

Systematic Analysis of Carotenogenesis in Microalgae for Model-Based Process Design

Dissertation

zur Erlangung des akademischen Grades

**Doktoringenieur
(Dr.-Ing.)**

von: Dipl.-Ing. Melanie Facht
geb. am: 2. Dezember 1986
in: Leisnig

genehmigt durch die Fakultät für Verfahrens- und Systemtechnik
der Otto-von-Guericke-Universität Magdeburg

Betreuer: Prof. Dr.-Ing. Kai Sundmacher
Gutachter: Prof. Dr. rer. nat. Thomas Bley
Prof. Dr. rer. nat. Jürgen Polle

eingereicht am: 31. März 2017
Promotionskolloquium am: 19. Juni 2017

Abstract

The topic of this thesis belongs to the broad field of algal biotechnology. This thesis presents a holistic approach for the analysis, optimization and design of microalgal bioprocesses from the systems engineering point of view. This is motivated by the fact that engineering of biosystems is accompanied by many hurdles in the biological and experimental field due to limited mechanistic knowledge and their inherent variability and complexity. The experimental foundations of this work were accelerated by recent advances in systems biology that led to new accurate and quantitative experimental techniques for the characterization of biosystems on the cellular level. A synergistic approach facilitating the combination of experimental and mathematical methods will provide a systems-level understanding of the microalgal metabolism under fluctuating environmental conditions and thereby drive the development of sustainable and economically-feasible phototrophic processes.

This thesis presents a systematic methodological framework for analysis and design of microalgal bioprocesses illustrated by the example of β -carotene production in *Dunaliella salina* in a lab-scale photobioreactor setup. For this purpose, an integrative approach is used that applies sophisticated experimental methods of systems biology to microalgal biosystems to predict how they change over time under varying input conditions. The approach combines flow cytometry, pulse amplitude modulation (PAM) fluorometry and fourier transform infrared (FTIR) spectroscopy with classical biochemical methods to enable a coherent view on the metabolism during the adaptational stress response of *Dunaliella salina* under carotenogenic conditions. It is shown that the approach is able to identify critical process parameters such as cell vitality and can provide implications for the optimal harvesting time point based on productivity and culture state.

In the next step, the experimental data is used to formulate mathematical models on various descriptive scales. First, a dynamic-kinetic reactor model is formulated that covers the effects of light and nutrient availability on biomass growth, internal nutrient status and pigment fraction in the biomass. A profile likelihood analysis is performed to ensure the identifiability of the model parameters and to point out targets for model reduction. The predictivity of the proposed model is proven by validation against independently conducted experiments under different cultivation conditions.

Second, the kinetic parameters obtained from the dynamic-kinetic growth model are used to formulate a dynamic flux balance analysis (DFBA) model that allows for predicting intracellular metabolites by incorporating biological knowledge. It is shown that the DFBA model is predictive and several model-based process strategies in fed-batch and continuous operation mode with the objective to maximize β -carotene productivity are suggested and validated experimentally. In this setup, the model-based design outperforms the classical batch process significantly in terms of biomass and β -carotene productivity (+187 % and +36 % for the fed-batch and +1120 % and +849 % for the continuous process).

Furthermore, the applicability of the interdisciplinary workflow composed of experiments and mathematical modeling is applied to *Dunaliella parva* to investigate the interspecies variability between the two close relatives in the *Dunaliella* genus. The results of the experimental and computational investigations indicate significant vari-

ability between *Dunaliella salina* and *Dunaliella parva* in terms of morphological differences, the biomass and β -carotene productivity as well as differences in photoacclimation and photoinhibition.

The integrative work flow of systematic experiments and predictive mathematical models is shown to be an effective approach to better apprehend for complexity of microalgal metabolism under dynamically changing environmental conditions leading to a progressive improvement of phototrophic bioprocesses.

Zusammenfassung

In der vorliegenden Arbeit wird ein hollistischer Ansatz für die Analyse, die Optimierung und das Design von mikroalgalen Bioprozessen aus der ingenieurwissenschaftlichen Perspektive präsentiert. Diese Vorgehensweise wird durch die Tatsache motiviert, dass die Optimierung von Biosystemen durch fehlendes mechanistisches Wissen, die inhärente Variabilität und Komplexität sowie von vielen biologischen und experimentellen Hürden beeinträchtigt wird. Dank jüngst erzielter methodischer Fortschritte in der quantitativen experimentellen Systembiologie werden neue Möglichkeiten für die akurate Analyse und Charakterisierung von Biosystemen auf der zellulären Ebene eröffnet. Das synergetische Konzept, welches experimentelle und mathematische Methoden kombiniert, führt zu einem tiefgreifenden Verständnis zellulärer Prozesse auf der Systemebene.

In dieser Arbeit wird die Herangehensweise für die Analyse und das Design von photosynthetischen Bioprozessen genutzt, welches am Beispiel der β -Carotin-Produktion in *Dunaliella salina* in einem Laborphotobioreaktor illustriert wird. Zu diesem Zweck wird ein systematisch, methodischer Ansatz verwendet, welcher anspruchsvolle experimentelle Methoden der Systembiologie auf mikroalgale Biosysteme anwendet, um deren dynamisches Verhalten unter fluktuierenden Umweltbedingungen zu untersuchen. Diese Methodik verbindet Durchflusszytometrie, Pulsamplitudenmodulation (PAM) und Fourier-Transform-Infrarotspektrometrie (FTIR-Spektrometrie) mit klassischen biochemischen Verfahren, die eine kohärente Sicht auf metabolische Prozesse während der adaptiven Stressantwort von *Dunaliella salina* unter carotino-genen Bedingungen ermöglichen. Es wird demonstriert, dass mit Hilfe dieses Verfahrens kritische Prozessparameter wie z.B. Zellvitalität überwacht werden können, um somit wichtige Indikatoren für die Bestimmung von optimalen Erntezeitpunkten basierend auf Produktivität und Kulturstatus zu liefern.

Im nächsten Schritt werden die experimentellen Daten genutzt um mathematische Modelle verschiedener Größenordnungen zu formulieren. Dafür wird zunächst ein dynamisch-kinetisches Wachstumsmodell präsentiert, welches den Effekt an veränderlichen Licht- und Nährstoffbedingungen auf das Biomassewachstum, den intrazellulären Nutrientenstatus und den Pigmentgehalt in der Biomasse beschreibt. Weiterhin liefert eine Profile-Likelihood-Analyse wichtige Anhaltspunkte über die Identifizierbarkeit der Modellparameter und zeigt damit auch potentielle Ziele für Modellreduktion auf. Die Prädiktivität des Modells wird durch unabhängige Experimente mit unterschiedlichen Kultivierungsbedingungen validiert.

Basierend auf den Parameterwerten des dynamisch-kinetischen Modells wird nachfolgend ein metabolisches Modell für dynamische Flussbilanzanalyse (DFBA) formuliert, welches durch die Einbindung von biologischem Wissen auch intrazelluläre Metabolitkonzentrationen vorhersagen kann. Es wird demonstriert, dass das DFBA-Modell einen prädiktiven Charakter aufweist und sowohl modellbasierte Prozessführungsstrategien für den Fed-Batch als auch für den kontinuierlichen Betrieb bei maximaler β -Carotin-Produktivität experimentell validiert werden konnten. In der modellbasierten Versuchsanordnung konnte sowohl der Fed-Batch-Prozess als auch die kontinuierlichen Kultivierungen signifikant höhere Biomasse- und β -Carotin-Produktivitäten erzielen (+187 % und +36 % für den Fed-Batch sowie +1120 % und +849 % für die kontinuierliche Kultivierung).

Desweiteren wird die Anwendbarkeit der interdisziplinären Vorgehensweise von Experimenten und Modellierung auf die Untersuchung der interspezies-spezifische Variabilität zwischen *Dunaliella salina* und der nah verwandeten Art *Dunaliella parva* demonstriert. Die Ergebnisse der experimentellen und theoretischen Untersuchungen zeigen, dass trotz der nahen Verwandtschaft der Organismen, eine große interspezies-spezifische Variabilität, vor allem im Bezug auf morphologische Unterschiede, Biomasse- und β -Carotin-Produktivität sowie Photoakklimierung und Photoinhibition auftritt.

Der integrative Ansatz aus systematischen Experimenten und prädiktiven mathematischen Modellen wird als effektives Werkzeug genutzt um die Komplexität metabolischer Prozesse in photosynthetischen Mikroorganismen unter fluktuierenden Umweltbedingungen besser zu erfassen, was schließlich zu einer schrittweisen Verbesserung von phototrophen Bioprozessen führt.

Acknowledgements

This thesis has been carried out from July 2011 until December 2016 in the Max Planck Institute for Dynamics of Complex Technical Systems in Magdeburg.

First and foremost, I would like to express my gratitude to Prof. Dr.-Ing. Kai Sundmacher for giving me the opportunity to write my thesis in his research group. I am very grateful for his guidance, the continuous support and trust as well as the scientific freedom in my project. My special thanks goes to Dr. Liisa Rihko-Struckmann for all the time spent on the supervision of my thesis and for her readiness for scientific discussion.

I am very grateful to Prof. Jürgen Polle for supporting this project. He did not only provide genetic information for *Dunaliella salina* but also takes the effort of travelling to Germany for examining this thesis. Also many thanks to Prof. Thomas Bley for accepting the invitation to act as a referee.

This work has also benefited from contributions of several lab technicians, engineers and students, which I was allowed to supervise. I owe many thanks to Saskia Nickel, Anne Christin Reichelt, Bianka Stein, Markus Ikert, Patrick Siegmund and Torsten Schröder for their excellent technical assistance and the nice working atmosphere. In these lines, I would like to thank the mechanical and electric workshop members Detlef Franz, Stefan Hildebrandt, Steve Haltenhof, Klaus-Dieter Stoll, Reiner Könning and Martin Stengel. I extend my thanks to the bachelor and master students Tobias Fries, Markus Janasch, Joel Thormeier, Jeanett Lärm, Steffi Gladebeck and Isabel Harriehausen for their support and enthusiasm. It was a pleasure to work with all of you.

Much gratitude to Kristin Pirwitz and Robert Flassig. I do not only value the helpful discussions, your continuous support and shared knowledge, but also the great moments we had working together. I am very grateful for the time I could spend with my colleagues and friends from the Max Planck Institute for Dynamics of Complex Technical Systems and Otto-von-Guericke University Magdeburg. In particular I want to mention Claudia Bednarz, Astrid and Boris Bensmann, Christoph Hertel, Florian Karst and Sebastian Kirsch.

Finally, I would like to express my gratitude to my family and friends for your motivation, support, trust and love. Special thanks goes to a very special person in my life who contributed in making this work possible. Thank you André for your patience, encouragement and love during these years.

There are many other persons, unfortunately too many to mention, who supported me during the time as a PhD student. Thank you all.

Preface

Several publications were prepared in the course of this thesis and are therefore incorporated in the manuscript. The chapters, which contain to some extent parts of these publications are listed in the following. In addition, the contributions of several students are mentioned here to acknowledge their support during the experimental and theoretical work of the present thesis.

- The experimental and theoretical methods used in this thesis are summarized in **Chapter 5** and were partly taken from Fachet et al. (2014), Fachet et al. (2016) and Flassig et al. (2016).
- **Chapter 6** deals with the experimental characterization of *Dunaliella salina* during the abiotic stress response. The methodological approach is partly taken from Fachet et al. (2016). However, the cultivation setup and the experimental data obtained is different from the aforementioned publication. Experimental support for the reactor operation and the optimization of the flow cytometric staining procedure was provided by Tobias Fries and Markus Janasch during their Bachelor theses. The FTIR measurements have been optimized by Maria Hentrich and Isabel Harriehausen during a research project and a Bachelor thesis.
- The dynamic-kinetic growth model for *Dunaliella salina* presented in **Chapter 7** is a modification of the equation system published in Fachet et al. (2014). The simulation and the profile likelihood analysis was conducted as described in Fachet et al. (2014). However, the equations contain minor modifications and the experimental data as well as the simulation results differ from the published version.
- In **Chapter 8**, the dynamic flux balance model for *Dunaliella salina* is introduced. The work flow and the majority of the model structure is taken from Flassig et al. (2016). If applicable, the values for kinetic parameters were set to the estimates obtained in **Chapter 7**. As already stated above, the equations contain minor modifications and the experimental data as well as the simulation results differ from the published version. Support in the implementation and the simulations was provided by Steffi Gladebeck in her Master thesis.
- In **Chapter 9**, an interspecies comparison between *Dunaliella salina* and *Dunaliella parva* is presented. The applicability of the interdisciplinary work flow composed of experiments and mathematical modeling as presented in Chapter 6 and 7 is applied to *Dunaliella parva* by using experimental data already published in Fachet et al. (2016) and submitted as Fachet et al. (2017).

M. Fachet, R. J. Flassig, L. Rihko-Struckmann, K. Sundmacher: A dynamic growth model of *Dunaliella salina*: Parameter identification and profile likelihood analysis, *Bioresource Technology*, 2014, 173C:21-31.

M. Fachet, D. Hermsdorf, L. Rihko-Struckmann, K. Sundmacher: Flow cytometry enables dynamic tracking of algal stress response: A case study using carotenogenesis in *Dunaliella salina*, *Algal Research*, 2016, 13:227-234.

R. J. Flassig[†], **M. Facht**[†], K. Höffner[†], P. I. Barton, K. Sundmacher: Dynamic flux balance modeling to increase the production of high-value compounds in green microalgae, *Biotechnology for Biofuels*, 2016, 9:165.

[†] Authors contributed equally.

M. Facht, R. J. Flassig, L. Rihko-Struckmann, K. Sundmacher: Carotenoid Production Process using Green Microalgae of the *Dunaliella* Genus: Model-Based Analysis of Interspecies Variability, *accepted by Industrial & Engineering Chemistry Research*, 2017.

Contents

Abstract	iv
Zusammenfassung	vi
Acknowledgements	vii
Preface	x
Notation	xv
Abbreviations	xvii
1. Introduction	1
1.1. Motivation	1
1.2. Aim of this work	2
2. Phototrophic pigment production	5
2.1. Carotenoid biosynthesis in photosynthetic organisms	5
2.2. Photoacclimation and photoinhibition	7
2.3. Carotenoid production in photosynthetic microorganisms	8
2.4. <i>Dunaliella salina</i> as a producer of natural β -carotene	9
3. Systematic analysis of microalgal metabolism	13
3.1. Flow cytometry	14
3.2. Pulse amplitude modulation (PAM)	16
3.3. Fourier transform infrared (FTIR) spectroscopy	18
4. Modeling of microalgal metabolism	21
4.1. Microalgal metabolism	21
4.2. Reconstruction of metabolic networks	22
4.3. Stoichiometric modeling frameworks	24
4.4. Dynamic-kinetic modeling frameworks	27
4.4.1. Macroscopic bioreactor modeling	27
4.4.2. Dynamic flux balance analysis	29
5. Experimental methods	33
5.1. Strain, growth medium and pre-cultivation	33
5.2. Cultivation experiments in flat-plate photobioreactors	33

5.3. Dry weight determination	34
5.4. Carbon and nitrogen fraction in the biomass	35
5.5. Ion chromatography	35
5.6. Determination of chlorophyll and carotenoid content	35
5.7. Determination of pigment composition using HPLC	36
5.8. Calculation of the optical cross section of chlorophyll <i>a</i>	37
5.9. Pulse amplitude modulation (PAM) fluorometry	37
5.10. Flow cytometric analysis	37
5.11. Analysis of biomass composition using FTIR spectroscopy	38
5.12. Analysis of biomass composition using biochemical assays	40
5.13. Calculation of biomass and β -carotene yield on absorbed light	41
6. Analysis of abiotic stress response during carotenogenesis	43
6.1. Flow cytometric characterization of the cell population	43
6.1.1. Cell growth	44
6.1.2. Abiotic stress related adaptation of pigment content	45
6.1.3. Relationship between carotenoid accumulation and granularity	47
6.2. Biotechnological parameters	47
6.3. Photosynthetic performance	49
6.3.1. Effective PSII quantum yield	49
6.3.2. Electron transport rate	49
6.3.3. Photosynthetic capacities under abiotic stress conditions	51
6.4. Macromolecular biomass composition	54
6.4.1. Optimization of FTIR spectroscopy for composition analysis	54
6.4.2. FTIR for relative macromolecular changes under abiotic stress	56
6.4.3. Comparison with conventional biochemical methods	57
7. Dynamic-kinetic modeling	59
7.1. Model formulation	60
7.1.1. Light attenuation in the photobioreactor	60
7.1.2. Nitrogen uptake rate	61
7.1.3. β -carotene synthesis rate	61
7.1.4. Photosynthesis rate	62
7.1.5. Growth rate	62
7.1.6. Profile likelihood analysis of model parameters	64
7.2. Determination of biomass-specific parameters	65
7.3. Parameter estimation	66
7.3.1. Biomass growth under fluctuating light and nutrient conditions	68
7.3.2. Extracellular nitrogen uptake	69
7.3.3. β -carotene fraction in the biomass	69
7.3.4. Total chlorophyll fraction in the biomass	69
7.4. Model predictions	69
7.4.1. Nitrogen cell quota and the nitrogen uptake rate	70
7.5. Model validation	71
7.6. Identifiability analysis using the profile likelihood	72
8. Dynamic flux balance analysis	75
8.1. Metabolic network analysis of the central carbon metabolism	76
8.1.1. Recent advances in genome sequencing of <i>D. salina</i>	76

8.1.2.	Comparison of enzymes in the carbon core metabolisms	77
8.2.	Dynamic flux balance model	80
8.2.1.	Flux balance model	81
8.2.2.	Exchange fluxes	81
8.2.3.	Dynamic photobioreactor model	83
8.2.4.	Model simulation	85
8.2.5.	Model validation	88
8.2.6.	Model-based optimization for fed-batch operation	88
8.2.7.	Model-based optimization for continuous operation mode	92
9.	Interspecies variations in the genus <i>Dunaliella</i>	97
9.1.	Strain identification of <i>D. salina</i> and <i>D. parva</i>	98
9.2.	Experimental analysis of interspecies variability	98
9.2.1.	Morphological variability between <i>D. salina</i> and <i>D. parva</i>	98
9.2.2.	Biotechnological parameters for <i>D. parva</i> under abiotic stress	99
9.2.3.	Photosynthetic performance of <i>D. parva</i>	99
9.2.4.	Correlation matrix for measured features of <i>D. salina</i> and <i>D. parva</i>	100
9.3.	Dynamic-kinetic growth model for <i>D. parva</i>	101
10.	Summary, Conclusion and Outlook	107
10.1.	Summary	107
10.2.	Conclusion	109
10.3.	Outlook	110
A.	Supplementary information for experimental analyses	113
A.1.	Description of experimental information according to MIFlowCyt	113
A.1.1.	Experimental overview	113
A.1.1.1.	Purpose	113
A.1.1.2.	Keywords	113
A.1.1.3.	Experiment Variables	113
A.1.1.4.	Organization	113
A.1.1.5.	Primary contact	114
A.1.2.	Quality control measures	114
A.1.3.	Flow sample	114
A.1.3.1.	Biological sample	114
A.1.3.2.	Sample characteristics	114
A.1.3.3.	Sample treatment description	114
A.1.3.4.	Fluorescence reagent description	114
A.1.3.5.	Characteristics being measured	114
A.1.4.	Instrument details	115
A.1.4.1.	Instrument manufacturer	115
A.1.4.2.	Instrument model	115
A.1.4.3.	Instrument configuration and settings	115
A.1.5.	Data analysis	116
A.1.5.1.	List-mode data files	116
A.1.5.2.	Data transformation details	116
A.1.5.3.	Gating details	116
A.2.	Supplementary information for FTIR analysis	118

B. Supplementary information for profile likelihood analysis	119
B.1. List of model parameters	119
B.2. Model equations for the dynamic-kinetic growth model of <i>D. parva</i> . . .	121
B.3. Interdependencies between model parameters	125
C. Supplementary information for metabolic network reconstruction	135
C.1. List of pathways and reaction	135
C.2. Metabolic network map of central carbon metabolism	144
Bibliography	145
List of Figures	160
List of Tables	162
Publications and statements on authorship	163
Supervision of bachelor and master theses	167
Curriculum Vitae	169

Notation

Greek symbols

γ_{\max}	Max. intracell. chlorophyll to nitrate ratio	$\text{g Chl g}^{-1} \text{N}$
θ_{eff}	Photon efficiency	-
λ	Duration of the <i>lag</i> phase	d
μ	Specific growth rate	d^{-1}
μ_{\max}	Maximal growth rate	d^{-1}
μ_{net}	Net specific growth rate	d^{-1}
$\bar{\nu}$	Wavenumber	cm^{-1}
ρ_{Chl}	Chlorophyll density in the reactor	g Chl m^{-3}
$\rho_{\text{N,ext}}$	Extracellular nitrogen density	g N m^{-3}
ρ_{X}	Biomass density on dry weight basis	g dw m^{-3}
Φ	Description of the <i>lag</i> phase	-
$\Phi_{\text{PSII,eff}}$	Effective quantum yield of PSII	-
$\Phi_{\text{PSII,max}}$	Maximum quantum efficiency of PSII	-
ω_{C}	Carbon content of biomass	$\text{g C g}^{-1} \text{dw}$
ω_{Chl}	Chlorophyll fraction of the biomass	$\text{g Chl g}^{-1} \text{dw}$
$\omega_{\text{Chl,N}}$	Chlorophyll-nitrogen ratio in the biomass	$\text{g Chl g}^{-1} \text{N}$
ω_{N}	Cell quota for nitrogen	$\text{g N g}^{-1} \text{dw}$
$\omega_{\text{N,crit}}$	Crit. nitrogen cell quota for β -carotene synthesis	$\text{g N g}^{-1} \text{dw}$
$\omega_{\text{N,max}}$	Maximal cell quota for nitrogen	$\text{g N g}^{-1} \text{dw}$
$\omega_{\text{N,min}}$	Minimal cell quota for nitrogen	$\text{g N g}^{-1} \text{dw}$

Latin symbols

a^*	Optical cross section of chlorophyll <i>a</i>	$\text{m}^2 \text{g}^{-1} \text{Chl}$
a	Absorption coefficient of chlorophyll	$\text{m}^2 \text{g}^{-1} \text{Chl}$
b	Absorption coefficient of β -carotene	$\text{m}^2 \text{g}^{-1} \text{Car}$
c	Backscattering coefficient of the biomass	m^{-1}
\bar{E}	Average photon flux density in the reactor	$\text{mol photons m}^{-2} \text{d}^{-1}$
E_0	Photon flux density at the reactor surface	$\text{mol photons m}^{-2} \text{d}^{-1}$
E_{abs}	Absorbed photon flux	$\text{mol photons d}^{-1}$
$E_{\text{car,crit}}$	Crit. light int. for β -carotene synthesis	$\mu\text{mol photons g}^{-1} \text{dw h}^{-1}$
\bar{E}_{sat}	Saturation light int. for chlorophyll to nitrate ratio	$\mu\text{mol photons m}^{-2} \text{s}^{-1}$
E_{out}	Transmitted photon flux density	$\text{mol photons m}^{-2} \text{d}^{-1}$

$E_{X,dw}$	Light intensity per biomass	$\text{mol photons m}^{-2} \text{d}^{-1} \text{g}^{-1} \text{dw}$
ETR	Relative electron transport rate	$\mu\text{mol electrons m}^{-2} \text{s}^{-1}$
F'	Light-adapted fluorescence steady-state	-
F_0	Minimal fluorescence of dark-adapted samples	-
F'_0	Minimal fluorescence of light-adapted samples	-
F_m	Maximal fluorescence of dark-adapted samples	-
F'_m	Maximal fluorescence of light-adapted samples	-
F_v	Variable fluorescence of dark-adapted samples	-
F'_v	Variable fluorescence of light-adapted samples	-
k	Hill coefficient	-
$K_{s,E}$	Half saturation coeff. for photosynthetic growth	$\text{mol photons m g}^{-1} \text{dw d}^{-1}$
$K_{i,\text{Chl},N}$	Inhibition coeff. for chlorophyll to nitrate ratio	$\mu\text{mol photons m}^{-2} \text{s}^{-1}$
$K_{i,E}$	Light inhibition coeff. for photosynthetic growth	$\text{mol photons m g}^{-1} \text{dw d}^{-1}$
$K_{s,N}$	Halfsaturation coeff. for nitrogen uptake	g N m^{-3}
ngam	Non-growth associated maintenance	$\text{mmol g}^{-1} \text{dw h}^{-1}$
NPQ	Non-photochemical quenching	-
$r_{\text{car},E}$	Light stress-induced β -carotene synthesis rate	$\text{g Car g}^{-1} \text{dw d}^{-1}$
$r_{\text{car},N}$	Nutrient stress-induced β -carotene synthesis rate	$\text{g Car g}^{-1} \text{dw d}^{-1}$
r_N	Nitrogen uptake rate	$\text{g N g}^{-1} \text{dw d}^{-1}$
$r_{N,\text{max}}$	Maximal nitrogen uptake rate	$\text{g N g}^{-1} \text{dw d}^{-1}$
r_P	Photosynthesis rate	$\text{g C g}^{-1} \text{Chl d}^{-1}$
$r_{P,\text{max}}$	Maximal theoretical photosynthesis rate	$\text{g C g}^{-1} \text{Chl d}^{-1}$
r_R	Respiration rate	d^{-1}
S_{PBR}	Illuminated reactor surface	m^2
$v_{\text{car},E}$	Light stress-induced β -carotene synthesis rate	$\text{mmol g}^{-1} \text{dw h}^{-1}$
$v_{\text{car},N}$	Nutrient stress-induced β -carotene synthesis rate	$\text{mmol g}^{-1} \text{dw h}^{-1}$
$v_{\text{NO}_3,\text{max}}$	Max. nitrogen uptake rate	$\text{g NO}_3 \text{g}^{-1} \text{dw h}^{-1} \text{L}^{-1}$
$v_{\text{NO}_3,\text{met},\text{max}}$	Max. nitrogen assimilation flux	$\text{mmol g}^{-1} \text{dw h}^{-1}$
V_{PBR}	Reactor volume	m^3
$Y_{X,E}$	Biomass yield on light energy	$\text{g dw mol}^{-1} \text{photons}$
z	Thickness of the reactor	m

Abbreviations

AU	Arbitrary units
BSA	Bovine serum albumin
CAM	Crassulacean acid metabolism
CCAP	Culture Collection of Algae and Protozoa
DAD	Diode array detector
DFBA	Dynamic flux balance analysis
DMAPP	Dimethylallyl pyrophosphate
DRUM	Dynamic reduction of unbalanced metabolism
EC	Enzyme commission
EFM	Elementary flux mode
ETR	Electron transport rate
FACS	Fluorescence-activated cell sorting
FBA	Flux balance analysis
FC	Flow cytometry
FCA	Flux coupling analysis
FLD	Fluorescence detector
FSC	Forward scatter
FTIR	Fourier transform infrared spectroscopy
FVA	Flux variance analysis
GC	Gas chromatography
GDS	Gene deletion studies
GGPP	Geranylgeranyl pyrophosphate
GPP	Geranyl pyrophosphate
HL	High light
HL-ND	High light and nitrogen-depleted
HPLC	High performance liquid chromatography
IC	Ion chromatography
IPP	Isopentyl pyrophosphate
KEGG	Kyoto Encyclopedia of Genes and Genomes
LED	Light-emitting diode
LL	Low light
LL-ND	Low light and nitrogen depletion
LL-NL	Low light and nitrogen limitation
LP	Linear program
MEP	Methylerythriol phosphate
NPQ	Non-photochemical quenching

OED	Optimal experimental design
ODE	Ordinary differential equation
PAM	Pulse amplitude modulation
PAR	Photosynthetically active radiation
PBR	Photobioreactor
PCA	Principle component analysis
PL	Profile likelihood
PLS	Partial least square
PPP	Pentose phosphate pathyway
PSII	Photosystem II
PSY	Phytene synthase
RFU	Relative fluorescence units
ROS	Reactive oxygen species
SSC	Side scatter
TAG	Triacylglyceride
TCA	Citric acid cycle

Chapter 1

Introduction

1.1 Motivation

Microalgae are a diverse group of phylogenetically unrelated photosynthetic microorganisms and are among the most important primary producers of organic matter on the planet. The exact number of algal species remains uncertain, but estimates vary between 30000 to several million species (Guiry, 2012). The diversity of microalgae results from an adaptation to the diverse habitats they are found in. Microalgae have evolved to tolerate a wide range of environmental conditions and consequently have proven to be a rich source of genetic and chemical diversity, comprising among others green algae (Chlorophyta), yellow-green algae (Xanthophyta), golden algae (Chrysophyta) and red algae (Rhodophyta) (Andersen, 1992). Some microalgal species show a remarkable degree of phenotypic plasticity to extend their tolerance against a wide range of environmental conditions, while other species specifically adapted to a smaller range (Stengel et al., 2011). Microalgal habitats range from freshwater (e.g.: *Chlorella vulgaris* (Mallick et al., 2011)) to hypersaline water (e.g. *Dunaliella salina* (Oren, 2010)), at negative temperatures (e.g. *Chlamydomonas nivalis* (Morgan-Kiss et al., 2006)), above 70 °C (e.g.: *Synechococcus lividus* (Meeks and Castenho, 1971)), at pH lower than 2 (*Dunaliella acidophila* (Pick, 1999)) to alkaline conditions above pH 10 (e.g. *Arthrospira platensis* (Sanchez-Luna et al., 2007))(Baroukh, 2014).

Currently, a minority of roughly 20 microalgal species has been used for production of biomass and high-value products demonstrating a large deficit of knowledge to fully exploit their potential (Barra et al., 2014). They have the ability to synthesize a remarkable amount of bioactive compounds of industrial relevance such as carotenoids, poly-unsaturated fatty acids, phytosterols, industrial enzymes and amino acids (Gimpel et al., 2015). In addition, their capacity to grow in saline water as well as wastewater is particularly interesting, since they do not necessarily compete with agriculture neither for land nor for water.

Although microalgae are a promising feedstocks for light driven biosynthesis of commodities and high-value products, advances in reactor optimization and strain engineering are needed to achieve profitability on industrial scale. Techno-economic analyzes have revealed that the three main influencing factors that significantly contribute to the overall production costs of microalgal metabolites are i) product con-

tent, ii) growth rate and iii) biomass density (Davis et al., 2011). These biological outputs are determined by a number of constraints including light intensity, nutrient supply and the unique metabolism of individual species. Improvements in all these areas are major drivers to create economically feasible and sustainable bioprocesses with photosynthetic microorganisms.

In order to identify the crucial factors influencing the profitability of microalgal processes, accurate measurement of a wide range of physiological parameters in dependence of the present input conditions (e.g. light and nutrients) are required. This goal will be supported by the recent advances in spectroscopic and fluorescent measurement techniques which aim at characterizing (among others) biomass density, content and composition of high value products and metabolic indicators for the cellular stress response. Although the potential productivities of phototrophic processes seem promising, many optimization steps are still necessary to achieve sustainable production and compatible prices at commercial scale (Hannon et al., 2010; Gangl et al., 2015). Mathematical modeling is beneficial for understanding the nonlinear behavior and organization of complex biosystems. Besides, mathematical models support rational process design and optimization due to their ability to predict unknown or non-measurable parameters, productivities in terms of biomass and high-value products and their influence on system performance and profitability.

1.2 Aim of this work

The understanding of the complex interaction between microalgal metabolism in the course of dynamically changing environmental conditions is an important prerequisite for the knowledge-based improvement of phototrophic bioprocesses. In the present thesis, this task is addressed by a new interdisciplinary approach for the systematic analysis and optimization of microalgal processes. The approach combines detailed experimental investigations with mathematical modeling on different levels of detail. As a model organism to demonstrate the applicability of the aforementioned approach, the halotolerant green microalga and commercial β -carotene producer *D. salina* is considered.

Within this approach advanced spectroscopic and fluorometric methods were applied together with fluorescent and colorimetric indicators to systematically track the morphological and metabolic changes of *Dunaliella* during carotenogenesis under various environmental conditions and in a dynamic manner. These properties were linked with biomass characteristics and economically relevant parameters for biomass and high-value products such as final densities, yields on absorbed light and volumetric productivities. Furthermore, mathematical modeling on different descriptive levels (macroscopic and metabolic models) were formulated and their predictions were validated against experimental data. Together, the combination of these approaches demonstrated that predictive mathematical models are powerful tools to improve bioprocesses significantly and provide new production strategies for photosynthetic organisms. The applicability of the phototrophic process characterization and design methodology has been demonstrated for carotenoid production in *D. salina* but has a large potential for application to uncharacterized algal strains and their products of

interest. The experimental and theoretical methods applied in this work are schematically illustrated in Fig. 1.1.

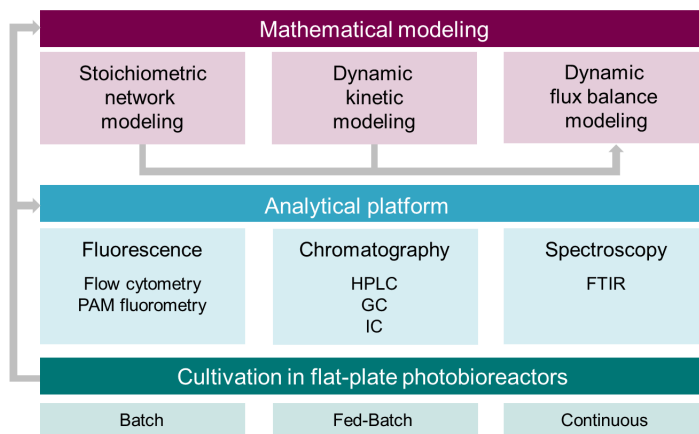


Figure 1.1.: Schematic outline of the thesis. The lower panel depicts the cultivations in flat-plate reactors as a basis to carry out experiments under reproducible conditions. The reactors were operated in different operation modes such as batch, fed-batch and continuous mode. The biomass obtained in this cultivations is subjected to various advanced experimental techniques for monitoring the abiotic stress response on different cellular levels (as illustrated in the middle panel). The experimental data obtained in the previous two levels were used to find a mathematical representation of the system on different descriptonal scales.

The thesis consists of ten Chapters. Chapter 2 introduces the biological foundations of pigment accumulation in photosynthetic organisms. Starting with the biosynthesis of carotenoids in green microalgae, the physiological role of photosynthetic pigments such as carotenoids and chlorophylls in photoprotection and energy dissipation is introduced. Moreover, the mechanisms of photosynthetic pigment acclimation under fluctuating light conditions are explained. With the biological fundamentals in mind, the most important producers of primary and secondary carotenoids are presented. The last part of Chapter 2 focuses on the morphology and physiology of *D. salina* and its unique ability to accumulate large amounts of β -carotene.

Chapter 3 presents an overview of the spectroscopic and fluorescent techniques to characterize microalgal metabolism during carotenogenesis. Of course, this is done in view of later applications. Therefore, the fundamentals and measuring principles of flow cytometry, pulse amplitude modulation (PAM) fluorometry and fourier transform infrared (FTIR) spectroscopy are introduced and their benefit for monitoring of phototrophic processes are discussed.

In Chapter 4, existing modeling frameworks for microorganisms are introduced. Due to the scope of this thesis, a special focus is laid on stoichiometric network models and dynamic-kinetic models based on ordinary differential equations. The mathematical representation of the system are shown as well as an extensive overview of recent contributions in this field especially with regard to microalgae is given. In the last part of the chapter, the concept of dynamic flux balance analysis is introduced, which combines the approaches of stoichiometric and dynamic-kinetic modeling.

The experimental methods used to analyze the microalgal metabolism are presented in Chapter 5.

Chapter 6 presents a systematic experimental investigation of the adaptational stress response of *D. salina* under carotenogenic conditions in batch cultivations. In particular, the influence of light and nutrients on growth, biomass composition and physiological parameters such as cell granularity is studied in a dynamic manner. The photosynthetic performance under abiotic stress is derived from maximum and effective quantum yield as well as non-photochemical quenching analyzed by PAM fluorometry. In addition, the applicability of FTIR spectroscopy for biomacromolecule composition analysis in *D. salina* is demonstrated.

In Chapter 7, a dynamic-kinetic reactor model is introduced which was formulated based on biological knowledge and the experimental data presented in Chapter 6. The application of mathematical modeling enables the determination of unknown kinetic parameters from the experimental data. Special attention was devoted to the analysis of parameter identifiability which is studied using the profile likelihood method. The proposed model is validated against independently conducted experiments under different cultivation conditions and verifiable predictions are given.

Chapter 8 illustrates the application of a metabolic network reconstruction to predict biomass composition using dynamic flux balance analysis (DFBA). The core idea of the approach, its assumptions and its justification are discussed. In addition, a metabolic network reconstruction of the central carbon metabolism of *D. salina* is presented based on genomic data. The accuracy of the model predictions is validated through independent experimental data followed by a subsequent model-based fed-batch optimization where the biomass and β -carotene density were increased by factors of about 2.5 and 2.1, respectively. In the last part of Chapter 8, two model-based continuous operation strategies with a fixed dilution rate D were predicted and experimentally validated. The continuous operation mode, where biomass and pigment content are in steady-state may lead to a major improvement in volumetric productivity due to the avoidance of the unproductive lag- and early exponential phase. The desired operation mode, where the dilution rate D equals the growth rate μ leads to a constant biomass and β -carotene density in steady-state and cannot be calculated on an empirical basis due to the complex interplay of light and nutrient stress on the growth rate μ . The experimental verification of the model-based continuous operation again led to a significantly improved biomass productivity by 3.3-fold and pigment productivity by 6-fold compared to the already optimized fed-batch operation.

Chapter 9 aims at a comparative evaluation between *D. salina* and a closely related organisms in the *Dunaliella* genus, namely *Dunaliella parva*. The interdisciplinary work flow composed of experiments and mathematical modeling as presented in Chapter 6 and 7 is applied to *D. parva* to demonstrate its applicability to other species in the *Dunaliella* genus. A special emphasis is placed on the morphological differences, the productivity in terms of biomass and β -carotene, the adaptational stress response as well as differences in photoacclimation and photoinhibition.

Finally, the thesis is summarized and concluded in Chapter 10. Furthermore, an outlook is given and future perspectives are discussed.

Chapter 2

Phototrophic pigment production

This chapter provides an overview about the physiological role of carotenoid pigments in light harvesting and photoprotection. Beside, the process of photoacclimation and their physiological relevance for optimal photosynthetic growth is explained. Furthermore, an overview about the most important commercial sources for microalgal carotenoids is given. This chapter is concluded by introducing the alga *D. salina* as a producer for β -carotene.

2.1 Carotenoid biosynthesis in photosynthetic organisms

Carotenoids are natural pigments belonging to the group of lipophilic isoprenoids. Most of the 600 carotenoid derivatives consist of 40 carbon atoms composed from eight isoprene units. Carotenoids can be divided into two groups: carotenes and xanthophylls. Carotenes (such as α -carotene and β -carotene) are pure hydrocarbons, whereas xanthophylls (such as lutein and zeaxanthin) contain additional oxygen atoms either as hydroxyl groups and/or by homolytic hydrogen substitution of carotenes or xanthophylls leading to the formation of epoxides (e.g. violaxanthin). Since carotenoid pigments primarily absorb light in the violet, blue and green wavelength region (400-550 nm,) their color ranges from yellow to red. Beside higher plants, some bacteria and fungi, all microalgae are capable of carotenoid biosynthesis. In general, carotenoid synthesis in photosynthetic organisms occur either via the cytosolic mevalonate pathway or the plastidial methylerythriol phosphate (MEP) pathway. However, there is no evidence that cytosolic mevalonate pathway is present in green microalgae (Lichtenthaler, 1999; Schwender et al., 2001).

The metabolites isopentyl pyrophosphate (IPP) and dimethylallyl pyrophosphate (DMAPP) are precursors for carotenoid synthesis in photosynthetic organisms. Initially, one molecule IPP and DMAPP are linked through a condensation reaction to form geranyl pyrophosphate (GPP). A further condensation reaction of two molecules IPP to GPP catalyzed by the enzyme geranylgeranyl pyrophosphate synthase leads to the formation of geranylgeranyl pyrophosphate (GGPP). GGPP is the building block for the synthesis of diterpenes (C₂₀). Subsequently, the formation of

phytoene catalyzed by the enzyme phytoene synthase (PSY) occurs through condensation of two GGPP molecules. Phytoene represents the precursor for synthesis of tetraterpenes (C₄₀) and is the first lipophilic compound in the carotenoid pathway. A sequence of desaturation reactions of phytoene results in the formation of ζ -carotene and lycopene. Subsequently, the carotenoid pathway splits into two branches. One branch leads to the formation of the yellow colored xanthophyll pigment lutein. The second branch leads to the formation of the orange-colored β -carotene. The enzymatic reaction converting β -carotene into zeaxanthin is catalyzed by β -carotene hydroxylase and is part of the violaxanthin cycle.

The violaxanthin cycle is a photoprotective mechanism that allows a reversible switch of the antenna of photosystem II (PSII) depending on the light conditions present. Under light limiting conditions PSII is in its light harvesting state. Consequently, violaxanthin is converted in a two-step de-epoxidation reaction to zeaxanthin with antheraxanthin being an intermediate (Jahns et al., 2009). Under over-saturating light conditions, PSII switches into a dissipative state where a reverse epoxidation reaction from violaxanthin to zeaxanthin is taking place. The two enzymes catalyzing this cycle are located on different sites of the thylakoid membrane. Violaxanthin de-epoxidase is present in the thylakoid lumen whereas zeaxanthin epoxidase is located in the chloroplast stroma. Furthermore, neoxanthin can be formed by an isomerization reaction from its precursor violaxanthin. The above mentioned pathways for carotenoid synthesis in microalgae have been studied intensively and a schematic representation is given in Fig. 2.1.

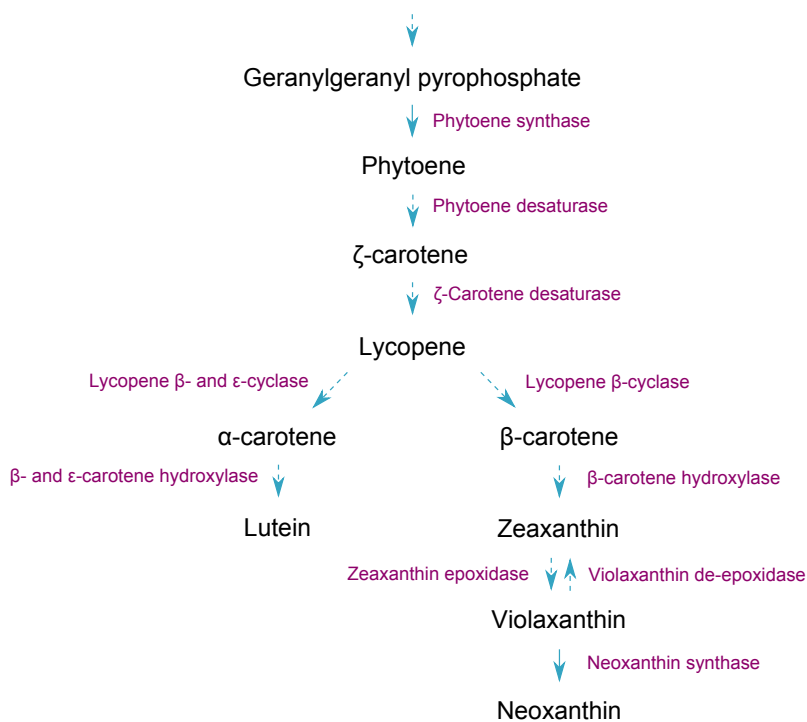


Figure 2.1.: Scheme of carotenoid biosynthesis pathway in microalgae. Direct (one-step) enzymatic reactions are depicted by bold arrows, whereas multi-step reactions with intermediate metabolites are depicted by dashed arrows. Adapted from Lamers et al. (2008) and Jin and Polle (2009).

The physiological functions of carotenoids are diverse and comprise accessory pigments for light harvesting, mediators of photosynthetic energy transfer and non-photochemical quenching as well as in the protection against photooxidative damage due to scavenging of reactive oxygen species (ROS) (reviewed in Mulders et al. (2014)). Due to their numerous conjugated double bonds, carotenoids are able to quench the triplet chlorophyll ($^3\text{Chl}^*$) and singlet oxygen ($^1\text{O}_2^*$) in the reaction center of photosystem II and in the antenna system (Krieger-Liszky, 2005). The photoprotective mechanism of action of carotenoids is illustrated in Fig. 2.2.

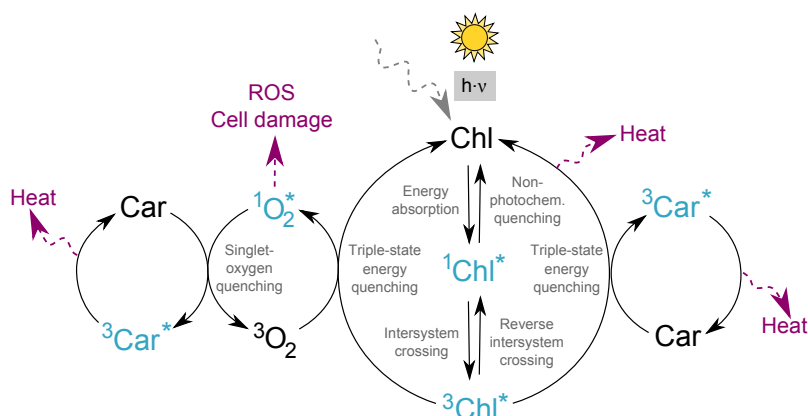


Figure 2.2.: Schematic overview of quenching mechanisms of carotenoid pigments. Excited states such as singlet oxygen ($^1\text{O}_2^*$), singlet chlorophyll ($^1\text{Chl}^*$) and triplet chlorophyll ($^3\text{Chl}^*$) are marked in blue. The specific mechanisms of action are colored in gray, whereas the cellular response and dissipation reactions are colored in purple. Adapted from Varela et al. (2015).

Carotenoid pigments can be divided into two subgroups, primary and secondary pigments, depending on their physiological role. Primary pigments are functionally and structurally related to the photosystem where they facilitate light harvesting as well as photoprotective roles due to quenching and scavenging mechanisms (see Fig. 2.2). In contrast, secondary pigments are neither functionally nor structurally bound to the photosynthetic apparatus and their photoprotective role results from a filtering mechanism preventing the formation of triplet chlorophyll ($^3\text{Chl}^*$) by absorbing oversaturating light. Since secondary pigments are not bound to the photosystem, they are usually accumulated in lipid globules in the interthylakoid space of the chloroplasts. According to the current state of knowledge, astaxanthin and β -carotene are the only known secondary carotenoids present in microalgae (Mulders et al., 2014).

2.2 Photoacclimation and photoinhibition

The light harvesting of all phototrophic algae is facilitated by chlorophylls (in the forms chlorophyll *a* and chlorophyll *b* present in Chlorophyta) and various accessory

pigments in the antenna complex which differ in a species-specific manner where a distinction is made between the presence phycobilins and carotenoids (Stengel et al., 2011). According to Stengel et al. (2011), all algal pigments can be classified based on their chemical structure as follows:

- Chlorophyll *a* and *b*: closed tetrapyrroles
- Phycobilipigments: open tetrapyrroles
- Carotenoids (carotenes and xanthophylls): isoprenoids with terminal cyclohexane rings.

Photoacclimation describes the phenotypic response of microalgae in which they adapt their photosynthetic pigment content to the particular light environment. Specifically, the number and size of the antenna complexes as well as the pigment composition in the antenna is adjusted to the present light conditions. Under optimal light conditions, all absorbed light is used for photochemistry and dissipating mechanisms are inactive. In this state, size of the antenna is large and mainly packed with chlorophylls and primary carotenoids. When the cell is exposed to over-saturating light conditions, the photosystem receive more light than required for photosynthesis. Consequently, the cell dissipates this energy as heat by emission as chlorophyll fluorescence. This process is referred to as non-photochemical quenching (NPQ), which protects the cell against oxidative damage from free radicals. In addition to the dissipating mechanisms, the cell adapts its pigment composition to the high light conditions. The pigment content in cells subjected to oversaturating light decreases to minimize light absorption and thereby photooxidation processes (MacIntyre et al., 2002). Specifically, the ratio of chlorophyll *a* to carbon is reduced by 60% compared to its maximal value. Beside, accessory pigments for light harvesting show the same tendencies (MacIntyre et al., 2002). Since chlorophyll *b* molecules are located on the outer part of the antenna complex, their decline is the initial step in pigment degradation. Chlorophyll *a* is the core pigment of the antenna complex but their content is also reduced in the course of exposure to over-saturating light. The light-induced damage of the photosystems is called photoinhibition and results in a decreasing photosynthetic efficiency. The photoinhibited reaction centers of PSII are continuously repaired via degradation and synthesis of the D1 protein. To reduce the damaging effect of high irradiance, the cell accumulates photoprotective pigments such as β -carotene as explained in Section 2.1.

2.3 Carotenoid production in photosynthetic microorganisms

The largest fraction of the current carotenoid production is manufactured by chemical synthesis of petroleum derivatives. Although synthetic carotenoids can be produced much cheaper compared to natural pigments, the consumer demand for natural pigments is rising (Wichuk et al., 2014). The global carotenoid market is expected to reach \$1.4 billion with an annual growth rate of 2.3% by 2018 (Research, Research). One main application area of carotenoids is the food and feed industry, where they are primarily used as colorants. Extensive studies have demonstrated a beneficial effect of carotenoids on health due to its anti-oxidant and anti-inflammatory proper-

ties (Bai et al., 2005; Choi et al., 2008; Xu et al., 2013), which has resulted in various applications of carotenoids for nutraceutical purposes. Beside the positive effects of carotenoids on human health, some studies also claimed that carotenoid treatment had no effect on the therapy of e.g. cardiovascular diseases (as reviewed in Zhang et al. (2014)). However, this outcome might be attributed to certain design aspects of the underlying clinical studies (Fassett and Coombes, 2012).

The pigment composition present in the organism depends on the metabolic pathways and their physiological role for adaption to the environmental conditions of the natural habitat. Table 2.1 summarizes several carotenoid-rich microalgal species with industrial relevance. For biotechnological applications, the amount of primary pigments in the biomass is usually too low to be economically feasible if considered as the main product. However, secondary carotenoids are present to a much higher extend compared to primary pigments and astaxanthin from *Haematococcus pluvialis* as well as β -carotene from *D. salina* are already produced at industrial scale. In addition to the species-specific pigment composition, advances in strain engineering, photobioreactor design and identification of metabolic pathways are required to further improve the organisms performance.

Table 2.1.: Carotenoid content of different carotenoid-rich microalgae. Adapted from Lamers et al. (2008).

Carotenoid	Strain	Carotenoid content (mg g ⁻¹ dw)	Reference
β -carotene	<i>Dunaliella salina</i>	100	Ben-Amotz et al. (1982)
Canthaxanthin	<i>Coelastrella striolata</i> var. <i>multistriata</i>	48	Abe et al. (2007)
Astaxanthin	<i>Haematococcus pluvialis</i>	77	Kang et al. (2007)
	<i>Chlorella zofingiensis</i>	6	Orosa et al. (2001)
Lutein	<i>Muriellopsis</i> sp.	8	Blanco et al. (2007)
	<i>Scenedesmus almeriensis</i>	6	Sanchez et al. (2008)

2.4 *Dunaliella salina* as a producer of natural β -carotene

The halotolerant green microalga *D. salina* is among the most important production organisms for natural β -carotene. Up to 10% of the total dry mass of *D. salina* can consist of β -carotene. The pigment is composed of eight isoprene units and eleven linearly arranged conjugated double bonds in the chemical structure form the light absorbing part of the β -carotene, also known as chromophore and causes its orange color. The accumulation of the pigment is an adaption upon the exposure to extreme environmental conditions such as high light intensity, high salinity and nutrient starvation as illustrated in Fig. 2.3. The overaccumulation of carotenoid pigments is due to a stress response which enables *Dunaliella* to survive in hypersaline environments. Therefore, hypersaline *Dunaliella* sp. occur in saline shallow lakes and evaporation ponds all over the world (Polle et al., 2009). Beside hypersaline species in the genus *Dunaliella* several euryhaline species of *Dunaliella* (e.g. *D. tertiolecta*, *D. primolecta*) have

been reported, which grow in marine water. However, only hypersaline species of the *Dunaliella* genus (e.g. *D. parva*, *D. viridis* and *D. salina*) play an important role in algal mass cultivation. Large scale facilities of *Dunaliella* for the production of β -carotene are operated in various countries (e.g. Australia, India, Israel, Spain, United States) (Ben-Amotz et al., 1991).

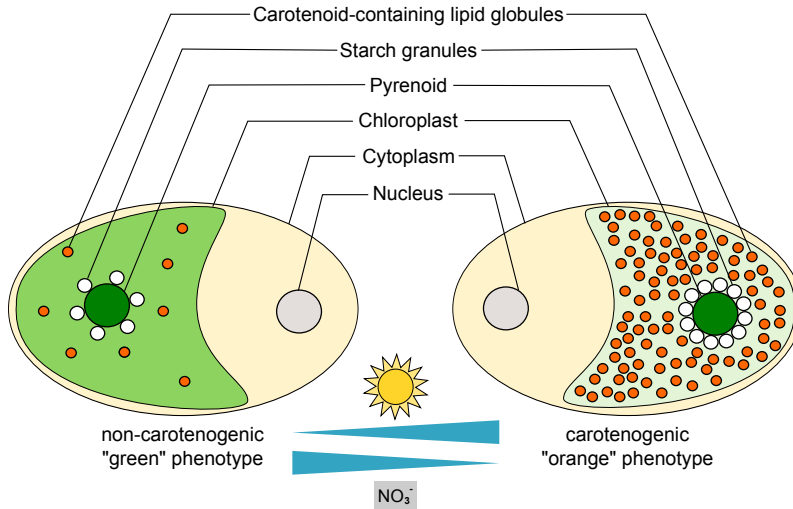


Figure 2.3.: Simplified representation of morphological changes in *D. salina* during carotenogenesis.

The cell shape of *Dunaliella* varies between ellipsoidal, ovoid, cylindrical and spherical with large differences in size (1-15 μm in length and 2-28 μm in width) (Polle et al., 2009). Hypersaline species of *Dunaliella* have the ability to survive in medium containing a wide range of NaCl concentrations from about 0.05 M to saturation (around 5.5 M) (Chen and Jiang, 2009). The optimal salinity for growth is considered to be in the range from 1.5 - 2 M NaCl (Vo and Tran, 2014).



Figure 2.4.: Microscopic pictures of carotenogenic (right) and non-carotenogenic (left) *D. salina* cells.

Even though, the overaccumulation of β -carotene in *D. salina* has been investigated extensively, only little is known about the cellular response and the regulatory mechanisms involved in the underlying adaptational stress response (Ben-Amotz et al., 1982; Lamers et al., 2010). Exposure of the cells to high irradiance is the main trigger

that induces photooxidative processes, which initiate the enrichment of photoprotective carotenoid pigments. The underlying photoprotective mechanisms of β -carotene are the prevention of oxidative damage by scavenging reactive oxygen species and the absorption of UV light, avoiding direct damage of cellular targets (Mulders et al., 2014). The overaccumulated β -carotene, which is mainly composed of the two isomers, 9-cis and all-trans, is stored in TAG-containing lipid globules in the interthylakoid space of the chloroplast (Ben-Amotz et al., 1982). Results from previous studies pointed out that TAG synthesis and β -carotene formation are interlinked, creating a metabolic sink avoiding end-product inhibition in the carotene biosynthesis pathway (Rabbani et al., 1998; Mendoza et al., 1999). This coincides with the fact, that massive carotene accumulation is enhanced with increasing abiotic stress, e.g. nutrient deprivation.

Thus, the ability to grow in hypersaline environments in combination with the high carotene content makes *Dunaliella* an excellent candidate for molecular farming of high value products. Since the impact of the abiotic stress response on biotechnological production parameters (such as volumetric biomass and carotene productivity) is not fully understood, further experimental and theoretical characterization are required to improve the process efficiency. These insights might also contribute to improvements in bioprocess development of other carotenogenic species.

Chapter 3

Systematic analysis of microalgal metabolism

A large variety of commercially interesting microalgal products, such as primary and secondary metabolites are nowadays produced in biotechnological processes (Koller et al., 2014). The recent advances in new analytical techniques for algal cell biology, which require only a minimal sample amount and enable fast preparation allow for a more detailed and comprehensive bioprocess characterization (Wagner et al., 2010; Havlik et al., 2013; Biller and Ross, 2014). A profound and extensive understanding of the process enables the determination of critical process parameters and set points, which strongly influence process stability and performance (Bohnen and Brück, 2013). Among other factors, the reactor setup, the nutrient composition in the growth medium and the environmental conditions, especially the light intensity, play the most important role to obtain a desired product content and quality. Unfavorable environmental conditions, such as high light intensity, high salinity or nutrient depletion can lead to metabolic imbalances and cause a complex adaptive physiological stress response (Mulders et al., 2014).

In the course of their evolution, microalgae have developed efficient strategies to tolerate and adapt to various types of abiotic stress. The sensing of abiotic stress induces a signaling cascade in the cell that leads to the activation of stress-responsive genes, the up-regulation of antioxidant pathways and the accumulation of secondary metabolites resulting in an adjustment of the cellular state to the new physiological conditions (Pérez-Clemente et al., 2013). Since most commercially relevant high value products, such as triacylglycerides (TAGs) and carotenoids, are accumulated under abiotic stress, changes in the cellular properties during the adaptational response can affect control strategies and process stability (Hyka et al., 2013). Therefore, a detailed characterization of these phenomena is necessary as a basis for robust process design for large scale cultivation systems. This chapter focuses on the recent progress in analytical methods including advanced fluorometric and spectroscopic techniques that facilitate the development of robust bioprocesses by providing a coherent picture of the microalgal metabolism under stress conditions. In the following, special attention is paid to the following methods:

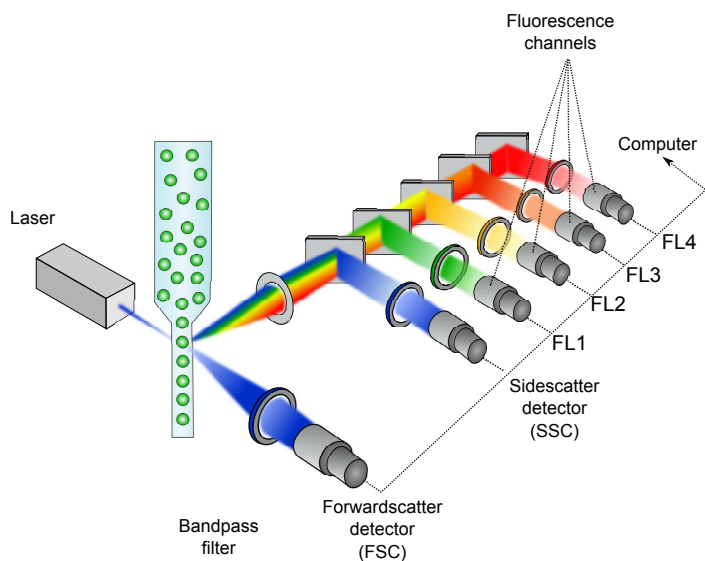


Figure 3.1.: Measuring principle of flow cytometry.

- Flow cytometry for detection of morphological and physiological changes during carotenogenesis.
- PAM fluorometry for the analysis of photosynthetic performance during adverse growth conditions.
- Fourier transform infrared (FTIR) spectroscopy for investigation of changes in biomass composition during the metabolic switch.

3.1 Flow cytometry

Flow cytometry is a widely used method in marine ecosystems research to investigate the structure and distribution of phytoplankton in natural seawater samples (Olson et al., 1985). The recent interest in oleaginous microalgae for the production of biofuels and edible oils has extended the application of flow cytometry to the staining of microalgal lipid bodies with lipophilic dyes, such as Nile Red and BODIPY (Chen et al., 2009; da Silva et al., 2009; Brennan et al., 2012). In addition, flow cytometry provides information about population heterogeneity and can therefore be used for fluorescence-activated cell sorting (FACS) to separate cells overproducing a target compound (Bougaran et al., 2012; Xie et al., 2014). Moreover, flow cytometry also supports the analysis of various morphological and biochemical features referring to physiological state of the cell (Mendoza Guzmán et al., 2012; de Winter et al., 2013). Depending on the environmental conditions, the cell cycle stage or the age of a cell, intrinsic light scattering and fluorescence emission properties of the biomass is changing. These changes in the cellular properties (e.g. cell size, granularity, pigmentation, vitality) have a large impact on the process performance and flow cytometry has therefore the potential to contribute to the rapid development of feasible bioprocesses.

A flow cytometric system as depicted in Fig. 3.1 consists of three parts:

1. The fluidic part: Alignment of the cells in the measurement stream by dilution of the sample with sheath fluid.
2. The optical part: Excitation of fluorescence with single or multiple lasers and detection of light scattering or fluorescence emission in appropriate detectors.
3. The electronic part: Conversion of light signals into electronic signals for data processing and analysis.

An overview of fluorescent dyes used to characterize physiological properties in microalgae is given in Table 3.1.

Table 3.1.: Selection of fluorescent dyes used for characterization of physiological properties in microalgae. Adapted from Hyka et al. (2013).

Property	Dye	Aim	Microalgae	Reference
Neutral lipid content	Nile Red	Identify lipid-rich strains	Chlorophyta	(Chen et al., 2009)
		Identify carotenoid-overproducing strains	<i>Dunaliella salina</i>	(Mendoza Guzmán et al., 2012)
	Identify lipid-overproducing mutants	BODIPY 505/515	<i>Isochrysis affinis galbana</i>	(Bougaran et al., 2012)
			<i>Chlamydomonas reinhardtii</i>	(Xie et al., 2014)
Lipid oxidation	C11-BODIPY 591/581	Lipid particle release	<i>Dunaliella viridis</i>	(Davis et al., 2015)
		Cell integrity	<i>Ophiocytium maius</i>	(Cooper et al., 2010)
	Determination of oxidative stress	DiOC ₆ (3)	<i>Chrysochromulina</i> sp.	(Brennan et al., 2012)
			<i>Mallomonas splendens</i>	
Membrane potential	DiBAC ₄ (3)	Identify lipid-rich strains	<i>Dunaliella tertioclecta</i>	(Gregori et al., 2002)
		Viability analysis of cells embedded in a hydrogel	<i>Chlamydomonas reinhardtii</i>	(Krujatz et al., 2015)
ROS	DHR123	Impact of cadmium exposure on ecotoxicity	<i>Chlorella sorokiniana</i>	(Jamers et al., 2009)
Cell viability	SYTOX blue	Impact of milking cadmium exposure on ecotoxicity	<i>Chlamydomonas reinhardtii</i>	(Jamers et al., 2009)
Cell vitality	Fluorescein diacetate (FDA)	Viability analysis with minimal autofluorescence overlap	<i>Emiliana huxleyi</i>	(Dashkova et al., 2016)
Cell integrity	SYTOX green	Investigate stages of cell death	<i>Dunaliella salina</i>	(Hejazi et al., 2004)
DNA content	Propidium iodide (PI)	Impact of cell cycle on biomass composition	Phytoplankton	(Veldhuis et al., 2001)
DNA content	Hoechst 33342		<i>Neochloris oleoabundans</i>	(de Winter et al., 2013)
DNA content	DAPI	Analysis of cell cycle	<i>Gonyaulax polyedra</i>	(Vicker et al., 1988)
			<i>Euglena</i> sp.	(Vitova et al., 2005)
	SYBR Green I	Analysis of cell cycle	<i>Porphyridium purpureum</i>	<i>Chlamydomonas reinhardtii</i>
			<i>Haematococcus pluvialis</i>	
			<i>Scenedesmus obliquus</i>	
			<i>Scenedesmus quadricauda</i>	

In summary, the use of flow cytometry for monitoring and optimization of phototrophic processes has great potential and benefits and is now slowly beginning to emerge. The majority of studies applying flow cytometry to microalgae focus only on single properties (e.g. lipid fluorescence) at a single time point rather than uncovering relationships in algal metabolism as an response to its dynamically changing environment.

Although the large scale production of natural β -carotene in *D. salina* is of high industrial relevance, a systematic and detailed analysis of cellular features corresponding to its physiological state during storage molecule accumulation under abiotic stress conditions is missing. Therefore, this thesis provides a unique resource for the dynamic exploration of the abiotic stress response in *D. salina* and its link to important

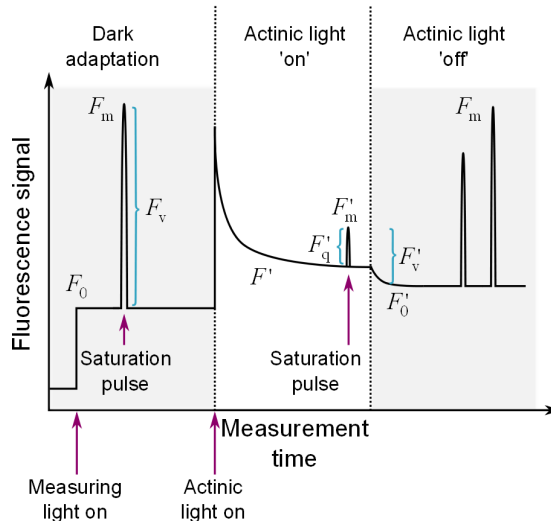


Figure 3.2.: Principle of PAM fluorometry.

bioprocess parameters, e.g. growth parameters, metabolic stress indicators, morphological properties and productivity.

3.2 Pulse amplitude modulation (PAM)

PAM fluorometry is a non-invasive analysis tool that monitors chlorophyll fluorescence as an indicator for the activity of photosystem II (PSII) and has broad application areas in algal and plant physiology (Schreiber, 1983). The activity of PSII is an indicator for the effect of fluctuating environmental conditions on the photosynthetic performance and the mechanisms leading to the adaptation of the photosynthetic machinery under adverse growth conditions. When photons are absorbed by chlorophyll molecules they can be valorized in the following ways: (i) drive photosynthetic electron transport; (ii) re-emission as heat; or (iii) re-emission as light (chlorophyll fluorescence) (Murchie and Lawson, 2013). Since the aforementioned processes compete with each other, an increase in one process results in a decreasing efficiency of the remaining ones. Hence, from the chlorophyll fluorescence signal relationships about photosynthetic efficiency and dissipation processes can be derived (Maxwell and Johnson, 2000). Although only a minor fraction of incident light can be used as measurement signal, the obtained signal/noise ratio of the measurement signal is high and the derived system properties can be estimated accurately.

The photosynthetic performance of the cells are calculated based on the fluorescence peak ratios observed during the illustrated time course (Fig. 3.2) where the cells are exposed to presence or absence of light in different durations and intensities such as constant actinic light (i.e. light that is absorbed by the photosynthetic machinery and will drive electron transport) or saturation light pulses. This procedure enables to distinguish between photochemistry and energy dissipation (e.g. due to non-photochemical quenching). The measurement usually starts with a dark-adaptation process of 5 to 10 min where the absence of actinic light leads to a stagnation in the

photosynthesis. In this period, all reaction centers of the photosystem are in an open state and the plastoquinone pool (Q_A) is fully oxidized. The basal fluorescence in the dark-adapted state is also referred to as F_0 and is detectable due to the presence of a low intensity measuring light, which is sufficient to induce fluorescence emission but too lower to start photosynthesis. At the end of the dark-adapted period, at short saturation pulse is applied to the culture which is able to fully saturate all reaction centers in the photosystem, which will change their state into the closed mode and the plastoquinone pool is in the reduced state. This saturation pulse induces the maximal fluorescence termed F_m . The difference between the maximal and minimal fluorescence F_m and F_0 is also called the variable fluorescence F_v . Numerous studies demonstrated the ratio between F_v and F_m represents a robust indicator for the maximum quantum efficiency of PSII (Eq. 3.1) (Butler, 1978).

$$\Phi_{\text{PSII,max}} = \frac{F_v}{F_m} = \frac{F_m - F_0}{F_m} \quad (3.1)$$

The presence of abiotic stress conditions such as high irradiance results in an light-induced decrease in the photosynthetic capacity due to inactivation of PSII (Long et al., 1994). This process is also referred to as photoinhibition. Cells which are exposed to photoinhibitory conditions shown a significantly lowered F_v/F_m ratio making it a suitable indicator for the detection of a light-induced physiological stress response (Demmig-Adams and Adams, 2006).

Subsequently, the actinic light is turned on to determine the photosynthetic parameters of the light adapted state. This phase is initiated by an instantaneous rise in the chlorophyll fluorescence which slowly declines until it reaches a steady-state value after several minutes (> 10 min) (Murchie and Lawson, 2013). The decline phase is caused by competing photochemical and non-photochemical quenching mechanisms. After the light-adapted fluorescence signal F' reached steady-state, a saturation pulse is applied to the culture which induces the closure of all reaction centers and the value for light-adapted maximal fluorescence F'_m is achieved. Note that the maximal fluorescence in the light-adapted state F'_m is always lower compared to the dark-adapted state F_m due to the presence of quenching mechanisms. The difference of the maximum light-adapted fluorescence F'_m and the steady-state value of fluorescence in actinic light F' normalized to F'_m is defined as the effective quantum yield of PSII ($\Phi_{\text{PSII,eff}}$) as shown in Eq. 3.2:

$$\Phi_{\text{PSII,eff}} = \frac{F'_q}{F'_m} = \frac{F'_m - F'}{F'_m} \quad (3.2)$$

Hence, $\Phi_{\text{PSII,eff}}$ is a measure of the efficiency of photochemistry under the present light conditions. The multiplication of $\Phi_{\text{PSII,eff}}$ with the average light intensity (\bar{E}) and the default ETR factor 0.42 leads to the derivation of the electron transport rate (ETR) which is given in Eq. 3.3:

$$\text{ETR} = 0.42 \cdot \Phi_{\text{PSII,eff}} \cdot \bar{E} \quad (3.3)$$

The default ETR factor originates from a "model" leaf and describes the fraction of the incident light intensity in the PAR region that is absorbed in PSII. The value of

0.42 originates from a study of Bjorkman and Demmig (1987) where 50 % of the PAR have been distributed to PSII and 84 % of the PAR was absorbed by photosynthetic pigments in a standard leaf (Schreiber et al., 2011).

NPQ is a mechanism to protect algae and plants from cellular damage due to over-saturating radiation by quenching singlet chlorophyll ($^1\text{Chl}^*$) as shown in Fig. 2.1 leading to the dissipation of excess energy as heat. As NPQ only occurs in light-adapted cells, its presence leads to a reduction of energy that can be converted into fluorescence. Therefore the fraction of NPQ in a sample can be estimated from the difference of the maximum fluorescence in the light-adapted state F'_m and the dark-adapted state F_m normalized to the light-adapted state (Eq. 3.4).

$$\text{NPQ} = \frac{F_m - F'_m}{F'_m} \quad (3.4)$$

Finally, the minimal fluorescence F'_0 can be estimated after turning of the actinic light. All parameters that can be derived from the chlorophyll fluorescence time course that is depicted in Fig. 3.2 are summarized in Table 3.2.

Table 3.2.: Frequently used parameters in PAM analysis and their physiological relevance. Adapted from Baker (2008).

Symbol	Definition	Physiological relevance
F_0	Minimal fluorescence of dark- and light-adapted samples	Level of fluorescence when Q_A is maximally oxidized and PSII centers are open
F_m	Maximal fluorescence of dark- and light-adapted samples	Level of fluorescence when Q_A is maximally reduced and PSII centers are closed
F_v	Variable fluorescence from dark- and light-adapted samples	Demonstrates the ability of PSII to perform photochemistry (Q_A reduction)
F_q	Difference in fluorescence between F'_m and F'	Photochemical quenching of fluorescence by open PSII centers
F_v/F_m	Maximum quantum efficiency of PSII photochemistry	Maximum efficiency at which light absorbed by PSII is used for reduction of Q_A
F'_q/F'_m	PSII operating efficiency	Estimates the efficiency at which light absorbed by PSII is used for Q_A reduction
F'_v/F'_m	PSII maximum efficiency	Relates the PSII maximum efficiency to the PSII operating efficiency
NPQ	Non-photochemical quenching	Monitors the apparent rate constant for heat loss from PSII

3.3 Fourier transform infrared (FTIR) spectroscopy

FTIR spectroscopy is a promising method for bioprocess characterization which combines several advantages. It is a rapid and non-invasive method which provides information on all molecules in the sample absorbing infrared light. In addition, the measurement is characterized by a high spectral resolution over a wide wavelength range. Due to the small sample amounts required (in the range of μg), the method enables highly flexible measurements with multiple replicates or short sampling times which makes it an excellent tool for bioprocess monitoring (Burgula et al.,

2007). Hence FTIR spectroscopy has gained significant importance in the field of biotechnology for identification and quantification of macromolecules, species comparison and analysis of biomass composition. Moreover, methods of multivariate data analysis (such as partial least square (PLS) analysis or principal component analysis (PCA)) promoted the interpretation of highly complex IR spectra of microorganisms with various IR-active molecules (Wagner et al., 2010).

The energy of a photon is defined by the product of its frequency ν and a proportionality factor h known as the Planck constant as described in Eq. 3.5.

$$E = h \cdot \nu \quad (3.5)$$

As the frequency ν and the wavelength λ are inversely proportional following equation can be derived:

$$\nu = \frac{c}{\lambda} \quad (3.6)$$

where c is the speed of light.

Therefore Eq. 3.5 leads to:

$$E = \frac{hc}{\lambda} \quad (3.7)$$

implying that shorter wavelength (or higher frequency) corresponds to higher energy.

The frequencies in a IR spectrum are usually expressed in wavenumbers $\bar{\nu}$ (cm^{-1}) which is typically used for infrared light and is the inverse of the wavelength. This has the advantage that the correlation between wavenumber and energy is directly proportional (the higher the wavenumber, the higher the energy).

$$\bar{\nu} = \frac{1}{\lambda} \quad (3.8)$$

Infrared spectroscopy makes use of the property of a compound to absorb characteristic wavelengths of infrared light which correspond to the functional groups present in the molecule. The absorbed light energy in the specific wavelength regions, is also called resonant frequencies and refers to the transition energy of the bond during vibration. Infrared light only induces vibrations if the bond is IR-active, meaning that a change in the dipole moment occurs (Berthomieu and Hienerwadel, 2009). Different vibrational modes such as stretching, bending, wagging and twisting can be present in a molecule (Carbonaro and Nucara, 2010). Therefore, IR spectroscopy is frequently applied to identify molecules or determine species based on the intensity and position of their characteristic bands in the IR spectrum. However, due to numerous different bonds in complex molecules, the resulting IR spectrum has many peaks which can render interpretation and quantification difficult. The positions of these characteristic bands is summarized in Table 3.3. The presence of a functional group is usually detected at higher wavenumbers ($4000 - 1600 \text{ cm}^{-1}$), whereas the wavelength region below 1500 cm^{-1} is referred to as "fingerprint" region (Bakker et al., 2003). Vibrations in this region are often complex and hard to assign to a specific functional group of the molecule.

Table 3.3.: Band assignment for major biomacromolecules found in FTIR spectra of microalgae. Adapted from Giordano et al. (2001) and Liu et al. (2013).

Wavenumber (cm ⁻¹)	Band assignment	Biomacromolecule
~ 3600-3300	symmetric O-H and N-H stretch	Water, protein
~ 3000-2800	asymmetric C-H stretch	Lipids (Methylene groups)
~ 1740	symmetric C=O stretch	Membrane lipids and fatty acids
~ 1650	symmetric C=O stretch	Proteins (Amide-I)
~ 1540	symmetric deformation of N-H and stretch of C-N	Proteins (Amide II)
~ 1245	asymmetric P=O stretch	Nucleic acids (DNA/RNA backbones)
~ 1200-900	symmetric C-O-C stretch	Polysaccharides
~ 1080-980	symmetric C-O stretch	Carbohydrates and polysaccharides

In summary, the quick and reliable estimation of the biomacromolecular composition is an indispensable step in the full exploitation and valorization of microalgal biomass towards the development of sustainable biorefineries. However, FTIR spectroscopy has been only rarely applied in algal biotechnology, mostly to prove the presence of lipids (e.g. by Giordano et al. (2001) for the diatom *Chaetoceros muellerii*, by Dean et al. (2010) for *Chlamydomonas reinhardtii* and *Scenedesmus subspicatus*, by Laurens and Wolfrum (2011) for *Nannochloropsis* sp., *Chlorococcum* sp. and *Spirulina* sp. and by Liu et al. (2013) for *D. salina*). A large proportion of the studies monitored the lipid accumulation only on a qualitative basis or as macromolecular ratios (lipid:protein or lipid:carbohydrates). Only very few studies addressed the quantification of FTIR spectra with respective standard molecules as done by Wagner et al. (2010) where the protein, lipid and carbohydrate content of *C. reinhardtii* has been measured and compared with conventional biochemical methods.

In the present work, a quantitative protocol for FTIR spectroscopy in *D. salina* has been developed and applied to link the morphological properties from the flow cytometric analysis and the photosynthetic performance derived from PAM measurements with the biomass level to get a consistent picture of β -carotene synthesis and its role in stress tolerance of the photosynthetic microorganisms.

Chapter 4

Modeling of microalgal metabolism

This chapter gives a comprehensive overview of the existing modeling frameworks for microalgae, their mathematical foundations and outline their applications in microalgal biotechnology. Mathematical modeling has become an essential tool to understand the complex organization of biological systems. Nevertheless, the applied methods of computational biology are very diverse and one single method is not able to cover the different temporal and spatial scales observed in a biological system. In order to get a coherent understanding of an organisms behavior under dynamically changing conditions the combination suitable computational approaches is required (Steuer et al., 2012).

4.1 Microalgal metabolism

Cellular systems perform a series of biochemical reactions where metabolites are converted from one compound into another. Metabolic networks and the underlying pathways link these reactions to fulfill physiological functions of the organism such as growth, respiration and adaptation to the environment. Studying metabolic networks can provide insights into the behavior of the system and provide useful targets for bioengineering strategies.

There is consensus regarding the fact that the carbon core metabolisms of green microalgae (Chlorophyta) is relatively conserved across the species and that the resulting metabolic networks show a large similarity (Reijnders et al., 2015). However, across different algal classes (e.g. diatoms and green microalgae) the structural organization of the central carbon metabolism is highly variable (Wilhelm et al., 2006; Hildebrand et al., 2013). The essential pathways in the central carbon metabolisms of green microalgae can be schematically represented as shown in Fig. 4.1.

The carbon core metabolism of microalgae covers the following pathways:

- **Photosynthesis:** Conversion of light energy into chemical energy, which is produced from the precursor molecules carbon dioxide and water and stored in form of carbohydrate molecules (e.g. starch).

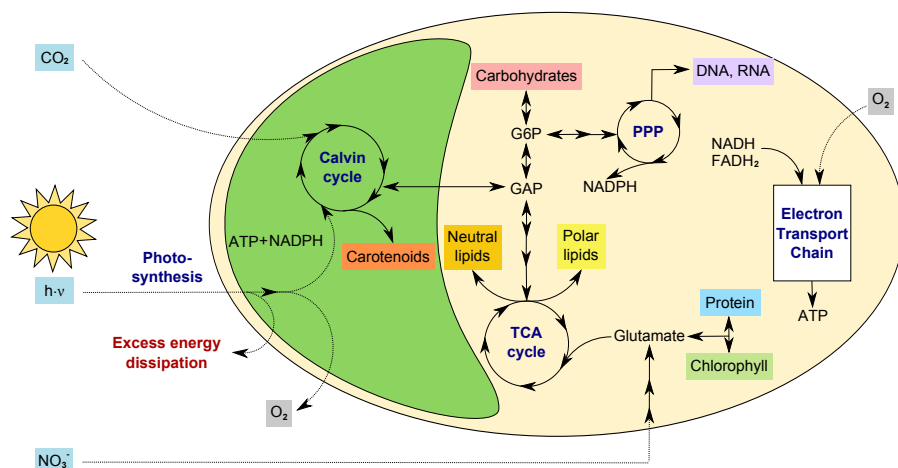


Figure 4.1.: Simplified graphical representation of the central carbon metabolism in *D. salina*. Adapted from Kliphuis et al. (2011).

- Glycolysis: Conversion of glucose into pyruvate to release energy in form of ATP or reducing equivalents (NADH) and generate precursor metabolites.
- Citric acid cycle (TCA): Generation of energy through the oxidation of acetyl-CoA derived from various sugar compounds, fatty acids or amino acids into carbon dioxide and energy.
- Oxidative phosphorylation: Formation of ATP due to electron transfer from donors to acceptors (NADH or FADH₂ to O₂) by a series of electron carriers.
- Pentose phosphate pathway (PPP): Generation of reductive power such as NADPH and C5-sugars as precursors for DNA and RNA synthesis.
- Carbohydrate and fatty acid synthesis: Supply of building blocks for formation of cell wall components and carbon storage.
- Carotenoid biosynthesis: Formation of pigments to fulfill the physiological requirements of photosynthetic light harvesting, photoprotection and energy sinks.
- In-cooperation of inorganic nutrients (e.g. nitrate): Supply of precursor molecules for the synthesis of nucleotide, amino acids and chlorophyll.

4.2 Reconstruction of metabolic networks

Due to large research investments in genome projects and the rapid advancement in sequencing technologies, the number of sequenced genomes is growing exponentially (Koussa et al., 2014). These sequences have great potential for the development of metabolic models, but their use is limited by the large time and effort required to annotate a genome. However, an annotated genome is an important prerequisite to link the present genes with metabolic reactions at the biochemical level (Thiele and Palsson, 2010). Metabolic network reconstructions aim at providing a

more comprehensive picture of the biochemical reactions taking place in an organisms. The reconstruction procedure follows a standardized protocol which has been described in detail by Thiele and Palsson (2010). After the metabolic network has been reconstructed, it needs to be translated into a mathematical model, which can be interpreted and analyzed using various software packages for network analysis such as MetaFluxNet (Lee et al., 2003), Cell Net Analyzer (Klamt et al., 2007) or the COBRA toolbox (Becker et al., 2007). The common format to facilitate the conversion of metabolic reaction networks into a mathematical network model is the Systems Biology Markup Language (SBML) (Hucka et al., 2003).

Currently, these approaches led to 10 studies that proposed 11 metabolic networks for 6 different algal species as summarized in Table 4.1 (Baroukh et al., 2015).

Table 4.1.: Existing metabolic networks for microalgae. Adapted from Koussa et al. (2014) and Baroukh et al. (2015)

Specie	References	Type of modeling framework	Scale	Reactions	Metabolites	Compartments
Chlorophyta						
<i>Chlorella protothecoides</i>	(Wu et al., 2015)	C13 metabolic flux analysis and FBA	Carbon core	272	270	4
<i>Chlorella sorokiniana</i>	(Yang et al., 2000)	FBA	Carbon core	67	61	1
<i>Chlorella</i> sp. FC2 IITG	(Muthuraj et al., 2013)	FBA and DFBA	Carbon core	161	114	1
<i>Chlamydomonas reinhardtii</i>	(Manichaikul et al., 2009)	Network reconstruction	Carbon core	259	467	6
	(Boyle and Morgan, 2009)	FBA	Carbon core	484	458	3
	(Kliphuis et al., 2011)	Calculation of energy requirements	Carbon core	160	164	2
<i>Ostreococcus tauri</i>	(Cogne et al., 2011)	FBA with thermodynamic and energetic constraints	Carbon core	280	278	1
	(Chang et al., 2011)	FBA	Genome-scale	2190	1068	9
	(Dal'Molin et al., 2011)	FBA	Genome-scale	1725	1869	3
<i>Ostreococcus tauri</i>	(Krumholz et al., 2012)	Microarray analysis and FBA	Genome-scale	871	1014	1
<i>Ostreococcus lucimarinus</i>	(Krumholz et al., 2012)	Microarray analysis and FBA	Genome-scale	964	1100	1
Haptophyta						
<i>Tisochrysis lutea</i>	(Baroukh et al., 2014)	Dynamic Reduction of Unbalanced Metabolism (DRUM)	Carbon core	162	157	3
Diatoms						
<i>Phaeodactylum tricornutum</i>	(Kim et al., 2016)	FBA	Genome-scale	849	587	4

The reasons why the existing metabolic networks differs in the number of reactions and metabolites are manifold. They mainly differ in level of detail used for description of the key metabolic pathways as extensively discussed in Baroukh (2014) and listed below:

- I. Photosynthetic reaction step (e.g. photophosphorylation, photorespiration)
- II. Biomacromolecule synthesis (e.g. lipids, carbohydrates, biomass)
- III. Synthesis of secondary metabolites (e.g. chlorophyll, carotenoids)
- IV. Compartmentalization and related exchange reactions
- V. Definition of reversible reactions (e.g. as two irreversible forward reactions in (Boyle and Morgan, 2009))
- VI. Consideration of isomeric forms (e.g.: α -D-glucose and β -D-glucose in Chang et al. (2011))

Still it remains questionable, if the different degree of detail for the representation of the metabolites and the biochemical reactions has a large impact on the accuracy of

the model predictions. Since the macroscopic reactions have a large similarity, it may therefore be concluded that the level of detail has only a minor impact on the simulation results (Baroukh, 2014). The incorporation of secondary metabolites is handled very different in metabolic models. Typically secondary metabolites contribute only to a very small fraction to the whole biomass and the presence varies greatly between the species. The majority of metabolic networks only include the synthesis of chlorophyll (Cogne et al., 2011; Kliphuis et al., 2011), whereas some studies consider detailed synthesis pathways of different pigment compounds and non-essential lipids (Chang et al., 2011). In most cases, secondary metabolites are not essential for growth and represent only a marginal fraction of the biomass. Though the fluxes related to their formation are supposed to be negligible compared to those of the carbon core metabolism and their impact on the prediction accuracy is estimated to be small (Baroukh, 2014). However, the analysis and optimization of secondary metabolite content is an important target in biotechnology since they are considered as high-value products or fine chemicals. Though, depending on the modeling task, their incorporation might be beneficial.

4.3 Stoichiometric modeling frameworks

This section introduces methods for stoichiometric network analysis of metabolic models. Such models rely only on structural aspects (stoichiometry) of the underlying reaction network and do not require kinetic information of the involved reactions. Despite of the limited predictive power, stoichiometric modeling allows deriving important functional and topological network properties and thus leading to a better understanding of metabolic network architecture. The metabolic network of a microorganism can be fully described by all biochemical reactions taking place in its metabolism. The dynamic changes in the concentration of a certain metabolite can be expressed by its stoichiometric coefficient and the reaction rate expressed by a set of ordinary differential equations (ODEs) as given in Eq. 4.1:

$$\frac{dx(t)}{dt} = \mathbf{N} \cdot \mathbf{v}(\mathbf{x}(t), \mathbf{u}(t), \mathbf{p}) \quad (4.1)$$

where \mathbf{N} is the stoichiometric matrix (with the dimension $m \times n$), m corresponds to the number of metabolites and n corresponds to the number of reactions taking place in the metabolic network. The vector \mathbf{v} is composed of the entries of all reaction fluxes contained in the network which depend on the state variables \mathbf{x} , the input \mathbf{u} and the kinetic parameters \mathbf{p} as well as t representing the cultivation time.

As the reaction rates and turnover number of intracellular metabolites are usually higher compared to those of regulatory processes (e.g. cellular growth rate or adaptation to changing environmental conditions), the quasi-steady state assumption is typically made, which relies on the fact that under constant external conditions and at longer time-scales, the metabolite concentrations and reaction rates are constant (Klamt et al., 2014). The steady-state of the metabolic network is described in terms of mass balance equation. This kind of assumption opens up the possibility to cal-

culate otherwise unknown internal fluxes of the reactions involved. Applying the steady-state assumption to Eq. 4.1 leads to the following expression:

$$\frac{dx(t)}{dt} = \mathbf{N} \cdot \mathbf{v} = 0 \quad (4.2)$$

Besides, biochemical conversion reactions, transport reactions can be present in flux vector \mathbf{v} which account for substrate uptake and shuttle of metabolites between certain compartments. Consequently, metabolites participating can be classified as intracellular or extracellular metabolites (e.g. substrate or excreted product) as depicted in Fig. 4.1. The entries in the stoichiometric matrix \mathbf{N} correspond to the stoichiometric coefficients of the reactions \mathbf{v} , where the i -th metabolite participates in the j -th reaction. The sign of the stoichiometric coefficient $N_{i,j}$ depends on its role in the reaction v_j (Baroukh, 2014). The relationship is as follows:

- $N_{i,j} = 0$ if metabolite i does not participate in reaction j
- $N_{i,j} > 0$ if metabolite i is an educt of reaction j
- $N_{i,j} < 0$ if metabolite i is a product of reaction j

The underlying biochemical reactions of the network can be distinguished between irreversible (\rightarrow) or reversible (\leftrightarrow) reactions. In general, each reaction is macroscopic and summarizes a set of elemental reactions involving enzyme complexes. As a consequence, the metabolic network (and its size) can vary depending on the description level.

In the problem formulation reversible reactions are not considered, but there are multiple ways to include them. First, reversible reaction can be represented by two irreversible reactions covering forward and backward reaction. Second, a reversibility vector can be introduced where the corresponding entry of a reaction j is zero if the reaction is irreversible or 1 if the reaction is reversible. Third, the reversibility can be coupled to the vectors accounting for the upper and lower bound where the corresponding entry of a reaction j is zero if the reaction is irreversible and negative if the reaction is reversible.

The frameworks for functional analysis of stoichiometric networks cover the following objectives along with the corresponding methods (Baroukh, 2014):

- Elementary flux modes (EFMs): Identification of all minimal functional pathways or sub-networks linking substrate uptake to biomass production inherent in a metabolic network (e.g. (Schuster et al., 1999)).
- Flux coupling analysis (FCA): Identification of coupled (directional, partial or full coupling) or blocked fluxes (e.g. Burgard et al. (2004)).
- Flux balance analysis (FBA): Determination of flux distribution under given input conditions by maximization of an objective function (e.g. Orth et al. (2010)).
- Flux variance analysis (FVA): Determination of variability in fluxes under given input conditions (e.g. Mahadevan and Schilling (2003)).
- Gene deletion studies (GDS): Study influence of gene deletion on flux distribution (e.g. Burgard et al. (2003)).

Flux balance analysis

The null space of the stoichiometric matrix \mathbf{N} gives important insights into the metabolic capabilities of a biochemical network and is a common step in the analysis of metabolic networks such as FBA or elementary mode analysis. In metabolic networks, the resulting system of linear equations is often underdetermined meaning that there are more unknown fluxes than equations (Klamt et al., 2002). Consequently, these systems do not have a unique solution because the defined constraints are not sufficient (Maarleveld et al., 2013). However, the definition of a reasonable objective function enables to find biologically relevant solutions by means of linear programming (Winterbach et al., 2011). A biological and evolutionary consistent objective is that the organism attempts to maximize its biomass growth rate and/or minimizes the formation of secondary products (Varma and Palsson, 1994; Schuetz et al., 2007). A biomass reaction that consumes precursor metabolites according to fixed stoichiometric coefficients is used to describe biomass production and predict the specific growth rate μ . However, also slightly sub-optimal flux distributions have been observed in biological systems giving rise to an easier transition under fluctuating environmental conditions.

To make the stoichiometric model more consistent with biological or thermodynamical knowledge of the organism, inequalities are often added to the equation system that define boundary conditions to the reaction fluxes \mathbf{v} (Orth et al., 2010). In addition, upper and lower bounds are introduced that specify the maximum and minimum reaction flux \mathbf{v} as given in Eq. 4.3. According to these constraints, the attainable region of flux space distribution is defined as

$$\mathbf{v}_{\text{lb}}(\mathbf{x}(t)) \leq \mathbf{v} \leq \mathbf{v}_{\text{ub}}(\mathbf{x}(t)) \quad (4.3)$$

where \mathbf{v}_{lb} and \mathbf{v}_{ub} are the lower and upper bounds of the reaction fluxes. The definition of inequalities and the objective function leads to a considerable reduction of the attainable region in the solution space.

The mathematical problem formulation of FBA is as follows:

$$\mathbf{v}(\mathbf{x}(t)) = \arg \max \mathbf{c}^T \mathbf{v} \quad (4.4)$$

$$\text{s.t.} \quad \begin{cases} \mathbf{N} \cdot \mathbf{v} = 0 \\ \mathbf{v}_{\text{lb}}(\mathbf{x}(t)) \leq \mathbf{v} \leq \mathbf{v}_{\text{ub}}(\mathbf{x}(t)) \end{cases} \quad (4.5)$$

where $\mathbf{c}^T \mathbf{v}$ is the objective function defined by the cost vector \mathbf{c} .

Most of the metabolic modeling efforts were devoted to organisms growing heterotrophically, especially to model organisms such as *Escherichia coli*. The questions they are aiming at are manifold and include:

1. Quantitative prediction of growth rates (Edwards et al., 2001; Ibarra et al., 2002).
2. Maximizing fluxes towards a certain product of interest by studying the influence of intervention strategies (e.g. gene knock-outs or overexpression) (Burgard et al., 2003; Trinh et al., 2008; Hädicke and Klamt, 2010).

3. Coupling of growth and formation of secondary products by means of intervention strategies (Klamt and Mahadevan, 2015).

The reason why stoichiometric network analysis and FBA only barely addresses photosynthetic organisms is based on the fact that dynamics in environmental fluctuations (e.g. light, temperature, nutrients etc.) cannot be addressed properly in this framework. Furthermore, the mathematical representation of light in this modeling framework is complex due to various regulatory levels in photosynthesis as described in Section 2.1 and 2.2. The photon flux is typically modeled as a constant input that is transformed into chemical energy according to stoichiometric constraints where the wavelength distribution of the light source or regulation (e.g. scattering of light from the algal surface and energy dissipation mechanisms) are not taken into account.

4.4 Dynamic-kinetic modeling frameworks

4.4.1. Macroscopic bioreactor modeling

The most common approach to formulate a dynamic mathematical model for biosystems is a macroscopic model using a set ODEs to describe the biochemical processes taking place. Similar to chemical processes, mass balance equations account for the concentration changes over time that include kinetic reaction parameters which account for biomass growth, substrate uptake and formation of secondary products. The main challenge in this modeling approach is to obtain a predictive model with reliable parameter estimates. Due to the large efforts necessary for generating suitable experimental data and the limited amount of measurable metabolic reaction rates this goal is often difficult to achieve, especially to represent the transient dynamics of intracellular metabolites. Nevertheless, constructing and solving of dynamic-kinetic models is relatively easy and computationally inexpensive making them an indispensable component for computational process optimization.

The ODE system, which general form is given in Eq. 4.6, is derived from a mass balance equation.

$$\frac{d\mathbf{x}(t)}{dt} = \mathbf{f}(\mathbf{x}(t), \mathbf{u}(t), \mathbf{p}) \quad (4.6)$$

where \mathbf{x} represents the state variables, \mathbf{u} the input and \mathbf{p} the kinetic parameters.

The biomass growth in a batch reactor given in Eq. 4.7:

$$\frac{d\rho_X}{dt} = \mu \cdot \rho_X \quad (4.7)$$

where μ is the specific growth rate (in d^{-1}) and ρ_X is the biomass density (in $g L^{-1}$). The specific growth rate μ depends on the availability of its limiting substrate S and the relationship is usually expressed using the Monod equation as follows:

$$\mu = \frac{\mu_{\max} \cdot S}{K_S + S} \quad (4.8)$$

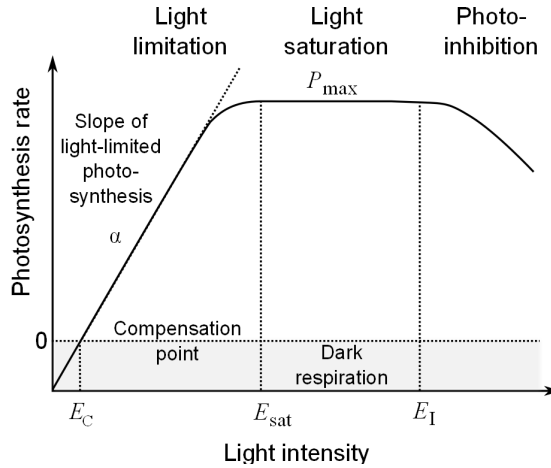


Figure 4.2.: Dynamic behavior of the photosynthesis-irradiance curve under various light regimes quantified by the oxygen evolution rate or the carbon fixation rate.

where S is the density of the limiting substrate (in g L^{-1}), μ_{\max} is the maximum growth rate (in d^{-1}) and K_S is the half-saturation coefficient (in g L^{-1}). The Eqs. 4.7 and 4.8 represent growth under heterotrophic conditions where one limiting substrate determines the value of the specific growth rate μ . Here, concentrations are expressed in terms of volumetric mass density, which is not always the case in literature. In the following, all concentrations are expressed as densities in g L^{-1} .

For photoautotrophic growth conditions commonly present in microalgal cultivations, Eq. 4.8 needs to be adjusted to account for light as "substrate". However, the relationship between photon flux density and growth rate is not straightforward since the photosynthesis rate is not directly proportional to the light absorption. The so-called P-E (also referred to as P-I) curve illustrates the relationship between photosynthesis rate and light intensity (E). As illustrated in Fig. 4.2, the P-E curve is characterized by the following four phases:

1. Dark respiration: The photosynthesis rate is zero due to absence of light until the compensation point (E_C) is reached and carbon storage is used to perform cellular respiration.
2. Light limitation: The photosynthesis rate increases linearly with increasing light intensity until a saturating light intensity (E_{sat}) is reached.
3. Light saturation: The photosynthesis rate is constant and at its maximal value meaning that a further increases in light does not lead to a higher photosynthesis rate. Above the saturation point, the light dependent reactions produce more ATP and NADPH than the light independent reactions consume to fix CO_2 .
4. Photoinhibition: A light intensity above the saturation point (E_{sat}) often leads to destruction of the photosynthetic apparatus (e.g. due to formation of ROS) and an impaired photosynthesis.

It should be noted that phototrophic batch cultivations under outdoor conditions but even lab-scale cultivations under constant incident light conditions lead to experience

of different light regimes in the system and can have either positive or negative influence on the growth rate. In some species, especially when adapted to high irradiance, photoinhibitory effects are not present or only of minor impact for the growth. All the aforementioned phenomena should be covered in the mathematical representation of the light-depend growth rate. A simple relationship between μ and the incident light intensity can be described by the following equation:

$$\mu_E = \mu_{\max} \cdot \frac{E_{av}}{E_{av} + K_{S,E} + \frac{E_{av}^2}{K_{i,E}}} \quad (4.9)$$

However, there are many other equation systems dealing with a mechanistic description of photosynthesis (Han, 2002; Rubio et al., 2003; Garcia-Camacho et al., 2012).

Beside the dependency of light on the growth rate, the absence of several nutrient can have an inhibitory effect on growth. In 1968, the researcher M. R. Droop developed a simple mathematical relationship for Vitamin B12 uptake in the marine phytoplankton *Monochrysis lutheri* which is still valid for various algal species and nutrients (Droop, 1968). Therefore, Eq. 4.10 is also often referred to as Droop equation. Since the accumulation of secondary metabolites such as carotenoids and TAG occur mostly under nitrogen starvation, this relationship is frequently applied to describe the growth reduction in dependence on the nitrogen availability in the medium as shown below:

$$\mu = \mu_E \cdot \left(1 - \frac{w_{N,\min}}{w_N}\right) \quad (4.10)$$

where $w_{N,\min}$ and w_N are the minimal and actual nitrogen quota of the biomass.

Dynamic-kinetic modeling has been successfully applied to various algal strains and substrate regime (autotrophic, mixotrophic and heterotrophic) to predict growth and the accumulation of metabolites (Packer et al., 2011; Quinn et al., 2011; Mairet et al., 2011; Blanken et al., 2016). A comprehensive overview on growth kinetic models of microalgae is presented in Lee et al. (2015).

4.4.2. Dynamic flux balance analysis

Depending on the degree of detail mathematical modeling approaches can be distinguished between models on macroscopic scale and intracellular scale. Macroscopic models use a reduced description of the biological reality to apprehend intrinsic phenomena and cellular dynamics. As explained in Sec. 4.4.1, such approaches use a system of ODEs to describe the evolution of state variables over time. Due to the limited amount of suitable experimental data, they are usually restricted to a small part of the metabolism or uses a simplified description of it. They are particularly well suited to describe biomass growth and nutrient uptake over time but can hardly be used for optimization of intracellular molecules of interest. In contrast, intracellular models are powerful approaches to unravel complex interactions and provide a mechanistic understanding of the cellular metabolism. In addition, they open up new possibilities for optimized production strategies for molecules of interest. How-

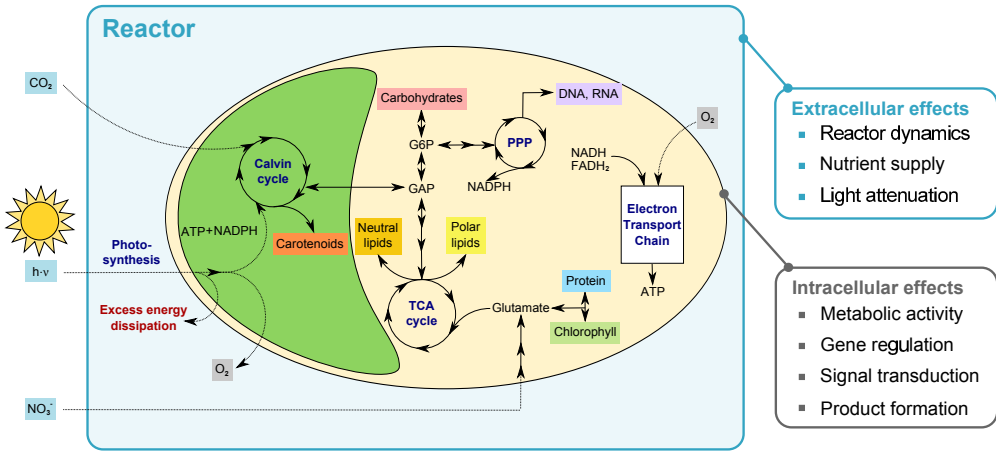


Figure 4.3.: Graphical representations of the DFBA approach taking into account intracellular and extracellular effects that influence microalgal metabolism.

ever, they rely on the availability of high-quality metabolic network reconstructions of annotated genetic data as explained in Section 4.2.

Since mass balance equations do not give insights into flux distributions, the analysis of metabolic networks is often carried out under steady-state conditions using constraint-based models. Within this framework the optimization objective is chosen in order to satisfy single or multiple optimality criteria. However, the cell population is constantly adapting its metabolism to fluctuating environmental conditions and steady-state models cannot account for temporal changes in biomass composition due to physiological adaptation processes. This exceptional property of biological organisms emerges from complex regulatory interactions between metabolism and enables the survival under harsh environmental conditions and prolonged starvation periods. The consideration of dynamic effects in metabolic networks is therefore of crucial importance to gain a mechanistic insights in metabolic adaptation and predict the accumulation of stress-related secondary metabolites, which are often of commercial interest due to its high value.

A method linking these two modeling approaches by adding additional dynamic constraints to metabolic network models is called dynamic flux balance analysis (DFBA). This framework is able to combine the aforementioned advantages of dynamic and steady-state frameworks to simulate growth transitions and predict the accumulation of commercially important metabolites. Therefore the system is divided into two parts: the dynamically changing environment and the intracellular metabolism, which is still in quasi steady-state (see Fig. 4.3). The FBA problem formulated in Eq. 4.4 is recalculated in quasi-steady state for each time step in the dynamic system (Fig. 4.4). Due to the introduction of dynamics in the FBA formulation, kinetic parameters (as mentioned in Section 4.4.1) need to be determined from experimental data in order to achieve high predictability. One major advantage of the DFBA approach is the possibility to include accumulation of storage molecules in a structured way by introduction of suitable kinetic equations.

To conclude, mathematical modeling is increasingly recognized as an indispensable research tool to understand the organization of biological systems. Nevertheless, the

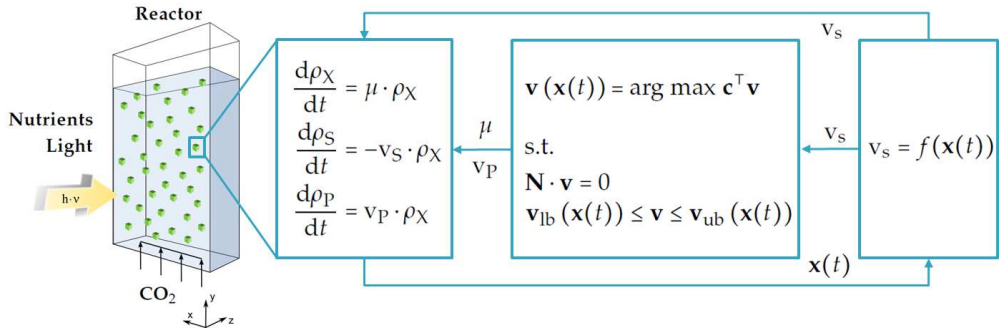


Figure 4.4.: Mathematical illustration of the DFBA workflow covering extracellular effects such as cell and reactor dynamics as well as intracellular stoichiometric of the underlying metabolic network.

methods and practices of mathematical modeling are highly diverse and no single methodology alone is able to cover the diverse temporal and spatial scales observed in biological systems. Therefore, the future of modeling resides in the utilization of a combination of methods, each suited to describe a particular aspect of biological reality giving rise to the challenge to combine these diverse conceptual and computational pictures into a coherent whole.

Chapter 5

Experimental methods

5.1 Strain, growth medium and pre-cultivation

The strains of *D. salina* and *D. parva* used in this work were obtained from the Culture Collection of Algae and Protozoa (Windermere, United Kingdom). Both strains were ordered as *D. salina* CCAP19/18 in 2011 and 2014. Since the cells showed pronounced differences in cell size and cellular dry weight, a 18S rRNA sequencing was performed by Cecilia Rad Menendez from CCAP. The sequence coverage of the sample ordered 2011 had a 100 % Query coverage (99 % Max. ID) with *D. parva*, whereas the sample ordered in 2014 had a 100 % Query coverage (99 % Max. ID) with *D. salina*. Therefore, the strains used in this work were named according to the sequencing results.

The growth of both stock cultures was performed in 500 mL shaking flasks containing 150 mL of the growth medium previously described by Lamers et al. (2010) on a rotary shaking incubator (Multitron, Infors AG, Switzerland) in air enriched with 3.5 % CO₂, at 26 °C, 100 rpm, with a light intensity of 30 μmol photons m⁻² s⁻¹ and alternating day/night cycles (16 h/8 h). The growth medium was composed of 1.50 M NaCl, 37.75 mM KNO₃, 22.50 mM Na₂SO₄, 4.87 mM K₂SO₄, 1.00 mM NaH₂PO₄, 0.37 mM MgCl₂, 19.35 mM Na₂EDTA, 18.9 mM CaCl₂, 11.25 mM NaFe EDTA, 1.89 mM MnCl₂, 1.48 mM ZnSO₄, 0.67 mM CuSO₄, 10.95 nM Na₂MoO₄, and 9.95 nM CoCl₂.

5.2 Cultivation experiments in flat-plate photobioreactors

Fermentations were performed in flat-plate photobioreactors either with 1 L cultivation volume (FMT 150, Photon Systems Instruments, 5 cm path length) equipped with white and red LEDs or with 1.8 L cultivation volume (Labfors Lux, Infors HT, 2 cm path length) equipped with warm white LEDs (Figs. 5.1 and 5.2). Both reactors were aerated with a gas mixture of 97 % air and 3 % CO₂ at a flow rate of 500 mL min⁻¹ controlled by mass flow controllers. The pH was adjusted to 7.5 by automated addition of 1 M HCl and 1 M KOH and the temperature was maintained at 24 °C. Dissolved oxygen was measured using an optical pO₂ electrode (Visiferm DO, Hamil-

ton Messtechnik GmbH, Switzerland). For inoculation, a stock culture grown under nitrogen-replete conditions was diluted to approximately 2×10^5 cells mL^{-1} for *D. salina* and 1×10^6 cells mL^{-1} for *D. parva* with the appropriate medium. The transmitted light intensity was measured by averaging the light intensity on the backside of the reactor using a light sensor (ULM-500, Walz or Infors HT).

Table 5.1.: Reactor constants of INFORS Labfors Lux and PSI FMT-150.

Constant	INFORS Labfors Lux	PSI FMT-150
Cultivation volume (L)	1.8	1
Reactor thickness (cm)	2	5
Illuminated surface area (m^2)	0.09	0.024

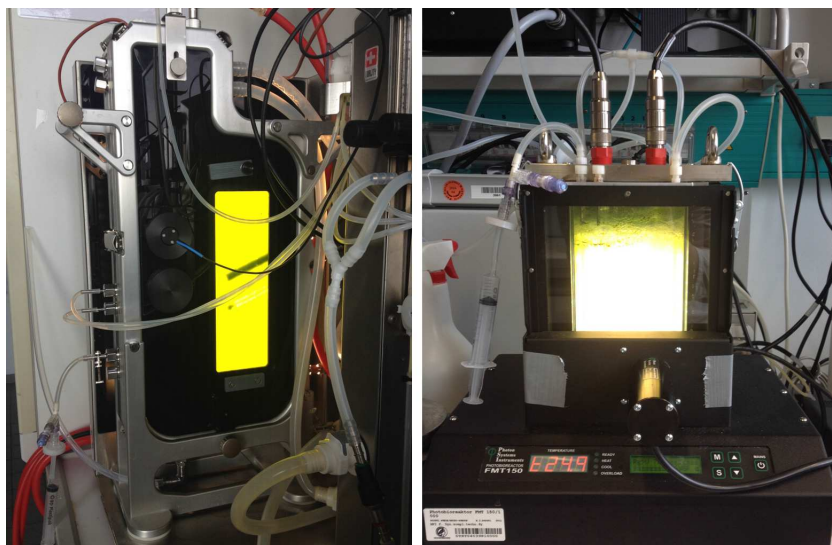


Figure 5.1.: Photographic pictures of the photobioreactor setup INFORS Labfors Lux (left) and PSI FMT-150 (right). (Courtesy of I. Harriehausen).

5.3 Dry weight determination

The determination of the cellular dry weight was performed according to Zhu and Lee (1997). Briefly, 5 mL of the cell suspension was filtered onto dry glass fiber filters (GF/F, $0.7 \mu\text{m}$, Whatman, UK) and washed with 0.5 M ammonium formate to remove remaining salts. The filter were dried in an oven (24 h, 70°C) until a constant weight was reached. Alternatively, samples of the cell suspension were transferred into 15 mL reaction tubes and were centrifuged for 10 min at 1,000 g. The supernatants were discarded and the cell pellets were washed with 0.5 M ammonium formate. Finally, the pellets were freeze-dried and the weights were determined on a balance.

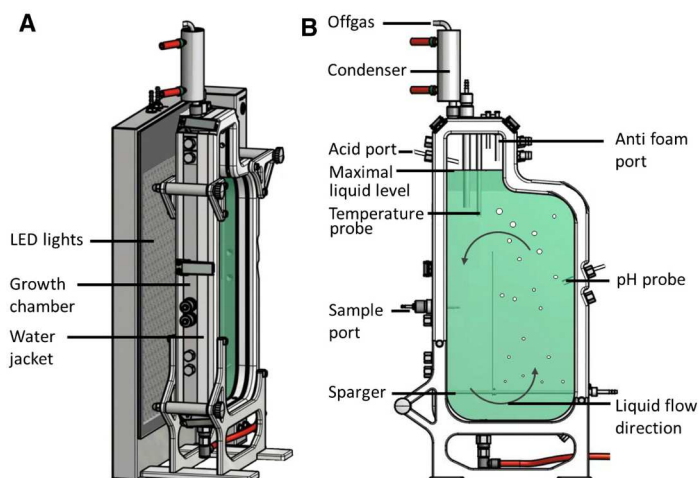


Figure 5.2.: Schematic view of INFORS Labfors Lux photobioreactor (A) side view and (B) front view. Adapted from Mulders et al. (2014) and Infors HT operation manual.

5.4 Carbon and nitrogen fraction in the biomass

The carbon fraction and the nitrogen cell quota of the inoculum were measured with a C/H/N analyzer from 3 mg freeze-dried biomass (Currenta, Germany).

5.5 Ion chromatography

Extracellular nitrogen density was measured using an ion chromatography system (Dionex ICS 1100, Thermo Scientific Dionex, USA) equipped with an Ion Pak AS22 column (Thermo Scientific Dionex, USA) with 4.5 mM sodium carbonate and 1.4 mM sodium bicarbonate as mobile phase, at a flow rate of 1.2 mL min^{-1} and with an injection volume of $50 \mu\text{L}$.

5.6 Spectrophotometrical determination of chlorophyll and carotenoid content

The chlorophyll and carotenoid fractions were determined using UV/VIS spectrophotometry. Depending on the cell density and the pigment fraction, a 3-10 mL sample was taken from the culture suspension. The cell suspension was filtered onto glass microfiber filters (GF/F, $0.7 \mu\text{m}$, Whatman, UK) using a vacuum pump (Fig. 5.3). Afterwards, the cells were washed with 0.5M ammonium formate, followed by 6 mL of 90 % acetone. The acetone-pigment extract was transferred into a 15 mL reaction tube. The suspension was incubated for 1 h at $4 \text{ }^\circ\text{C}$ in a mixing block at 100 rpm. In order to separate the cell debris from the pigment extract, the mixture was centrifuged 5 min at $3,000 g$. The supernatant was collected and measured using a UV/VIS spectrophotometer (Specord S600, Analytik Jena, Germany) at the follow-

ing wavelengths (470, 645 and 661.5 nm). The pigment densities of the sample were calculated according to Lichtenthaler (2001).



Figure 5.3.: Filtered carotenogenic (right) and non-carotenogenic (left) *D. salina* biomass. (Courtesy of I. Harriehausen).

$$\rho_{\text{Chla}} = (11.24 \cdot A_{661} - 2.04 \cdot A_{645}) \cdot \rho_{\text{Acetone}} = A_A \cdot \rho_{\text{Acetone}} \quad (5.1)$$

$$\rho_{\text{Chlb}} = (20.13 \cdot A_{645} - 4.19 \cdot A_{661}) \cdot \rho_{\text{Acetone}} = A_B \cdot \rho_{\text{Acetone}} \quad (5.2)$$

$$\rho_{\text{Car}} = \frac{(1000 \cdot A_{470} - 1.9 \cdot A_A - 63.14 \cdot A_B)}{214} \cdot \rho_{\text{Acetone}} \quad (5.3)$$

5.7 Determination of pigment composition using HPLC

Pigment extraction

Samples of the cell suspension were centrifuged for 10 min at 1,000 *g*. The supernatant was discarded and the cell pellet was washed with 0.5 M ammonium formate. The sample volume was adapted to result in a biomass dry weight of approximately 3 mg. The pellet was freeze-dried and stored at -20 °C until extraction. The extraction of the microalgal pigments was performed according to the method proposed by Lamers et al. (2010).

Analysis of pigment composition

The content of β -carotene, chlorophyll *a* and chlorophyll *b* in the biomass was quantified by High Performance Liquid Chromatography (HPLC) (Agilent 1100, Agilent Technology, USA), using a Reversed-Phase C18 column (Zorbax Eclipse Plus, 1.8 μm pore size, 100 mm x 2.1 mm). An injection volume of 2 μL was used for analysis. The elution was performed by a linear gradient from 100 % A (84 % acetonitrile, 2 % methanol, 14 % Tris buffer (0.1 M, pH 8.0)) to 10 % A and 90 % B (68 % methanol, 32 % ethyl acetate) for 2 min followed by elution with 100 % B for 3 min at a flow rate of 0.5 mL min⁻¹ (Polle et al., 2001). Detection of the pigments was performed with a diode array detector (DAD) and a fluorescence detector (FLD) in a range from 400 to 800 nm. The pigments were identified by comparing retention time and spec-

tral properties with commercial pigment standards (Sigma Aldrich, USA). The pigment content in the biomass was quantified by constructing a calibration curve with the respective standard.

5.8 Calculation of the optical cross section of chlorophyll *a*

The optical cross section of chlorophyll *a* was measured with a spectrophotometer (V-670, JASCO, United States) equipped with a 60 mm integrating sphere (ISN 723, JASCO, United States). The chlorophyll *a* specific absorption coefficient a^* was determined in baseline-corrected spectra at a wavelength of 664 nm. Using Eq. 5.4, the optical cross section of chlorophyll *a* was calculated (Wagner et al., 2006):

$$a^* = \frac{2.3 \cdot A(\lambda)}{d \cdot \rho_{\text{Chl}}} \quad (5.4)$$

5.9 Pulse amplitude modulation (PAM) fluorometry

The maximum photochemical quantum yield of PSII Φ_{II} was analyzed using a Dual-PAM 100 fluorometer (Walz, Germany). For this propose, 1.5 mL culture suspension was dark adapted in a glass cuvette for 10 min at 26 °C. Afterwards, the minimal fluorescence level (F_0) and maximal fluorescence level (F_m) induced by a saturating actinic light pulse (635 nm, 2000 $\mu\text{mol photons m}^{-2} \text{s}^{-1}$, 0.5 s) were determined with a measuring radiation of 5 $\mu\text{mol m}^{-2} \text{s}^{-1}$. The maximal photochemical quantum yield of PSII was calculated according to the following equation:

$$\Phi_{\text{PSII,max}} = \frac{F_m - F_0}{F_m} \quad (5.5)$$

For the saturation pulse analysis, the actinic light intensity was manually adjusted to the average incident light present in the reactor at the sampling time point. Prior measurement, the cells were subjected to a dark adaptation period of 10 min where the culture is only illuminated by the non-actinic measurement light that was used to determine the basal chlorophyll fluorescence level. A magnetic stirrer ensured a homogeneous distribution within the sample.

5.10 Flow cytometric analysis

All samples were diluted with cultivation medium to a cell density of approximately 1×10^6 cells mL^{-1} prior to the analysis. The cell density was monitored in diluted samples using volumetric counting of 200 μL cell suspension. Intrinsic cellular properties, such as cell integrity and granularity were monitored in unstained cell samples using the light scattering properties of the biomass in the forward (FSC) and side scatter (SSC) channels.

Instrument settings, data acquisition and analysis

The analysis of the above mentioned cellular properties was carried out in a flow cytometer (CyFlow Space, Sysmex-Partec, Germany) equipped with a blue argon solid state (488 nm) excitation laser. The signal intensities were calculated from the geometric mean values of the histograms and were displayed as arbitrary units (AU) per particle for the FSC and SSC signals or as relative fluorescent units (RFU) per particle for the different fluorescence emission channels FL1 - FL3 (see Table S1 for emission ranges). The sample flow rate was adjusted to $1 \mu\text{L s}^{-1}$, which corresponds to approximately 1,000 particles/s measured in a degassed 1.5 M NaCl solution as sheath fluid. Discrimination between the cellular signal and the background signal was performed by applying a gate on the red chlorophyll fluorescence emission signal (FL3) corresponding to the cellular signal. The algal cell populations inside the gate range were the dominant type of event detected. Data acquisition, gating and analysis were performed with FloMax software (Version 2.70). For further information regarding the instrument settings and data acquisition, please see the documentation according to the MIFlowCyt standard in the Supplementary material.

Fluorescence microscopy

The flow cytometric measurements were validated using a light and epifluorescence microscope (Axio Imager A1, Carl Zeiss, Germany) equipped with a digital camera system.

5.11 Analysis of macromolecular biomass composition using FTIR spectroscopy

The determination of the microalgal biomass composition was conducted using the Nicolet 6700 FTIR spectrometer (Thermo Scientific, Germany) equipped with a X-Y-Autosampler (Pike Technologies, USA).

Preparation of standards and samples

For all major biomass compounds in the microalgal biomass (proteins, carbohydrates and lipids), calibration curves with a appropriate reference substance according to Wagner et al. (2010) were recorded. The standards used for this calibration are listed in Table 5.2 together with their appropriate solvents. bovine serum albumine (BSA) was used as a standard for proteins and the polysaccharide laminarin for carbohydrates. The TAG molecule glycerol tripalmitate was shown to be a suitable standard for polar lipids. In initial experiments conducted with laminarin the distribution of the standard on the plate surface was very heterogeneous and due to that the corresponding peak heights for calibration had a high relative standard deviation. This problem has been overcome by dissolving laminarin in a mixture of $6 \mu\text{g } \mu\text{L}^{-1}$ BSA in water as shown in Table 5.2.

Table 5.2.: Concentration of standards for FTIR spectroscopy.

Macromolecular group	Substance	Solvent	Density range ($\mu\text{g } \mu\text{L}^{-1}$)
Proteins	BSA	Water	1 - 10
Carbohydrates	Laminarin	Water/BSA mix	4 - 14
Lipids	Glycerol tripalmitate	Trichloromethane	0.5 - 8

The measurement of the FTIR spectra was conducted on a 96-well microplate using $2 \mu\text{L}$ of cell suspension adjusted to a cell density $1 \times 10^8 \text{ cells mL}^{-1}$ (Fig. 5.4). The optimal cell density per spot was tested in a prior optimization step and was a trade-off between a high signal/noise ratio and a low sample volume. In order to reduce measurement and handling errors, 12 replicates were measured for each sampling time point. Subsequently, the microplate was placed in a incubator chamber at 40°C for 10 min to allow drying of the samples. In addition, the solvents listed in 5.2 were applied on the plate to serve as blank as well as for baseline correction.

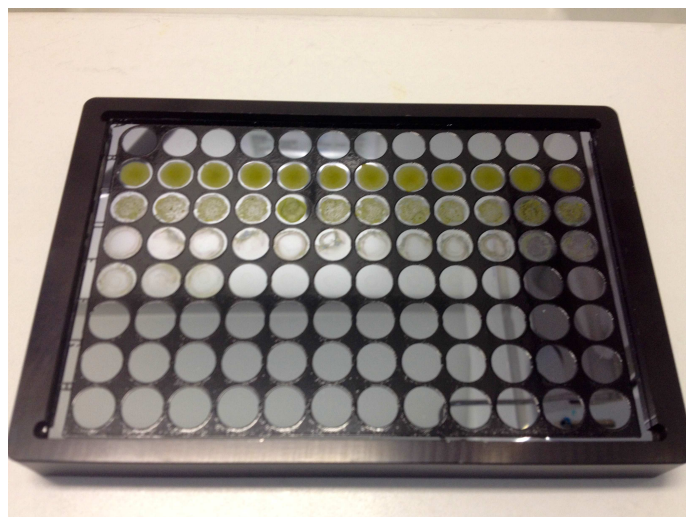


Figure 5.4.: FTIR plate with blank and cell suspensions dissolved in water and trichloromethane/methanol. Row A1: Blank with water, Row B1-12: cells solved in water, Row C1-12: cells solved in trichloromethane:methanol, Row D1-12: lipids extracted in trichloromethane:methanol. (Courtesy of I. Harriehausen).

Device settings and measurement procedure

To acquire the FTIR spectra of the samples, the microplate was inserted into the XY autosampler. The measurements were conducted using the following settings (32 scans per spot, spectral resolution of 4 cm^{-1} , wavenumber region from 3000 cm^{-1} to 750 cm^{-1}). The device and sample settings were set in the corresponding software (AutoPro Control and OMNIC (Thermo Scientific, Germany)). Afterwards, the spectra were baseline-corrected manually based on the blank measurements. The analysis of the resulting spectra was done with the TQAnalyst software (Thermo Scientific, Germany) by examining area and relative or absolute height of the absorption peaks.

5.12 Analysis of macromolecular biomass composition using biochemical assays

Protein determination using the Lowry method

The protein determination was conducted according to the protocol described by (Lowry et al., 1951). Briefly, the following solutions were prepared: solvent A (1 M NaOH), solvent B (5 % Na₂CO₃), solvent C (0.5 % CuSO₄ and 1 % sodium-potassium-tartrate) and solvent D (mixture of 2 mL solvent C and 50 mL solvent B). Solvent E was the Folin reagent. Subsequently, 1-2 mg algal dry mass were solved in 0.5 mL of bidistilled water and 0.5 mL solvent A. The mixture was heated at 60 °C for 10 min. After cooling the solution down to room temperature, 2.5 mL of solvent D was added and the mixture incubated for additional 10 min at room temperature. Afterwards, 0.5 mL of solvent E was added and followed by 15 min incubation at room temperature. Finally, the formation of the blue complex (due the reaction copper ions with the peptide bonds) can be determined by measuring the absorption at 595 nm using a UV/VIS spectrophotometer (Specord S600, Analytik Jena, Germany). The protein amount in the sample was calculated based on a calibration curve recorded with BSA.

Carbohydrate determination using the phenol-sulphuric acid method

The total carbohydrate fraction in the biomass was determined using the phenol-sulfuric acid method. Therefore, 0.5-1 mg dry biomass were dissolved in 400 μL bidistilled water. Afterwards, 400 μL of 90 % phenol solution was added to the solution. Subsequently, 2 mL concentrated sulphuric acid was added and the mixture was incubated for 30 min. The resulting absorption at 488 nm was determined using a UV/VIS spectrophotometer (Specord S600, Analytik Jena, Germany). The carbohydrate amount in the sample was calculated based on a calibration curve recorded with starch.

Lipid determination using the soxhlet extraction

The lipid content was determined using the soxhlet extraction based on a protocol described by Wang and Weller (2006). Prior to extraction, 5-10 g dry algal biomass was placed in a thimbleholder. Subsequently, 200 mL of *n*-hexane was filled into a pre-weighted solvent flask. The flask was then heated to 70 °C for 5 h. Afterwards, the *n*-hexane was vaporized at 30 °C and at 335 mbar in a rotary evaporator (Büchi, Switzerland) at 85 rpm until all *n*-hexane was evaporated. The algal lipid extract was dried in a climate chamber MKF 240 (Binder, Germany) at 70 °C overnight. Finally, the weight of lipid extract was determined on a balance.

5.13 Calculation of biomass and β -carotene yield on absorbed light

For the evaluation of the process performance, the biomass and β -carotene density as well as the volumetric productivity of biomass ($\text{g dw L}^{-1} \text{d}^{-1}$) and β -carotene ($\text{mg dw L}^{-1} \text{d}^{-1}$) were calculated as a function of cultivation time:

$$P_{\text{av,P}} = \frac{\rho_{\text{P}}(t) - \rho_{\text{P}}(0)}{t} \quad (5.6)$$

where t represent the cultivation time (d) and ρ_{P} is the product density (g dw L^{-1} or mg dw L^{-1}). Furthermore, the time-averaged yields of biomass $Y_{X,E}$ and β -carotene on absorbed light energy $Y_{\beta,E}$ were calculated by dividing the time-averaged productivity ($\text{mg L}^{-1} \text{d}^{-1}$) by the volumetric photon absorption rate of the evaluated time period ($\text{mol PAR photons L}^{-1} \text{d}^{-1}$) according to Mulders et al. (2014):

$$Y_{\text{P,E}} = \frac{P_{\text{av,P}}}{\frac{E_{\text{abs}} \cdot s_{\text{R}}}{V_{\text{R}}}} \quad (5.7)$$

where E_{abs} is the absorbed light ($\text{mol PAR photons m}^{-2} \text{d}^{-1}$), s_{R} is the reactor surface (m^2) and V_{R} is the reactor volume (L).

Chapter 6

Analysis of abiotic stress response during carotenogenesis

Although the large scale production of natural β -carotene in *D. salina* is of high industrial relevance, a systematic and detailed analysis of cellular features corresponding to its physiological state during storage molecule accumulation under abiotic stress conditions has not been analyzed in detail. The goal of this Chapter is to systematically explore the influence of abiotic stress on important bioprocess parameters, e.g. growth parameters, metabolic stress indicators, morphological properties and productivity in batch cultures of *D. salina* in a fully controlled flat-plate bioreactor setup.

6.1 Flow cytometric characterization of the cell population

D. salina was cultivated in the INFORS flat-plate photobioreactor system in batch mode under three different cultivation conditions (Table 6.1). The adaptational abiotic stress response and their influence on the bioprocess performance represented by the biomass and β -carotene yield on absorbed light was analyzed under the presence of high light and nutrient stress.

Table 6.1.: Overview of experimental conditions for batch cultures of *D. salina* under abiotic stress conditions.

Reactor system	Condition	Abbr.	Light intensity per biomass ($\mu\text{mol m}^{-2} \text{s}^{-1} \text{g}^{-1} \text{dw L}$)	Extracellular nitrogen density (g N L^{-1})
Infors Labfors Lux	Low light	LL	300	0.51
	High light	HL	3000	0.51
	High light and nitrogen deprivation	HL-ND	3000	0.05

6.1.1. Cell growth

The most important parameter for growth monitoring is the determination of the cell density. Absolute cell counting with a flow cytometer is a rapid and statistically reliable method to monitor the number of cells in a culture.

The cell densities of the batch cultures were monitored until the early stationary growth phase was reached using true volumetric cell counting in samples diluted to approximately 1×10^6 cells mL^{-1} . The forward scatter signal collected from 488 nm excitation was corrected for the non-algal background by applying a manual gate on the chlorophyll signal for all analyzed samples. Under control conditions, the algal cell population is the dominant type of event (>90%) detected compared to the background signal.

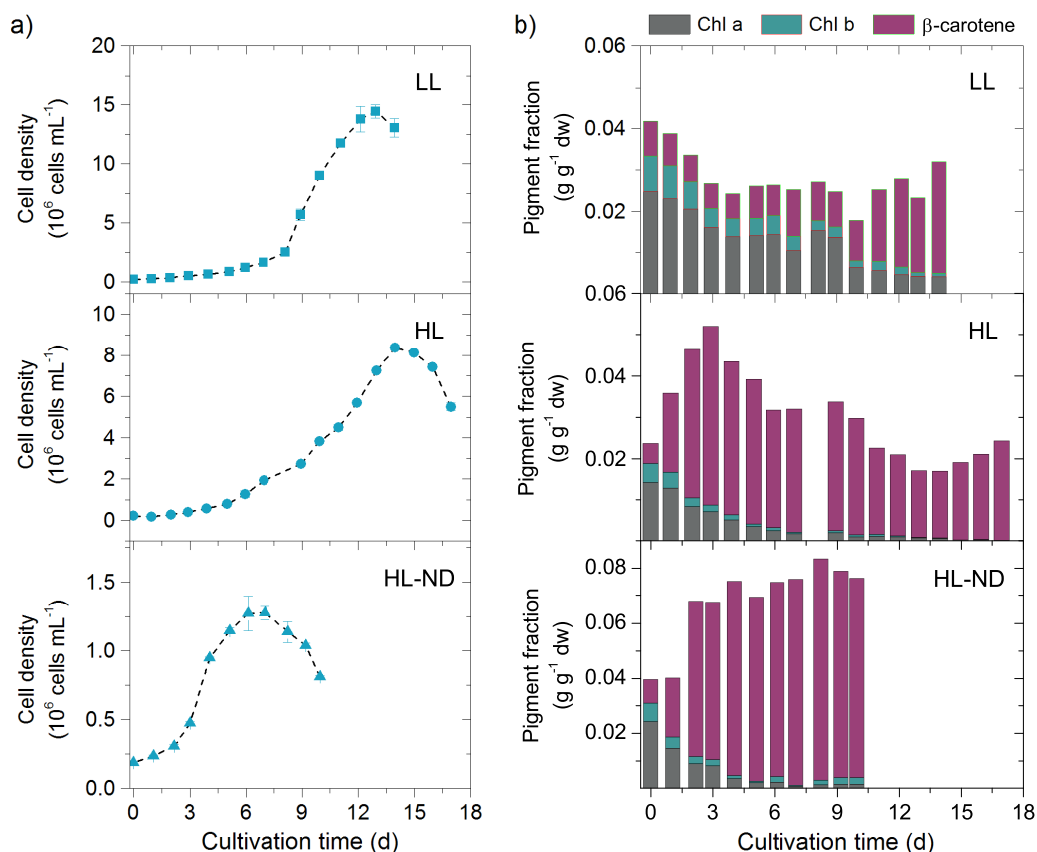


Figure 6.1.: Effect of abiotic stress type on the cell growth and pigment composition of *D. salina*. a) Cell density growth curves and b) Mass fractions of chlorophyll *a*, *b* and β -carotene for the three investigated cultivation conditions; LL - low light, HL - high light, HL-ND - high light and nitrogen depletion. The symbols represent the mean values and the error bars correspond to the deviation from the average value of duplicate measurements.

The time series for the biomass growth is shown in Fig. 6.1a. Comparing all three cultivation conditions, the low light culture (LL) reached the highest final cell density, 1.4×10^7 cells mL^{-1} . The final cell density reached in the stationary growth phase for the cultivation under high light (HL) was only slightly lower compared to the LL con-

ditions, namely 8.4×10^6 cells mL^{-1} . The stationary cell density under high light and nitrogen depletion (HL-ND) was 1.3×10^6 cells mL^{-1} and 10 times lower compared to the LL conditions (Fig. 6.1a). All cultures had an initial *lag* phase of approximately two days until they entered the exponential growth phase. Depending on the cultivation conditions, the early stationary phase was reached at different time points. In the HL-ND culture, the stationary growth phase was reached at day 6, three days after the depletion of the extracellular nitrogen source. The nitrogen-replete cultures reached the stationary phase at day 13 and 14 for the LL and HL culture, respectively. Since the light intensity of the reactor was adjusted to the biomass growth (according to the specifications in Table 6.1), the determination of the extracellular nitrogen density confirmed that the growth under all three conditions was always nutrient-limited. In terms of biomass density on dry weight basis, the LL cultivation resulted in 7.2 g dw L^{-1} , the HL cultivation in 6.5 g dw L^{-1} and the HL-ND in 1.1 g dw L^{-1} (Fig. 6.2a).

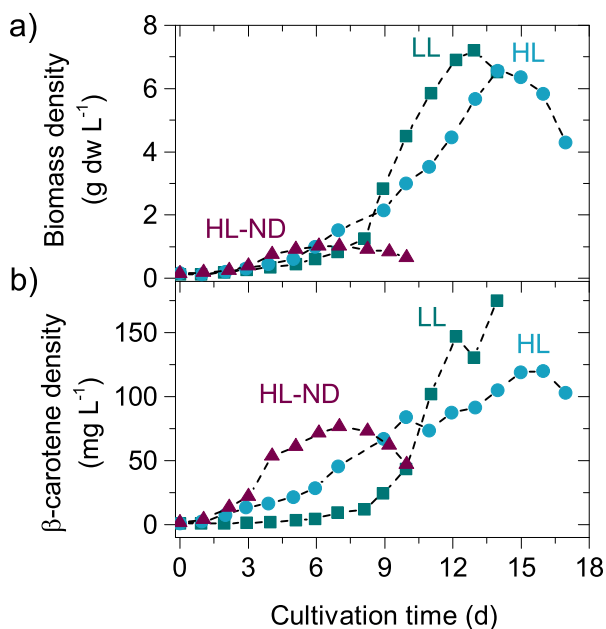


Figure 6.2.: Effect of abiotic stress type on the a) biomass density on dry weight basis and b) β -carotene density for the three investigated cultivation conditions.

6.1.2. Abiotic stress related adaptation of pigment content

Fig. 6.1b illustrates the time course of the pigments β -carotene, chlorophyll *a* and *b* as a function of cultivation time. The presence of high light conditions (HL, HL-ND) led to an instantaneous accumulation of light-stress induced β -carotene (Fig. 6.1b). At day 1 after light-stress induction the β -carotene fraction was already 3 to 4 times higher compared to the basal level. The highest β -carotene fraction has been detected under HL-ND conditions. When nutrient limitation started at day 3 after inoculation, a β -carotene level of 8.0% (w/w) at day 8 was achieved. The maximal β -carotene fraction under HL conditions was achieved at day 3 with 4.3% (w/w) and was constantly

high until the fixed light stress of $3000 \mu\text{mol m}^{-2} \text{s}^{-1} \text{g}^{-1} \text{dw L}$ could be maintained. At day 7, the physical limitation of the light panel with a maximum light intensity of $3000 \mu\text{mol m}^{-2} \text{s}^{-1}$ has been reached since the biomass density achieved 1 g dw L^{-1} . Due to the decreased light stress, the β -carotene fraction lowered from 3.0 to 1.6% (w/w). When the nutrient starvation of the HL culture occurred the β -carotene fraction increased again to 2.3% (w/w) in the stationary phase. Under LL conditions, the β -carotene fraction was low and at its basal level of 0.7% (w/w) under nitrogen-replete conditions. When nitrogen becomes limited at day 11, the β -carotene fraction increased to 2.6% (w/w) in the stationary phase which is comparable to the level obtained in the HL culture. Although the β -carotene fractions under LL and HL conditions are low compared to the HL-ND cultivations, the β -carotene density is significantly higher due to the high biomass densities achieved under this conditions. The maximum β -carotene density was reached under LL conditions with 175 mg L^{-1} , followed by 120 mg L^{-1} under HL conditions and 76 mg L^{-1} under HL-ND conditions (Fig. 6.2b).

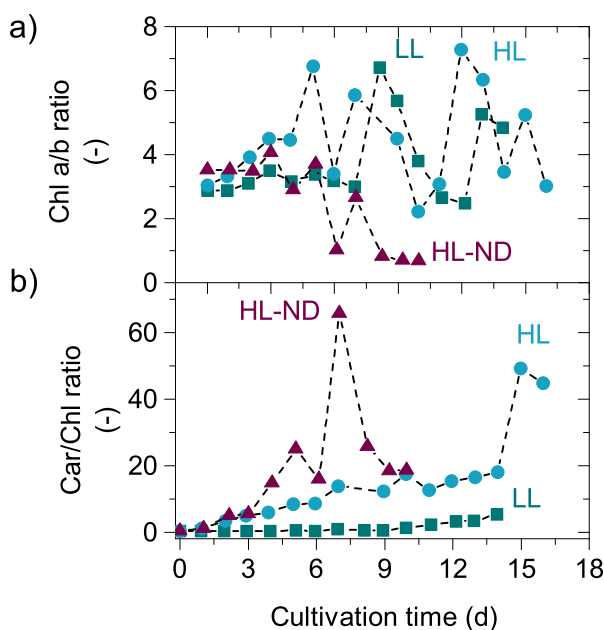


Figure 6.3.: Effect of abiotic stress type on the a) chlorophyll a/b ratio and b) β -carotene/chlorophyll ratio.

The stock cultures used as inoculum for batch cultivations were in late exponential phase and after inoculation they photoacclimate to the light conditions in the flat-plate photobioreactor. Under all three cultivation conditions (LL, HL and HL-ND), the amount of absorbed light energy in the initial cultivation phase is higher than the energy required for growth. This imbalance led to a reduction in the chlorophyll pigment fraction due to photoacclimation processes (Fig. 6.1b). Since, chlorophyll b is located in the upper layer of the antenna complex the degradation occurs faster compared to chlorophyll a , especially under high light conditions. During high light stress and nutrient depletion (HL-ND) the rate of chlorophyll b degradation is higher compared to that of chlorophyll a leading to a higher chlorophyll a/b ratio (Fig. 6.3a). Under low light conditions, the chlorophyll a/b ratio remains high, which is in agree-

ment with previous studies from Webb and Melis (1995). The simultaneous reduction in the chlorophyll fraction and accumulation of β -carotene led to a significant increase in the carotene/chlorophyll ratio (Fig. 6.3b).

6.1.3. Formation of carotenoid-containing lipid globules led to increased granularity of the cells

The accumulation of neutral lipid globules is a prerequisite for β -carotene accumulation. During the environmental stress response, an increased intracellular granularity has been observed in microalgal cultures making this property a potentially useful marker for the physiological state of a cell (Hyka et al., 2013). The presence of abiotic stress often leads to the accumulation of storage molecules such as starch, neutral lipids and β -carotene, resulting in a more complex internal structure and a larger proportion of scattered light. The variations in the cell granularity were analyzed using the geometric mean value of the side scatter signal in the flow cytometric analysis. The dynamics of cell granularity correlate with the β -carotene accumulation in a linear manner (Fig. 6.4). Upon exposure to abiotic stress an increase of the cell granularity up to 4-fold compared to the basal level was detected. This finding illustrates that the formation of neutral lipid globules results in more complex internal structure of the cell detected by a higher proportion of side-scattered light.

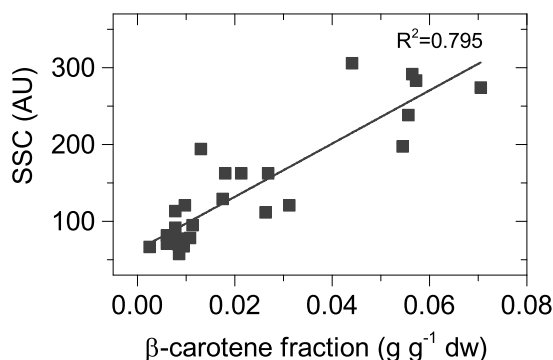


Figure 6.4.: Relationship between cell granularity (SSC) and β -carotene fraction in the biomass.

6.2 Biotechnological parameters

The most productive cultivation conditions in terms of volumetric biomass productivity was the LL culture with a maximal value of $0.56 \text{ g dw L}^{-1} \text{ d}^{-1}$ followed by the HL culture with $0.45 \text{ g dw L}^{-1} \text{ d}^{-1}$, whereas the HL-ND culture reached only $0.15 \text{ g dw L}^{-1} \text{ d}^{-1}$ (Fig. 6.5a). Especially the pronounced photoinhibitory effects on growth under high light conditions led to the lowered volumetric productivities compared to the light limiting conditions. For the biomass yield on absorbed light energy $Y_{X,E}$ the LL culture clearly outperforms the high light cultures (HL and HL-ND). Due to the lower incident light on biomass ratio the highest $Y_{X,E}$ of $0.12 \text{ g dw mol}^{-1} \text{ photons}$

was calculated, whereas the HL and HL-ND cultures had only 0.016 and 0.010 g dw mol⁻¹ photons (Fig. 6.5c).

The highest volumetric β -carotene productivity has been reached in the HL-ND culture with 12.8 mg L⁻¹ d⁻¹, followed by the LL culture with 12.0 mg L⁻¹ d⁻¹ and the HL culture with 8.3 mg L⁻¹ d⁻¹ (Fig. 6.5b). Although the β -carotene density under HL-ND conditions is significantly lower compared to the LL and HL conditions, the shorter batch time of only 10 days led to the highest volumetric productivity. The β -carotene yield on absorbed light reached its maximum value in the initial phase of the light-stressed culture (Fig. 6.5d), namely 2.1 and 1.3 mg mol⁻¹ photons. The β -carotene yield on absorbed light for the LL culture was almost constant during the whole cultivation period at a value around 0.6 mg mol⁻¹ photons.

The yield of secondary carotenoids on absorbed photons is an important process parameter in order to estimate the performance and to optimize large scale systems, but has only rarely been addressed in previous studies. Mulders et al. (2014) published a comparable secondary carotenoid yield on absorbed light of 2.75 mg mol⁻¹ photons for *Chlorella zofingiensis* cultivated under nitrogen-depleted conditions. The detailed studies performed by Lamers et al. (2010) and Lamers et al. (2012) cultivating *D. salina* under high light conditions (1400 μ mol photons m⁻² s⁻¹ incident light) as well as under low light (200 μ mol photons m⁻² s⁻¹ incident light) and nutrient-limited conditions in a turbidostat achieved higher volumetric β -carotene productivities (37 mg L⁻¹ d⁻¹ under HL conditions, 18.5 mg L⁻¹ d⁻¹ under LL conditions) and β -carotene yield on light (4.6 mg mol⁻¹ under HL conditions, 16.2 mg mol⁻¹ under LL conditions) compared to this study using batch operation mode. This outcome clearly indicates that innovative process design approaches have a large potential to optimize the performance of biotechnological production systems.

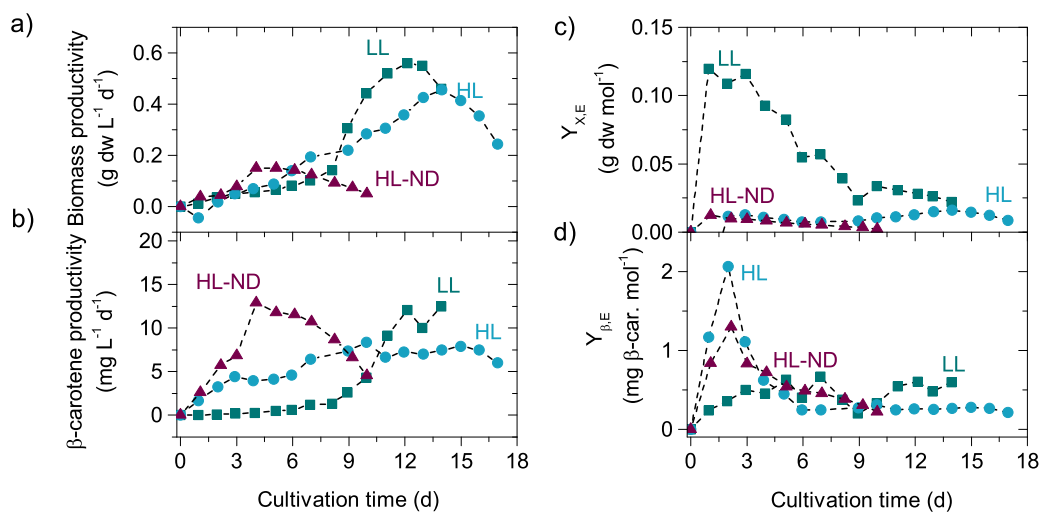


Figure 6.5.: Effect of abiotic stress type on a) the biomass productivity on dry weight basis, b) the β -carotene productivity, c) the time-averaged biomass yield on absorbed light and d) the time-averaged β -carotene yield on absorbed light.

Table 6.2.: Performance of the batch cultivations.

Property	Unit	LL	HL	HL-ND
Max. biomass density	g dw L ⁻¹	7.22	6.55	1.02
Max. biomass productivity	g L ⁻¹ d ⁻¹	0.55	0.45	0.15
Max. β -carotene density	mg L ⁻¹	175.18	120.04	76.42
Max. β -carotene fraction	mg g ⁻¹ dw	26.86	43.28	80.30
Max. β -carotene productivity	mg L ⁻¹ d ⁻¹	12.05	7.90	12.88

6.3 Photosynthetic performance

In order to regulate their photosynthesis, algae have developed mechanisms to adapt to fluctuating light conditions by regulating light absorption and efficiency of light conversion into chemical energy. When comparing the content of light-harvesting pigments with the photosynthetic light curve, conclusions on the physiological changes in different light-adapted states can be drawn. For this purpose, additional cultivations in batch operation mode under static light conditions (constant incident light intensity) were carried out as shown in Table 6.3.

Table 6.3.: Overview of experimental conditions for PAM and FTIR measurements.

Reactor system	Condition	Abbr.	Light intensity ($\mu\text{mol m}^{-2} \text{s}^{-1}$)	Extracellular nitrogen density (g N L ⁻¹)
PSI FMT-150	Low light	LL	180	0.52
	High light	HL	1500	0.49
Infors Labfors Lux	High light and nitrogen deprivation	HL-ND	1500	0.12

6.3.1. Effective PSII quantum yield in low- and high-light acclimated cells

The effective PSII quantum yield ($\Phi_{\text{PSII,eff}}$) is a qualitative measure for efficiency at which the incident light is absorbed and used for photochemistry. The photon uptake rate correlates with the number of photosystems and the efficiency at which they operate. Consequently, under high irradiance conditions the photosystems operate at low efficiency. Fig. 6.6 shows the dependency of the effective PSII quantum yield on the average light intensity. In both, the low light and high light acclimated cells, the initial effective quantum yield was around 0.55 which is in agreement with Herrmann et al. (1997). With increasing illumination, the fraction of photons used for photochemistry declined linearly for low- and high-light acclimated cells. At 1300 $\mu\text{mol photons m}^{-2} \text{s}^{-1}$, the effective quantum yield reached a constant value of 0.1.

6.3.2. Electron transport rate in low- and high-light acclimated cells

The relative electron transport rate (ETR) is an indicator for the photosynthetic capacity of the cells and therefore the ability to provide energy for cell growth and metabolism. It is calculated as described in Eq. 3.3 by multiplication of the average

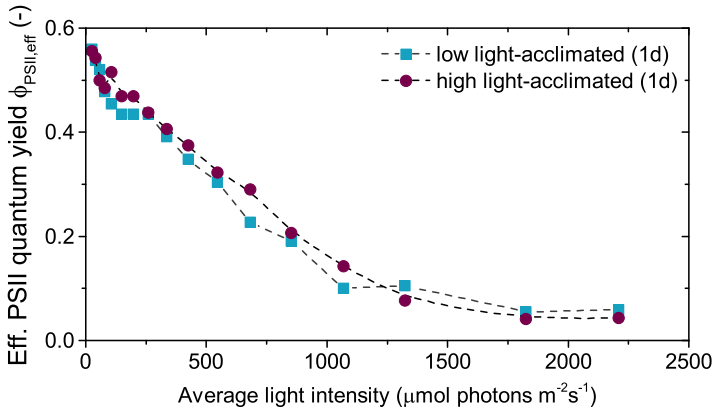


Figure 6.6.: Relationship between effective quantum yield of PSII and average light intensity for cells acclimated to low-light and high-light conditions.

light intensity with the effective PSII quantum yield and the default ETR factor of 0.42 (Schreiber et al., 2011). The default ETR factor originates from a "model" leaf and describes the fraction of the incident light intensity in the PAR region that is absorbed in PSII. The value of 0.42 originates from a study of Bjorkman and Demmig (1987) where 50 % of the PAR have been distributed to PSII and 84 % of the PAR was absorbed by photosynthetic pigments in a standard leaf (Schreiber et al., 2011). Though the calculated value for the relative ETR is only an estimate without detailed knowledge about of PSII content and the PSII absorption cross-section (Schreiber et al., 2011). Thereby, the relative ETR does not dependent on the chlorophyll content of the sample but since the ETR curves were recorded with the same light source and the same wavelength of actinic light they are still comparable to each other.

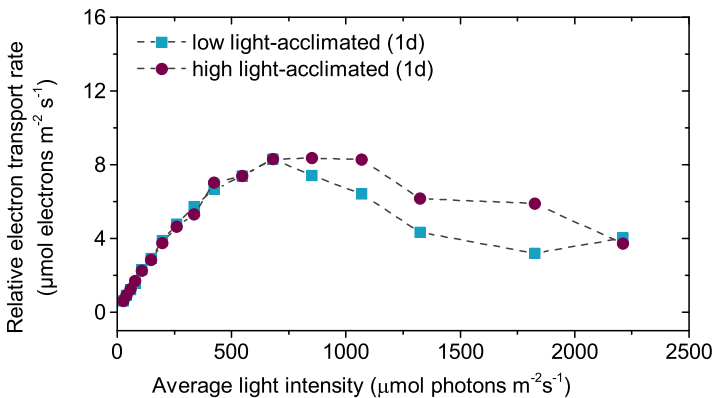


Figure 6.7.: Relationship between relative electron transport rate and average light intensity for cells acclimated to low-light and high-light conditions.

The relationship between relative ETR and average light intensity is shown in Fig. 6.7. As already illustrated in Fig. 4.2, the curve shows three characteristic phases (light limitation, light saturation and photoinhibition). Under both conditions (low- and high-light acclimated cells), the ETR increased linearly until a light intensity of 550 $\mu\text{mol photons m}^{-2}\text{s}^{-1}$ was reached. In this light regime, the light intensity

directly correlates with the rate of photosynthesis. Both cultures reached a maximal ETR value of 6.9 to 8.3 $\mu\text{mol electrons m}^{-2} \text{s}^{-1}$. The light saturation range for the low light-acclimated culture was from 550 - 860 $\mu\text{mol photons m}^{-2} \text{s}^{-1}$, whereas the high light-acclimated culture showed a prolonged light saturation phase from 550 - 1070 $\mu\text{mol photons m}^{-2} \text{s}^{-1}$. The light saturation phase was followed by a photoinhibition phase where the ETR declined to about 4 $\mu\text{mol electrons m}^{-2} \text{s}^{-1}$ at 2200 $\mu\text{mol photons m}^{-2} \text{s}^{-1}$.

6.3.3. Photosynthetic capacities under abiotic stress conditions

Low light conditions

Fig. 6.8 illustrates how the photosynthetic performance of *D. salina* changes for cultivation under low light conditions presented by the time course of the three photosynthetic parameters: operating efficiency of the photosystem II ($\Phi_{\text{PSII,eff}}$), maximum quantum yield of PSII ($\Phi_{\text{PSII,max}}$) and non-photochemical quenching (NPQ). The time course for maximum and effective quantum yield showed comparable trends over the whole cultivation period as both increase from 0.42 to 0.67. This indicates that the photochemistry works effectively under LL conditions since effective and maximum quantum yield of PSII show only low deviations from each other. In addition, the value for NPQ remained at a relatively low level over the cultivation period, namely 0.2 from day 1 to day 3 and decreased to 0.1 from day 4 until the end of the cultivation period. This is in agreement with the trends observed for $\Phi_{\text{PSII,eff}}$ and $\Phi_{\text{PSII,max}}$ as under conditions where photosynthesis works effectively, dissipation mechanisms such as NPQ are inactive. However, the lower maximum quantum yield of 0.42 in the initial cultivation stage illustrates the photosynthetic performance was not fully exploited at this time. Possible explanations for the lowered $\Phi_{\text{PSII,eff}}$ could be nutrient limitations in the inoculum culture which led to an impaired photosynthetic potential. Moreover, the turbulent flow regime in the flat plate reactor might have induced a lag phase in the culture affecting metabolic activity and growth after inoculation. After recovery, the quantum yield remained high until the end of the cultivation and reached the maximal values for the quantum yield of 0.65 reported for *D. salina* by Herrmann et al. (1997).

High light conditions

In comparison to the LL cultivation, the photosynthetic parameters for HL cultivation show pronounced fluctuations as illustrated in Fig. 6.9. Effective and maximum quantum yield of PSII was at 0.6 in the initial cultivation phase and close to its maximal value determined under LL conditions and reported by Herrmann et al. (1997). The NPQ value for inoculum was 0.23 and is low as the stock culture was grown under LL conditions. In the course of the cultivation when the light stress becomes persistent the decrease of the effective quantum yield to 0.15 - 0.3 is accompanied by a simultaneous increase of the NPQ from 0.23 to 1.4. In the early exponential phase, the maximum quantum yield decline in the same way as observed for the effective quantum yield. However from day 4 on, the maximal quantum yield increased again and reached its maximal value again at day 5. The drop in the quantum yield under HL conditions was caused by two adaptational processes: photoinhibition and photoac-

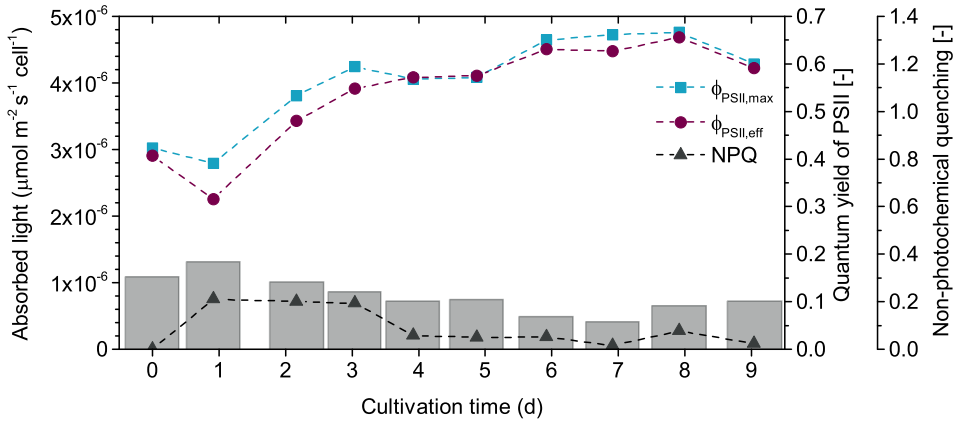


Figure 6.8.: Photosynthetic performance expressed as maximum ($\Phi_{\text{PSII,max}}$) and effective quantum yield of PSII ($\Phi_{\text{PSII,eff}}$) as well as non-photochemical quenching (NPQ) under LL conditions in correlation to the incident light per cell.

climation as already observed for *D. salina* by Herrmann et al. (1997) and Ghetti et al. (1999). First, the presence of over-saturating light in the culture led to photoinhibitory effects. Secondly, the cell adjusted its pigment composition in the antenna by degradation of chlorophyll pigments and truncates its size, as explained in Section 2.2 and observed by Neidhardt et al. (1998). As a consequence, photon absorption and photochemistry work less efficient protecting the cell from oxidative stress. To further increase the photoprotective response, the accumulation of carotenoids assist the absorption of oversaturating light and the quenching of ROS which explains the continuous increase of the NPQ value over the cultivation time. On day 1 after inoculation the NPQ value was still low although the light stress was already pronounced leading to overexcited chlorophyll states in the photosystem as explained in Section 2.1. This observation could be attributed to the presence to the xanthophyll cycle where an epoxidation mechanisms leads to the conversion of violaxanthin to zeaxanthin, which is an alternative dissipative path compared of non-photochemical quenching (see Section 2.1). The xanthophyll cycle acts on the time scale of minutes and its role in *D. salina* was investigated in detail by Jin et al. (2003). The simultaneous acting of xanthophyll cycle and non-photochemical quenching are effective in photoprotection of *D. salina* as the recovery of the maximum PSII quantum yield to its maximal value demonstrated.

High light and nutrient-depleted conditions

The observations made for the cultivation under HL-ND conditions are similar to the HL conditions to a large degree. The maximal quantum yield of the inoculum is 0.62 and close to the maximal literature value (Herrmann et al., 1997). The effective quantum yield was 0.56 and just slightly lower than the maximal quantum yield. One day after induction of the light stress, maximal as well as effective PSII quantum yield dropped significantly to 0.38 and 0.29. In the further course of the cultivation, the effective quantum yield remains at a stable level of 0.26-0.30, whereas the maximum quantum yield declined slightly to 0.36 until day 2 and started to recover to 0.48 on day 4. When the extracellular nitrogen in the medium was completely depleted,

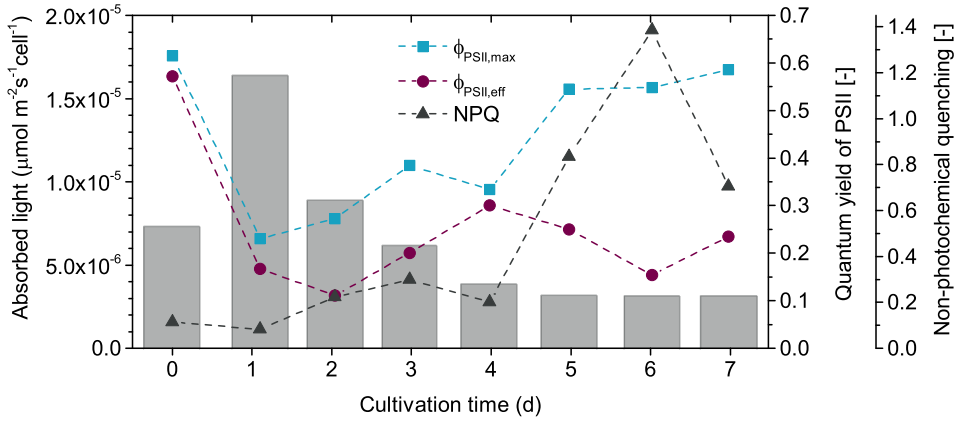


Figure 6.9.: Photosynthetic performance expressed as maximum ($\Phi_{\text{PSII,max}}$) and effective quantum yield of PSII ($\Phi_{\text{PSII,eff}}$) as well as non-photochemical quenching (NPQ) under HL conditions in correlation to the incident light per cell.

the maximum quantum yield dropped again to 0.29 in the stationary phase of cell growth. Except of day 5, for the effective and maximum quantum yield showed similar trends as under HL conditions. In contrast to the HL cultivation, no significant rise in the NPQ level was detected under HL-ND conditions. The initial NPQ value was with 0.43 already twice as high as under LL or HL conditions. Surprisingly, the presence of light stress does not correlate with an increasing NPQ value. It rather follows the same tendency as observed for the maximum quantum yield. The signal-to-noise ratio for the PAM measurement under HL-ND as relatively low compared to the cultivations under nitrogen-replete conditions due to the very low chlorophyll content in the biomass. Since the measuring principle of PAM is the emission of chlorophyll fluorescence, the detection in diluted cell suspension with low chlorophyll content is more challenging and error-prone than in biomass with higher chlorophyll content. However, the observed behavior should still adequately reflect the changes in photosynthetic performance.

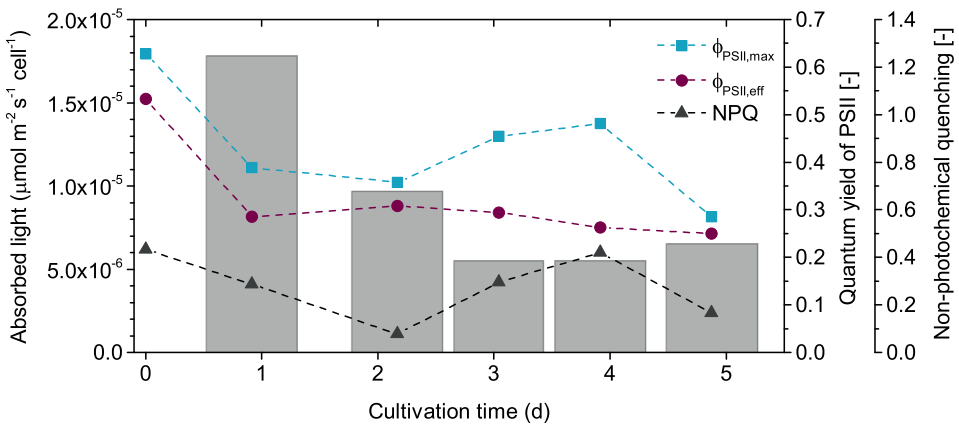


Figure 6.10.: Photosynthetic performance expressed as maximum ($\Phi_{\text{PSII,max}}$) and effective quantum yield of PSII ($\Phi_{\text{PSII,eff}}$) as well as non-photochemical quenching (NPQ) under HL-ND conditions in correlation to the incident light per cell.

6.4 Macromolecular biomass composition

The content of high-value products, such as carotenoids or polyunsaturated fatty acids, in the biomass is typically below 10% and a large fraction of residual biomass mainly composed out of carbohydrates and proteins remains unused. In contrast, the economic feasibility of microalgal processes is often difficult to achieve because of energy and cost-intensive harvesting and extraction steps. Therefore, microalgal process design requires tailor-made biorefinery approach to valorize most of the biomass fractions. An important prerequisite is the fast characterization of the macromolecular biomass composition since conventional biochemical assays are time-consuming and often require large sample amounts. Therefore, the following section presents infrared spectroscopy as a fast and reliable method to determine the macromolecular biomass composition of *D. salina* under various abiotic stress conditions.

Algae biomass is mainly composed out of three biomacromolecules; proteins, carbohydrates as well as polar and apolar lipids. Commonly their amount in the biomass is quantified by single biochemical methods (see Chapter 5). FTIR spectroscopy is able to analyze several IR-active compounds in a multi-component mixture (such as biomass) in one sample and in a short time (see Section 3.3). In the following section, the applicability of FTIR spectroscopy to biomass composition analysis of *D. salina* is discussed.

6.4.1. Optimization and validation of FTIR spectroscopy for analysis of biomass composition

The main requirement for a standard substance is that it possesses the same characteristic atomic bonds and consequently peaks at the same characteristic wavenumber, as the macromolecule it represents. In Table 3.3, the most important atomic bonds that were confirmed by Giordano et al. (2001) and Liu et al. (2013) are shown with the characteristic wavenumbers at which they absorb and the macromolecule they are assigned to. Previous research by Wagner et al. (2010) demonstrated the applicability of BSA as protein standard, glycerol tripalmitate for lipids and laminarin for carbohydrates for microalgae biomass. Therefore, absorption spectra for the aforementioned standards were collected and depicted in Fig. 6.11. The absorption spectra of BSA, laminarin and glycerol tripalmitate agree in wavenumber and relative height of the characteristic absorption peaks with Wagner et al. (2010). A comparison of the characteristic wavenumbers is shown in Table 6.4.

Table 6.4.: Characteristic wavenumbers identified for *D. salina* in this work compared to Wagner et al. (2010).

Macromolecular group	Substance	Wavenumber (cm ⁻¹) in this study	Wavenumber (cm ⁻¹) by Wagner et al. (2010)
Carbohydrates	Laminarin	1157	1150
Proteins	BSA	1545	1545
Lipids	Glycerol tripalmitate	1736	1740

The protein standard BSA showed two major peaks corresponding to the amide I and II bands at 1545 and 1658 cm⁻¹. Glycerol tripalmitate has been proven to be an appropriate standard for lipids due to its characteristic peaks at 2849 and 2915 cm⁻¹, which

can be assigned to the C-H bond of saturated carbons and at 1736 cm^{-1} for symmetric C=O stretch of membrane lipids and fatty acids. The polysaccharide laminarin consists of 23-25 glucose units. Its absorption spectrum is comparable to glucose in several wavenumber regions, e.g in the characteristic area for the symmetric C-O stretch of monosaccharides from $1100-1000\text{ cm}^{-1}$. Beside, laminarin also show characteristic bands in the region of $1200-1100\text{ cm}^{-1}$ which can be assigned to the symmetric C-O-C stretch of polysaccharides. The laminarin absorption spectrum exhibits a local maximum at 1157 cm^{-1} .

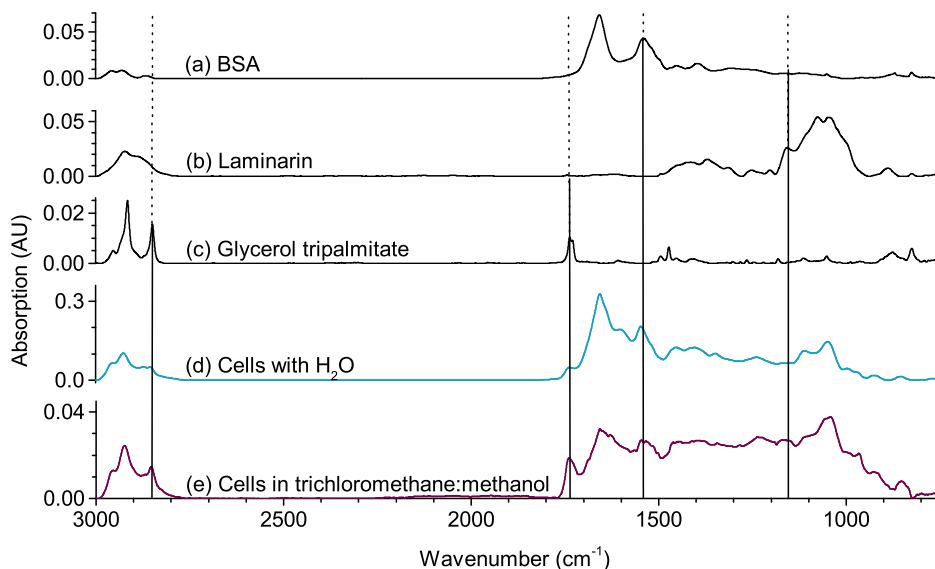


Figure 6.11. FTIR absorption spectra for the three macromolecular standards: a) BSA, b) laminarin and c) glycerol tripalmitate as well as the algal cells diluted in d) water and e) a trichloromethane:methanol mixture.

In order to evaluate whether the above mentioned standards are appropriate to enable a quantification of *Dunaliella* biomass, the characteristic peaks identified in Table 6.4 were tested for various cell densities of *D. salina* ranging from $0.5-1 \times 10^8$ cells mL^{-1} grown under low light and nutrient-replete conditions (see Table 6.3 for cultivation conditions). Fig. 6.11 shows that all characteristic peaks identified in Table 6.4 for the chosen macromolecular standards were also present in the cellular spectra. However, as already found by Wagner et al. (2010) there is a spectral overlap with the amide I band at 1650 cm^{-1} and the symmetric C=O stretch at 1736 cm^{-1} which is characteristic for fatty acids.

Subsequently, a calibration curve for the selected standards was constructed to enable a quantification of the cellular macromolecule content based on the height of the characteristic peaks listed in Table 6.4. The coefficient of determination (R^2) was 0.99 for BSA and glycerol tripalmitate and 0.98 for laminarin which indicates a good linear correlation between the peak height and the molecular density in the sample.

6.4.2. Application of FTIR spectrometry for relative macromolecular changes under abiotic stress

Based on the identified characteristic peaks (see Table 6.4), the macromolecular composition of *D. salina* under abiotic stress conditions was investigated (see Table 6.3 for cultivation conditions). Fig. 6.12 depicts the changes in biomass composition when cultivated under LL, HL and HL-ND conditions compared to the inoculum. A visual comparison of the peak heights of the at the characteristic wavenumbers already provide insights about the relative changes in the biomacromolecules. The results of the macromolecular ratios calculated for the stationary phase compared to the inoculum grown under low light and nutrient-replete conditions is shown in Fig. 6.13.

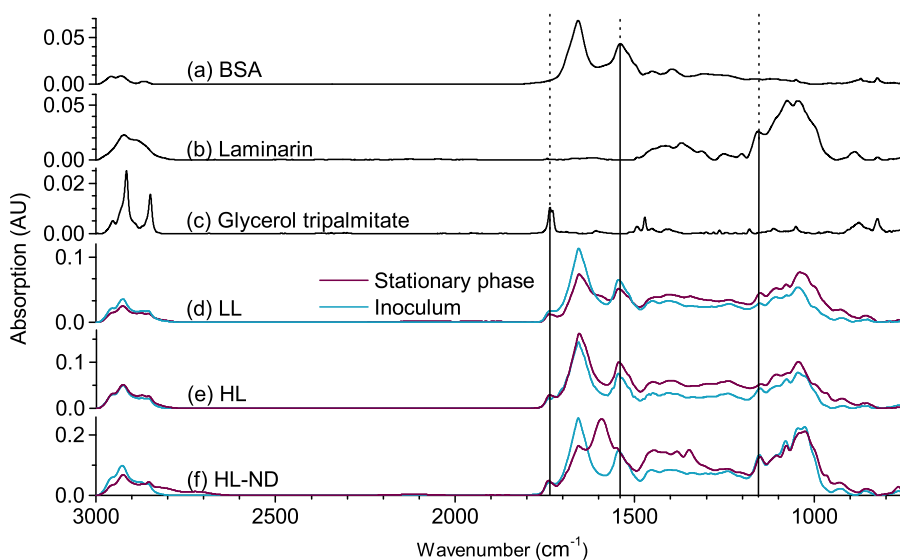


Figure 6.12.: FTIR absorption spectra for the three macromolecular standards: a) BSA, b) laminarin and c) glycerol tripalmitate) as well as algal cells of the inoculum and stationary phase cultivated under the following conditions: d) LL, e) HL and f) HL-ND.

It is clearly visible that the macromolecular composition under nitrogen-replete conditions (LL and HL) showed only minor changes compared to the inoculum. Only under prolonged nutrient-starvation a significant effect on the biomass composition was detected (Fig. 6.12). In the HL-ND cultivation, the peak height of the amide-I band at 1650 cm⁻¹ (symmetric C=O stretch) corresponding to the protein fraction decreased significantly. This is in line with current knowledge where biochemical analysis of *D. tertiolecta* by Fabregas et al. (1989) already revealed a positive correlation between nitrate density in the medium and protein fraction in the biomass. Additionally, an unknown peak was detected between the amide I and amide II peak at 1600 cm⁻¹. According to Günzler and Gremlich (2003), the strong absorption at this wavenumber is (among others) characteristic for the carbon double bond (C=C) of aromatic compounds. Another explanation for the peak at 1600 cm⁻¹ could be a structural change in the protein structure as a consequence of prolonged nitrogen starvation. Günzler and Gremlich (2003) names a substitution of a neighboring atom of the amide band or a mesomeric effects as a possible reason for the peak shift as already shown in Halverson et al. (1991), where a shift of the amide I band from 1640 cm⁻¹ to 1610 cm⁻¹ is caused by an isotopic replacement of a C atom in an anti-parallel β -sheet.

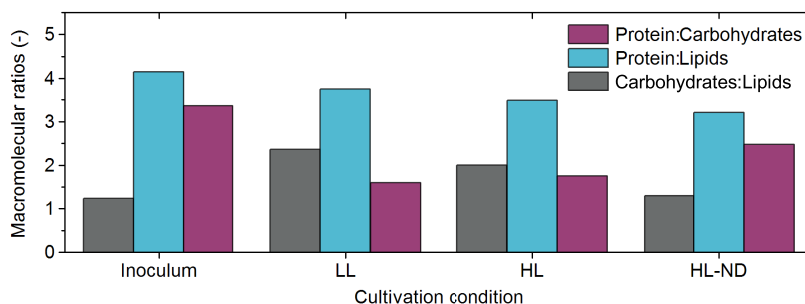


Figure 6.13.: Macromolecular ratios of carbohydrates, protein and lipids in the inoculum and stationary phase of batch cultivations.

Based on the peak heights of the characteristic peaks, the macromolecular ratios of protein:carbohydrate, protein:lipid and carbohydrate:lipid were calculated and shown in Fig. 6.13. The protein:carbohydrate ratio ranges from 1.23 in the inoculum to 2.3 under LL conditions. The higher protein:carbohydrate ratio under LL conditions was caused by a higher protein fraction and lower carbohydrate fraction in the stationary phase compared to the inoculum. The protein:lipid ratio decreases under all three cultivation conditions from 4.14 to 3.20 under HL-ND conditions indicating a slightly higher lipid fraction in the stationary phase compared to the inoculum. The carbohydrate:lipid fraction indicates that the highest fraction was achieved in the inoculum with a ratio of 3.36, where the starch is the preferred short term storage energy sink which provide energy for cell growth and division. In the stationary cultures, the carbohydrate:lipid ratio increases with increasing abiotic stress. The LL culture had a ratio of 1.59, the HL culture of 1.74 and the HL-ND culture 2.47. The relatively high carbohydrate:lipid ratio under HL-ND conditions indicates that under nutrient depletion where protein synthesis is strongly impaired starch is a good energy sink beside carotenoid-containing lipid globules.

6.4.3. Comparison of quantitative biomass analysis using FTIR spectroscopy with conventional biochemical methods

After proving that FTIR spectroscopy is able to determine relative changes in biomacromolecules under abiotic stress, its ability to provide quantitative information about biomass composition was investigated. Therefore, the biomass was analyzed with conventional biochemical methods for protein, carbohydrate and lipid determination and compared with FTIR spectroscopy calibration based on peak height. The results of this comparison are shown in Table 6.5. The biochemical biomass analysis was

Table 6.5.: Comparison of quantitative biomass analysis using FTIR spectroscopy with conventional biochemical methods.

Macromolecular group	Protein (% w/w)	Carbohydrates (Starch) (% w/w)	Lipids (% w/w)
Biochemical methods	43	4	9
FTIR spectroscopy	38	3	7

conducted with conventional assays as described in Section 5.12 and the results are

depicted in Table 6.5. Additionally, the biomass was measured by FTIR spectroscopy and a calibration curve with the above mentioned standards was measured. The quantification of the cellular macromolecule content was calculated based on the peak height. The protein determination revealed a close match between the values for the Lowry method and FTIR method, namely 43 % (w/w) and 38 %. The same applies to the carbohydrate determination, where almost comparable values for the phenol-sulfuric acid method (3 % (w/w) of starch) and the FTIR method (4 % (w/w) of polysaccharides) were measured. Finally, the results for the lipid-extracted biomass analyzed with conventional soxhlet extraction with a lipid content of 9 % (w/w) confirmed the value of 7 % lipids measured by FTIR spectroscopy. When comparing the results of biochemical assays with FTIR spectroscopy it is evident that there is only a minor deviation between the two methods and FTIR spectroscopy is well suited to evaluate microalgal biomass composition in a fast and reliable way.

Chapter 7

Dynamic-kinetic modeling

Mathematical models can help identifying new details of the metabolism for economically feasible production of added-value compounds. Detailed knowledge from laboratory scale cultivations can support operating and controlling large-scale cultivation systems. Here, a reliable mathematical model is an important prerequisite for understanding effects of various cultivation conditions on growth and pigmentation. Some successful approaches to model microalgal metabolism on the basis of nutrient uptake and light utilization linked to biomass growth and storage molecule accumulation have been reported in literature. The majority of published microalgal growth models consist of ODEs to describe the dynamic changes in the biomass in a kinetic manner for different green microalgal species (Mairet et al., 2011; Packer et al., 2011; Quinn et al., 2011; Klok et al., 2013; Adesanya et al., 2014).

These kind of models offer the advantage of providing a flexible platform for including biochemical knowledge of the metabolism and provide the opportunity to predict cellular properties for different cultivation scenarios and operation modes. This is of particular advantage since it allows for extrapolation inside or even outside of the experimental region and reduces the number of further time-consuming experiments. The crucial issue of predictivity covers two important aspects in mathematical modeling. First, a valid model structure based on mechanistic model equations formulated with biochemical knowledge of the system and secondly well determined and identifiable model parameters. Only few of the previously published studies addressed the importance of parameter identifiability on predictivity and model state uncertainties. This is a crucial modeling task, since depending on the detail of the proposed equation system, all presented growth models share a high number of model parameters needed to describe the complex phenomena of nutrient uptake and light adaption finally leading to biomass growth and product formation. Parameter identifiability and related predictive power of the model is a crucial issue towards model-based application for large scale cultivation scenarios and robust microalgal process design as it analyzes the reliability of the parameter estimates and thus model predictions in the light of the given data (Muñoz-Tamayo et al., 2014).

This chapter aims at formulating a predictive model for growth and pigmentation of *D. salina* that includes the utilization of light and nitrogen as the primary influencing factors. A special focus was directed towards a potential parameter reduction, the

estimation of the model parameters from measured data points and the analysis of their identifiability.

Table 7.1.: Summary of experimental conditions of *D. salina* cultivated in batch mode used to calibrate the dynamic-kinetic growth model.

Purpose	Reactor	Abbr.	Light intensity per biomass ($\mu\text{mol m}^{-2} \text{s}^{-1} \text{g}^{-1} \text{dw L}$)	Duration of lag phase (d)	Extracellular nitrogen density (g N L^{-1})
Model calibration	INFORS	LL	408	3	0.51
		HL	2124	4	0.51
		HL-ND	3870	1	0.05
Model validation		LL-ND	372	1	0.04
		LL-NL	372	2	0.09

7.1 Model formulation

In the following section, the important factors affecting microalgal growth are briefly described. After that the essential assumptions and equations of the model to provide all necessary information for understanding and assessing the simulation results are given. The model equations formulated to describe the state variables for the cellular processes in *D. salina* during growth are subdivided into two categories. Firstly, the dynamic changes in the state variables are represented by ordinary differential equations. Secondly, the kinetic expressions and microalgal biomass characteristics are expressed by algebraic equations. The presented dynamic model equations consider the following five state variables:

- Biomass density ρ_X (g dw m^{-3})
- Extracellular nitrogen density ρ_N (g N m^{-3})
- Intracellular nitrogen fraction ω_N ($\text{g N g}^{-1} \text{dw}$)
- Chlorophyll fraction ω_{Chl} ($\text{g Chl g}^{-1} \text{dw}$)
- β -carotene fraction ω_{Car} ($\text{g Car g}^{-1} \text{dw}$)

7.1.1. Light attenuation in the photobioreactor

The absorption and scattering of light by microalgal biomass are major determinants for the efficiency of growth in photosynthetic cultivation systems. Therefore, it is important to describe the light attenuation in the photobioreactor in an appropriate manner. The amount of absorbed light is mainly determined by the fraction of photosynthetic pigments such as chlorophylls and carotenoids in the biomass. Beside light absorption, light scattering acts as an important phenomenon in light harvesting in a biomass-dependent manner leading to a reduction in the photosynthetic efficiency. The incident light falling on the reactor surface E_0 decreases exponentially along the optical path coordinate L according to the law of Lambert-Beer.

$$E(L) = E_0 \cdot \exp[-(a \cdot \rho_{\text{Chl}} + b \cdot \rho_{\text{Car}} + c) \cdot L] \quad (7.1)$$

where a , b and c represent the absorption and scattering coefficients of the biomass and ρ_{Chl} and ρ_{Car} are the pigment densities in the reactor. Given a PBR with the optical path length $L=z$, the transmitted photon flux density E_{out} is calculated as follows:

$$E_{\text{out}} = E(L=z) = E_0 \cdot \exp[-(a \cdot \rho_{\text{Chl}} + b \cdot \rho_{\text{Car}} + c) \cdot z] \quad (7.2)$$

The average photon flux density \bar{E} in the photobioreactor is calculated by integration of $E(L)/L$ between $L=0$ and the optical path length $L=z$:

$$\bar{E} = \frac{E_0}{(a \cdot \rho_{\text{Chl}} + b \cdot \rho_{\text{Car}} + c) \cdot z} \cdot (1 - \exp[-(a \cdot \rho_{\text{Chl}} + b \cdot \rho_{\text{Car}} + c) \cdot z]) \quad (7.3)$$

The absorbed photon flux E_{abs} is calculated from the difference of incident and transmitted photon flux density normalized to the reactor surface S_{PBR} :

$$E_{\text{abs}} = (E_0 - E_{\text{out}}) \cdot S_{\text{PBR}} \quad (7.4)$$

The light intensity per biomass $E_{\text{X,dw}}$ is calculated from the ratio of average photon flux density \bar{E} and the biomass density ρ_{X} normalized to the reactor volume V_{PBR} :

$$E_{\text{X,dw}} = \frac{\bar{E}}{\rho_{\text{X}} \cdot V_{\text{PBR}}} \quad (7.5)$$

7.1.2. Nitrogen uptake rate

The uptake rate of inorganic nitrogen r_{N} from the medium was assumed to follow Michaelis-Menten kinetics (Eq. 7.6). By including the Droop function into the uptake rate, the expression ensures that nitrogen uptake is terminated under nitrogen-repleted conditions (Droop, 1968):

$$r_{\text{N}} = r_{\text{N,max}} \cdot \frac{\rho_{\text{N,ext}}}{\rho_{\text{N,ext}} + K_{\text{S,N}}} \cdot \left(1 - \frac{\omega_{\text{N}}}{\omega_{\text{N,max}}}\right) \quad (7.6)$$

where $r_{\text{N,max}}$ and $K_{\text{S,N}}$ represent the maximal uptake rate and the half-saturation coefficient for nitrogen as well as $\omega_{\text{N,max}}$ which is the maximal nitrogen quota in the biomass.

7.1.3. β -carotene synthesis rate

The synthesis of β -carotene mainly depends on the presence and intensity of light and nutrient stress. Therefore, the equation for its synthesis couples a light-dependent and nutrient-dependent synthesis term as formulated below (Eq. 7.7):

$$r_{\text{Car}} = r_{\text{Car,E}} \cdot \frac{E_{\text{X,dw}}^k}{E_{\text{Car,crit}}^k + E_{\text{X,dw}}^k} + r_{\text{Car,N}} \cdot \left(1 - \frac{\omega_{\text{N}}^k}{\omega_{\text{N,crit}}^k + \omega_{\text{N}}^k}\right) \quad (7.7)$$

where $r_{\text{Car,E}}$ and $r_{\text{Car,N}}$ represent the maximal synthesis rate under light and nutrient stress. The half saturation coefficients for light and nutrient stress are denoted as $E_{\text{Car,crit}}$ and $\omega_{\text{N,crit}}$. The Hill coefficient is represented by k . The dependency of the

light intensity per biomass ($E_{X,dw}$) and nitrogen cell quota (ω_N) on the β -carotene synthesis rate (r_{Car}) is illustrated in Fig. 7.1.

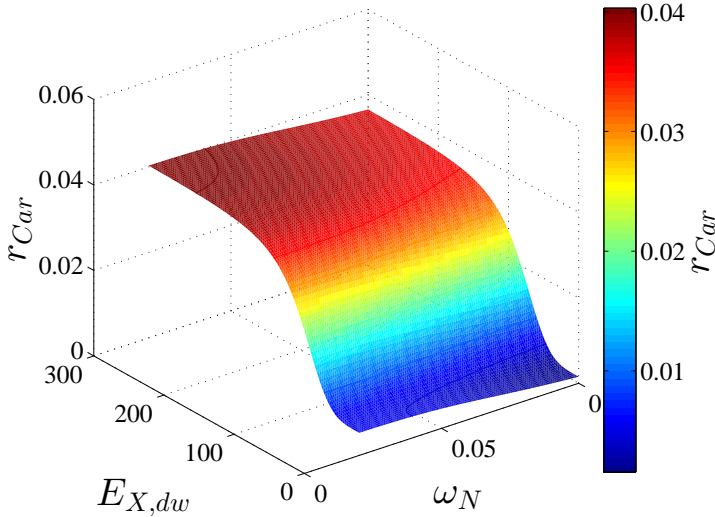


Figure 7.1.: Dependency of the light intensity per biomass ($E_{X,dw}$) and nitrogen cell quota (ω_N) on the β -carotene synthesis rate (r_{Car}).

7.1.4. Photosynthesis rate

The carbon-specific, light-limited photosynthesis rate can be expressed using Eq. 7.8:

$$r_P = r_{P,max} \cdot \left(1 - \frac{\omega_{N,min}}{\omega_N}\right) \cdot \left(1 - \exp\left[\frac{-a \cdot Y_{X,E} \cdot \bar{E}}{r_{P,max}}\right]\right) \quad (7.8)$$

where $r_{P,max}$ is the maximal photosynthesis rate, $\omega_{N,min}$ is the minimal nitrogen quota of the biomass and $Y_{X,E}$ is the biomass yield on light energy. This relationship developed by Geider et al. (1998) includes the dependencies on the average photon flux density, the light absorption properties, the photon efficiency and the nutrient status of the biomass.

7.1.5. Growth rate

Since pronounced photoinhibitory effects were observed under HL and HL-ND conditions, a growth rate approach containing an inhibition term has been formulated to describe the specific biomass growth rate μ (Mairet et al., 2011). In addition, a Droop

term has been added to the equation to ensure growth arrest under nitrogen depletion as shown in Eq. 7.9:

$$\mu = \mu_{\max} \cdot \frac{E_{X,dw}}{E_{X,dw} + K_{s,E} \cdot \frac{\rho_X}{\rho_{Chl}} + \frac{E_{X,dw}^2}{K_{i,E}}} \cdot \left(1 - \frac{\omega_{N,\min}}{\omega_N}\right) \quad (7.9)$$

The dependency of the light intensity per biomass ($E_{X,dw}$) and nitrogen cell quota (ω_N) on the maximal growth rate (μ_{\max}) is illustrated in Fig. 7.2. Since the cells need

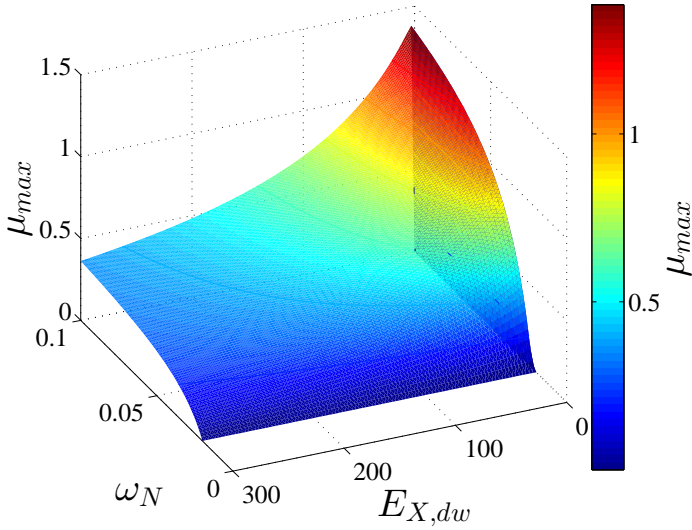


Figure 7.2.: Dependency of the light intensity per biomass ($E_{X,dw}$) and nitrogen cell quota (ω_N) on the maximal growth rate (μ_{\max}).

to adapt to the conditions in the photobioreactor, at time $t = 0$ an initial *lag* phase was observed in the experimental data. Therefore, the specific growth rate was adjusted using a Hill function:

$$\Phi = \frac{t^k}{\lambda^k + t^k} \quad (7.10)$$

to estimate the *lag* phase Φ where k is the exponential factor describing the transition from *lag* to exponential phase and λ is the duration of the *lag* phase. Taking the respiration rate into account, the following equation for the net specific growth rate μ_{net} was derived:

$$\mu_{\text{net}} = \Phi \cdot (\mu - r_R) \quad (7.11)$$

The biomass yield on light energy $Y_{X,E}$ is calculated according the following expression:

$$Y_{X,E} = \frac{\mu \cdot \rho_X \cdot V_{\text{PBR}}}{E_{\text{abs}}} \quad (7.12)$$

where V_{PBR} is the reactor volume.

After the formulation of the kinetic expressions, Eqs. 7.2 - 7.12, the following five dynamic equations are deduced in order to describe biomass growth, chlorophyll and β -carotene fraction, extracellular nitrogen density and nitrogen quota:

$$\frac{d\rho_X}{dt} = \mu_{net} \cdot \rho_X \quad (7.13)$$

$$\frac{d\rho_{N,ext}}{dt} = -r_N \cdot \rho_X \quad (7.14)$$

$$\frac{d\omega_N}{dt} = r_N - \mu \cdot \omega_N \quad (7.15)$$

$$\frac{d\omega_{Chl}}{dt} = \frac{\omega_{Chl,N} \cdot \mu \cdot r_N}{r_P \cdot \left(\frac{\omega_{Chl}}{\omega_C}\right)} - \mu_{net} \cdot \omega_{Chl} \quad (7.16)$$

$$\frac{d\omega_{Car}}{dt} = r_{Car} - \mu_{net} \cdot \omega_{Car} \quad (7.17)$$

The model equations contain nine parameters (optimization variables) and eleven biomass and three reactor constants (see Table 7.2). The presented model equations were formulated with special emphasis on limiting the number of model parameters to a minimum, e.g. the biomass yield on light energy $Y_{X,E}$ (Eq. 7.12) was calculated from the state variables instead.

The proposed model was implemented in MATLAB (MathWorks) and solved by using CVODES (Hindmarsh et al., 2005). The model simulations were compared with experimental data of *D. salina* grown under different cultivations conditions (Table 7.1) in a flat-plate photobioreactor in batch mode. The nine model parameters were estimated using the nonlinear optimization algorithm `fmincon` initialized with parameter values taken from literature and experimental data. This algorithm attempts to find a set of parameters that minimizes the objective function defined in Eq. 7.18.

7.1.6. Profile likelihood analysis of model parameters

In most cases the model parameters Θ are unknown and need to be estimated numerically from experimental data and proposed model equations. During parameter identification, the agreement of experimental data $y_k(t_i)$ with the simulation results $y_k(t_i, \Theta)$ is evaluated by the weighted sum of squared residuals $\chi^2(\Theta)$ as an objective function:

$$\chi^2(\Theta) = \sum_{k=1}^m \sum_{i=1}^{d_k} \frac{1}{\sigma_{ki}^2} (y_k(t_i) - y_k(t_i, \Theta))^2, \quad (7.18)$$

where m is the number of measured outputs, d_k is the number of measurement times, y_k and \hat{y}_k are the k -th measured output variable and corresponding model prediction and σ_{ki}^2 is the variance in the measured data. For independent, normally distributed, additive measurement noise, $\chi^2(\Theta)$ is proportional to the negative log-likelihood function. In this case, parameter estimation based on minimizing the residual sum

of squares is equivalent to maximizing the likelihood function and can therefore be used instead.

An often used method to proof the reliability of an estimated parameter set is the analysis of parameter identifiability. In this work, an approach proposed by Raue et al. (2009) using constrained likelihood profiles was applied. The strength of the approach is to systematically explore the high-dimensional parameter space for each parameter individually (Kreutz et al., 2013). In detail, for each parameter Θ_i a section along the least increase in $\chi^2(\Theta)$ with respect to all other parameters $\Theta_{j \neq i}$ is computed:

$$\chi_{\text{PL}}^2(\Theta_i) = \min_{\Theta_{j \neq i}} [\chi^2(\Theta)] \quad (7.19)$$

The shape of $\chi_{\text{PL}}^2(\Theta_i)$ can be used to assess the identifiability of each parameter for given data. Identifiable parameters have a parabolically shaped profile likelihood $\chi_{\text{PL}}^2(\Theta_i)$. Given that $\chi_{\text{PL}}^2(\Theta_i)$ follows a χ^2 distribution, one may derive a critical value χ_{PL}^2 for a confidence level of typically 95 %, which can be used to derive the corresponding confidence interval for the respective parameter.

In case of non-identifiability, one can distinguish between structural and practical non-identifiability. Non-identifiability is indicated by a flat shape of χ_{PL}^2 either in direction of one confidence bound (practical non-identifiability) or in direction of both confidence bounds (structural non-identifiability). Structural non-identifiability arises from the model structure, whereas practical non-identifiability results from a lack in the amount and quality of experimental data. For model parameters which are non-identifiable, a change of the parameter value has no significant influence on the likelihood value and hence does not influence observed model outputs. However, internal non-observed model states can vary significantly, rendering model predictions on internal states questionable.

The MATLAB implementation of the profile likelihood algorithm was based on a pseudocode provided by Raue et al. (2009) and was parallelized by Robert J. Flassig. Absolute and relative tolerances have been set to 10^{-7} and 10^{-6} , respectively.

7.2 Determination of biomass-specific parameters

In order to achieve a high predictability of the model and to reduce the number of estimated parameters, biomass-specific constants were directly determined from experimental data.

Duration of the *lag* phase

The duration of the lag phase λ was estimated from the cell density growth curve (see Table 7.1). According to Baty and Delignette-Muller (2004), the Hill coefficient was set to $k = 4$.

Elemental biomass composition

The minimal and maximal nitrogen quota ($\omega_{N,\min}$ and $\omega_{N,\max}$) as well as the carbon fraction ω_C in the biomass were determined C/H/N analysis as described in Chapter 5.

Absorption properties of the biomass

The chlorophyll content in the microalgal biomass is strongly dependent on the light conditions in the photobioreactor and consequently is subject to substantial fluctuations during the cultivation. The optical cross section of chlorophyll *a* (a^*) is an important variable describing the packaging of this pigment in the PSII. As depicted in Fig. 7.3 a - c, a^* is subject to significant variations under fluctuating light conditions. The values for the optical cross section of chlorophyll *a* range from 6.8 to 19.8 $\text{m}^2 \text{g}^{-1}$ Chl under low light conditions (LL), from 9.6 to 21.2 $\text{m}^2 \text{g}^{-1}$ Chl under high light conditions (HL) and from 6.8 to 11.1 $\text{m}^2 \text{g}^{-1}$ Chl under high light and nitrogen-depleted conditions (HL-ND). In order to keep the kinetic model as simple as possible, the optical cross section of chlorophyll *a* (a^*) was fixed to 11.84 $\text{m}^2 \text{g}^{-1}$ Chl *a* according to the average measurement value under the three tested cultivation conditions as shown in Fig. 7.3. The pigment specific absorption and backscattering coefficients (a , b and c) were estimated by maximizing the match between the measured values of incident and transmitted light intensity.

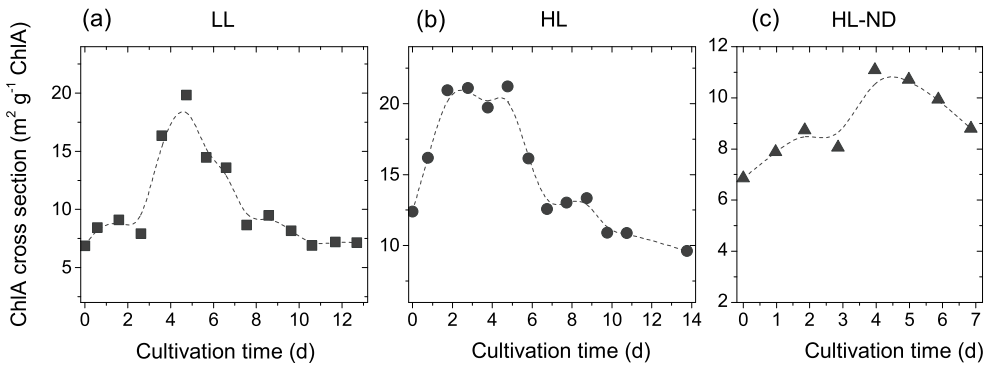


Figure 7.3.: Effect of various cultivation conditions on the time-variant input variables, optical cross section of chlorophyll *a*. Optical cross section of chlorophyll *a* for cultivation under LL (a), HL (b) and HL-ND conditions (c). The dashed line represents the cubic spline interpolation between the experimental data points (symbols).

According to the measurement results the values for the biomass-specific parameters were set as shown in Table 7.2.

7.3 Parameter estimation

The presented model was used to estimate a set of nine model parameters for the equation system, which describes the dynamic changes in the biomass density, the chlorophyll and β -carotene fraction as well as the extracellular nitrogen density in

Table 7.2.: Summary of biomass-specific parameters for *D. salina* derived from experiments and literature data.

Description	Symbol	Value	Unit	Source
Optical cross section of chlorophyll <i>a</i>	a^*	11.84	$\text{m}^2 \text{g}^{-1} \text{Chl } a$	Average of experimental data
Absorption coeff. of chlorophyll <i>a</i> and <i>b</i>	a	5.134	$\text{m}^2 \text{g}^{-1} \text{Chl}$	Fitting of absorption model to exp. data
Absorption coeff. of β -carotene	b	2.202	$\text{m}^2 \text{g}^{-1} \text{Car}$	Fitting of absorption model to exp. data
Backscattering coeff. of the biomass	c	16.591	m^{-1}	Fitting of absorption model to exp. data
Hill coefficient	k	4	-	Literature (Baty and Delignette-Muller, 2004)
Duration of the lag phase	λ	variable	d	Estimation from exp. data (see Table 7.1)
Maximal theoretical photosynthesis rate	$r_{p,\max}$	1526	$\text{g C g}^{-1} \text{Chl d}^{-1}$	Estimation from exp. data
Carbon fraction	ω_{C}	0.49	$\text{g N g}^{-1} \text{dw}$	Direct measurement
Maximal cell quota for nitrogen	$\omega_{\text{N},\max}$	0.03	$\text{g N g}^{-1} \text{dw}$	Direct measurement
Minimal cell quota for nitrogen	$\omega_{\text{N},\min}$	0.10	$\text{g N g}^{-1} \text{dw}$	Direct measurement
Critical N cell quota for β -carotene synthesis	$\omega_{\text{N},\text{crit.}}$	0.08	$\text{g N g}^{-1} \text{dw}$	Estimation from exp. data
Reactor thickness	z	0.02	m	Reactor constant
Reactor volume	V_{PBR}	0.0018	m^{-3}	Reactor constant
Reactor surface	s_{PBR}	0.09	m^{-2}	Reactor constant

largest agreement to the experimental data. For this purpose, the objective function was defined to minimize the weighted sum of squared residuals (Eq. 7.18) for ρ_X , ω_{Chl} , ω_{Car} and $\rho_{\text{N,ext}}$ for three experimental conditions (see LL, HL and HL-ND in Table 8.2). During parameter estimation, box constraints were imposed on the parameters. The box bounds have been chosen according to bio-physical limitations, e.g. the respiration rate r_{R} can not be smaller than zero. The measurement variances were parameterized as $\sigma_{\text{ki}}^2 = 0.1 \max(y_k(t))$, i.e. each measurement is assumed to have a variance of 10 % from the maximal value of the respective time course. This variance parameterization most likely overestimates the true variance but should at least give an upper bound on the true variance levels. The parameter set $\hat{\Theta}$ obtained from the constrained least squares fit is given in Table 7.3. At the optimal parameter vector, a $\chi^2 = 950$ was calculated for a total number of measurement points of $n_y = 172$.

Table 7.3.: Summary of the obtained optimal parameter values $\hat{\Theta}$ as well as the individual confidence intervals $[\sigma_i^-; \sigma_i^+]$ corresponding to a confidence level of 95 % from constrained non-linear optimization and profile likelihood analysis for *D. salina*.

Symbol	$\hat{\Theta}$	σ_i^-	σ_i^+	Identifiability
$r_{\text{N},\max}$	0.346	0.249	0.531	Structurally and practically identifiable
$K_{\text{s},\text{N}}$	0.05	0.0003	3.591	Structurally and practically identifiable
μ_{\max}	1.708	1.406	2.130	Structurally and practically identifiable
$K_{\text{s},\text{E}}$	0.033	0.018	0.055	Structurally and practically identifiable
$K_{\text{i},\text{E}}$	68.719	48.186	97.744	Structurally and practically identifiable
$E_{\text{car,crit}}$	77.718	74.102	80.138	Structurally and practically identifiable
$r_{\text{car},\text{E}}$	0.032	0.022	0.041	Structurally and practically identifiable
$r_{\text{car},\text{N}}$	0.005	0.0045	0.0055	Structurally and practically identifiable
r_{R}	0.142	0.131	0.152	Structurally and practically identifiable

7.3.1. Biomass growth under fluctuating light and nutrient conditions

The simulation results shown in Fig. 7.4 a-c demonstrate that the model describes the dynamics of biomass growth under various light and nutritional conditions with the estimated parameter set $\hat{\Theta}$ (Table 7.3) in a good manner. The maximum biomass density from all three experimental conditions was achieved in the cultivation under low light (LL), namely 7.2 g dw L^{-1} . This corresponds to a final cell density of $1.4 \times 10^7 \text{ cells mL}^{-1}$ cultivation volume. The final biomass density reached in the stationary phase for the cultivations under high light (HL) is 6.5 g dw L^{-1} and almost comparable to the low light condition (LL). Under high light and nitrogen depletion (HL-ND) the biomass growth was significantly lowered due to nutrient abundance and only 1.1 g dw L^{-1} biomass was achieved.

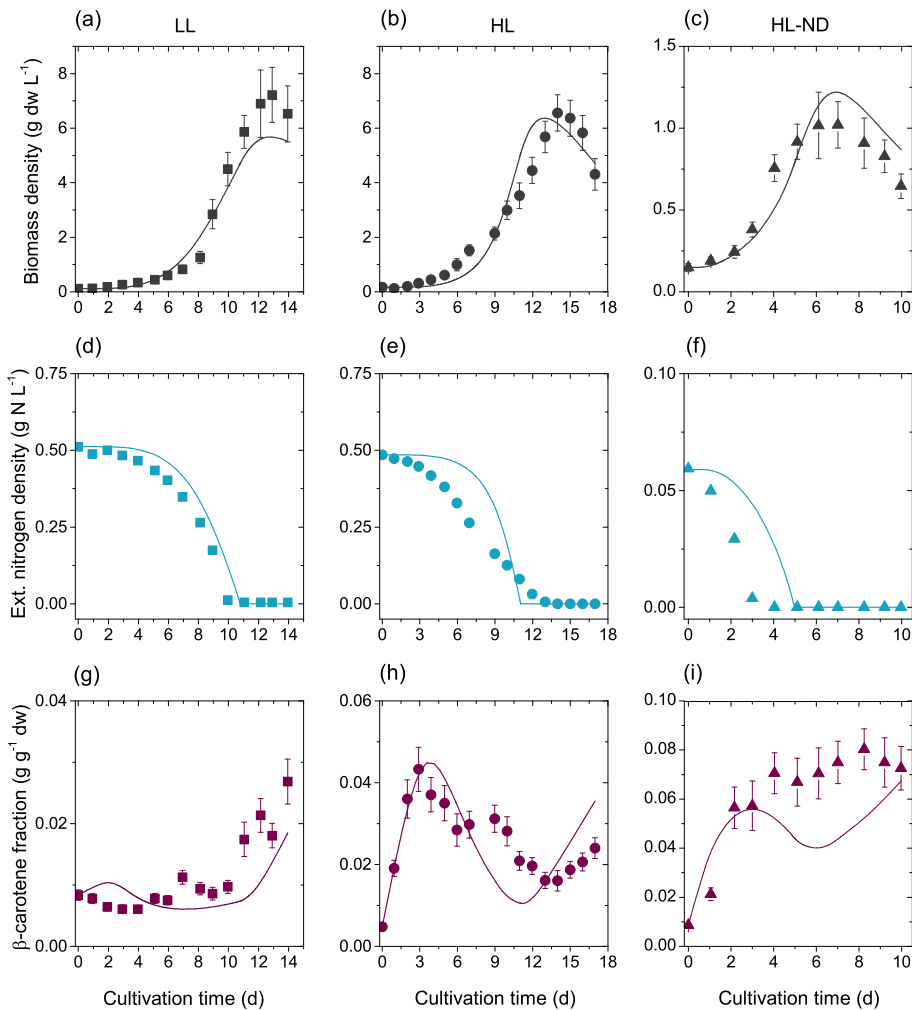


Figure 7.4.: Model simulations for the effect of various cultivation conditions on the biomass density $\rho_{X,dw}$ (a-c), the extracellular nitrogen density $\rho_{N,ext}$ (d-f) and the β -carotene fraction ω_{Car} (g-i). Comparison of the simulated time course (lines) with experimental data (symbols).

7.3.2. Extracellular nitrogen uptake

The simulated time course for the extracellular nitrogen density agreed well with the experimental data (Fig. 7.4 d-f). The results revealed that the growth under all three conditions was always nutrient and never light-limited. As expected, the growth under nutrient-depleted conditions (HL-ND) was governed by the lowest external nutrient availability and the internal nutrient status of the cells. The external nitrogen was totally depleted four days after inoculation in the nitrogen starved culture (HL-ND). The simulation results clearly indicate, that nitrogen uptake is strongly reduced in the *lag* phase under nitrogen-repleted conditions (LL, HL), since the nitrogen cell quota is close to its maximal value $\omega_{N,max}$ (Fig. 7.4 d-f).

7.3.3. β -carotene fraction in the biomass

The model simulations agree well with the experimental data for the β -carotene fraction ω_{Car} in the cells (Fig. 7.4 g-i). The data clearly indicate that light and nutrient stress alone are able to induce the accumulation of the photoprotective pigments. However, when both stress conditions are combined under HL-ND conditions the β -carotene synthesis exceeds the fractions achieved under LL or HL conditions. The highest β -carotene fraction was detected in the HL-ND culture with 8.0% (w/w), followed by the HL culture with 4.3% (w/w) at day 3 and 2.7% (w/w) in the stationary culture under LL conditions. Under HL conditions the initially high β -carotene accumulation induced by the presence of light stress declined as soon as the incident light intensity fell below the fixed light stress of $3000 \mu\text{mol m}^{-2} \text{s}^{-1} \text{g}^{-1} \text{dw L}$ due to the physical limitation of the LED light panel to a maximal light intensity of $3000 \mu\text{mol m}^{-2} \text{s}^{-1}$. Under LL conditions, the β -carotene synthesis started when a critical nitrogen quota of approximately $0.075 \text{g N g}^{-1} \text{dw}$ was reached.

7.3.4. Total chlorophyll fraction in the biomass

The model simulations agree reasonably well with the experimental data for the chlorophyll fraction ω_{Chl} , which is crucial for predicting the light attenuation in the reactor (Fig. 7.5 a-c). During the initial cultivation period more light energy is supplied per cell than is required for growth, resulting in a considerable decline of the total chlorophyll fraction under all three conditions. The minimal total chlorophyll content in the biomass is almost comparable under three cultivation conditions, namely $0.004 \text{g Chl g}^{-1} \text{dw}$.

7.4 Model predictions

The estimated parameter set (Table 7.3) was used to predict dynamic changes of the non-measured dynamic state, namely the internal nitrogen cell quota ω_N for the measured experimental conditions (LL, HL, HL-ND) as presented in Fig. 7.5 d-f.

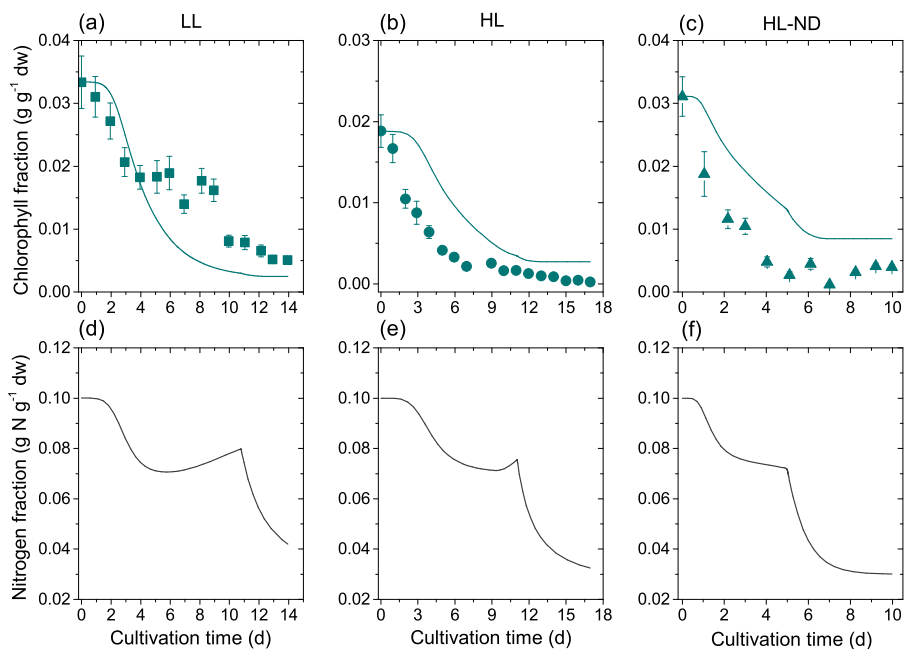


Figure 7.5.: Model simulations for the effect of various cultivation conditions on the the chlorophyll fraction ω_{Chl} (a-c) and the nitrogen quota in the biomass ω_{N} (d-f). Comparison of the simulated time course (lines) with experimental data (symbols).

7.4.1. Nitrogen cell quota and the nitrogen uptake rate

In this study, the nitrogen cell quota of the inoculum grown under nitrogen-repleted conditions was set to $0.10 \text{ g N g}^{-1} \text{ dw}$, which has been determined by C/H/N analysis and corresponds to the maximal nitrogen quota in the biomass $\omega_{\text{N,max}}$ (see Table 7.2). Experimental data for minimal and maximal cell quota have been published for the closely related species *Dunaliella tertiolecta* (Goldman and Peavey, 1979). The reported minimal nitrogen cell quota was $0.03 \text{ g N g}^{-1} \text{ dw}$ and the maximal nitrogen cell quota was $0.08 \text{ g N g}^{-1} \text{ dw}$, which is close to our experimentally determined values.

The predicted maximal nitrogen uptake rate is $0.346 \text{ g N g}^{-1} \text{ dw d}^{-1}$. The value for the calculated nitrogen uptake rate r_{N} , (see Eq. 7.6) under all three conditions is approx. $0.05 \text{ g N g}^{-1} \text{ dw d}^{-1}$, which is in good agreement with measurements ranging from 0.05 - $0.015 \text{ g N g}^{-1} \text{ dw d}^{-1}$ measured for several green microalgal species by Hein et al. (1995). However, it is lower than measured nitrogen uptake rates for the same strain used in this study, namely *D. salina* CCAP 19/18, grown in a low light turbidostat culture ($0.085 \text{ g N g}^{-1} \text{ dw d}^{-1}$) measured by Lamers et al. (2012) and $0.08 \text{ g N g}^{-1} \text{ dw d}^{-1}$ from Lomas and Glibert (2000) measured for the closely related organism *D. tertiolecta*.

7.5 Model validation

The proposed model with the estimated parameter set was validated with two independent cultivation experiments in batch operation mode under low light and nutrient limited or depleted conditions (LL-ND and LL-NL) as illustrated in Table 7.1. The time courses for biomass density, external nitrogen density, β -carotene and chlorophyll fraction are in good agreement with the experimental data (Fig. 7.6 and 7.7). Both cultures were nutrient limited indicated by an β -carotene synthesis at day 6 of the LL-ND culture and day 8 of LL-NL culture. Due to the higher initial nitrogen density (0.09 g N L^{-1} compared to 0.04 g N L^{-1}) in the LL-NL culture, the final biomass density achieved in the stationary phase was also higher 1.7 g dw L^{-1} compared to 1.0 g dw L^{-1} . The β -carotene fraction was almost similar to the cultivation under LL conditions ($2.3\% \text{ (w/w)}$ under LL-ND and $2.9\% \text{ (w/w)}$ under LL-NL compared to $2.7\% \text{ (w/w)}$).

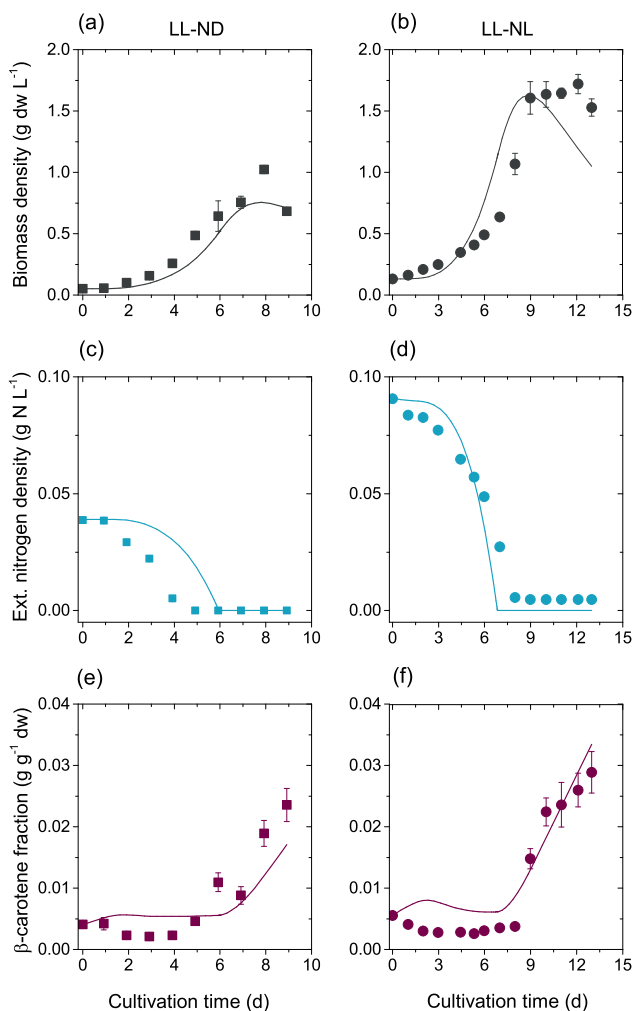


Figure 7.6.: Model validation for the effect of various cultivation conditions on the cell density $\rho_{X,dw}$ (a-b), the extracellular nitrogen density $\rho_{N,ext}$ (c-d) and the β -carotene fraction ω_{Car} (e-f). Comparison of the simulated time course (lines) with experimental data (symbols).

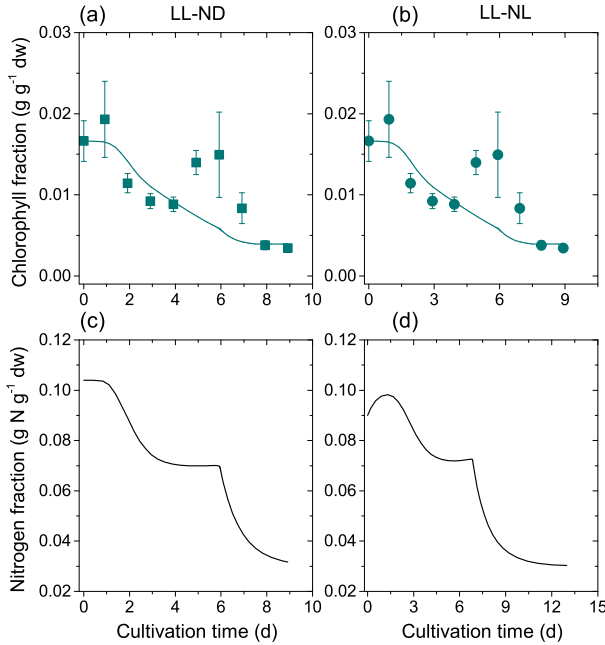


Figure 7.7.: Model simulation for the effect of various cultivation conditions on the the chlorophyll fraction ω_{Chl} (a-b) and the nitrogen quota in the biomass ω_{N} (c-d). Comparison of the simulated time course (lines) with experimental data (symbols).

7.6 Identifiability analysis using the profile likelihood

The results of the identifiability analysis of all model parameters using likelihood profiles are presented in Fig. 7.8. This approach allows distinguishing between structurally non-identifiable, practically non-identifiable and identifiable parameters depending on the shape of χ_{PL}^2 (Section 7.1.6). The lower and upper bounds of the 95 % confidence intervals are given in Table 7.3. All nine model parameters are identifiable indicated by the shape of the χ_{PL}^2 curve and the finite size of the derived confidence intervals (Fig. 7.8 a - i, black solid line and Table 7.3). Besides profile likelihood, likelihood analysis is frequently performed to evaluate the predictive power of a proposed model. In contrast to the profile likelihood, where one parameter Θ_i is varied and all other parameters $\Theta_{j \neq i}$ are re-optimized, for likelihood analysis only the parameter value for Θ_i is changed and the remaining parameters $\Theta_{j \neq i}$ are kept constant. Due to this fact, the parameter identifiability analysis using the likelihood function is less strict than the profile likelihood based identifiability analysis. This is illustrated in Fig. 7.8 (gray dashed lines vs. black solid lines). Still, likelihood analysis is useful to identify potentially non-identifiable parameters.

The likelihood of the nine identifiable model parameters seem to be in an asymptotic setting indicated by the parabolic shape with finite size of the 95 % confidence interval (Fig. 7.8 a - i). Due to the negligence of the parameter interdependencies, the confidence interval derived for each parameter are significantly smaller for the

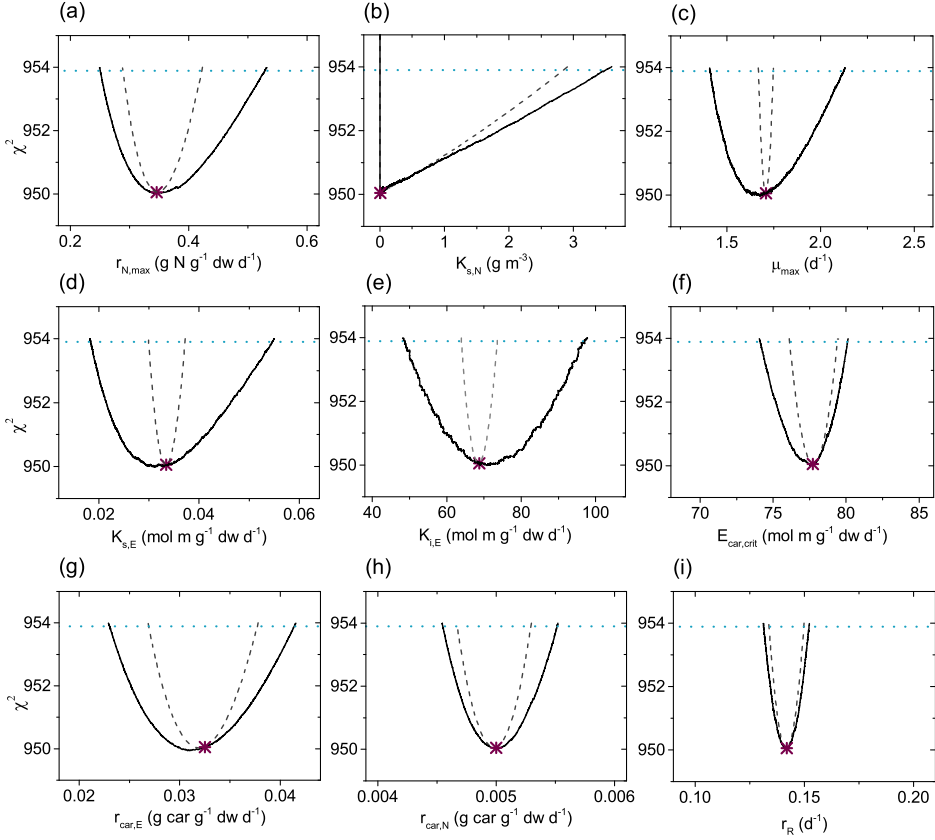


Figure 7.8.: Profile likelihood-based identifiability for all model parameters: a) Maximal nitrogen uptake rate r_{\max} , b) Halfsaturation coefficient for nitrogen uptake $K_{s,N}$, c) Maximal growth rate μ_{\max} , d) Half saturation coefficient for photosynthetic growth $K_{s,E}$, e) Light inhibition coefficient for photosynthetic growth $K_{i,E}$, f) Critical light intensity for β -carotene synthesis $E_{\text{car,crit}}$, g) Light stress-induced β -carotene synthesis rate $r_{\text{car,E}}$, h) Nutrient stress-induced β -carotene synthesis rate $r_{\text{car,N}}$ and i) Respiration rate r_R . The profile likelihood-based sensitivity curve, where Θ_i is varied and all other parameters $\Theta_{j \neq i}$ are kept constant, is indicated by the dashed gray line. The profile likelihood-based identifiability curves are indicated by the black solid line. The blue dotted horizontal line indicates the threshold utilized to assess likelihood-based 95% confidence interval and the asterisk corresponds to the optimal parameter value.

likelihood-based derivation compared to the profile likelihood. This example illustrates the strength of the identifiability analysis based on profile likelihoods leading to detailed information about parameter interdependencies and reliable confidence intervals. Non-identifiability of model parameters originate from either unknown functional dependencies between different parameters - in such a case, a change in a model parameter can be compensated by several other model parameters - or structural non-observability. In order to overcome this limitation, additional system outputs need to be quantified. The application of optimal experimental design (OED) approaches could be beneficial in order to determine the measurement signal with the highest information content (Muñoz-Tamayo et al., 2014; Flassig et al., 2015).

In summary, a dynamic-kinetic model has been proposed, which describes growth and the pigmentation of *D. salina* under fluctuating light and nutritional conditions with nine model parameters. The results revealed that model simulation describes the experimental data accurately. The identifiability analysis using the profile likelihood indicated that all nine parameters are structurally and practically identifiable. The resulting predictive growth model allows the prediction of biomass productivity and pigmentation under different cultivation conditions and bioreactor operation modes.

Chapter 8

Dynamic flux balance analysis

The construction of dynamic-kinetic bioreactor models using ODEs is a well-established formalism in bioprocess engineering. These models allow for prediction of biomass growth, nutrient uptake and metabolite production and enable the identification of bottlenecks in the process setup. These simplified growth models as presented in Chapter 7 are robust and computationally inexpensive but might be only valid for a certain range of environmental conditions and thus have limited predictive capabilities for extrapolation outside the experimental region (Höffner et al., 2013). The limitations in dynamic-kinetic models are attributed to a variety of reasons such as model non-linearity, parameter identifiability, estimability and uncertainty (Srinivasan et al., 2015).

It is known that metabolic processes are based on complex reaction pathways throughout different subcellular compartments and its integration into a metabolic model is a prerequisite to get insight into the formation and regulation of metabolites (Grafahrend-Belau et al., 2013). Although the methodological progress in quantitative biology is advancing quickly, it is still not possible to fully parametrize a dynamic model of a microorganisms' metabolism at genome scale (Wu et al., 2016). Usually, methods such as FBA are used to determine the flux distribution in a metabolic network under given input conditions by maximization of an objective function (see Chapter 4). However, FBA methods only account for growth under balanced conditions and are limited to predicting steady state flux distributions. DFBA is an extension of classical FBA that allows the dynamic effects of the extracellular environment on intracellular metabolism to be predicted and optimized (Henson and Hanly, 2014). This enables exploration of metabolic flux distributions consistent with stoichiometric and thermodynamic constraints as well as constraints formulated according to experimental data (Wu et al., 2016).

The present chapter introduces an extension of the DFBA formulation to stress-induced β -carotene accumulation in *D. salina*. The objective is to develop and validate a detailed and structured model for *D. salina* with focus on quantitative prediction of stress-induced β -carotene production dependent on different external cultivation conditions. An important prerequisite for the formulation of the DFBA model is the reliable parametrization of the dynamically changing reactor environment (as presented in Chapter 7) since the large number of reactions in a genome-scale metabolic

network (see Table 4.1) results in a bi-level optimization problem that is computationally expensive and challenging to solve.

Existing modeling formulations for dynamic prediction of microalgal metabolism focus on lipid production, as a feedstock for the next generation of biofuels and do not include stress-induced accumulation of other metabolites. DRUM (Dynamic Reduction of Unbalanced Metabolism) is a dynamic metabolic modeling framework which includes accumulation of intracellular metabolites Baroukh et al. (2014). This approach relies on the definition of subnetworks and EFM analysis of each of the subnetworks. Since EFM analysis can become computationally expensive, this may not be applicable to large (genome-scale) networks. Furthermore, prior knowledge regarding the division into subnetworks must be available and kinetic expressions have to be assigned to each of the subnetworks. In contrast, the current formulation does not require EFM and therefore can be applied to genome-scale networks. Another approach that has been presented recently is MetDFBA (Willemsen et al., 2015). This extension of DFBA assumes that metabolic measurements are available. Such an assumption may not be feasible for large-scale production systems. The derivation of the model presented in this work also takes advantage of existing detailed metabolic models. The recent advances in development of genome-scale metabolic network reconstructions for microalgae have been outlined in Chapter 4.

8.1 Metabolic network analysis of the central carbon metabolism

8.1.1. Recent advances in genome sequencing of *D. salina*

Algae and higher plants possess three different DNA-containing compartments: the nucleus, the plastid and the mitochondrion. The nomenclature of the respective genomes is derived from the compartment they originate from. Therefore, the genetic information in the nucleus is called the nuclear genome, whereas the mitochondrial and plastidal genomes are located inside the mitochondrion and the plastid. Collectively, they are referred to as organelle genomes (Del Vasto, 2015). The majority of genes in the organelle genome are attributed to metabolic functions in respective organelle such as cellular respiration in the mitochondrion and plastidal photosynthesis. Beside photosynthesis, many other metabolic functions are associated with the plastid such as fatty-acid biosynthesis, nitrogen assimilation, amino acid and starch biosynthesis (Del Vasto, 2015).

The sequencing of the organelle genomes of *D. salina* CCAP19/18 isolated from the Hutt Lagoon in Western Australia was completed in 2010 (Smith et al., 2010). Unexpectedly, the mitochondrial and plastidal genome of *D. salina* were with 28 kb and 269 kb quite large and more than half of it consisted of non-coding DNA and introns (Smith et al., 2010).

Moreover, researchers around Jon Magnuson completed the sequencing of the nuclear *D. salina* CCAP 19/18 genome funded by the Department of Energy Joint Genome Institute (<http://genome.jgi.doe.gov/DunsalCCAP1918/DunsalCCAP1918.info.html>). However, the assembly of the nuclear genome is challenging since it

contains a high number of introns and extensive palindromic repeats preventing the assembly of larger sets of overlapping DNA segments and hindering its assembly (Del Vasto et al., 2015). Since, the annotated genes for all enzymes in the *Dunaliella* metabolism are not available, the reconstruction of a metabolic network map could not have been achieved so far. Though it might be adequate to make use of a metabolic network reconstruction of a close relative. As listed in Table 4.1, for the green alga *C. reinhardtii* various carbon core and genome-scale network models have been developed. Moreover algae of the genus *Dunaliella* and *Chlamydomonas* both belong to the order of Volvocales (Gonzalez et al., 2009). In addition, there is a broad consensus that the carbon core metabolisms of green microalgae is conserved along several lineages since almost 90 % of the functional annotated proteins of *C. reinhardtii* and of other microalgal proteins are homologs of *Arabidopsis thaliana* proteins (Reijnders et al., 2015).

8.1.2. Comparison of enzymes in the carbon core metabolisms of *D. salina* and *C. reinhardtii*

Although the central carbon metabolism is generally assumed to be conserved, a comparison of annotated enzymes in the Calvin cycle, the carbon-core metabolism and the isoprenoid biosynthesis of *D. salina* were compared with a reconstruction of the central carbon metabolism of *C. reinhardtii* published by Kliphuis et al. (2011). The basis for this comparison with *D. salina* is formed by a collection of annotated enzymes in the respective pathways was provided by Prof. Jürgen Polle (Brooklyn College, New York), a collaborator of the above mentioned *D. salina* nuclear genome project. Fig. 8.1, 8.2 and 8.3 show the network map for the cytosol, the chloroplast and the mitochondrium. The summarized network map containing all three considered compartments in one figure can be found in Appendix C (Fig. S1).

As can be seen in the following figures, there is a high degree of similarity in the metabolic pathways for the calvin cycle, the photorespiration, the glycolysis, and the pentose phosphate pathway between *C. reinhardtii* and *D. salina*. In addition, the reaction pathways highlighted in green were added to the network because the corresponding enzymes have been identified in *D. salina*, specifically the carotenoid biosynthesis, the crassulacean acid metabolism (CAM) and the starch synthesis. However, this pathways also occur in *C. reinhardtii* but have been neglected by Kliphuis et al. (2011) for reasons of simplicity. A prediction tool called PredAlgo, developed by Tardif et al. (2012) was designed to determine the subcellular localization of nuclear-encoded enzymes in *C. reinhardtii*. For that, PredAlgo differs between the following three compartments: the mitochondrium, the chloroplast and the cytosol. The study of Tardif et al. (2012) showed that application of PredAlgo led to an improved discrimination between plastidal and mitochondrial-localized proteins. As stated by the authors, PredAlgo works most accuratere for the genus of *Chlamydomonas* and related green algal species (Chlorophyta). The algorithm of this program was applied to the annotated enzymes in the nuclear genome of *D. salina* by Prof. Jürgen Polle. The a comprehensive list of reactions and compounds in the metabolic network can be found in Appendix C (Table S1 and S2). All entries in the list of reactions (see Table S1) carrying an EC number (Enzyme commission number)

and KEGG ID (Kyoto Encyclopedia of Genes and Genomes) are annotated enzymes of the *D. salina* genome according to the compilation provided by Prof. Jürgen Polle.

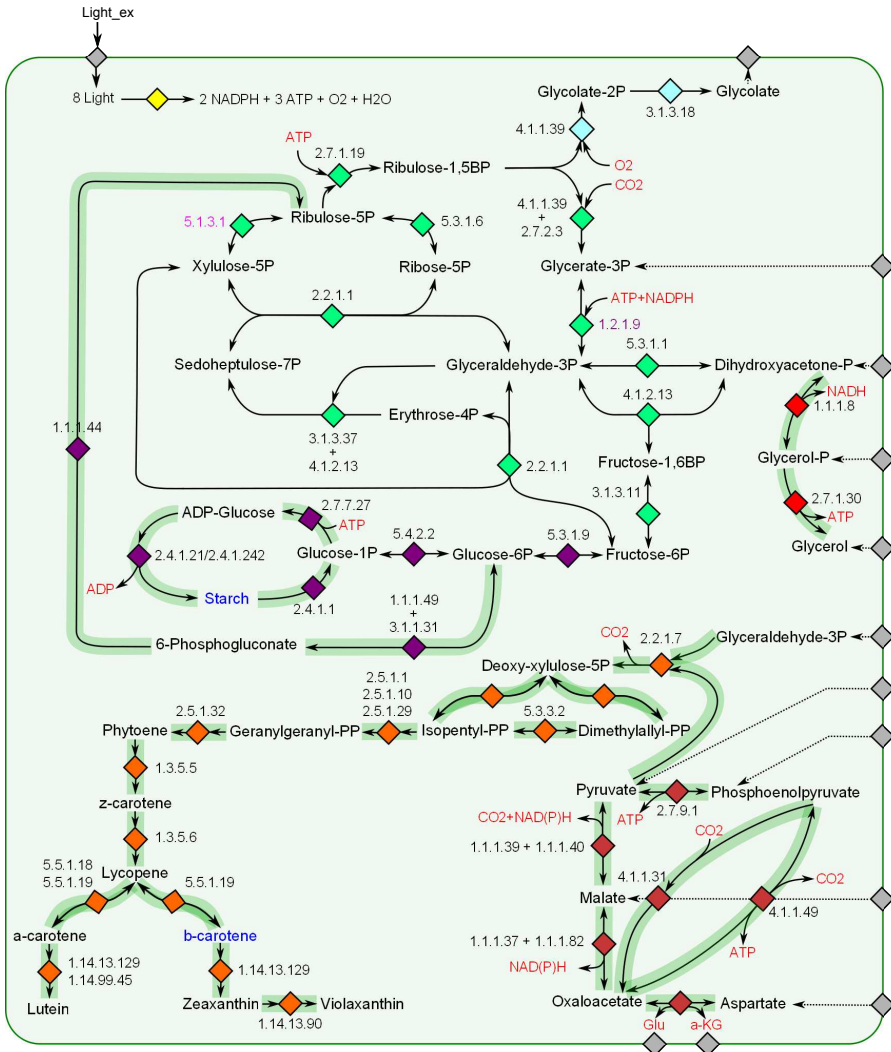


Figure 8.2.: Network map of carbon core metabolism in the chloroplast. The arrows indicate the direction and reversibility of the reactions. The gray boxes indicate shuttling of metabolites between the considered compartments. The reaction arrows in highlighted in green correspond to reactions that have been added to the network. The blue font color refers to metabolites modeled as biomass compounds and the red font color refers to key reaction components such as energy and reduction equivalents. The magenta colored EC numbers belong to enzymes where the corresponding genes were absent but which are necessary to connect the metabolites of the previous and following reactions.

The subcellular localization of some of the annotated enzymes differed from the expectations. For instance, the enzyme glyceraldehyde 3-phosphate dehydrogenase (EC 1.2.1.9) which is part of the calvin cycle was predicted to be localized in the cytosol rather than in the chloroplast. Furthermore, also cytosolic forms of glyceraldehyde 3-phosphate dehydrogenase (EC 1.2.1.13/1.2.1.12) acting in the glycolysis have been identified in the genome. For the triose-phosphate isomerase enzyme (EC

5.3.1.1), PredAlgo predicted a chloroplast localization, although usually a cytosolic localization is assumed.

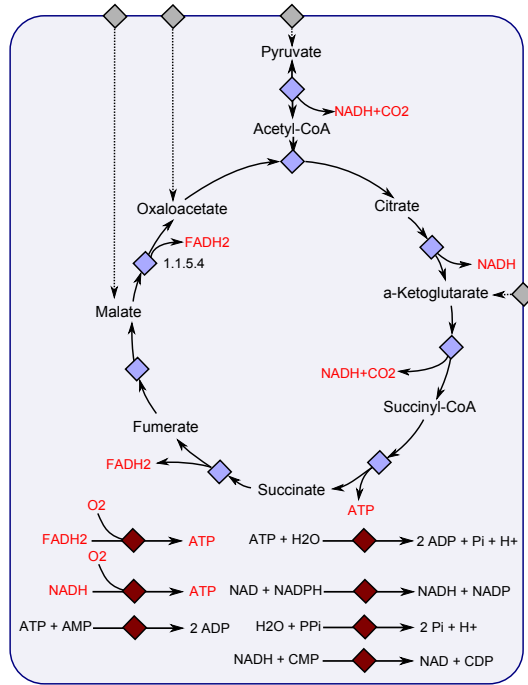


Figure 8.3.: Network map of carbon core metabolism in the mitochondrion. The arrows indicate the direction and reversibility of the reactions. The gray boxes indicate shuttling of metabolites between the considered compartments. The blue font color refers to metabolites modeled as biomass compounds and the red font color refers to key reaction components such as energy and reduction equivalents.

In some essential parts of the metabolism such as the pentose phosphate pathway and the photorespiration also missing enzymes were found, namely ribulose-phosphate 3-epimerase (EC 5.1.3.1) and glyoxylate reductase (EC 1.1.1.26). According to Cordwell (1999), the occurrence of missing enzymes can have various reasons such as failed identification due to low sequence similarity, the reaction is performed by an yet unknown enzyme, multi-enzyme complexes that catalyze different reactions, incorrect assignment of gene identities in genome databases or known enzymatic reactions which have not been assigned to a gene sequence so far. Since the enzymes acting in the up-stream and down-stream reactions are present and the catalyzed reaction is of physiological significance, it was not excluded from the reaction network.

8.2 Dynamic flux balance model

In FBA, models are based on the assumption that the intracellular reaction network has reached a quasi-steady state (balanced-growth assumption). In DFBA, it is assumed that the intracellular dynamics are fast compared to extracellular dynamics such that the quasi-steady state approximation for the FBA model remains valid. For photosynthetic organisms that undergo constant environmental fluctuation this

assumption is not justifiable. Indeed, dynamic intracellular accumulation and consumption are essential in the metabolism of the cells. Therefore, in the current formulation, this is modeled by introducing intracellular dynamic states. The DFBA model developed here consists of two main components, a metabolic model of the microalga and a dynamic model of the photobioreactor environment. The dynamic state variables of the model are the extracellular dynamic states, which are the biomass concentration on dry weight basis ρ_X and the extracellular nitrate concentration ρ_{NO_3} , in addition to the intracellular dynamic states, which are the chlorophyll fraction of total biomass ω_{Chl} , the β -carotene fraction of total biomass ω_{Car} , and the nitrogen cell quota ω_N .

8.2.1. Flux balance model

Since a genome-scale metabolic network representation of *D. salina* is not available, a metabolic network reconstruction of the green fresh water alga *C. reinhardtii* is used to demonstrate the applicability of this network for prediction of the pigment production of *D. salina* under different abiotic stress conditions (Chang et al., 2011; Dal'Molin et al., 2011). A key aspect of this study is the prediction of light- and nitrogen-dependent growth and production of β -carotene. The stoichiometric network of the FBA model is extended to account for the accumulation of chlorophyll and β -carotene. In particular, reversible accumulation fluxes are added to the mass balance of these metabolites. Their upper and lower bounds are determined by the regulatory models described below. The newly defined fluxes are conceptually the same as the exchange fluxes, except that they describe exchange with an intracellular storage.

8.2.2. Exchange fluxes

In addition to the modification of the FBA model, the upper and lower bounds on the exchange and accumulation fluxes are specified as follows and are derived from the dynamic-kinetic model described in Chapter 7.

Light attenuation

The average photon flux density \bar{E} in the photobioreactor is calculated as described in Eq. 7.3. The optical depth is determined as the product of absorption coefficients and densities of the major light absorbing pigments chlorophyll and β -carotene. The average biomass specific light intensity that is the input to the FBA model is determined as follows.

$$E_{X,dw} = \frac{\theta_{dim}\theta_{eff}\bar{E}}{\rho_X \cdot z}, \quad (8.1)$$

where θ_{dim} is a unit conversion factor such that the unit of $E_{X,dw}$ is consistent with existing FBA model input unit and θ_{eff} is dimensionless efficiency factor as in Chang et al. (2011) and $\rho_X \cdot z$ is the biomass density per surface area of the bioreactor in g dw m⁻². Finally, the upper and lower bound on the light exchange flux are

set to the average biomass specific light intensity.

Nitrate metabolism flux

The rate at which the internal nitrate storage is metabolized is denoted by $v_{\text{NO}_3,\text{met}}$. As with all other exchange fluxes, the sign convention implies that a negative value indicates a consumption of nitrate. In analogy with 7.6 of the dynamic-kinetic model, the lower bound on nitrate metabolism rate is given by

$$v_{\text{NO}_3,\text{met}}^{\text{LB}} = -v_{\text{NO}_3,\text{met},\text{max}} \left(1 - \frac{\omega_{\text{N},\text{min}}}{\omega_{\text{N}}} \right), \quad (8.2)$$

where the maximal flux value $v_{\text{NO}_3,\text{met},\text{max}}$ is considered as a model parameter. The metabolism is inhibited as the nitrogen cell quota ω_{N} reaches its minimal value $\omega_{\text{N},\text{min}}$. Furthermore, it is assumed that no nitrate is synthesized through this flux and therefore the upper bound of the nitrate metabolism flux is set to zero.

Chlorophyll accumulation flux

An empirical model for the chlorophyll accumulation is developed based on the observation that the ratio between chlorophyll and nitrogen in various photosynthetic microorganisms can be approximated by a simple inhibition function of the incident light (Thompson et al., 1990; Mairet et al., 2010). Specifically, it is assumed that the ratio is given by

$$\gamma(\bar{E}) = \gamma_{\text{max}} \frac{K_{\text{i,Chl,N}}}{\bar{E} + K_{\text{i,Chl,N}}}, \quad (8.3)$$

where γ_{max} is the maximal ratio and $K_{\text{i,Chl,N}}$ is an inhibition constant. Furthermore, since the data in Thompson et al. (1990) is collected under low and medium light conditions, it is assumed that the ratio is constant for irradiance higher than a critical value \bar{E}_{sat} . The synthesis of chlorophyll in the metabolic network is enforced by varying the bounds on the chlorophyll accumulation flux. If the lower bound is greater than zero, only flux distributions with positive chlorophyll accumulation flux are feasible in the FBA model. This redirects part of the metabolic activity towards chlorophyll synthesis. Hence, to model the regulation of chlorophyll synthesis the lower bound on the chlorophyll flux is assumed to be of the form

$$v_{\text{Chl}}^{\text{LB}} = \left(\gamma(\bar{E}) - \frac{\omega_{\text{Chl}}}{\omega_{\text{N}}} \right). \quad (8.4)$$

If $\frac{\omega_{\text{Chl}}}{\omega_{\text{N}}} < \gamma(\bar{E})$, then the lower bound is greater than zero, which enables accumulation of chlorophyll. If $\frac{\omega_{\text{Chl}}}{\omega_{\text{N}}} > \gamma(\bar{E})$, then the lower bound is less than zero, which enables metabolism of chlorophyll. This regulation can be considered as a proportional control structure with the aim to track the ratio between chlorophyll and nitrogen. The analogy between biochemical regulation and control structures is illustrated in detail in Cloutier and Wellstead (2010). The maximal chlorophyll to nitrogen ratio

γ_{\max} was determined based on experimental data, whereas the inhibition constant $K_{i,\text{Chl},\text{N}}$ and the saturation light intensity are model parameters.

Carotene exchange flux

The photoprotective pigment β -carotene is produced in algae to increase the dissipation of energy at high photon flux densities. Under these conditions the microorganisms cannot utilize all light energy in the photosystem and the excess is harmful to the cell. Furthermore, the mechanism is energetically preferable only if the amount of available nitrogen is low. If sufficient nitrogen (and carbon) is available, then the light energy is used to generate more biomass.

As already stated in Chapter 7 (Eq. 7.7), it is assumed that for high photosynthesis rates, which are measured by average biomass specific light intensity, the biosynthesis of β -carotene as a secondary carotenoid and energy sink is induced, while for low light limiting conditions no accumulation occurs. In addition to the light dependent regulation, the dependency on intracellular nitrogen availability has to be taken into account. At high nitrogen quota, the β -carotene synthesis rate is down regulated since sufficient nitrogen is available for biomass synthesis. Combining these two mechanisms yields that the lower bound of the β -carotene exchange flux in the FBA model is similar to the equation presented in Chapter 7 (Eq. 7.7).

$$v_{\text{Car}}^{\text{LB}} = v_{\text{car},\text{E}} \cdot \frac{E_{\text{X},\text{dw}}^k}{E_{\text{car},\text{crit}}^k + E_{\text{X},\text{dw}}^k} + v_{\text{car},\text{N}} \cdot \left(1 - \frac{\omega_{\text{N}}^k}{\omega_{\text{N},\text{crit}}^k + \omega_{\text{N}}^k} \right) \quad (8.5)$$

Similar to the chlorophyll flux, a positive value for this lower bound implies the accumulation of β -carotene. The upper bound on the β -carotene accumulation flux is set to be infinite. The upper and lower bounds of all exchange fluxes including the flux for non-growth associated ATP maintenance are multiplied by the Hill function Φ such that all metabolic activities are effected during the *lag* phase.

8.2.3. Dynamic photobioreactor model

The flat-plate photobioreactor environment is assumed to be well-mixed such that there are no gradients in nutrients or biomass concentration in the reactor volume. The mass balance for nitrate as an extracellular metabolite is explicitly included in the reactor model. Dissolved CO_2 is provided in excess and is assumed to be not growth-limiting, hence the exchange flux for CO_2 in the FBA model is unbounded and the CO_2 mass balance is not included in the dynamic model. Furthermore, it is assumed that the dissolved O_2 concentration is constant and at equilibrium with the environment, hence the exchange flux for O_2 is unbounded and the O_2 mass balance is not included in the dynamic model.

Nitrogen quota

The Droop model is a widely used formulation to represent limitation of substrate uptake due to internal accumulation (Droop, 1968). The model promotes the idea that growth depends on the stored intracellular pool of nutrients and not directly on

the extracellular concentration. The nitrogen quota ω_N is described by the following ordinary differential equation

$$\dot{\omega}_N = \frac{m_N}{m_{\text{NO}_3}} v_{\text{NO}_3} - \mu \omega_N, \quad (8.6)$$

where v_{NO_3} in the first term is the nitrate uptake rate determined by Michaelis-Menten kinetics, and μ is the growth rate, which is determined by the solution of the FBA model. The Michaelis-Menten kinetic uptake model is formulated similar to Eq. 7.6 and given by

$$v_{\text{NO}_3} = v_{\text{NO}_3, \text{max}} \frac{\rho_{\text{NO}_3}}{K_{S,N} + \rho_{\text{NO}_3}} \left(1 - \frac{\omega_N}{\omega_{N, \text{max}}} \right), \quad (8.7)$$

where the second term models the saturation, i.e. when the nitrogen quota reaches its maximum value $\omega_{N, \text{max}}$. It is assumed that the intracellular nitrogen is stored in form of nitrate. The maximal nitrogen quota is a biomass specific constant and given in Table 7.2.

The complete equation system for the dynamic photobioreactor model is given by:

$$\frac{d\rho_X}{dt} = \mu \cdot \rho_X \quad (8.8)$$

$$\frac{d\rho_{\text{NO}_3}}{dt} = -v_{\text{NO}_3} \cdot \rho_X \quad (8.9)$$

$$\frac{d\omega_N}{dt} = \frac{M_N}{M_{\text{NO}_3}} \cdot v_{\text{NO}_3} - \mu \cdot \omega_N \quad (8.10)$$

$$\frac{d\omega_{\text{Chl}}}{dt} = m_{\text{Chl}} \cdot v_{\text{Chl}} - \mu \cdot \omega_{\text{Chl}} \quad (8.11)$$

$$\frac{d\omega_{\text{Car}}}{dt} = m_{\text{Car}} \cdot v_{\text{Car}} - \mu \cdot \omega_{\text{Car}} \quad (8.12)$$

where μ , v_{Car} , v_{Chl} and $v_{\text{NO}_3, \text{met}}$ are determined by the FBA model via lexicographic optimization as described in Gomez et al. (2014). Specifically, DFBA1ab requires the specification of lexicographic optimization objectives to avoid the common problem of nonunique exchange fluxes that render the ODE system impossible to integrate.

The hierarchy (or lexicographic ordering) chosen is shown in Table 8.1. The ordering is motivated by the assumption that the primary objective is the maximization of growth, then the remaining resources prioritized based on their importance to maintain metabolic activity and finally minimizing the uptake of nutrients under the constraints that all previous objectives are met.

Table 8.1.: Priority list order for the lexicographic linear programs

Level	Objective
1	Maximize biomass production (autotrophic)
2	Minimize chlorophyll accumulation
3	Minimize β -carotene accumulation
4	Minimize nitrate metabolization flux

The numerical solution of the proposed model involves the use of DFBA1ab, a MATLAB code that performs reliable and efficient DFBA simulations (Gomez et al., 2014).

Widespread implementation of DFBA has been hindered by numerical complications resulting from linear programs (LPs) becoming infeasible and having nonunique solution vectors. Infeasible LPs cause simulation failure as the right-hand side of the ODEs becomes undefined, and nonunique solution vectors cause this same right-hand side to be nonunique, producing an ODE system that integrators are unable to solve. DFBA1ab is a MATLAB implementation of the DFBA simulator presented in Höffner et al. (2013) that avoids infeasibilities and lexicographic optimization to provide unique exchange fluxes. It reformulates the LP locally as an algebraic system and integrates a differential-algebraic equation system instead of ODEs with LPs embedded to increase speed.

Parameter estimation is performed by minimizing the cost function

$$J(\mathbf{p}) = \chi^2(\mathbf{p}) + \alpha\Theta(\mathbf{p})^2 \quad (8.13)$$

where the residual sum of squares χ^2 is given by Equation 8.13, Θ is a penalty function and α is a positive weighting factor. The output variables are the biomass density, the extracellular nitrogen density, the chlorophyll and β -carotene fractions of the biomass.

The penalty function is included such that the optimal solution of the parameter estimation is a feasible DFBA simulation. It is possible that for arbitrary parameter values, the linear programs embedded in the DFBA model are not feasible at every time instance during a batch simulation. DFBA1ab provides a penalty value that is zero if the simulation is feasible and strictly great than zero otherwise (see Gomez et al. (2014) for further details). Hence, a large weighting factor ensures that infeasible DFBA simulations are penalized in the optimization problem. Heuristic optimization algorithms for the parameter estimation problem that are not based on gradient information were able to provide a good solution, even though no guarantee of optimality could be issued. The best solution was found by a genetic algorithm using the ga function in MATLAB.

8.2.4. Model simulation

The DFBA approach was applied to simulate biomass growth, nutrient uptake and pigment fraction in a more structured manner than the dynamic-kinetic growth model presented in Chapter 7. The time evolution of the model solutions, with parameters values given in Table 8.2, compared to the experimental data under different light and nutrient conditions are illustrated in Figs. 8.4 and 8.5. The model simulations agree very well with the experimental data for all measured outputs. The biomass constants and parameter values were taken from Chapter 7 (7.3) and the units were converted in order to be compatible with the DFBA model (see Table 8.2).

The total number of model parameters is ten, where five parameters originate from the dynamic-kinetic growth model in Chapter 7 which were proven as identifiable and five DFBA-specific parameters.

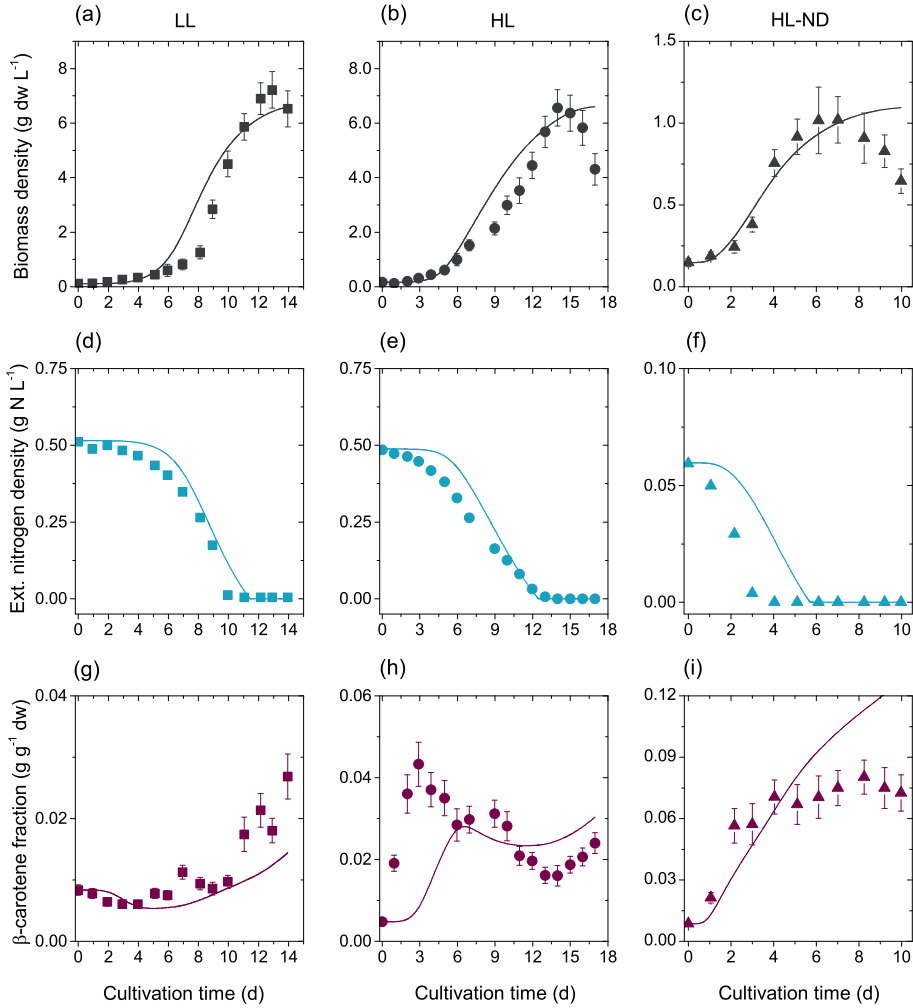
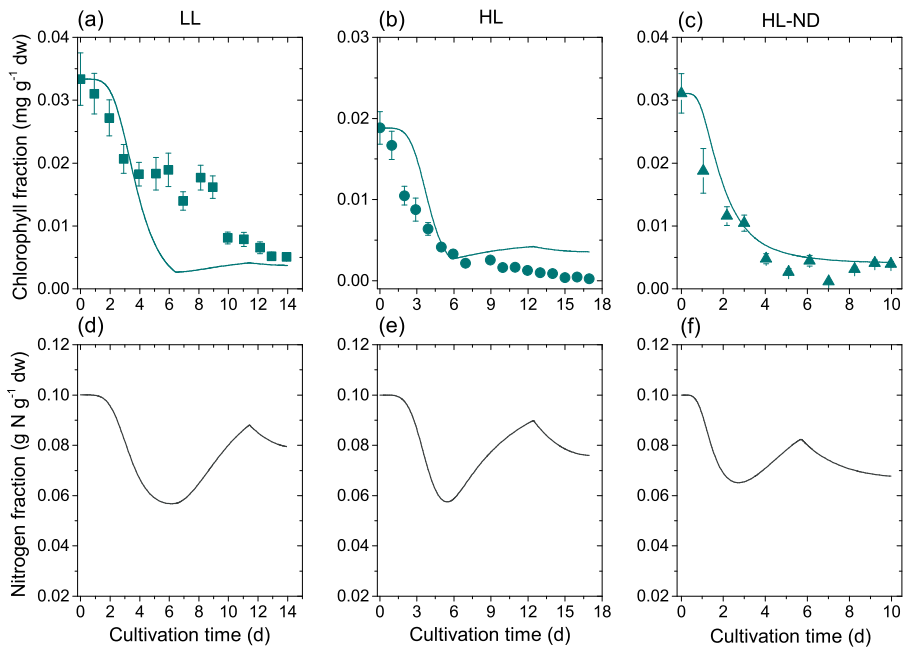


Figure 8.4: Model simulation for the effect of various cultivation conditions on the biomass density ρ_X (a-c), the extracellular nitrogen density $\rho_{N,\text{ext}}$ (d-f) and the β -carotene fraction ω_{Car} (g-i) in the DFBA model. Comparison of the simulated time course (lines) with experimental data (symbols).

Table 8.2.: Biomass constants and parameter values for the DFBA model. The values for the biomass constants and model parameters were taken from Chapter 7.

Symbol	Description	Value	Unit
Biomass constants			
γ_{\max}	Max. intracell. chlorophyll to nitrate ratio	0.33	$\text{g Chl g}^{-1} \text{N}$
λ	Duration of the lag phase		d
$\omega_{\text{N,crit}}$	Crit. nitrogen cell quota for β -carotene synthesis	0.08	$\text{g N g}^{-1} \text{dw}$
$\omega_{\text{N,min}}$	Min. nitrogen cell quota	0.03	$\text{g N g}^{-1} \text{dw}$
$\omega_{\text{N,max}}$	Max. nitrogen cell quota	0.10	$\text{g N g}^{-1} \text{dw}$
k	Hill coefficient	4	-
Dynamic-kinetic model parameters			
$E_{\text{car,crit}}$	Crit. light int. for β -carotene synthesis	1.94×10^5	$\mu\text{mol photons g}^{-1} \text{dw h}^{-1}$
$K_{\text{s,N}}$	Michaelis-Menten coeff. for NO_3 uptake	6.82×10^{-4}	$\text{g NO}_3 \text{ L}^{-1}$
$v_{\text{car,E}}$	Light stress-induced β -carotene synthesis rate	4.64×10^{-3}	$\text{mmol g}^{-1} \text{dw h}^{-1}$
$v_{\text{car,N}}$	Nutrient stress-induced β -carotene synthesis rate	4.11×10^{-4}	$\text{mmol g}^{-1} \text{dw h}^{-1}$
$v_{\text{NO}_3,\text{max}}$	Max. nitrogen uptake rate	0.0167	$\text{g NO}_3 \text{ g}^{-1} \text{dw h}^{-1} \text{L}^{-1}$
DFBA specific parameters			
E_{sat}	Saturation light int. for chlorophyll to nitrate ratio	75.5	$\mu\text{mol photons m}^{-2} \text{s}^{-1}$
$K_{\text{i,Chl,N}}$	Inhibition coeff. for chlorophyll to nitrate ratio	12.5	$\mu\text{mol photons m}^{-2} \text{s}^{-1}$
$v_{\text{NO}_3,\text{met,max}}$	Max. nitrogen assimilation flux	0.19	$\text{mmol g}^{-1} \text{dw h}^{-1}$
ng_{am}	Non-growth associated maintenance	light and nutrient dependent	$\text{mmol g}^{-1} \text{dw h}^{-1}$
	for LL conditions	0.915	
	for HL conditions	1.00	
	for HL-ND conditions	1.28	
	for LL-ND conditions	0.915	
	for LL-NL conditions	1.28	
θ_{eff}	Photon efficiency	light dependent	-
	for LL conditions	3.0×10^{-4}	
	for HL conditions	9.0×10^{-5}	
	for HL-ND conditions	4.3×10^{-5}	
	for LL-ND conditions	2.2×10^{-4}	
	for LL-NL conditions	2.0×10^{-4}	

**Figure 8.5.:** Model simulation for the effect of various cultivation conditions on the the chlorophyll fraction ω_{Chl} (a-c) and the nitrogen quota in the biomass ω_{N} (d-f) in the DFBA model. Comparison of the simulated time course (lines) with experimental data (symbols).

8.2.5. Model validation

The model predictions are validated through comparison with an independent set of experimental data that was not used for the parameter estimation. The experiments were performed under light light and nitrogen depletion (LL-ND) and light light and nitrogen limitation (LL-NL). The model prediction and validation data are illustrated in Figs. 8.6 and 8.7.

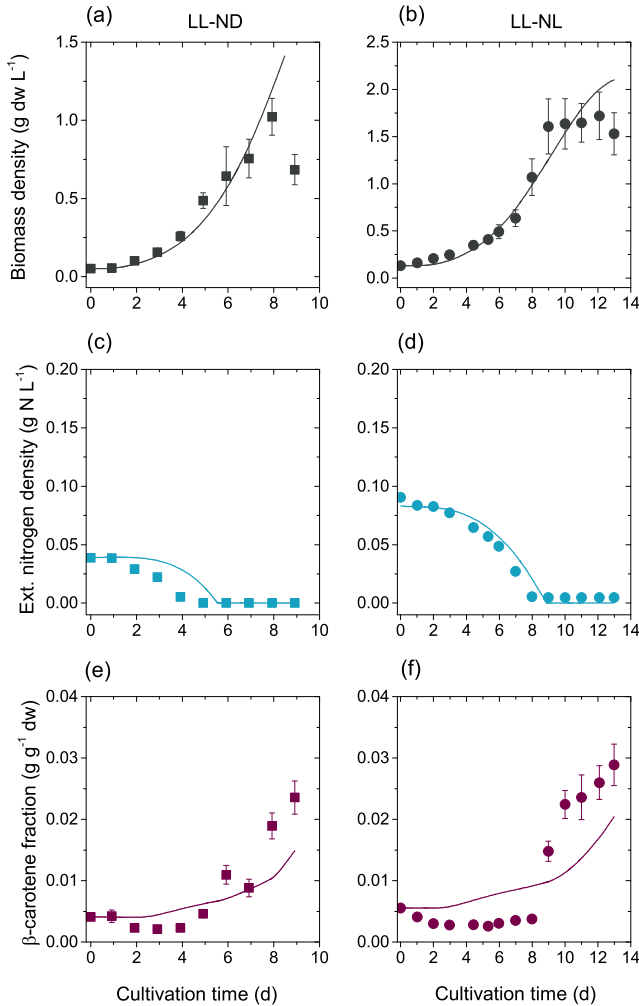


Figure 8.6.: Model validation for the effect of various cultivation conditions on the cell density ρ_X (a-b), the extracellular nitrogen density $\rho_{N,ext}$ (c-d) and the β -carotene fraction ω_{Car} (e-f) in the DFBA model. Comparison of the simulated time course (lines) with experimental data (symbols).

8.2.6. Model-based optimization for fed-batch operation

As can be seen from Figs. 8.4 and 8.5, *D. salina* grows well for low to high light conditions at sufficient supply of nitrate. In the stress condition of high light and nutrient depletion, a strong β -carotene accumulation was observed, however, the growth rate

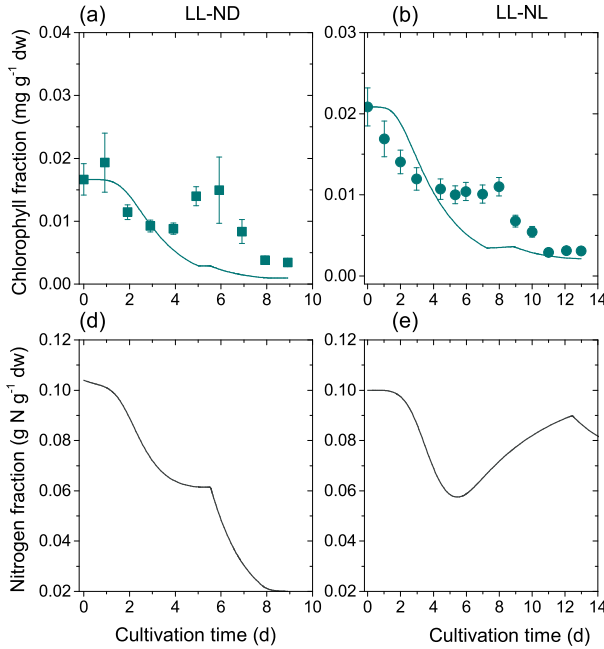


Figure 8.7.: Model validation for the effect of various cultivation conditions on the the chlorophyll fraction ω_{Chl} (a-b) and the nitrogen quota in the biomass ω_{N} (c-d). Comparison of the simulated time course (lines) with experimental data (symbols).

is considerably smaller than for nutrient-replete conditions. Given a validated computational model of *D. salina*, an optimal fed-batch cultivation to trade-off growth and β -carotene accumulation optimally was designed based on the model structure published in Flassig et al. (2016), where two input variables (i) light intensity per biomass and (ii) nitrogen feeding rate were optimized.

As can be seen in Eq. 8.5, there is an interplay between light and nutrient stress that drives β -carotene accumulation. Therefore, the optimization can be simplified in a first step via exertion of a fixed light stress per cell. After inoculation an initial 1 day adaptation phase at incident light intensity $E_0 = 100 \mu\text{mol photons m}^{-2}\text{s}^{-1}$ was performed followed by the light intensity profile

$$E_{0,opt}(t) = I_0 \cdot \rho_X. \quad (8.14)$$

The factor $I_0 = 3000 \mu\text{mol photons m}^{-2}\text{s}^{-1} \text{ g}^{-1} \text{ dw L}$ was motivated by natural sunlight conditions in open pond operation systems. Note that until a ρ_X of 1 g L^{-1} , the light intensity profile can sustain a fixed incident light stress per cell. With this light feed, an optimal nitrogen feeding profile based on the model published in Flassig et al. (2016) was identified. The nitrogen feeding profile was parameterized as a Hill function with the Hill coefficient n_D and nitrogen fraction ratio $\omega_{\text{N,min}}/\omega_{\text{N}}(t)$,

$$N_{feed,opt}(t) = N_D \frac{(\omega_{\text{N,min}}/\omega_{\text{N}}(t))^{n_D}}{1 + (\omega_{\text{N,min}}/\omega_{\text{N}}(t))^{n_D}}. \quad (8.15)$$

The parameters were set as follows: $n_D = 10$ and $\omega_{N,\min} = 0.02$. Other parameterizations are of course possible. However, firstly the S-shape of the Hill function seems natural for a growing culture, and secondly, for a fixed light stress the nitrogen quota at its minimal value is the most dominating factor for β -carotene synthesis in combination with cell growth.

Given these two feed parametrizations, the model was used to simulate the behavior of biomass growth and β -carotene accumulation for a fed-batch time of 9 days with the model structure given above. As can be seen in Fig. 8.8 regimes for optimal growth are suboptimal for β -carotene accumulation and vice versa. Fig. 8.8 also indicates the β -carotene density in the reactor ($\rho_{Car} = \omega_{Car} \cdot \rho_X$). The optimal design point can be chosen along a line of different combinations of internal nitrogen and nitrogen feeding factor N_D . Since the internal nitrogen at the beginning of the fed-batch cultivation is determined by the inoculation, the nitrogen feeding factor was determined to $N_D = 0.02 \text{ g}_N \text{ L}^{-1} \text{ h}^{-1}$.

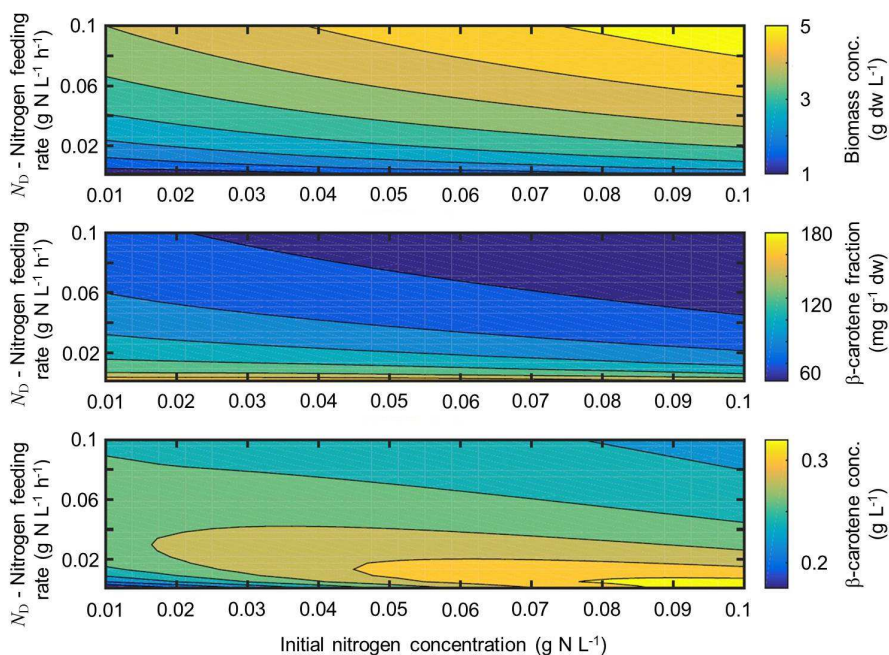


Figure 8.8.: Influence of inoculum nitrate concentration and nitrogen feeding factor N_D on biomass (top), β -carotene fraction (middle) and β -carotene density (bottom). For the experiment, the inoculum nitrate concentration was at 0.08 g L^{-1} . Thus $N_D = 0.02 \text{ g}_N \text{ L}^{-1} \text{ h}^{-1}$ was chosen.

The resulting input profiles were realized in an experimental run, where both profiles have been discretized in daily integrated applications (Fig. 8.9). Seven days after inoculation, the culture reached a saturation in the maximal light stress and the β -carotene amount started to decline (Fig. 8.9). Inducing an additional stress via nitrogen depletion, the β -carotene fraction could again be raised. At the optimal harvesting time point, a β -carotene density of 0.140 g L^{-1} at a fraction of $0.06 \text{ g Car g}^{-1} \text{ dw}$ and a biomass density of 3.4 g dw L^{-1} was achieved. This is about 83% more β -carotene and 233% more biomass compared to the standard batch (see Tab. 8.3).

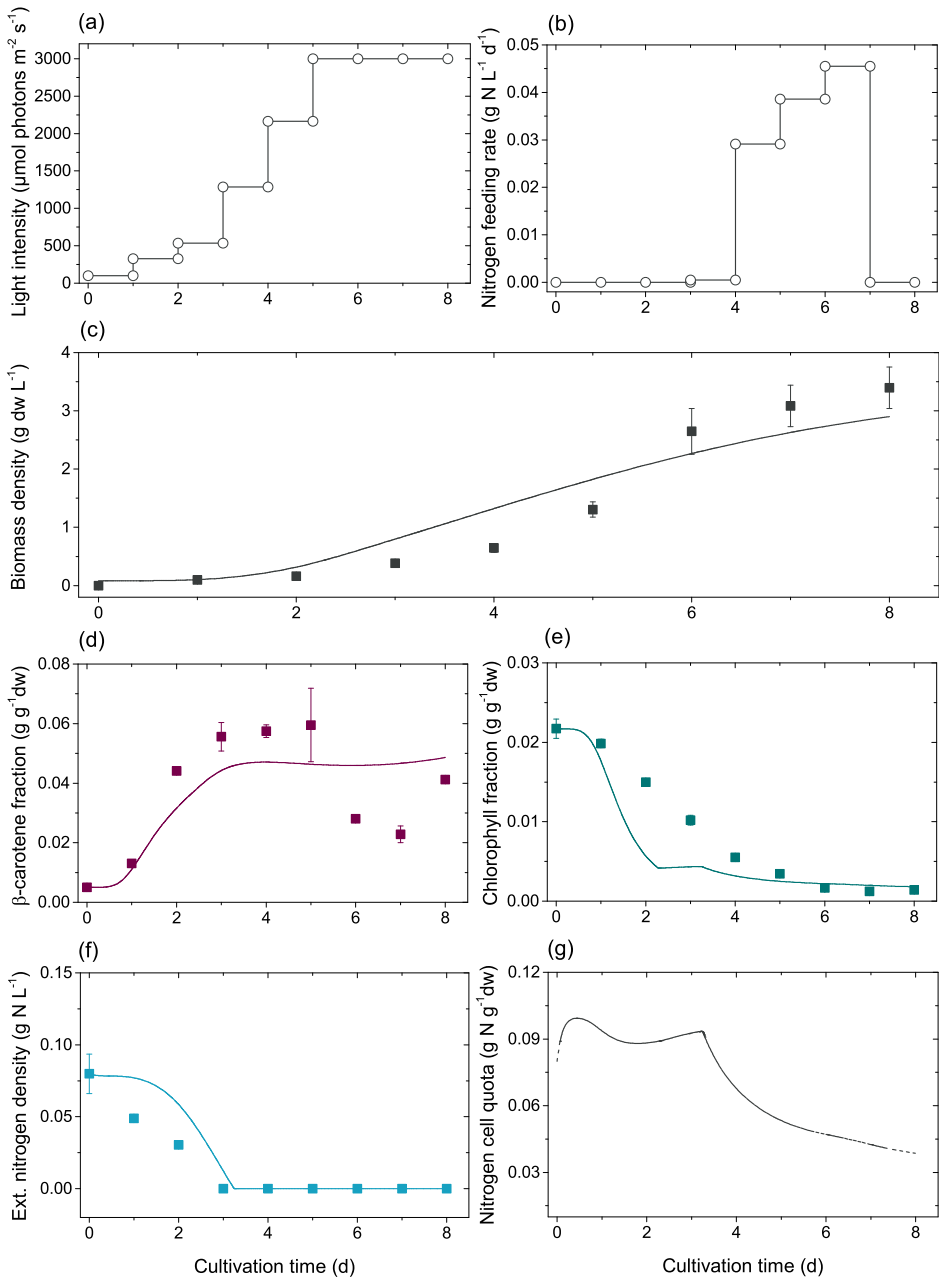


Figure 8.9.: Simulation results of the optimized fed-batch cultivation. Simulations results of c) biomass density, d) β -carotene fraction, e) chlorophyll fraction, f) nitrogen density and g) nitrogen cell quota (lines), experimental data (symbols) and error bars. The two top panels show the applied a) light and b) nutrient profile.

Table 8.3.: Performance of the fed-batch cultivation compared to the batch cultivation. The percentage of increase to the HL-ND batch is given in brackets.

Property	Unit	LL	HL	HL-ND	Opt. Fed-Batch
Max. biomass density	g dw L ⁻¹	7.22	6.55	1.02	3.40 (+233 %)
Max. biomass productivity	g dw L ⁻¹ d ⁻¹	0.56	0.46	0.15	0.43 (+187 %)
Max. β -carotene density	mg L ⁻¹	175.18	120.04	76.42	140.06 (+83 %)
Max. β -carotene fraction	mg g ⁻¹ dw	26.86	43.28	80.30	59.53 (-26 %)
Max. β -carotene productivity	mg L ⁻¹ d ⁻¹	12.05	7.90	12.88	17.48 (+36 %)

8.2.7. Model-based optimization for continuous operation mode

A major reason for the low biomass and pigment production and batch- and fed-batch cultivations is the long lag- and early exponential phase which accounts to almost one third of the overall cultivation time. Continuous reactor operation, where biomass and pigment accumulation are in steady-state may lead to a significant increase in volumetric productivity. In order to test this hypothesis, the validated DFBA equation system was extended from batch to continuous operation mode by adding the dilution rate D to the biomass equation. The desired operation mode, where the dilution rate D equals the growth rate μ leads to a constant biomass and β -carotene density in steady-state and cannot be calculated on an empirical basis due to the complex interplay of light and nutrient stress on growth. Therefore, the model-based optimization approach presented for the fed-batch cultivation was extended to the continuous operation mode. Two different steady-state conditions were chosen, namely 1 g dw L⁻¹ at a dilution rate of 0.46 d⁻¹ and a fixed light stress of 3000 $\mu\text{mol m}^{-2} \text{s}^{-1} \text{g}^{-1} \text{dw}$ and 3 g dw L⁻¹ at a dilution rate of 0.55 d⁻¹ and a fixed light stress of 1000 $\mu\text{mol m}^{-2} \text{s}^{-1} \text{g}^{-1} \text{dw}$. Thus, under both light conditions the maximal light intensity of the reactor panel is 3000 $\mu\text{mol m}^{-2} \text{s}^{-1}$. The corresponding nitrogen feeding rate was calculated based on Eq. 8.15. The experimental conditions for the model-based continuous cultivations are given in Table 8.4.

Table 8.4.: Overview of experimental conditions for model-based continuous cultivations of *D. salina*.

Name	Steady state light intensity per biomass ($\mu\text{mol m}^{-2} \text{s}^{-1} \text{g}^{-1} \text{dw}$)	Dilution rate (d ⁻¹)	Nitrogen feeding rate (g N L ⁻¹ d ⁻¹)
Continuous I	3000	0.46	0.008
Continuous II	1000	0.55	0.04

Similar to the model-based fed-batch cultivation, the computed input profiles were experimentally realized in daily integrated applications. Again, the experimental data and the simulation results agree to a large extend (Figs. 8.11 and 8.12) demonstrating the validity of the suggested model. Although both cultivations used the maximal light intensity of the reactor panel, the volumetric β -carotene productivity differed significantly (Table 8.5). The high light continuous process with a fixed light stress 3000 $\mu\text{mol m}^{-2} \text{s}^{-1} \text{g}^{-1} \text{dw}$ is almost comparable with the fed-batch process in terms of biomass- and β -carotene productivity. Thereby, not only the fed-batch but also the high light continuous process significantly outperformed the HL-ND batch. However, when comparing to the second continuous process with a fixed light stress of only 1000 $\mu\text{mol m}^{-2} \text{s}^{-1} \text{g}^{-1} \text{dw}$ at 3 g dw L⁻¹ biomass, a tremendous increase in productivity was observed. Compared to the already optimized fed-batch process a

3.2-fold increase in biomass productivity and a 6-fold increase in β -carotene productivity was achieved. Compared to the HL-ND batch the increase in productivity is even more pronounced, namely 11.2-fold increase in biomass and 8.5-fold increase in β -carotene productivity. As can be seen in Figs. 8.11 and 8.12, the nitrogen cell quota was in both culture at its minimal value of $0.03 \text{ g N g}^{-1} \text{ dw}$ indicating the validity of our parameterization approach (Eq. 8.15) and the predictivity of the nitrogen metabolism in the DFBA model.

Table 8.5.: Performance of the continuous cultivations in steady-state compared to the optimized fed-batch cultivation. The percentage of increase to the optimized fed-batch is given in brackets.

Property	Unit	Opt. Fed-Batch	Continuous I	Continuous II
Biomass density	g dw L^{-1}	3.40	0.75 (-78 %)	3.30 (-3 %)
Biomass productivity	$\text{g dw L}^{-1} \text{ d}^{-1}$	0.43	0.35 (-35 %)	1.83 (+326 %)
β -carotene fraction	$\text{mg g}^{-1} \text{ dw}$	59.53	62.30 (+5 %)	66.80 (+12 %)
β -carotene productivity	$\text{mg L}^{-1} \text{ d}^{-1}$	17.48	21.18 (+21 %)	122.24 (+600 %)

Finally, to illustrate the "process" routes in which β -carotene is synthesized under different cultivation conditions, a state space representation is given in Fig. 8.10, where the β -carotene density is plotted over the biomass density.

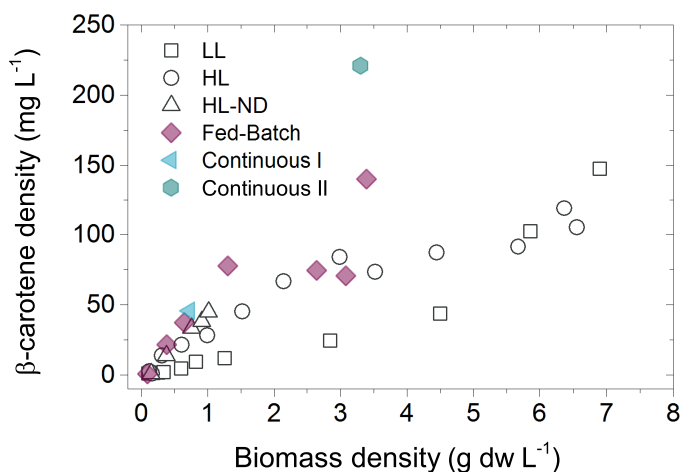


Figure 8.10.: State space diagram depicting the β -carotene density over the biomass density of all cultivation experiments in batch, fed-batch or continuous mode.

In conclusion, Chapter 7 and 8 illustrate the advantages and drawbacks of these two modeling approaches for the construction of predictive growth and product accumulation. However, to the best of our knowledge, there is no direct comparison of results obtained from classical ODE models and DFBA models.

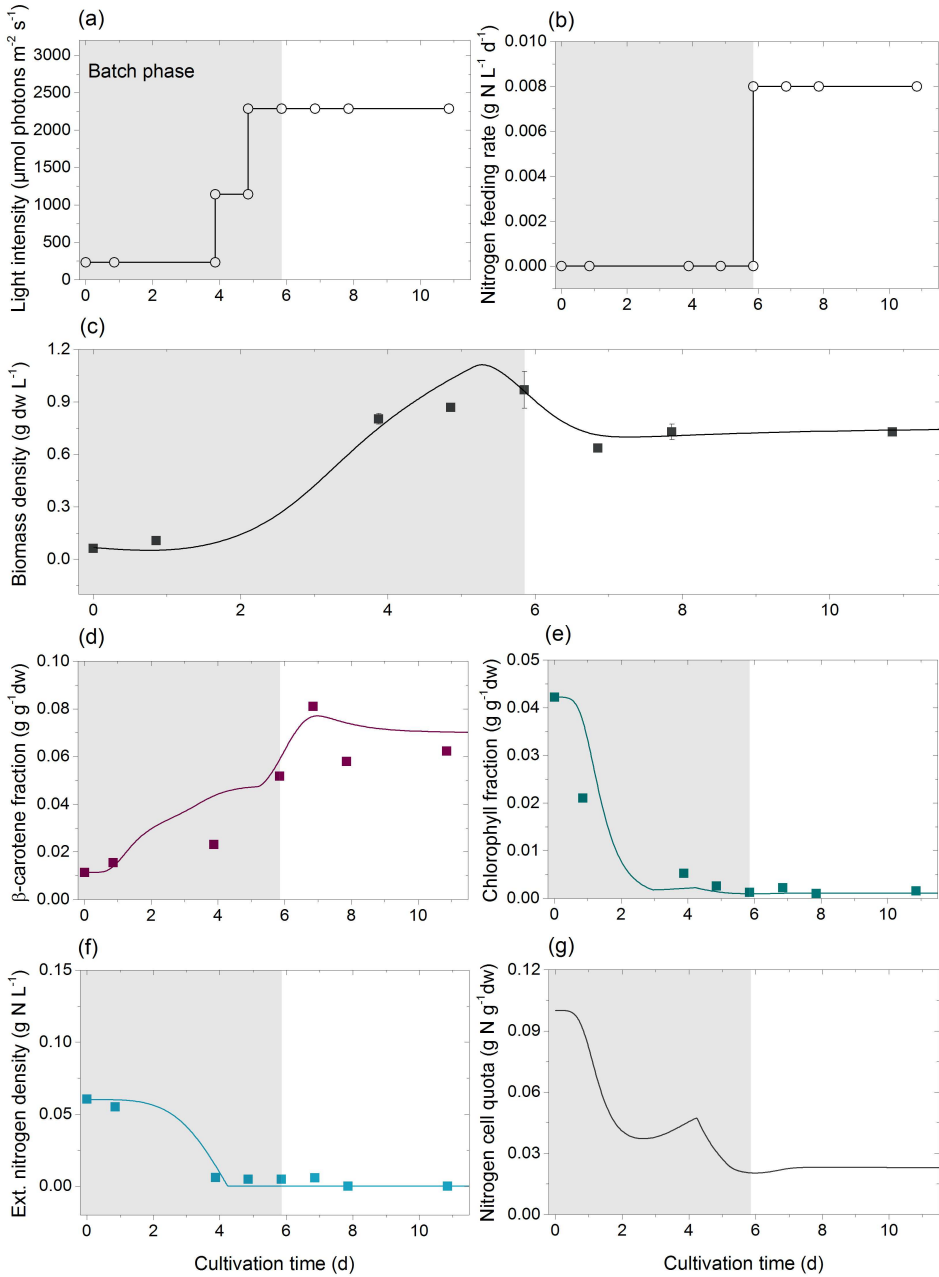


Figure 8.11.: Simulation results of the continuous cultivation at $3000 \mu\text{mol m}^{-2} \text{s}^{-1} \text{g}^{-1} \text{dw}$. Simulations results of c) biomass density, d) β -carotene fraction, e) chlorophyll fraction, f) nitrogen density and g) nitrogen cell quota (lines), experimental data (symbols) and error bars. The two top panels show the applied a) light and b) nutrient profile.

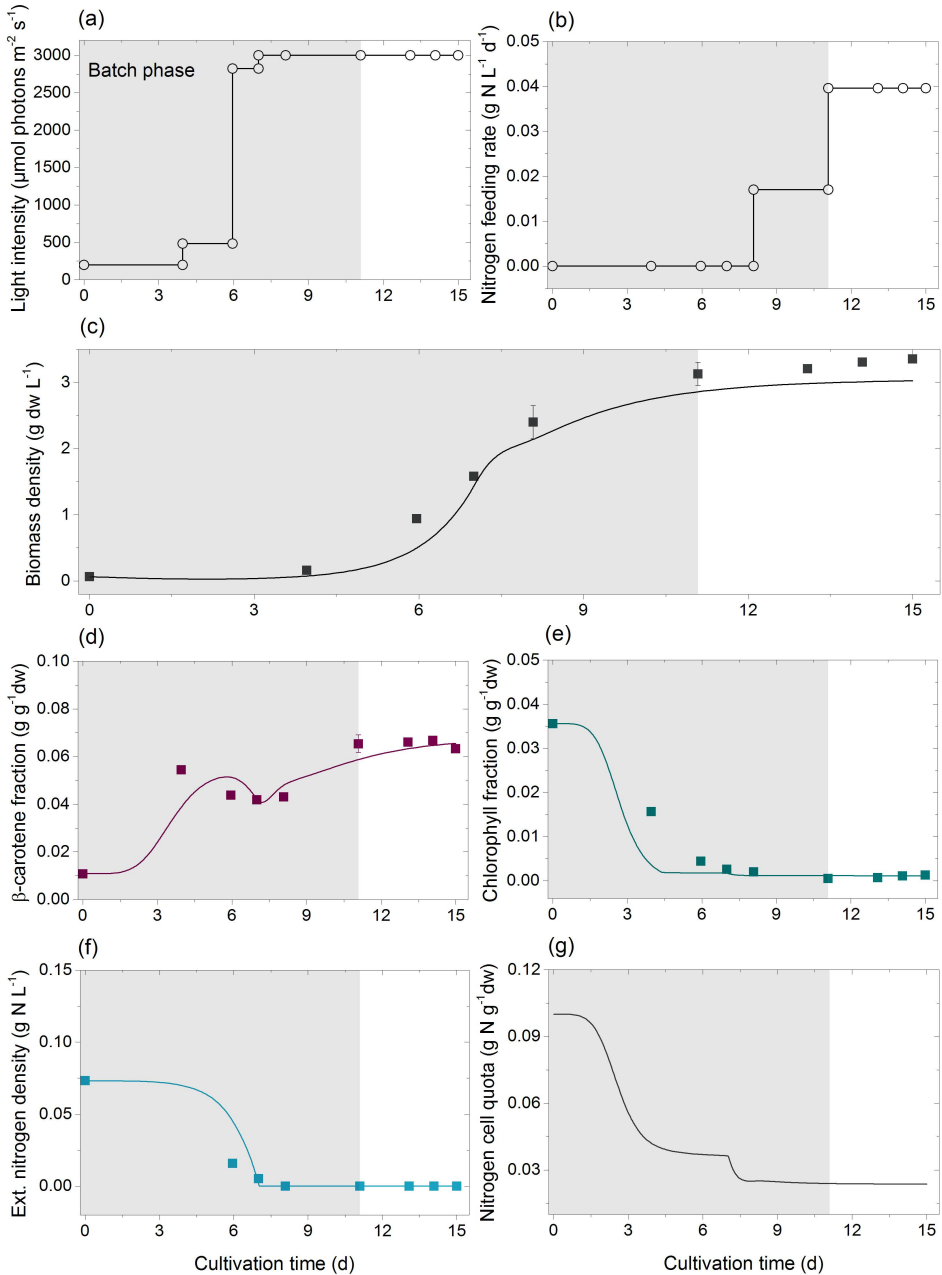


Figure 8.12.: Simulation results of the continuous cultivation at $1000 \mu\text{mol m}^{-2} \text{s}^{-1} \text{g}^{-1} \text{dw}$. Simulations results of c) biomass density, d) β -carotene fraction, e) chlorophyll fraction, f) nitrogen density and g) nitrogen cell quota (lines), experimental data (symbols) and error bars. The two top panels show the applied a) light and b) nutrient profile.

Chapter 9

Interspecies variations in the genus *Dunaliella*

Unicellular green microalgae of the genus *Dunaliella* are among the most studied members of the Chlorophyceae (Polle et al., 2009). The lack of a rigid cell wall is common to all of them. The majority of the species in the *Dunaliella* genus can be found in salt water habitats all around the world. According to a re-evaluation of the *Dunaliella* genus published by Borowitzka and Siva (2007) 22 species were classified, including 17 halophilic organisms with salt optima between 6 and 12% (w/w) and comprises among others *D. salina*, *D. parva*, *D. viridis*, *D. minuta*, *D. gracilis* and *D. bioculata*.

There have been very few studies dealing with a comparative evaluation of physiological and biochemical differences among microalgal strains or species. However, when they exist they generally indicate a significant intra- and interspecies variability (Gonzalez et al., 2009). Although this variability makes comparison of results and deduction of valuable conclusions challenging among different strains, this strategy will promote the "survival of the fittest" in outdoor cultures subjected to significant environmental fluctuations. Physiological variability within *D. salina* was observed in numerous publications (Cifuentes et al., 1992; Markovits et al., 1993; Gomez and Gonzalez, 2005) and the major outcomes and conclusions are summarized in Gonzalez et al. (2009). In general, the results of the previously mentioned studies investigating growth and β -carotene content of *D. salina* isolates from different geographical regions found tremendous physiological variability. Since this variability has also been observed under controlled and comparable lab conditions, the origin of the variability must be related to the genome.

The ability to grow in hypersaline habitats make algae of the genus *Dunaliella* an attractive candidate for algal mass culture. Due to its high β -carotene content, the majority of the studies focused on the biotechnological potential of *D. salina*. This chapter aims at investigating the interspecies differences between *D. salina* and *D. parva*. A special emphasis is placed on the morphological differences, the productivity in terms of biomass and β -carotene, the adaptational stress response as well as differences in photoacclimation and inhibition. Furthermore, the applicability of the interdisciplinary workflow composed of experiments and mathematical modeling as presented in Chapter 6 and 7 is applied to *D. parva*.

9.1 Strain identification of *D. salina* and *D. parva*

Various culture collections located across the world provide an important repository for different algal strains collected from diverse natural habitats. Their task to protect and maintain the biodiversity and thus the genetic material are of inestimable value for algal research. As it holds true for all living organisms, it is inevitable that the genome of all species is subject to constant modifications and mutations. In addition due to the handling of thousands of different strains in the laboratories of culture collections, the samples are prone to contamination by different algae, bacteria or fungi.

Both strains were ordered as *D. salina* CCAP19/18 in 2011 and 2014 at the Culture Collection of Algae and Protozoa (CCAP). Since the cells showed pronounced differences in cell size and cellular dry weight, a 18S rRNA sequencing was performed by Cecilia Rad Menendez from CCAP. The sequence coverage of the sample ordered 2011 had a 100 % Query coverage (99 % Max. ID) with *D. parva*, whereas the sample ordered in 2014 had a 100 % Query coverage (99 % Max. ID) with *D. salina*. The distinction between *D. salina* and *D. parva* was done on the basis of the 18S rRNA gene sequences, where *D. salina* contained only one intron compared *D. parva* which contained two introns (Olmos et al., 2000).

9.2 Experimental analysis of interspecies variability

9.2.1. Morphological variability between *D. salina* and *D. parva*

Beside *D. salina*, *D. parva* and *D. pseudosalina* are known to belong to the carotenogenic species of the *Dunaliella* genus (Borowitzka and Siva, 2007). Like *D. salina*, *D. parva* is a hypersaline alga tolerating NaCl fractions from 3 % (w/w) NaCl to saturation and an optimal salinity range from 6 to 8 % (w/w) (Borowitzka and Siva, 2007). In contrast to *D. salina*, the maximum carotenoid fraction reported for *D. parva* is about 5 % (w/w) (Borowitzka and Siva, 2007).

The most distinctive features between *D. salina* and *D. parva* were the cell size and the dry weight. The results of the comparison are shown in Table 9.1 and showed a high morphological and physiological variability among the studied species. The length of a single *D. parva* cell was only half the cell length of *D. salina* and the cell width was only one third of *D. salina*. The significant differences in the cell size also translated into the cellular dry weight. An average *D. parva* cell had a weight of only 33.5 pg cell⁻¹, whereas the *D. salina* cell had a weight of 520 pg cell⁻¹ when cultivated under low-light and nutrient-repleted conditions. The size measurements were in line with the values published by Borowitzka and Siva (2007) and are given in Table 9.1 for comparison.

Table 9.1.: Size and weight comparison for *D. salina* and *D. parva*. The size determination was performed by manual length and width measurement of 30 representative cells from light microscopic images acquired with the Axio Imager A1 (Carl Zeiss, Germany).

Species	Av. length (μm)		Av. width (μm)		Av. cellular dry weight (pg cell^{-1})
	this work	literature	this work	literature	
<i>D. parva</i>	7.6	8-10	3.8	3-5	33.5
<i>D. salina</i>	14.7	10-15	11.6	5-10	520

9.2.2. Biotechnological parameters for *D. parva* under abiotic stress

Batch cultivations of *D. parva* were carried out in order to identify interspecies differences in biomass formation and pigment accumulation (Table 9.2). The biotechnological parameters are listed in Table 9.3 and the percentage decrease or increase is given in brackets behind. In almost all cases *D. salina* outperformed *D. parva*. The highest content of β -carotene was observed with 4.9% (w/w) under HL-ND conditions and is in line with the 5.0% (w/w) reported by Borowitzka and Siva (2007). Although the initial nitrate density of the HL-ND batch of *D. parva* was lower compared to the HL-ND batch of *D. salina* (0.017 g N L^{-1} compared to 0.05 g N L^{-1}), the incorporation into the biomass seems to be more efficient since the final biomass density for *D. parva* was 35% higher. Indeed, the elemental composition analysis revealed a minimum nitrogen cell quota of $0.02 \text{ g N g}^{-1} \text{ dw}$ for *D. parva* whereas $0.03 \text{ g N g}^{-1} \text{ dw}$ was measured for *D. salina*.

Table 9.2.: Overview of experimental conditions for batch cultures of *D. parva*.

Abbreviation	Description	Light intensity ($\mu\text{mol m}^{-2} \text{ s}^{-1}$)	Duration of lag phase (d)	Extracellular nitrogen density (g N L^{-1})
LL	Low light	175	3	0.5
HL	High light	1950	3	0.5
HL-ND	High light and nitrogen depletion	1950	2.5	0.017

Table 9.3.: Biotechnological performance of *D. parva* compared to the percentage of increase or decrease measured for *D. salina* for cultivations under abiotic stress in batch operation mode. Details on the cultivation conditions of *D. parva* are given in Fatchet et al. (2014).

Property	Unit	LL	HL	HL-ND
Max. biomass density	g dw L^{-1}	1.50 (-79%)	4.45 (-32%)	1.38 (+35%)
Max. biomass productivity	$\text{g L}^{-1} \text{ d}^{-1}$	0.16 (-71%)	0.50 (+8%)	0.22 (+47%)
Max. β -carotene density	mg L^{-1}	4.48 (-97%)	15.92 (-87%)	67.73 (-11%)
Max. β -carotene fraction	$\text{mg g}^{-1} \text{ dw}$	3.0 (-89%)	24.4 (-44%)	49.1 (-39%)
Max. β -carotene productivity	$\text{mg L}^{-1} \text{ d}^{-1}$	1.41 (-88%)	1.82 (-76%)	11.53 (-11%)

9.2.3. Photosynthetic performance of *D. parva*

Beside the differences in morphology and biotechnological parameters, further variability compared to *D. salina* was observed in the response upon exposure to oversat-

urating light conditions as illustrated in Fig. 9.1, where the dependency of the ETR on the average light intensity is given. In the case of *D. salina*, photosaturation occurred between 550–860 $\mu\text{mol photons m}^{-2} \text{s}^{-1}$ and the photoinhibitory phase was reached from 1070 $\mu\text{mol photons m}^{-2} \text{s}^{-1}$ on (Fig. 6.7). In contrast, a pronounced saturation and photoinhibitory phase could not be observed, neither for low light nor for high light-acclimated *D. parva* cells (Fig. 9.1). Due to the absence of a photoinhibition phase in *D. parva*, the maximal ETR of 25 $\mu\text{mol electrons m}^{-2} \text{s}^{-1}$ is 3 times higher compared to the maximal ETR achieved for *D. salina*.

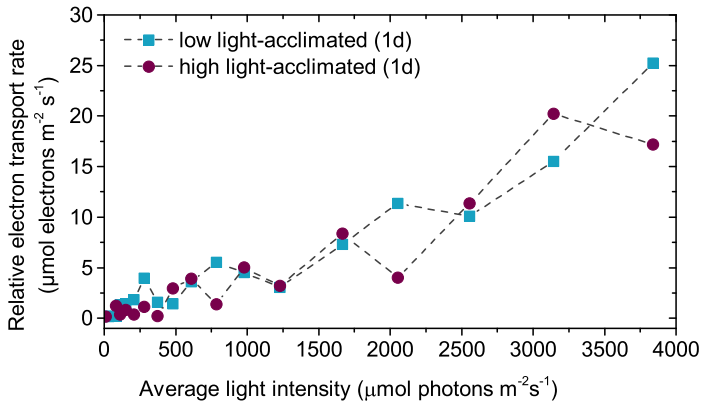


Figure 9.1.: Relationship between electron transport rate and average light intensity in *D. parva*.

9.2.4. Correlation matrix for measured features of *D. salina* and *D. parva*

In order to present the results of the multiparametric biomass analysis in a structured way, correlation matrices of the various measured biomass features of *D. parva* and *D. salina* were constructed and shown in Fig. 9.2. The correlation matrices were calculated with the Matlab functions `cov` and `corrcoef`, where in an intermediate step the covariance matrix was calculated from which the final correlation matrix was computed (Davis et al., 2015). In Fig. 9.2, the various parameters are grouped by category from left to right and bottom to top: input conditions, biomass-related parameters, flow cytometric parameters and PAM parameters. Correlations among members of the same category are boxed along the diagonal of the matrix and data points reflected across the diagonal are redundant (Davis et al., 2015). In general, the biomass features of *D. parva* exhibit a higher correlation intensity compared to *D. salina*, although the correlation pattern show a high degree of similarity. In principle, the PAM parameters ($\Phi_{\text{PSII,max}}$, $\Phi_{\text{PSII,eff}}$ and NPQ) and flow cytometry parameters (Debris content, FSC and SSC) are well correlated, whereas the biomass-related parameters show only weak correlation.

The positively correlated biomass features for *D. parva* and *D. salina* can be summarized as follows:

- Incident light per biomass and β -carotene content with debris content and cell granularity

- Chlorophyll content with nitrogen density
- Maximum and effective quantum yield of PSII with chlorophyll content
- Maximum quantum yield of PSII and NPQ with cell density and biomass density on dry weight basis

Noteworthy, among the features with highly negative correlation coefficients (less than -0.8) are the β -carotene content and the external nitrogen density.

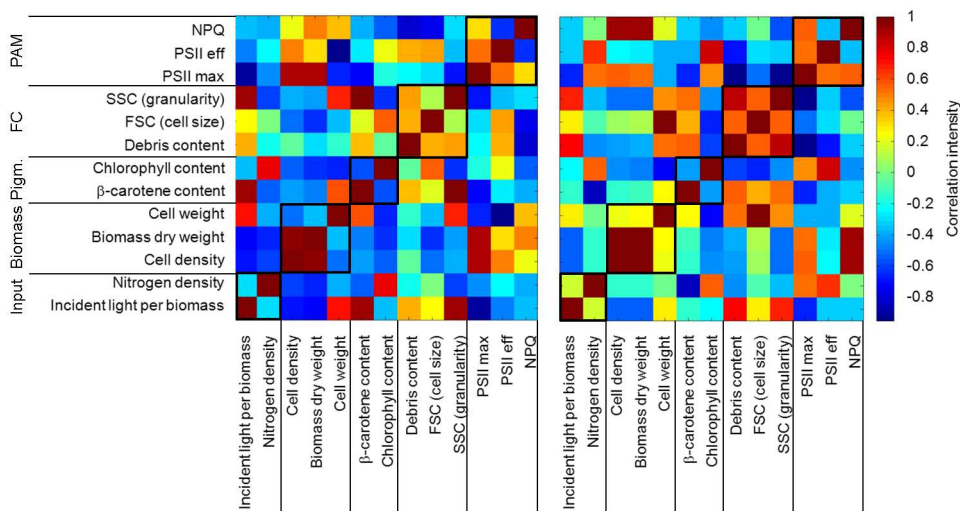


Figure 9.2: Correlation matrix for the measured biomass features of *D. salina* (left) and *D. parva* (right). Black boxes indicate groupings of related parameters, i.e., along the diagonal from lower left to upper right: Input conditions, biomass-related parameters, pigments, flow cytometric parameters and PAM parameters. Diagonal elements (from lower left to upper right) of the matrix represent correlation of each parameter with itself.

9.3 Dynamic-kinetic growth model for *D. parva*

In the following section, the interspecies variability between *D. salina* and *D. parva* was analyzed with a model-based approach, namely the dynamic-kinetic growth model presented in Chapter 7. The experimental data for the simulations were obtained as specified in Table 9.2.

Due to the large degree of similarity in the model structure, the model equations and biomass-specific constants (Table S2) are given in Appendix B. Similar to the results for *D. salina*, the simulation results for *D. parva* are in good agreement with the experimental data (Figs. 9.3 and 9.4). The observed growth behavior under HL conditions confirmed the result of the PAM analysis that *D. parva* showed no pronounced photoinhibitory effects (Fig. 9.1). The maximum biomass density from all three experimental conditions was achieved in the cultivation under HL conditions, namely 4.9 g dw L^{-1} . The maximal biomass densities reached in the stationary phase for the cultivations under LL conditions as well as under HL-ND conditions are almost comparable, namely 1.5 g dw L^{-1} and 1.4 g dw L^{-1} .

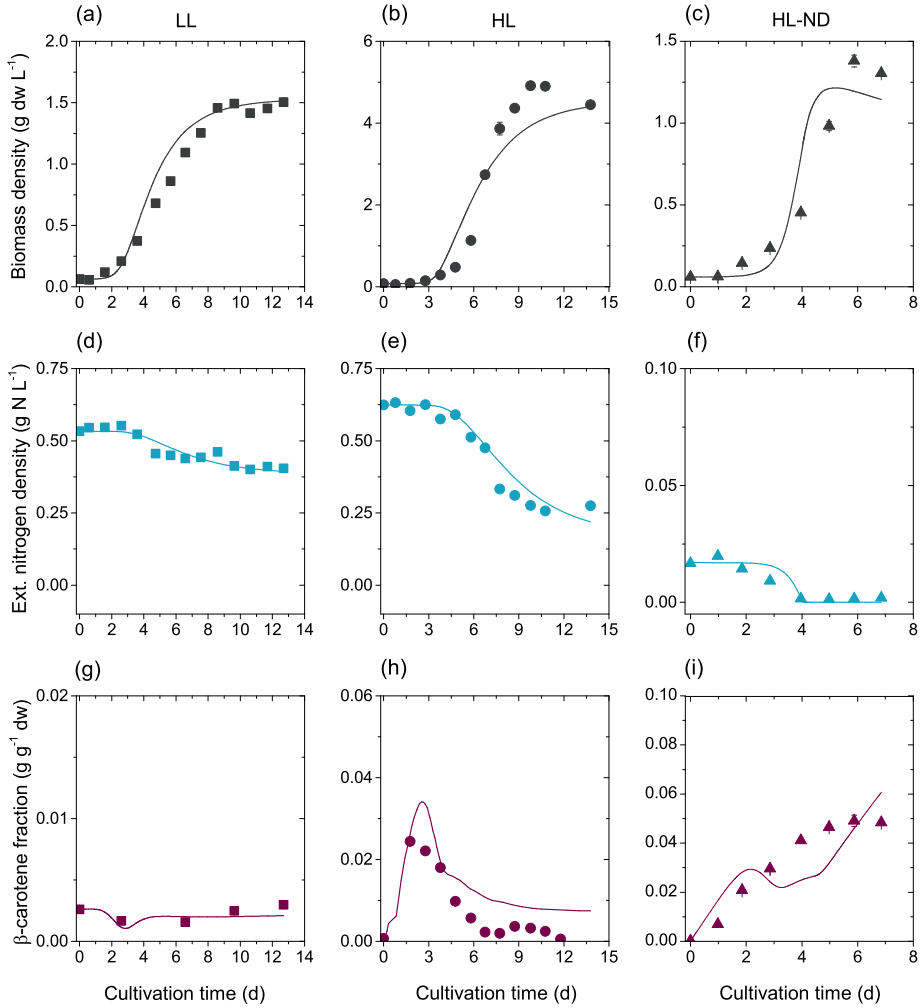


Figure 9.3.: Model simulations for *D. parva* for the effect of various cultivation conditions on the biomass density ρ_X (a-c), the extracellular nitrogen density $\rho_{N,ext}$ (d-f) and the β -carotene fraction ω_{Car} (g-i). Comparison of the simulated time course (lines) with experimental data (symbols).

The simulated time course for the extracellular nitrogen density agreed well with the experimental data (Fig. 9.3). The results revealed that the growth under nitrogen-repleted conditions (LL, HL) was always light limited. As expected, the growth under nutrient-depleted conditions (HL-ND) was governed by the external nutrient availability and the internal nutrient status of the cells. The external nitrogen was totally depleted four days after inoculation in the nitrogen starved culture (HL-ND). The simulation results clearly indicate that nitrogen uptake is strongly reduced in the early exponential and late stationary growth phase under nitrogen-repleted conditions (LL, HL), since the nitrogen cell quota is close to its maximal value $\omega_{N,max}$.

The light and nutrient dependency on the β -carotene synthesis works in the same way for *D. parva* as observed for *D. salina* (Eq. 7.7). The highest β -carotene fraction was achieved during a combination of light- and nutrient stress. However, the maximal mass fraction for *D. parva* is with 4.9% (w/w) significantly lower compared to that of *D. salina* with 8.0% (w/w).

The model simulations agree very well with the experimental data for the chlorophyll fraction ω_{Chl} , which is crucial for predicting the light attenuation in the reactor (Fig. 9.4). During the initial cultivation period more light energy is supplied per cell than is required for growth, resulting in a considerable decline of the total chlorophyll fraction under all three conditions. The extent of the initial decrease in chlorophyll strongly depends on the applied photon flux density. For cells acclimated to low photon flux densities, the chlorophyll reduction was more intense during growth under high irradiance (HL) compared to growth under low irradiance (LL). Under nitrogen-repleted conditions (LL, HL), cells start to synthesize chlorophyll when they enter the exponential growth phase, because the enhanced growth led to a reduced average photon flux density in the reactor. Due to the fact, that growth and chlorophyll synthesis are strongly hindered during nitrogen-depleted conditions, the chlorophyll fraction in the biomass steadily declines from 42 mg g⁻¹ dw to 5 mg g⁻¹ dw.

The optimal parameter estimates and the identifiability of the nine model parameters for *D. parva* are given in Fig. 9.5 and Table 9.4. Whereas in the *D. salina* growth model all parameters were identifiable, in the *D. parva* growth model one parameter was practical non-identifiable, namely the light inhibition coefficient for photosynthetic growth $K_{i,E}$. Since *D. parva* showed no pronounced photoinhibitory effects it is biologically plausible that the corresponding parameter $K_{i,E}$ is not identifiable indicated by the flat profile likelihood in direction of the upper confidence bound. The halfsaturation coefficient for nitrogen uptake $K_{S,N}$ was fixed to a value of 0.155 g m⁻³, which was recalculated from experimental data for *Dunaliella tertiolecta* from Lomas and Glibert (2000) and has already been used for the growth model published by Facht et al. (2014).

In agreement with the PAM measurements (Figs. 6.7 and 9.1) were *D. parva* showed a significantly higher ETR compared to *D. salina*, the better photosynthetic growth potential is also reflected by the parameter estimates for the maximal growth rate (μ_{max}) and the half saturation coefficient for photosynthetic growth ($K_{s,E}$) as shown in Table 9.4. The optimal parameter estimates obtained for *D. parva* are notably higher compared to *D. salina*, namely 6.980 to 1.708 d⁻¹ for μ_{max} and 0.396 to 0.033 mol photons m g⁻¹ dw d⁻¹ for $K_{s,E}$. Due to the small cell weight of *D. parva* (Table 9.1), the higher photosynthetic growth potential does not translate into a more productive cultivation process since the biomass productivity of *D. parva* is considerably lower compared to

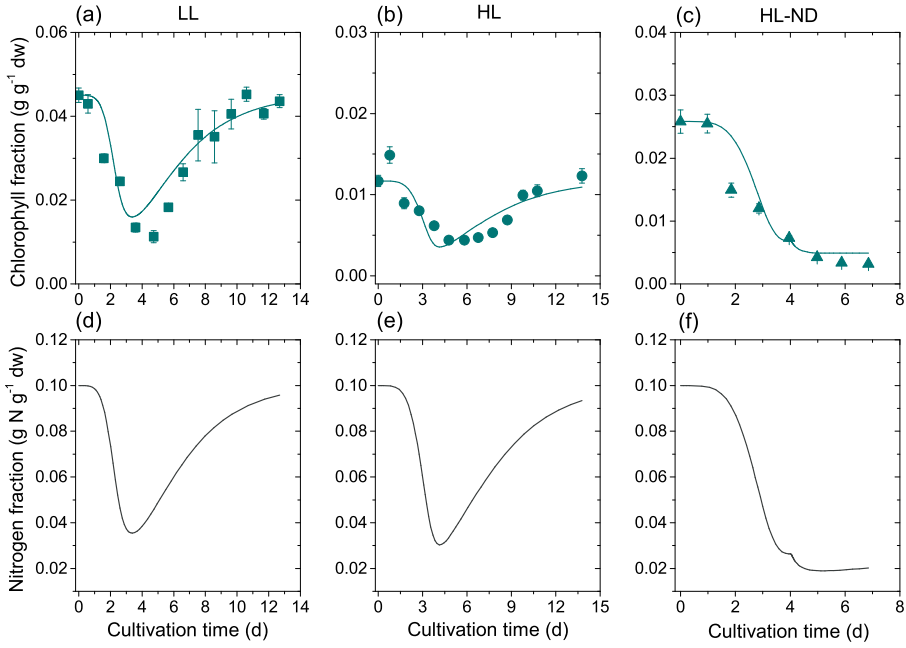


Figure 9.4.: Model simulations for *D. parva* for the effect of various cultivation conditions on the the chlorophyll fraction ω_{Chl} (a-c) and the nitrogen quota in the biomass ω_{N} (d-f). Comparison of the simulated time course (lines) with experimental data (symbols).

Table 9.4.: Summary of the obtained optimal parameter values $\hat{\Theta}$ as well as the individual confidence intervals $[\sigma_i^-; \sigma_i^+]$ corresponding to a confidence level of 95% from constrained non-linear optimization and profile likelihood analysis for *D. parva* in comparison with *D. salina*.

Symbol	$\hat{\Theta}$ for <i>D. salina</i>	$\hat{\Theta}$ for <i>D. parva</i>	σ_i^-	σ_i^+	Identifiability
$r_{\text{N,max}}$	0.346	0.058	0.049	0.069	Structurally and practically identifiable
$K_{\text{s,N}}$	0.05	0.155	0	7.832	Structurally and practically identifiable
μ_{max}	1.708	6.980	6.176	8.533	Structurally and practically identifiable
$K_{\text{s,E}}$	0.033	0.396	0.272	0.682	Structurally and practically identifiable
$K_{\text{i,E}}$	68.7190	499	328.078	$+\infty$	Practically non-identifiable, biologically plausible
$E_{\text{car,crit}}$	77.718	70.202	53.564	101.429	Structurally and practically identifiable
$r_{\text{car,E}}$	0.032	0.016	0.012	0.026	Structurally and practically identifiable
$r_{\text{car,N}}$	0.005	0.036	0.029	0.043	Structurally and practically identifiable
r_{R}	0.142	0.327	0.200	0.531	Structurally and practically identifiable

D. salina (see Table 9.3). However, the strain selection of *D. parva* for an outdoor cultivation process might be beneficial because of its absence of photoinhibition under high irradiance.

In this work, the β -carotene content under HL-ND conditions for *D. salina* was with $80 \text{ mg g}^{-1} \text{ dw}$ 63 % higher than the $49 \text{ mg g}^{-1} \text{ dw}$ measured for *D. parva*. Therefore, also the parameter for the light stress-induced β -carotene synthesis rate $r_{\text{car,E}}$ is 2-fold higher for *D. salina* ($0.032 \text{ g Car g}^{-1} \text{ dw d}^{-1}$ to $0.016 \text{ g Car g}^{-1} \text{ dw d}^{-1}$ for *D. parva*). However, the critical light intensity for β -carotene synthesis ($E_{\text{car,crit}}$) is almost comparable ($70 \text{ mol photons g}^{-1} \text{ dw d}^{-1}$ for *D. parva* and $78 \text{ mol photons g}^{-1} \text{ dw d}^{-1}$ for *D. salina*).

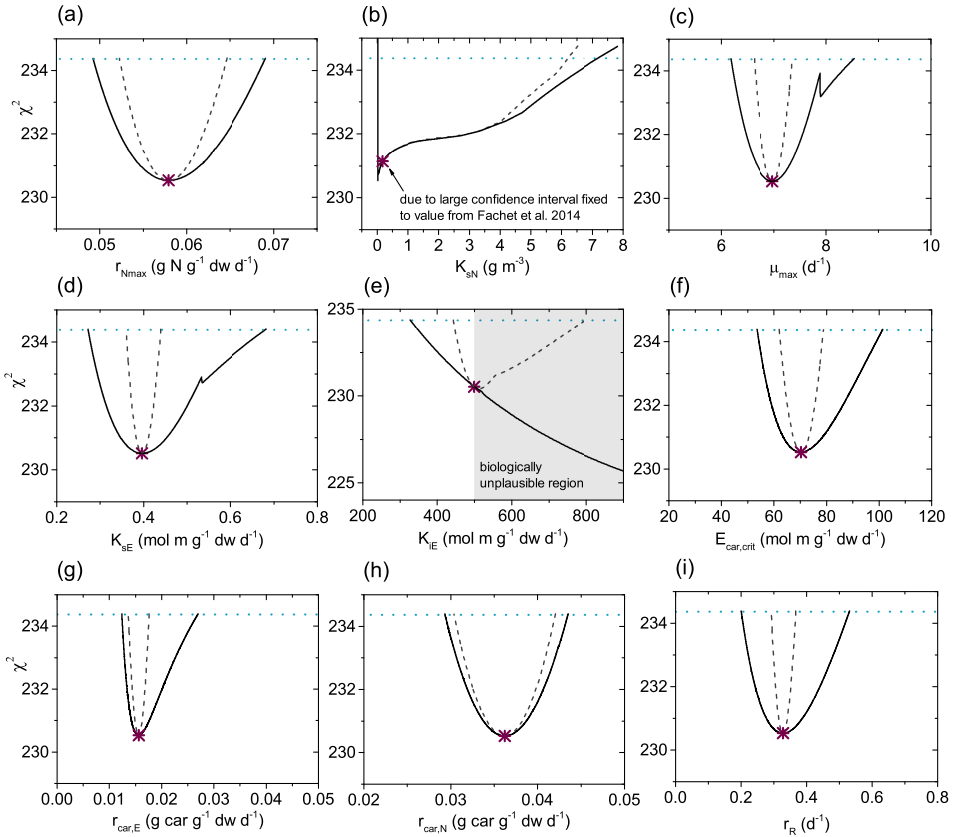


Figure 9.5: Profile likelihood-based identifiability for all model parameters: a) Maximal nitrogen uptake rate r_{max} , b) Halfsaturation coefficient for nitrogen uptake $K_{\text{s,N}}$, c) Maximal growth rate μ_{max} , d) Half saturation coefficient for photosynthetic growth $K_{\text{s,E}}$, e) Light inhibition coefficient for photosynthetic growth $K_{\text{I,E}}$, f) Critical light intensity for β -carotene synthesis $E_{\text{car,crit}}$, g) Light stress-induced β -carotene synthesis rate $r_{\text{car,E}}$, h) Nutrient stress-induced β -carotene synthesis rate $r_{\text{car,N}}$ and (i) Respiration rate r_{R} . The profile likelihood-based sensitivity curve, where Θ_i is varied and all other parameters $\Theta_{j \neq i}$ are kept constant, is indicated by the dashed gray line. The profile likelihood-based identifiability curves are indicated by the black solid line. The blue dotted horizontal line indicates the threshold utilized to assess likelihood-based 95 % confidence interval and the asterisk corresponds to the optimal parameter value.

Chapter 10

Summary, Conclusion and Outlook

10.1 Summary

The topic of this thesis belongs to the wide field of algal biotechnology. The thesis presents a systematic methodological framework for the optimization of phototrophic bioprocesses from the engineering point of view. However, the task of biosystems engineering is associated with many theoretical, biological and experimental challenges due to our limited mechanistic knowledge and its inherent variability and complexity. The foundations of the multidisciplinary approach presented in this thesis have been driven by recent advances in accurate, quantitative experimental approaches in the field of systems biology. An integration of experimental and computational methods provide synergy for a systems-level understanding of photosynthetic organisms and thereby facilitate the development of sustainable and economically-viable algae processes.

In this thesis, a holistic approach for analysis and design of a microalgal bioprocesses with the case study of β -carotene production in *D. salina* in a lab-scale photobioreactor setup is presented. The task is addressed in an integrative manner by applying sophisticated experimental techniques of systems biology to microalgal biosystems to predict how they change over time and under varying input conditions. The experimental data was used to formulate mathematical models on various scales. The major outcomes of this thesis are (i) robust and predictive models for β -carotene production in *D. salina* that enable model-based process analysis and design and (ii) a modular and interdisciplinary framework coupling experiments and modeling that can be transferred to other green algal species. A detailed summary of the results obtained in this thesis is given below.

The systematic experimental approach with special focus on the adaptational stress response of *D. salina* under carotenogenic conditions was developed and presented in Chapter 6 supported by the methodological foundations explained in Chapter 3. The approach was applied to cells cultivated under batch conditions to monitor morphological changes during carotenogenesis in a dynamic manner.

Based on the experimental results obtained in Chapter 6, a dynamic-kinetic reactor model was formulated and presented in Chapter 7. The ordinary differential equation system accounted for biomass growth, nutrient uptake and pigment fraction in the

biomass. The proposed model structure was a tradeoff between the justification of the experimentally observed behavior under various abiotic stress conditions with a minimal number of parameters. The identifiability of the model parameters was investigated using profile likelihood giving implications for model reduction. The proposed model is validated against independently conducted experiments under different cultivation conditions and verifiable predictions are given.

The derived parameters from the dynamic-kinetic growth model in Chapter 7 were included into a dynamic flux balance model presented in Chapter 8 and validated against experimental data obtained from batch cultivations. The dynamic part of the DFBA model considers the same dynamic states as in the dynamic-kinetic model presented in Chapter 7, namely biomass growth, nitrogen uptake, internal nitrogen status as well as chlorophyll and β -carotene fraction in the biomass. Thus, the DFBA formulation allows for predicting intracellular metabolites by incorporating biological knowledge in a structured manner. The DFBA model was further used to predict a model-based fed-batch and two model-based continuous operation strategy with the objective to maximize β -carotene productivity. In this setup, the biomass and β -carotene productivity was significantly increased compared to the empirically operated batch process.

Furthermore, the applicability of the interdisciplinary workflow composed of experiments and mathematical modeling as presented in Chapter 6 and 7 was applied to *D. parva* to investigate the interspecies variability between the two close relatives in the *Dunaliella* genus. The results of the experimental and computational investigations presented in Chapter 9 indicate significant variability between *D. salina* and *D. parva* in terms of morphological differences, the biomass and β -carotene productivity as well as differences in photoacclimation and photoinhibition.

The achievements of this thesis can be summarized as follows:

- Development and employment of an experimental platform to systematically analyze the abiotic stress response in *D. salina* with innovative spectroscopic and fluorometric techniques.
- Flow cytometry and FTIR spectroscopy have only been scarcely used for algal process monitoring and this work can provide a reference for their successful application in future studies.
- First comprehensive dynamic-kinetic growth model for *D. salina* and *D. parva* covering nutrient uptake, light attenuation and pigmentation.
- Parameter identifiability analysis using profile likelihood approach to characterize model state uncertainties.
- Connection of the metabolic network level with the dynamic reactor environment to a dynamic flux balance model.
- First dynamic flux balance model for green microalgae, which is calibrated and validated against experimental data.
- Model-based operation strategies in fed-batch and continuous mode were experimentally validated and confirmed.

- Optimized design outperformed the classical batch process significantly in terms of biomass and β -carotene productivity (+187% and +36% for the fed-batch and +1120% and +849% for the continuous process).

10.2 Conclusion

The main objective of this thesis was to gain a systems-level understanding of carotenogenesis in *D. salina* to identify promising operation strategies for their production. The major conclusions that can be drawn from this work are:

- I. Recent advances in sophisticated experimental techniques for systems-level characterization of biosystems improved bioprocess monitoring. These methods take advantage of:
 - Small amount of sample required for analysis
 - Fast and reliable analysis with high statistical significance
- II. Improved possibilities for process monitoring lead to robustification of bioprocesses due to:
 - Fast identification of critical process parameters such as cell vitality
 - Detection of population heterogeneity
 - Optimal harvesting time point determined based on productivity and culture state
- III. Sophisticated experimental approaches from systems biology and the low sample amount required for them promote shorter sampling intervals resulting in more experimental data of higher quality and finally leading to the development of models with higher predictivity.
- IV. The model-based fed-batch and continuous operation strategies aiming at high carotenoid-productivity clearly outperformed the batch process operated on an empirical basis.

Clearly, this thesis is able to contribute to the final goal of profitable, sustainable and highly productive microalgal processes. The integrative work flow illustrated here strengthens the iterative approach of modeling and experiments to better apprehend for cellular complexity under fluctuating environmental conditions.

Doubtlessly, the ongoing methodological advances in the experimental as well as the computational area will further broaden our knowledge on the metabolic adaptation of microalgae and lead to a progressive improvement of mathematical models. This task includes the investigation of unknown and non-validated gene and protein functions, the extension of sequencing projects for industrially relevant strains, the reconstruction of genome-scale metabolic models and coupling with other -omics data e.g. from transcriptomics or proteomics. Thereby, the engineering of industrially valuable strains is accelerated and provides the basis for effective biotechnology, metabolic engineering and even synthetic biology with green microalgae.

10.3 Outlook

Once an annotated algal genome is available, a genome-scale metabolic model can be reconstructed and its topology can be analyzed (Reijnders et al., 2014). As stated in Chapter 8, the genome of *D. salina* is already sequenced but annotation is not completed so far. Owing to the lack of the *Dunaliella* genome-scale metabolic network, the stoichiometric network was apprehended by the metabolism of the model green algae *C. reinhardtii*. A genome-scale of metabolic model of *D. salina* is expected to increase the predictive power of the DFBA model. Beside of autotrophic growth, the model might be used to simulate and validate the flux distribution, β -carotene and biomass productivity under mixotrophic or heterotrophic growth conditions. Significant contributions in the field of metabolic engineering can only be achieved by studying (i) the influence of gene knock-outs on the production of certain metabolites and (ii) the interlinkages of algal metabolic networks to the networks of associated bacteria to unravel the growth-promoting or growth-inhibiting effect in algal-bacterial consortia.

The production of biofuels, commodities and fine chemical requires the cultivation in large-scale photobioreactors. The majority of this cultivation systems are operated outdoor in open raceway ponds, shallow lakes or closed photobioreactor systems. These systems are subjected to significant spatiotemporal variations in environmental conditions during the day, week, month or even year. The daily light intensity is highly variable and is influenced by the day/night cycle, the solar radiation angle and the percentage of cloud coverage. Furthermore, the biomass productivity strongly depends on the cultivation temperature which themselves is influenced by the ambient temperature, the solar irradiance, the wind speed as well as reactor design. Mixing of large-scale photobioreactors is another critical issue to avoid photoinhibition and growth arrest through CO₂ gas-liquid mass transfer limitations. The complex interplay of environmental fluctuations in outdoor cultivations makes it very challenging to estimate reliable parameters from these systems. This thesis used controlled lab-scale cultivations to estimate kinetic growth parameters of *Dunaliella* to calibrate and validate the models presented in Chapter 7 and 8. As the availability of multifactorial experimental data for outdoor systems is expected to increase rapidly in the next years for a variety of industrially-relevant strains. Thus, the proposed model could be extended to predict growth in large-scale photobioreactors or to facilitate a rational selection of appropriate strains for a certain geographic location.

The omnipresent imperfections discussed above might lead to the presence of population heterogeneity in large-scale cultivation systems. Microbial heterogeneity is not only influenced by the stochastic nature of gene expression, it is also caused by variations in intracellular compounds such as regulatory proteins and transcription factors. Since microbial heterogeneity affects bioprocess performance, it can be a target for future metabolic engineering strategies for microalgae.

The content of high-value products, such as carotenoids or polyunsaturated fatty acids, in the biomass is typically low (below 10%) and a large fraction of residual biomass remains unused. In contrast, the economic feasibility is often difficult to achieve because of energy and cost-intensive harvesting and extraction steps. Therefore, microalgal process design requires tailor-made downstream processing strategies and a biorefinery approach to valorize most of the biomass fractions. The FTIR

spectroscopy and the DFBA approach presented in this thesis are valuable synergistic tools for a model-based description of biomass composition and can contribute to the design an optimal algae-based biorefinery and/or to improve performance of existing bioproduction processes for achieving an economic feasible overall process operation under the consideration of all essential up- and downstream steps.

In summary, it remains to be stated that the tools of this work ought to be used in the future for the optimization and design of microalgal processes. This can involve the adaption of the methods to different algae species, the development of systematic operation strategies for photobioreactors such as tailor-made light profiles or optimized nutrient and media feeding strategies. Concerning the model structure, a further development towards the incorporation of fluctuating input conditions without neglecting the effects of light/dark cycles, imperfect mixing and variable temperature on biomass productivity is a challenging task. However, this is not straightforward due to the inherent complexities of the different processes and time scales involved in photosynthesis and acclimation. But first and foremost, the maximization of the photosynthetic carbon capture efficiency and advanced metabolic engineering strategies is the field in which successful methodologies and techniques will have the largest impact.

Appendix A

Supplementary information for experimental analyses

A.1 Description of experimental information according to MIFlowCyt

A.1.1. Experimental overview

A.1.1.1. Purpose

The purpose of the experiment was to analyze changes in the cellular properties of *Dunaliella salina* during β -carotene accumulation under the presence of abiotic stress using flow cytometry.

A.1.1.2. Keywords

Dunaliella salina, β -carotene, flow cytometry, cellular properties

A.1.1.3. Experiment Variables

The presence of high light intensity and nitrogen deprivation were chosen to be suitable inducers of carotenogenesis and their effect on cell growth, granularity, vitality and neutral lipid fluorescence was studied in a time-dependent manner.

A.1.1.4. Organization

Max Planck Institute for Dynamics of Complex Technical Systems
Sandtorstrasse 1
39106 Magdeburg, Germany

A.1.1.5. Primary contact

Melanie Fachet (fachet@mpi-magdeburg.mpg.de), Dr. Dana Hermsdorf (hermsdorf@mpi-magdeburg.mpg.de)

A.1.2. Quality control measures

To verify the performance and system alignment, Calibration Beads of 3 μm diameter (Catalogue number: 05-4018) were measured before each batch cultivation.

A.1.3. Flow sample

A.1.3.1. Biological sample

The algae *Dunaliella salina* (strain CCAP 19/18) and *Dunaliella parva* used in this study were obtained from the Culture Collection of Algae and Protozoa (Windermere, United Kingdom).

A.1.3.2. Sample characteristics

The alga is known to accumulate high amounts of β -carotene upon exposure to abiotic stress conditions.

A.1.3.3. Sample treatment description

All samples were diluted with cultivation medium to a cell density of approximately 1×10^6 cells mL^{-1} prior to the analysis. The vitality staining was performed by adding 20 μL of the FDA stock solution (2 mg mL^{-1}) to 1 mL of cell suspension leading to a final concentration of 40 μg mL^{-1} . For the neutral lipid determination, the cell suspension was stained with a final concentration of 0.5 μg mL^{-1} Nile Red and incubated for 15 minutes in the dark.

A.1.3.4. Fluorescence reagent description

- Nile Red: N3013, Sigma Aldrich
- Fluorescein diacetate: F1303, Invitrogen

A.1.3.5. Characteristics being measured

- Unstained cells:
 - SSC: Population identification
 - SSC: Cell granularity
 - FL3: Chlorophyll fluorescence, population identification
- Stained cells:

- FL1: Cell vitality
- FL1: Nile Red

A.1.4. Instrument details

A.1.4.1. Instrument manufacturer

Sysmex-Partec GmbH (www.sysmex-partec.com)

A.1.4.2. Instrument model

CyFlow Space

A.1.4.3. Instrument configuration and settings

Flow cell and fluidics

The instrument has not been altered; fixed-alignment cuvette flow cell.

Light sources

The instrument has not been altered:

- 488 nm blue argon solid state laser (20 mW)
- 375 nm ultra-violet diode laser (16 mW)

Excitation optics configuration

The instrument has not been altered.

Optical filters

The instrument has not been altered, all filters are original and came with the instrument (March 07, 2012).

Optical detectors

The instrument has not been altered. Detector voltages have been set to: FSC=140V; SSC=200V; FL1=380V; FL2=416V; FL3=400V; FL4=450V; FL5=660V.

Optical paths

The instrument has not been altered. The following table shows the filter configuration:

Table S1.: Configuration of the emission ranges for the flow cytometric detector channels

Laser	Detector channel	Filter	Fluorochrome detected
Blue (488 nm)	FL1	536/40	Nile Red, Fluorescein, BODIPY 505/515
	FL2	590/40	Nile Red
	FL3	675/20	Nile Red, Chlorophyll autofluorescence
	FL4	>748	-
UV (375 nm)	FL5	455/50	-

A.1.5. Data analysis

A.1.5.1. List-mode data files

FCS data files can be obtained by contacting Melanie Fachet or Dr. Dana Hermsdorf.

A.1.5.2. Data transformation details

Purpose of data transformation

Visualization and gating.

Data transformation description

FlowMax (Sysmex-Partec GmbH, Version 2.7) default visualization settings have been used for gating. The calculation of the geometric mean values for light scattering and fluorescence emission was conducted with FloMax.

A.1.5.3. Gating details

The same gating strategy has been used for all data files.

Gating description

The gating strategy involves the following gates:

- FSC-FL3 gate to define the intact algal cell population (Fig. 1a) in data files of stained and unstained cells
- For Nile Red-stained cells: FL1 gate to determine mean fluorescence intensity (Fig. 3)
- For FDA-treated cells: FL1 gate to define the number of vital algal cells (Fig. 5)

The following figure illustrates the gating strategy of unstained cells:

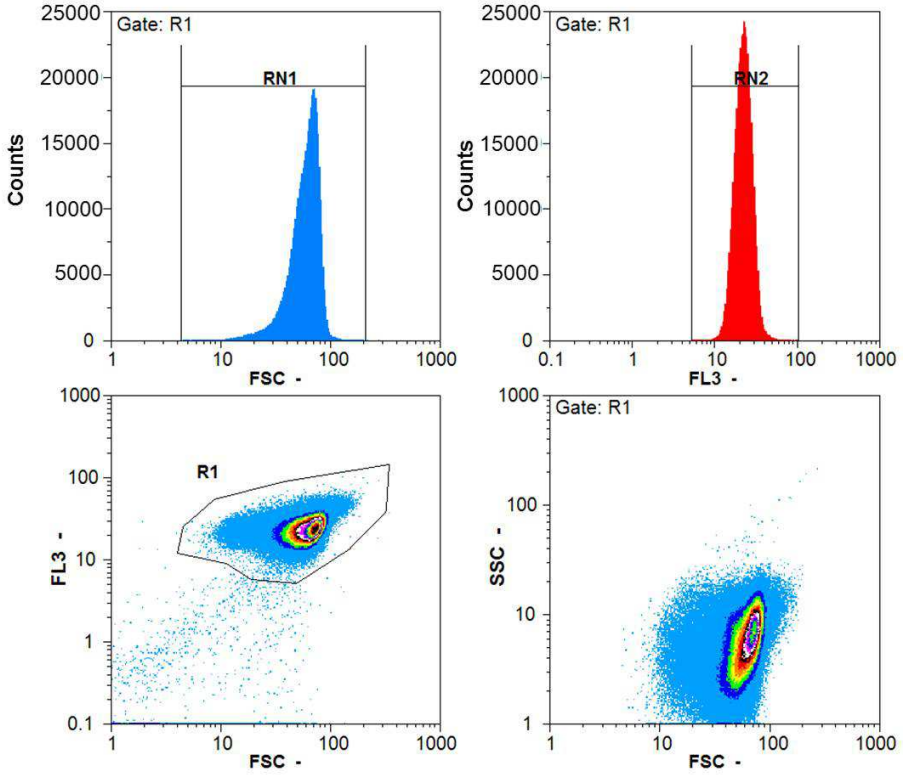


Figure S5.: Gating strategy for unstained cells

A.2 Supplementary information for FTIR analysis

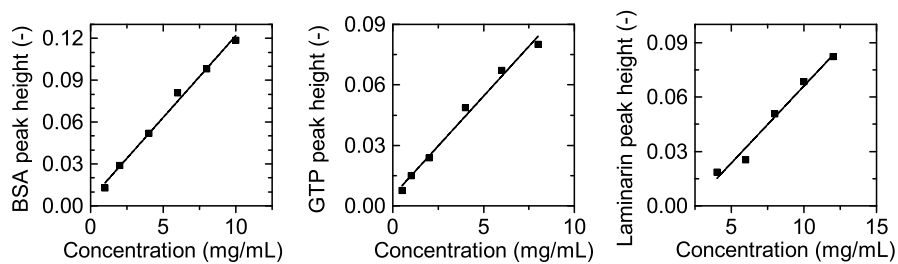


Figure S6.: Calibration curve for FTIR analysis with respective standards. a) BSA, b) Glycerol tripalmitate (GTP) and c) Laminarin.

Appendix B

Supplementary information for profile likelihood analysis

B.1 List of model parameters

Table S1.: Overview of parameters from dynamic-kinetic model.

Symbol	Description	Unit
λ	Duration of the <i>lag</i> phase	d
μ	Specific growth rate	d ⁻¹
μ_{\max}	Maximal growth rate	d ⁻¹
μ_{net}	Net specific growth rate	d ⁻¹
ρ_{Chl}	Chlorophyll density in the reactor	g Chl m ⁻³
$\rho_{\text{N,ext}}$	Extracellular nitrogen density	g N m ⁻³
ρ_X	Biomass density on dry weight basis	g dw m ⁻³
Φ	Description of the <i>lag</i> phase	-
ω_C	Carbon content of biomass	g C g ⁻¹ dw
ω_{Chl}	Chlorophyll fraction of the biomass	g Chl g ⁻¹ dw
$\omega_{\text{Chl,N}}$	Chlorophyll-nitrogen ratio in the biomass	g Chl g ⁻¹ N
ω_N	Cell quota for nitrogen	g N g ⁻¹ dw
$\omega_{\text{N,max}}$	Maximal cell quota for nitrogen	g N g ⁻¹ dw
$\omega_{\text{N,min}}$	Minimal cell quota for nitrogen	g N g ⁻¹ dw
a^*	Optical cross section of chlorophyll <i>a</i>	m ² g ⁻¹ Chl
a	Absorption coefficient of chlorophyll	m ² g ⁻¹ Chl
b	Absorption coefficient of β -carotene	m ² g ⁻¹ Car
c	Backscattering coefficient of the biomass	m ⁻¹
E_0	Photon flux density at the reactor surface	mol photons m ⁻² d ⁻¹
E_{abs}	Absorbed photon flux	mol photons d ⁻¹
$E_{\text{car,crit}}$	Crit. light int. for β -carotene synthesis	mol photons g ⁻¹ dw d ⁻¹
$E_{X,\text{dw}}$	Light intensity per biomass	mol photons m ⁻² d ⁻¹ g ⁻¹ dw
E_{out}	Transmitted photon flux density	mol photons m ⁻² d ⁻¹
\bar{E}	Average photon flux density in the reactor	mol photons m ⁻² d ⁻¹
k	Hill coefficient	-
$K_{s,E}$	Half saturation coeff. for photosynthetic growth	mol photons m g ⁻¹ dw d ⁻¹
$K_{i,E}$	Light inhibition coeff. for photosynthetic growth	mol photons m g ⁻¹ dw d ⁻¹

$K_{s,N}$	Halfsaturation coeff. for nitrogen uptake	g N m^{-3}
$r_{\text{car},E}$	Light stress-induced β -carotene synthesis rate	$\text{g Car g}^{-1} \text{dw d}^{-1}$
$r_{\text{car},N}$	Nutrient stress-induced β -carotene synthesis rate	$\text{g Car g}^{-1} \text{dw d}^{-1}$
r_N	Nitrogen uptake rate	$\text{g N g}^{-1} \text{dw d}^{-1}$
$r_{N,\text{max}}$	Maximal nitrogen uptake rate	$\text{g N g}^{-1} \text{dw d}^{-1}$
r_P	Photosynthesis rate	$\text{g C g}^{-1} \text{Chl d}^{-1}$
$r_{P,\text{max}}$	Maximal theoretical photosynthesis rate	$\text{g C g}^{-1} \text{Chl d}^{-1}$
r_R	Respiration rate	d^{-1}
s_{PBR}	Illuminated reactor surface	m^2
V_{PBR}	Reactor volume	m^3
$Y_{X,E}$	Biomass yield on light energy	$\text{g dw mol}^{-1} \text{photons}$
z	Thickness of the reactor	m

B.2 Model equations for the dynamic-kinetic growth model of *D. parva*

The model equations formulated to describe the state variables for the cellular processes in *D. parva* during growth are subdivided into two categories. Firstly, the dynamic changes in the state variables are represented by ordinary differential equations. Secondly, the kinetic expressions and microalgal biomass characteristics are expressed by algebraic equations. The presented dynamic model equations consider the following four state variables:

- Biomass density ρ_X (g dw m⁻³)
- Extracellular nitrogen density ρ_N (g N m⁻³)
- Intracellular nitrogen fraction ω_N (g N g⁻¹ dw)
- Chlorophyll fraction ω_{Chl} (g Chl g⁻¹ dw)
- β -carotene fraction ω_{Car} (g Car g⁻¹ dw)

Light attenuation in the photobioreactor

The incident light falling on the reactor surface E_0 decreases exponentially along the optical path coordinate L according to the law of Lambert-Beer.

$$E(L) = E_0 \cdot \exp[-(a \cdot \rho_{Chl} + b \cdot \rho_{Car} + c) \cdot L] \quad (B.1)$$

where a , b and c represent the absorption and scattering coefficients of the biomass and ρ_{Chl} as well as ρ_{Car} are the pigment densities in the reactor. The transmitted photon flux density E_{out} is given by:

$$E_{out} = E(L = z) = E_0 \cdot \exp[-(a \cdot \rho_{Chl} + b \cdot \rho_{Car} + c) \cdot z] \quad (B.2)$$

The average photon flux density \bar{E} in the photobioreactor is calculated by integration of $E(L)/L$ between $L = 0$ and the optical path length $L = z$:

$$\bar{E} = \frac{E_0}{(a \cdot \rho_{Chl} + b \cdot \rho_{Car} + c) \cdot z} \cdot (1 - \exp[-(a \cdot \rho_{Chl} + b \cdot \rho_{Car} + c) \cdot z]) \quad (B.3)$$

The absorbed photon flux E_{abs} is calculated from the difference of incident and transmitted photon flux density normalized to the reactor surface s_{PBR} :

$$E_{abs} = (E_0 - E_{out}) \cdot s_{PBR} \quad (B.4)$$

The photon flux density $E_{X,dw}$ per biomass is calculated from the ratio of average photon flux density \bar{E} and the biomass density ρ_X normalized to the reactor volume V_{PBR} :

$$E_{X,dw} = \frac{\bar{E}}{\rho_X \cdot V_{PBR}} \quad (B.5)$$

Nitrogen uptake rate

The uptake rate of inorganic nitrogen r_N from the medium was assumed to follow Michaelis-Menten kinetics. By including the Droop function into the uptake rate, the expression ensures that nitrogen uptake is terminated under nitrogen-repleted conditions (Droop, 1968):

$$r_N = r_{N,\max} \cdot \frac{\rho_{N,\text{ext}}}{\rho_{N,\text{ext}} + K_{S,N}} \cdot \left(1 - \frac{\omega_N}{\omega_{N,\max}}\right) \quad (\text{B.6})$$

where $r_{N,\max}$ and $K_{S,N}$ represent the maximal uptake rate and the half-saturation coefficient for nitrogen as well as $\omega_{N,\max}$ which is the maximal nitrogen quota in the biomass.

β -carotene synthesis rate

The synthesis of β -carotene mainly depends on the presence and intensity of light and nutrient stress. Therefore, the equation for its synthesis couples a light-dependent and nutrient-dependent synthesis term as formulated below:

$$r_{\text{Car}} = r_{\text{Car},E} \cdot \frac{\bar{E}^k}{E_{\text{car,crit}}^k + \bar{E}^k} + r_{\text{Car},N} \cdot \left(1 - \frac{\omega_N^k}{\omega_{N,\text{crit}}^k + \omega_N^k}\right) \quad (\text{B.7})$$

where $r_{\text{Car},E}$ and $r_{\text{Car},N}$ represent the maximal synthesis rate under light and nutrient stress. The half saturation coefficients for light and nutrient stress are denoted as $E_{\text{car,crit}}$ and $\omega_{N,\text{crit}}$. The Hill coefficient is represented by k .

Photosynthesis rate

The carbon-specific, light-limited photosynthesis rate can be expressed as follows:

$$r_P = r_{P,\max} \cdot \left(1 - \frac{\omega_{N,\min}}{\omega_N}\right) \cdot \left(1 - \exp\left[\frac{-a \cdot Y_{X,E} \cdot \bar{E}}{r_{P,\max}}\right]\right) \quad (\text{B.8})$$

where $r_{P,\max}$ is the maximal photosynthesis rate, $\omega_{N,\min}$ is the minimal nitrogen quota of the biomass and $Y_{X,E}$ is the biomass yield on light energy. This relationship developed by Geider et al. (1998) includes the dependencies on the average photon flux density, the light absorption properties, the photon efficiency and the nutrient status of the biomass.

Growth rate

The equation for the light- and nutrient-dependent effects on the specific growth rate is expressed in the following equation:

$$\mu = \mu_{\max} \cdot \frac{E_{X,dw}}{E_{X,dw} + K_{s,E} \cdot \frac{\rho_X}{\rho_{Chl}} + \frac{E_{X,dw}^2}{K_{i,E}}} \cdot \left(1 - \frac{\omega_{N,\min}}{\omega_N}\right) \quad (B.9)$$

Since the cells need to adapt to the conditions in the photobioreactor, at time $t = 0$ an initial *lag* phase was observed in the experimental data. Therefore, we adjusted the specific growth rate using a Hill function:

$$\Phi = \frac{t^k}{\lambda^k + t^k} \quad (B.10)$$

to estimate the *lag* phase Φ where k is the exponential factor describing the transition from *lag* to exponential phase and λ is the duration of the *lag* phase. Taking the respiration rate into account, the following equation for the net specific growth rate μ_{net} was derived:

$$\mu_{\text{net}} = \Phi \cdot (\mu - r_R) \quad (B.11)$$

The biomass yield on light energy $Y_{X,E}$ is calculated according the following expression:

$$Y_{X,E} = \frac{\mu \cdot \rho_X \cdot V_{\text{PBR}}}{E_{\text{abs}}} \quad (B.12)$$

where V_{PBR} is the reactor volume.

After the formulation of the kinetic expressions, the following five dynamic equations are deduced in order to describe biomass growth, chlorophyll and β -carotene fraction, extracellular nitrogen density and nitrogen quota:

$$\frac{d\rho_X}{dt} = \mu_{\text{net}} \cdot \rho_X \quad (B.13)$$

$$\frac{d\rho_{N,\text{ext}}}{dt} = -r_N \cdot \rho_X \quad (B.14)$$

$$\frac{d\omega_N}{dt} = r_N - \Phi \cdot \mu \cdot \omega_N \quad (B.15)$$

$$\frac{d\omega_{\text{Chl}}}{dt} = \frac{\omega_{\text{Chl},N} \cdot \mu \cdot r_N}{r_P \cdot \left(\frac{\omega_{\text{Chl}}}{\omega_C}\right)} - \mu_{\text{net}} \cdot \omega_{\text{Chl}} \quad (B.16)$$

$$\frac{d\omega_{\text{Car}}}{dt} = r_{\text{Car}} - \mu_{\text{net}} \cdot \omega_{\text{Car}} \quad (B.17)$$

Table S2.: Summary of biomass-specific parameters for *D. parva* derived from experiments and literature data.

Description	Symbol	Value	Unit	Source
Optical cross section of Chl <i>a</i>	a^*	11.84	$\text{m}^2 \text{g}^{-1} \text{Chl } a$	Average of experimental data
Absorption coeff. of Chl <i>a</i> and <i>b</i>	a	5.134	$\text{m}^2 \text{g}^{-1} \text{Chl}$	Fitting of absorption model to exp. data
Absorption coeff. of β -carotene	b	2.202	$\text{m}^2 \text{g}^{-1} \text{Car}$	Fitting of absorption model to exp. data
Backscattering coeff. of the biomass	c	16.591	m^{-1}	Fitting of absorption model to exp. data
Hill coefficient	k	4	-	Literature (Baty and Delignette-Muller, 2004)
Duration of the lag phase	λ	2	d	Estimation from exp. data
Maximal theoretical photosynthesis rate	$r_{P,\text{max}}$	2000	$\text{g C g}^{-1} \text{Chl d}^{-1}$	Estimation from exp. data
Carbon fraction	ω_{C}	0.49	$\text{g N g}^{-1} \text{dw}$	Direct measurement
Maximal cell quota for nitrogen	$\omega_{\text{N,max}}$	0.10	$\text{g N g}^{-1} \text{dw}$	Direct measurement
Minimal cell quota for nitrogen	$\omega_{\text{N,min}}$	0.015	$\text{g N g}^{-1} \text{dw}$	Direct measurement
Crit. cell quota for β -carotene synthesis	$\omega_{\text{N,crit}}$	0.02	$\text{g N g}^{-1} \text{dw}$	Estimation from exp. data
Reactor thickness	z	0.05	m	Reactor constant
Reactor volume	V_{PBR}	0.001	m^{-3}	Reactor constant
Reactor surface	s_{PBR}	0.024	m^{-2}	Reactor constant

B.3 Interdependencies between model parameters

Growth model for *D. salina*

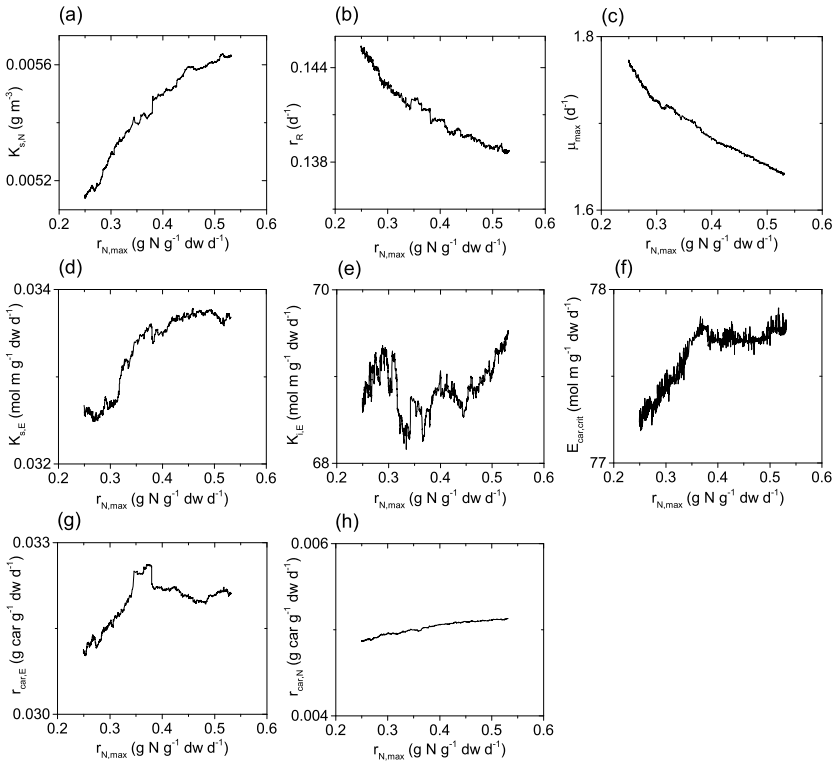


Figure S1.: Profile likelihood of $r_{N,max}$ and its dependencies on the remaining parameters in terms of relative change of each kinetic parameter for *D. salina*.

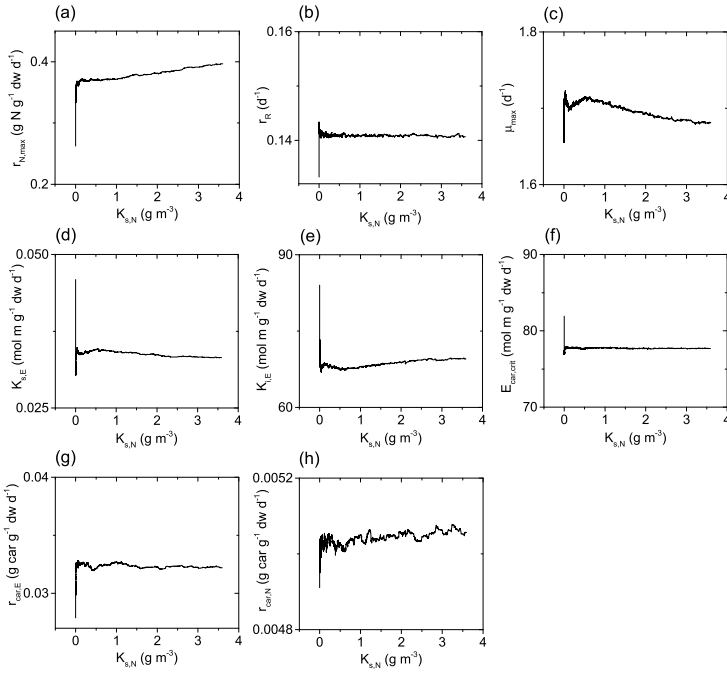


Figure S2.: Profile likelihood of $K_{s,N}$ and its dependencies on the remaining parameters in terms of relative change of each kinetic parameter for *D. salina*.

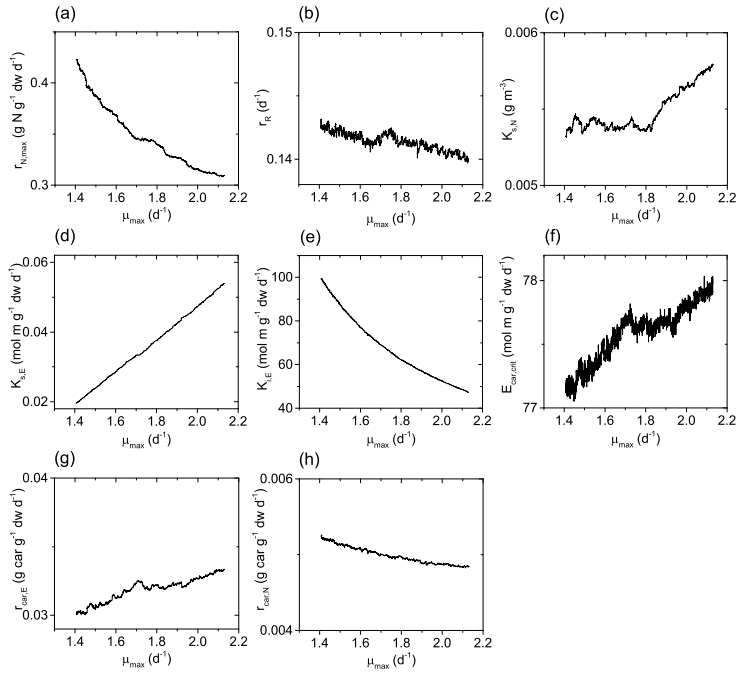


Figure S3.: Profile likelihood of μ_{max} and its dependencies on the remaining parameters in terms of relative change of each kinetic parameter for *D. salina*.

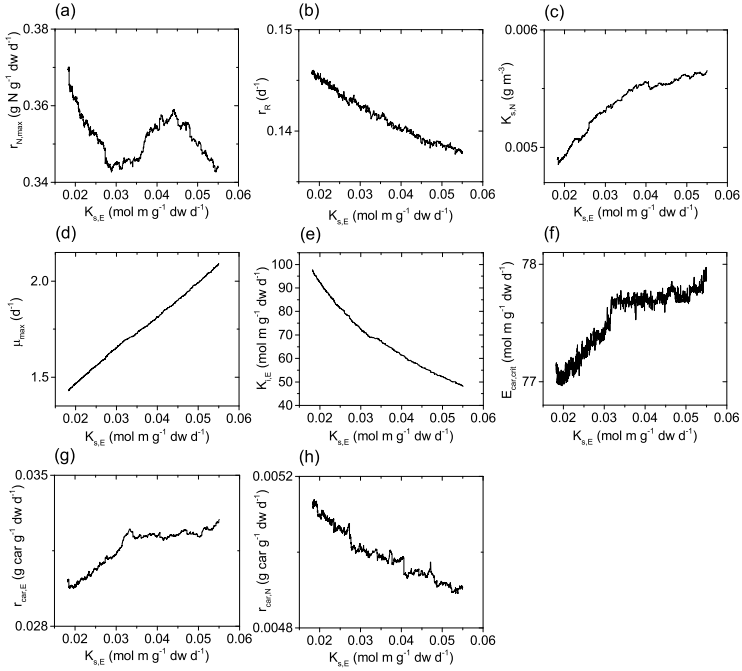


Figure S4. Profile likelihood of $K_{s,E}$ and its dependencies on the remaining parameters in terms of relative change of each kinetic parameter for *D. salina*.

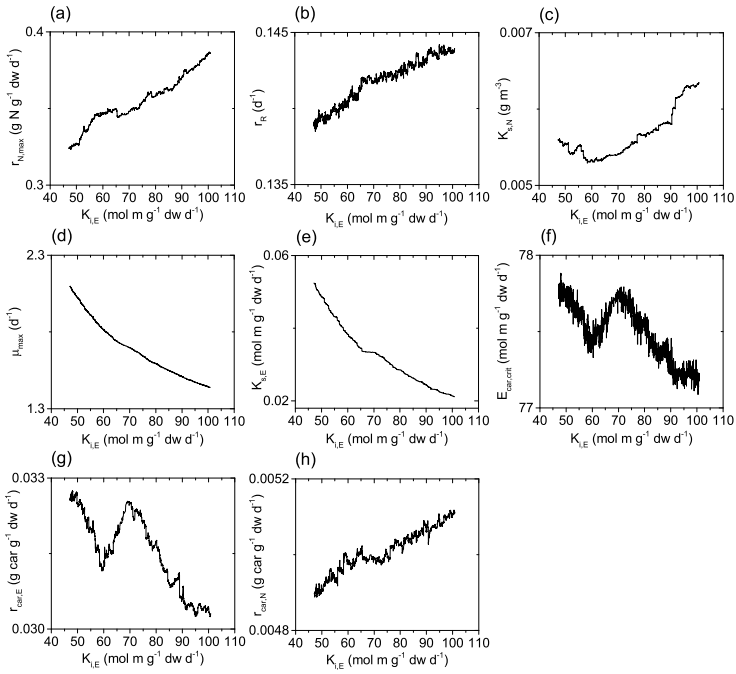


Figure S5. Profile likelihood of $K_{i,E}$ and its dependencies on the remaining parameters in terms of relative change of each kinetic parameter for *D. salina*.

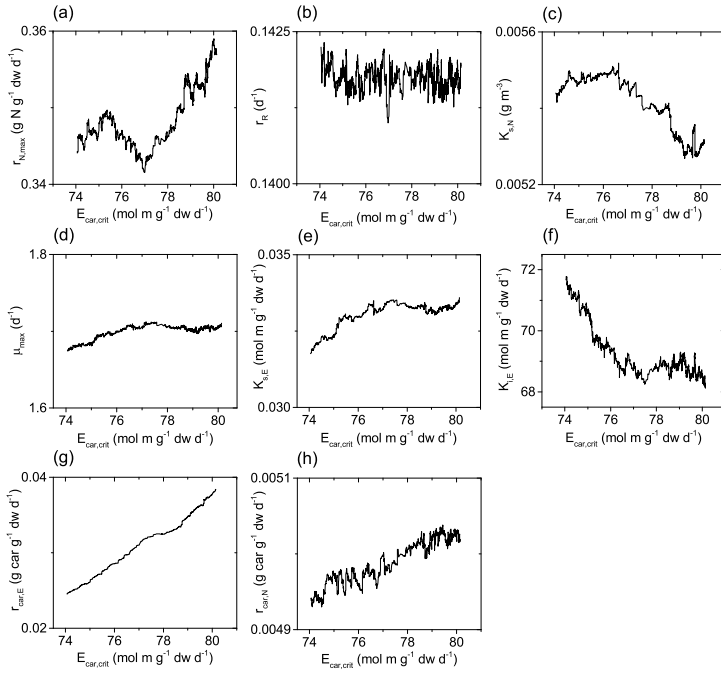


Figure S6.: Profile likelihood of $E_{\text{car,crit}}$ and its dependencies on the remaining parameters in terms of relative change of each kinetic parameter for *D. salina*.

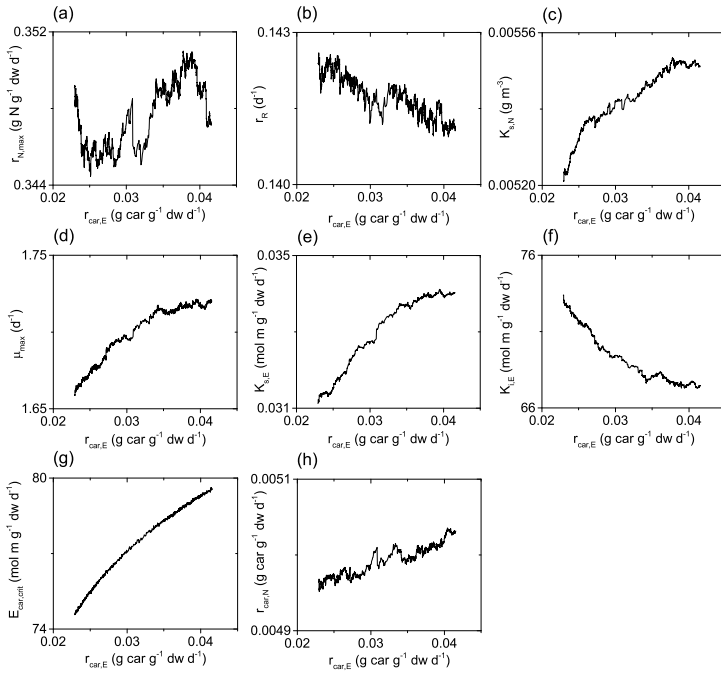


Figure S7.: Profile likelihood of $r_{\text{car,E}}$ and its dependencies on the remaining parameters in terms of relative change of each kinetic parameter for *D. salina*.

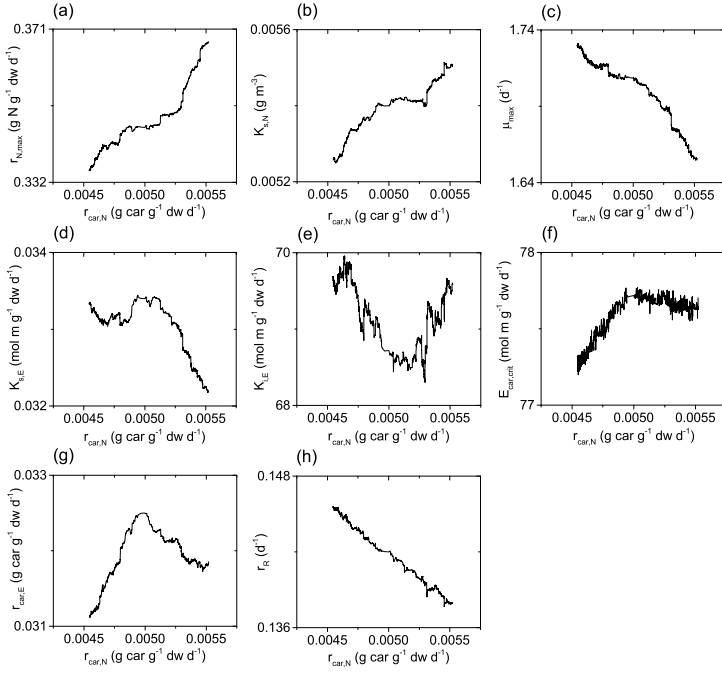


Figure S8. Profile likelihood of $r_{\text{car},N}$ and its dependencies on the remaining parameters in terms of relative change of each kinetic parameter for *D. salina*.

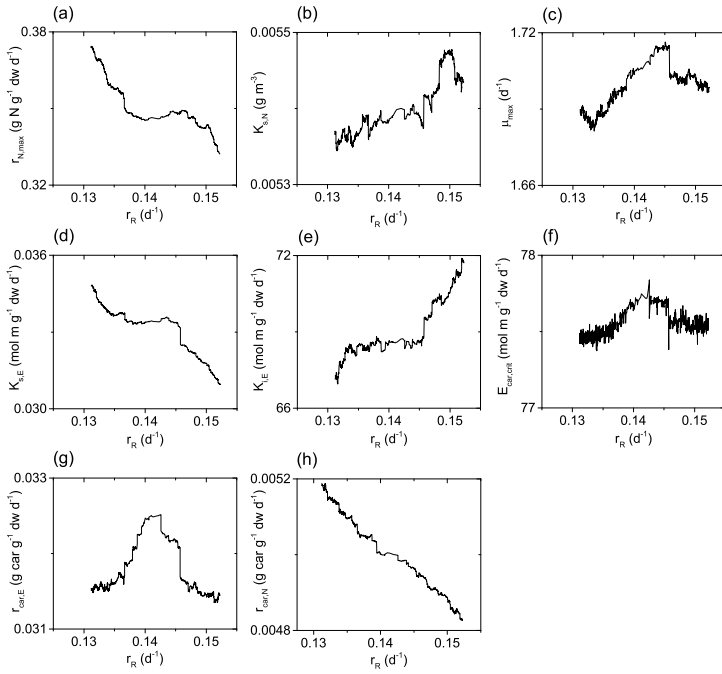


Figure S9. Profile likelihood of r_R and its dependencies on the remaining parameters in terms of relative change of each kinetic parameter for *D. salina*.

Growth model for *D. parva*

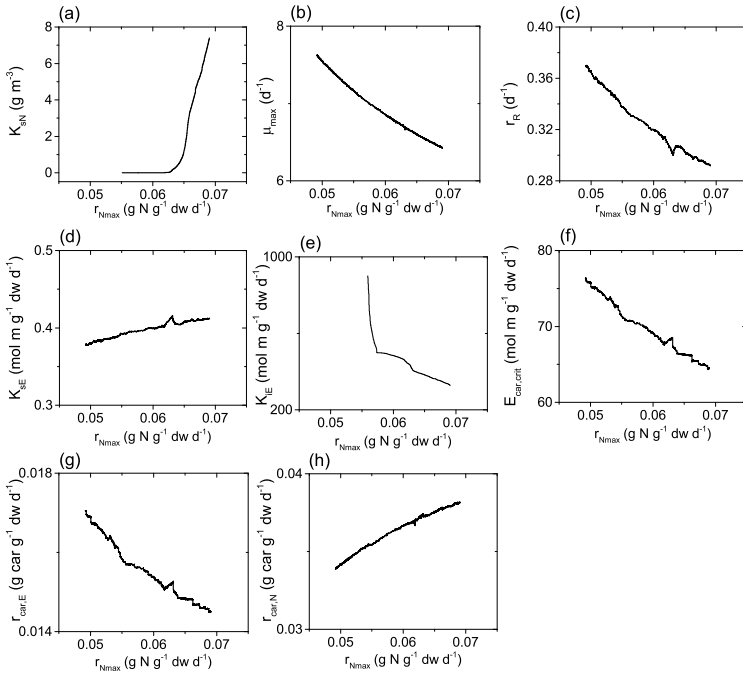


Figure S10: Profile likelihood of $r_{N,max}$ and its dependencies on the remaining parameters in terms of relative change of each kinetic parameter for *D. parva*.

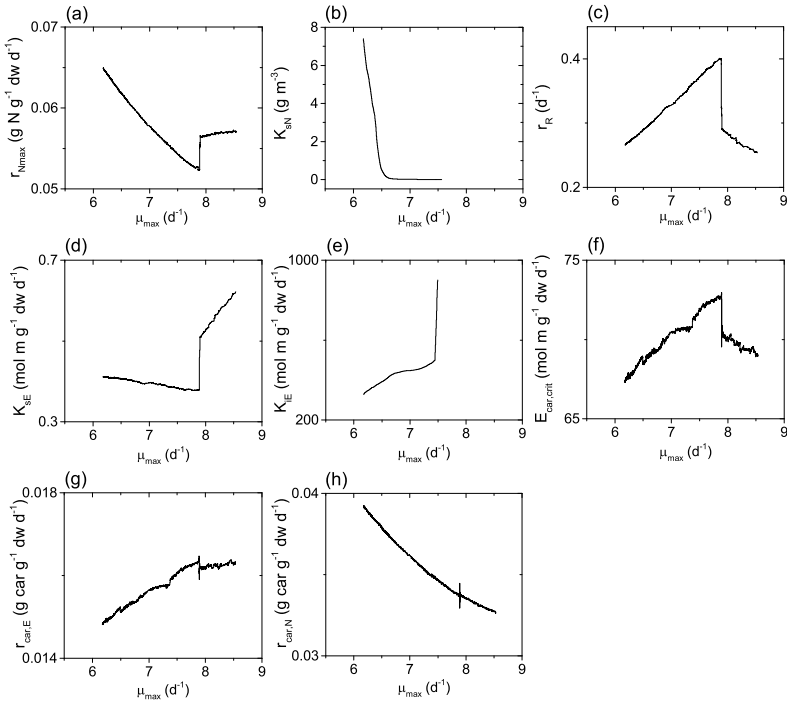


Figure S11.: Profile likelihood of μ_{\max} and its dependencies on the remaining parameters in terms of relative change of each kinetic parameter for *D. parva*.

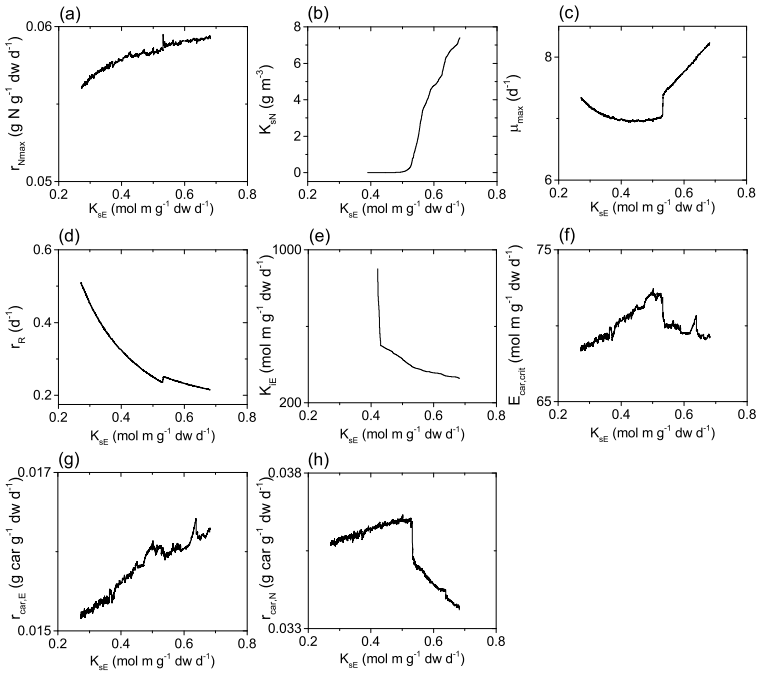


Figure S12.: Profile likelihood of $K_{S,E}$ and its dependencies on the remaining kinetic parameters in terms of relative change of each kinetic parameter for the dynamic-kinetic model of *D. parva*.

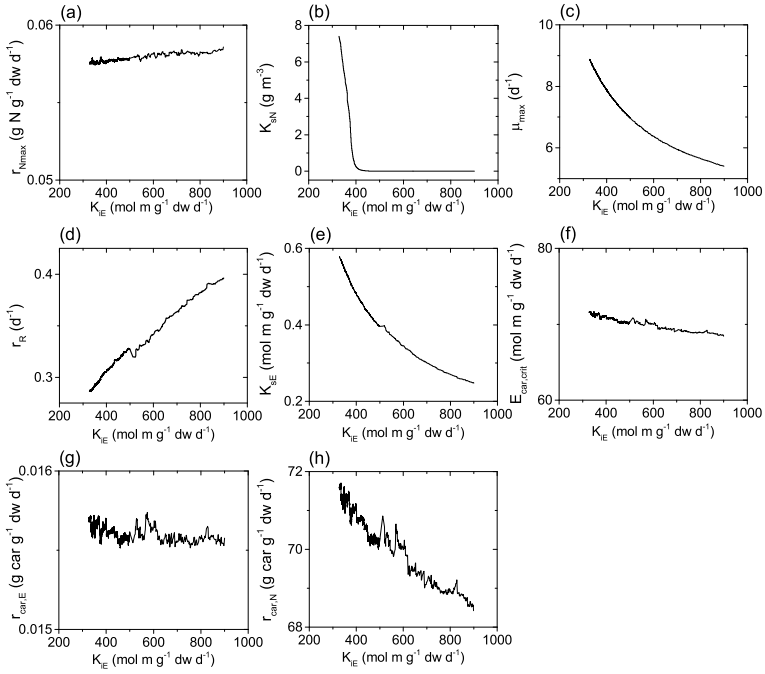


Figure S13.: Profile likelihood of $K_{i,E}$ and its dependencies on the remaining parameters in terms of relative change of each kinetic parameter for *D. parva*.

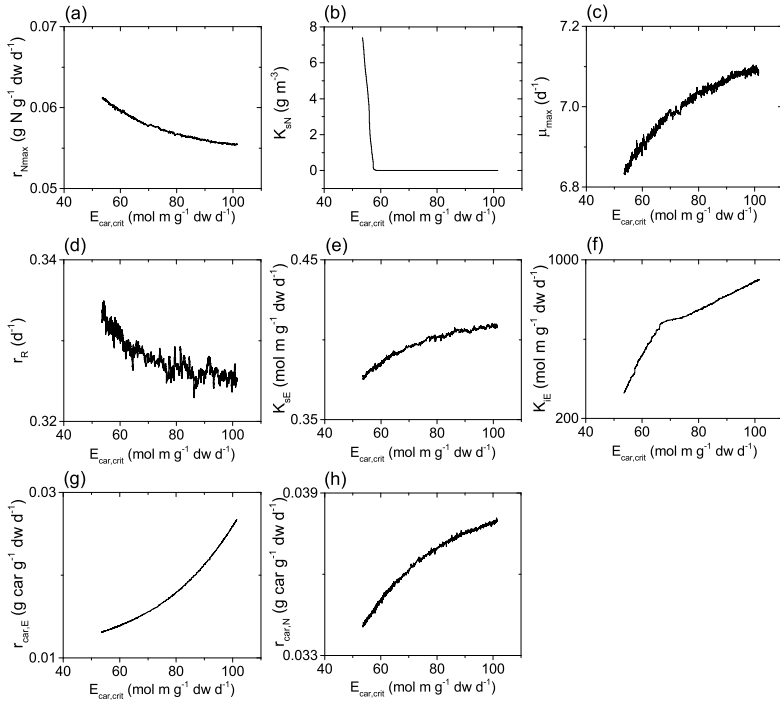


Figure S14.: Profile likelihood of $E_{car,crit}$ and its dependencies on the remaining parameters in terms of relative change of each kinetic parameter for *D. parva*.

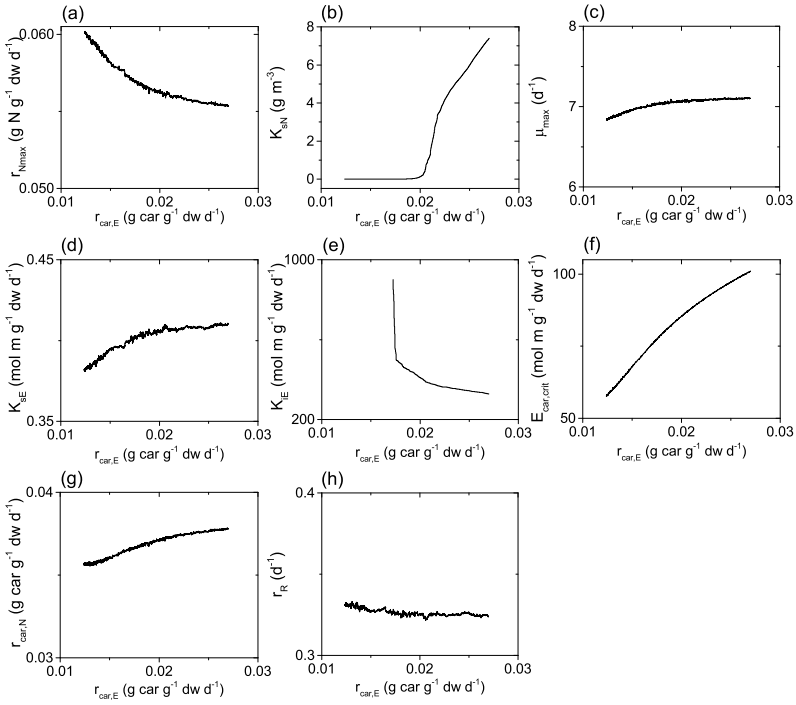


Figure S15.: Profile likelihood of $r_{\text{car,E}}$ and its dependencies on the remaining parameters in terms of relative change of each kinetic parameter for *D. parva*.

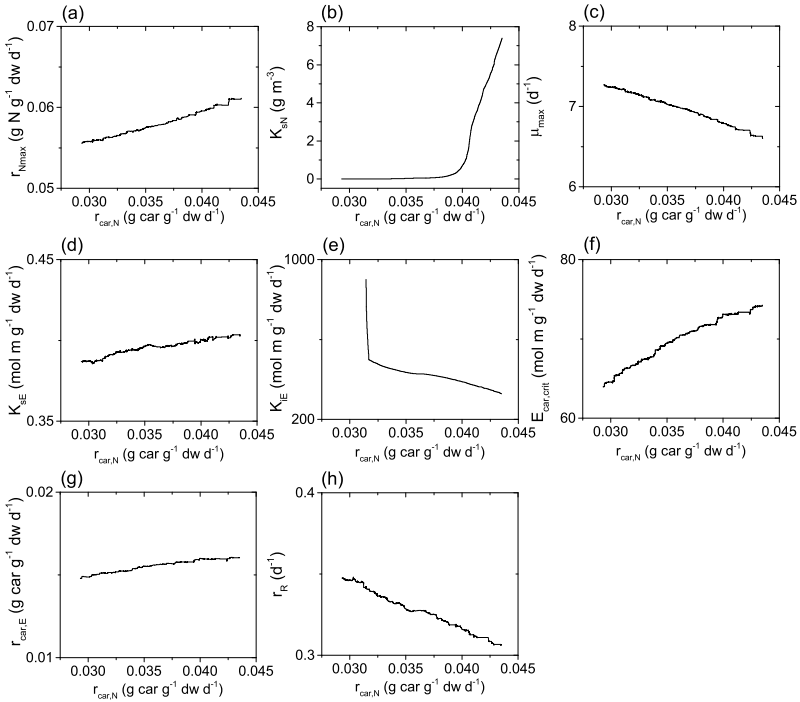


Figure S16.: Profile likelihood of $r_{\text{car,N}}$ and its dependencies on the remaining parameters in terms of relative change of each kinetic parameter for *D. parva*.

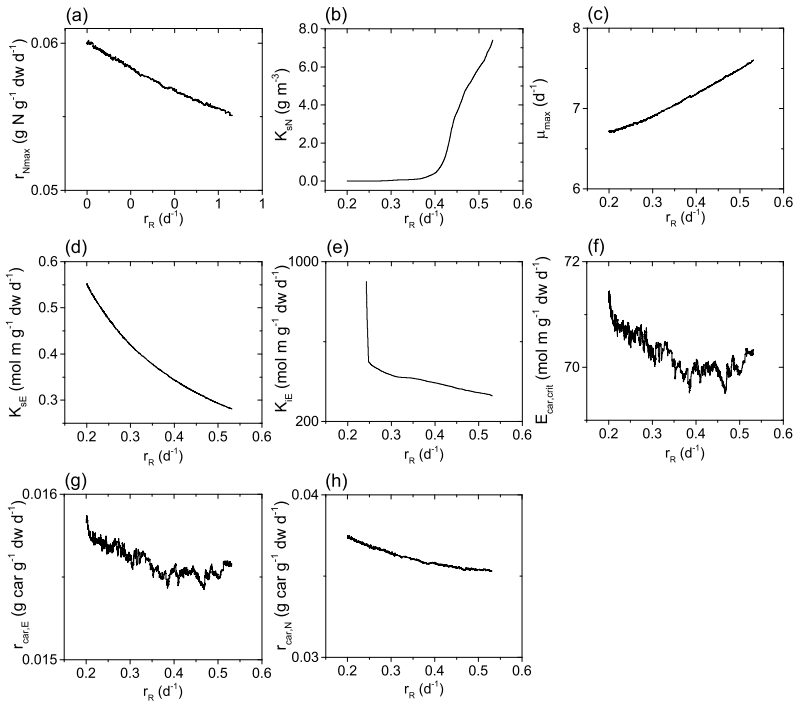


Figure S17.: Profile likelihood of r_R and its dependencies on the remaining parameters in terms of relative change of each kinetic parameter for *D. parva*.

Appendix C

Supplementary information for metabolic network reconstruction

C.1 List of pathways and reaction

Table S1.: List of reactions in the carbon core metabolism. The arrows indicate the direction and reversibility of the reactions. Metabolites in the chloroplast are notated with a **c** and metabolites in the mitochondrion are notated with a **m** before the abbreviation.

No.	ID	Reaction	E.C.	KEGG ID
R001	Light1	8 Light + 3 ADP + 3 Pi + H[+] + 2 cNADP → O2 + H2O + 2 cNADPH + 3 ATP	-	-
R002	Cal1	CO2 + H2O + cRu15DP → 2 c3PG + 2H[+]	4.1.1.39	R00024
R003	Cal2	ATP + c3PG → ADP + H[+] + c13DPG	2.7.2.3	R01512
R004	Cal3	H[+] + NADPH + c13DPG ↔ NADP + H2O + cGAP	1.2.1.9	R01058
R005	Cal4	cGAP ↔ cDHAP	5.3.1.1.	R01015
R006	Cal5	cDHAP + cGAP ↔ cF16P	4.1.2.13	R01068
R007	Cal6	H2O + cF16P ↔ Pi + cF6P	3.1.3.11	R00762
R008	Cal7	cF6P + cGAP ↔ cE4P + cX5P	2.2.1.1	R01067
R009	Cal8	H2O + cE4P + cGAP ↔ Pi + cS7P	3.1.3.37	R01845
R010	Cal9	cGAP + cS7P ↔ cR5P + cX5P	4.1.2.13	R01829
R011	Cal10	cX5P ↔ cRu5P	2.2.1.1	R01641
R012	Cal11	cR5P ↔ cRu5P	5.1.3.1	R01529
R013	Cal12	ATP + cRu5P → ADP + cRu15DP	5.3.1.6	R01056
R014	Gluc1	cG6P + H2O + NADP ↔ c6PG + NADPH + H[+]	2.7.1.19	R01523
R015	Gluc2	c6PG + NADP ↔ CO2 + NADPH + cRU5P + H[+]	1.1.1.49	R00835
R016	Gluc3	cF6P ↔ cG6P	3.1.1.31	R02035
R017	Gluc4	cG6P ↔ cG1P	1.1.1.44	R01528
R018	Gluc5	ATP + cG1P → cADP-G + PPi	5.3.1.9	R00771
R019	Gluc6	cADP-G → ADP + Starch	5.4.2.2	R08639
R020	Gluc7	Starch+ Pi → cG1P	2.7.7.27	R00948
R021	CAM1	AMP + cPEP + PPi ↔ ATP + cPYR + Pi	2.4.1.21	R06049
R022	CAM2	cMAL + NAD ↔ cPYR + CO2 + NADH	2.4.1.1	R06185
R023	CAM3	cMAL + NADP ↔ cPYR + CO2 + NADPH	2.7.9.1	R00206
R024	CAM4	cMAL + NAD ↔ cOXA + NADH + H[+]	1.1.1.39	R00214
			1.1.1.40	R00216
			1.1.1.37	R00342

R025	CAM5	$cMAL + NADP \leftrightarrow cOXA + NADPH + H[+]$	1.1.1.82	R00343
R026	CAM6	$ATP + cOXA \leftrightarrow ADP + CO_2 + cPEP$	4.1.1.49	R00341
R027	CAM7	$CO_2 + H_2O + cPEP \rightarrow H[+] + cOXA + Pi$	4.1.1.31	R00345
R028	CAM8	$cASP + cAKG \leftrightarrow cOXA + cGLU$	2.6.1.1	R00355
R029	CAM9	$MAL + NAD \leftrightarrow PYR + CO_2 + NADH$	1.1.1.39	R00214
R030	CAM10	$MAL + NADP \leftrightarrow PYR + CO_2 + NADPH$	1.1.1.40	R00216
R031	CAM11	$ATP + OXA \leftrightarrow ADP + CO_2 + PEP$	4.1.1.49	R00341
R032	CAM12	$CO_2 + H_2O + PEP \rightarrow H[+] + OXA + Pi$	4.1.1.31	R00345
R033	CAM13	$ATP + CO_2 + H_2O + PYR \rightarrow ADP + OXA + Pi + 2 H[+]$	6.4.1.1	R00344
R034	Pres1	$cRu15DP + O_2 \rightarrow c3PG + cGLYCOL2P$	4.1.1.39	R03140
R035	Pres2	$cGLYCOL2P + H_2O \rightarrow cGLYCOL + Pi$	3.1.3.18	R01334
R036	Pres3	$GLYCOL + NAD \rightarrow GLYOX + NADH + H[+]$	1.1.1.26	R00717
R037	Pres4	$SER + GLYOX \rightarrow GLY + HydPyr$	2.6.1.45	R00588
			2.6.1.51	
R038	Pres5	$H[+] + HydPyr + NADH \rightarrow GLYCA + NAD$	1.1.1.29	R01388
R039	Pres6	$ATP + GLYCA \rightarrow ADP + 3PG$	2.7.1.31	R01514
R040	Pres7	$GA + NAD + H_2O \rightarrow$ $GLYCA + NADH + H[+]$	1.2.1.3	R01752
R041	Pres8	$GLYC + NAD \rightarrow GA + NADH + H[+]$	1.1.1.21	R01036
R042	Pres9	$GLYC + NADP \rightarrow GA + NADPH + H[+]$	1.1.1.2	R01041
R043	Pres10	$GLY + H_2O + METHF \leftrightarrow SER + THF$	-	-
R044	Pres11	$GLY + NAD + THF \leftrightarrow CO_2 + METHF + NADH + NH_4[+]$	-	-
R045	Pres12	$GLY + H[+] + PYR \leftrightarrow ALA + GLYOX$	-	-
R046	Gly1	$G6P \leftrightarrow G1P$	5.4.2.2	R08639
R047	Gly2	$F6P \leftrightarrow G6P$	5.3.1.9	R00771
R048	Gly3	$ATP + F6P \rightarrow ADP + F16P$	2.7.1.11	R00756
R049	Gly4	$F16P + H_2O \rightarrow F6P + Pi$	3.1.3.11	R00762
R050	Gly5	$DHAP + GAP \leftrightarrow F16P$	4.1.2.13	R01068
R051	Gly6	$DHAP \leftrightarrow GAP$	5.3.1.1	R01015
R052	Gly7	$GAP + NADP + Pi \rightarrow 13DPG + H[+] + NADPH$	1.2.1.13	R01063
R053	Gly8	$13DPG + ADP \leftrightarrow 3PG + ATP$	2.7.2.3	R01512
R054	Gly9	$3PG \leftrightarrow 2PG$	5.4.2.12	R01518
R055	Gly10	$2PG \leftrightarrow H_2O + PEP$	4.2.1.11	R00658
R056	Gly11	$ADP + PEP \rightarrow ATP + PYR$	2.7.1.40	R00200
R057	Gly12	$ATP + GLUC \leftrightarrow ADP + G6P$	2.7.1.1	R00299
R058	Gly13	$G1P \leftrightarrow CARB + Pi$	-	-
R059	PP1	$G6P + H_2O + NADP \leftrightarrow 6PG + NADPH + 2 H[+]$	1.1.1.49	R00835
			3.1.1.31	R02035
R060	PP2	$6PG + NADP \leftrightarrow CO_2 + NADPH + RU5P + H[+]$	1.1.1.44	R01528
R061	PP3	$RU5P \leftrightarrow R5P$	5.3.1.6	R01056
R062	PP4	$RU5P \leftrightarrow X5P$	5.1.3.1	R01529
R063	PP5	$R5P + X5P \leftrightarrow GAP + S7P$	2.2.1.1	R01641
R064	PP6	$GAP + S7P \leftrightarrow E4P + F6P$	2.2.1.2	R08575
R065	PP7	$F6P + GAP \leftrightarrow E4P + X5P$	2.2.1.1	R01067
R066	TCA1	$CoA + NAD + mPYR \rightarrow mAcCoA + CO_2 + NADH$	-	-
R067	TCA2	$mAcCoA + H_2O + mOXA \leftrightarrow mCIT + CoA + H[+]$	-	-
R068	TCA3	$mCIT + NAD \leftrightarrow mAKG + CO_2 + NADH$	-	-
R069	TCA4	$mAKG + CoA + NAD \rightarrow CO_2 + NADH + mSUCCoA$	-	-
R070	TCA5	$ADP + Pi + mSUCCoA \leftrightarrow ATP + CoA + mSUC$	-	-
R071	TCA6	$FAD + mSUC \leftrightarrow FADH_2 + mFUM$	-	-
R072	TCA7	$mFUM + H_2O \leftrightarrow mMAL$	-	-
R073	TCA8	$FAD + mMAL \leftrightarrow FADH_2 + mOXA$	1.1.5.4	R01257
R074	Glyc1	$DHAP + ADP \leftrightarrow DHA + ATP$	2.7.1.29	R01011
R075	Glyc2	$DHA + H[+] + NADPH \leftrightarrow GLYC + NADP$	1.1.1.156	R01039
R076	Glyc3	$ADP + cGLYC3P \rightarrow ATP + cGLYC$	2.7.1.30	R00847
R077	Glyc4	$GLYC3P + FAD \leftrightarrow DHAP + FADH_2$	1.1.5.3	R00848
R078	Glyc5	$cGLYC3P + NAD \leftrightarrow cDHAP + H[+] + NADH$	1.1.1.8	R00842
R079	Glyc6	$ADP + GLYC3P \rightarrow ATP + GLYC$	2.7.1.30	R00847

R080	NS1	$H[+] + NADH + NO_3 \leftrightarrow H_2O + NAD + NO_2$	-	-
R081	NS2	$5 H[+] + 3 NADPH + NO_2 \leftrightarrow NH_4[+] + 2 H_2O + 3 NADP$	-	-
R082	NS3	$ATP + SO_4 \rightarrow APS + P_i$	-	-
R083	NS4	$APS + NADH \rightarrow AMP + NAD + SO_3$	-	-
R084	NS5	$5 H[+] + 3 NADPH + SO_3 \leftrightarrow H_2S + 3 H_2O + 3 NADP$	-	-
R085	Ox1	$1.5 ADP + 1.5 H[+] + 1.5 P_i + FADH_2 + 0.5 O_2 \rightarrow$ $FAD + 1.5 ATP + 2.5 H_2O$	-	-
R086	Ox2	$3.5 H[+] + 2.5 ADP + 2.5 P_i + NADH + 0.5 O_2 \rightarrow$ $NAD + 2.5 ATP + 3.5 H_2O$	-	-
R087	Ox3	$NAD + NADPH \rightarrow NADH + NADP$	-	-
R088	Ox4	$H_2O + P_i \rightarrow H[+] + 2 P_i$	-	-
R089	Ox5	$AMP + ATP \rightarrow 2 ADP$	-	-
R090	Ox6	$ATP + H_2O \rightarrow ADP + H[+] + P_i$	-	-
R091	Ox7	$1 NADH + 1 CMP \rightarrow 1 NAD + 1 CDP$	-	-
R092	AA1	$AKG + H[+] + NADPH + NH_4[+] \rightarrow GLU + H_2O +$ $NADP$	-	-
R093	AA2	$ATP + GLU + NH_4[+] \rightarrow ADP + GLN + H[+] + P_i$	-	-
R094	AA3	$AKG + GLN + H[+] + NADPH \leftrightarrow NADP + 2 GLU$	-	-
R095	AA4	$3PG + GLU + H_2O + NAD \leftrightarrow$	1.1.1.95	R01513
		$AKG + H[+] + NADH + P_i + SER$	2.6.1.52	R04173
			3.1.3.3	R00582
R096	AA5	$SER \rightarrow NH_4[+] + PYR$	-	-
R097	AA6	$AcCoA + H_2S + SER \leftrightarrow Ace + CYS + CoA + H[+]$	-	-
R098	AA7	$ATP + Ace + CoA \rightarrow ADP + AcCoA + P_i$	-	-
R099	AA8	$GLU + PYR \rightarrow AKG + ALA$	-	-
R100	AA9	$H[+] + THR \leftrightarrow 2OXOB + NH_4[+]$	4.3.1.19	R00996
R101	AA10	$2OXOB + GLU + H[+] + NADPH + PYR \leftrightarrow$ $AKG + CO_2 + H_2O + ILE + NADP$	-	-
R102	AA11	$2 H[+] + ALA + NADPH + PYR \leftrightarrow$ $CO_2 + H_2O + NADP + VAL$	-	-
R103	AA12	$2 PYR + AcCoA + GLU + H[+] + NAD + NADPH \leftrightarrow$ $AKG + CoA + LEU + NADH + NADP + 2 CO_2$	-	-
R104	AA13	$2 PEP + ATP + E4P + NADPH \rightarrow$ $ADP + CHO + NAD P + 4 P_i$	-	-
R105	AA14	$CHO \leftrightarrow PRE$	-	-
R106	AA15	$GLU + H[+] + PRE \leftrightarrow AKG + CO_2 + H_2O + PHE$	-	-
R107	AA16	$GLU + NAD + PRE \leftrightarrow AKG + CO_2 + NADH + TYR$	-	-
R108	AA17	$CHO + GLN \leftrightarrow ANTH + GLU + H[+] + PYR$	-	-
R109	AA18	$ANTH + H[+] + PRPP + SER \leftrightarrow$ $CO_2 + GAP + P_i + TRYP + 2 H_2O$	-	-
R110	AA19	$3 H_2O + 2 NAD + ATP + GLN + PRPP \rightarrow$ $AICAR + AKG + HIS + P_i + 2 NADH + 2 P_i + 5 H[+]$	-	-
R111	AA20	$GLU + OXA \leftrightarrow AKG + ASP$	2.6.1.1	R00355
R112	AA21	$ASP + ATP + GLN + H_2O \rightarrow ADP + ASN + GLU + H[+]$ $+ P_i$	-	-
R113	AA22	$2 ATP + 2 H_2O + CO_2 + GLN \rightarrow$ $CaP + GLU + P_i + 2 ADP + 3 H[+]$	-	-
R114	AA23	$2 GLU + ASP + ATP + CaP + NADH \rightarrow$ $AKG + AMP + ARG + FUM + H_2O + NAD + P_i + P_i$	-	-
R115	AA24	$3 H[+] + 2 NADH + GLU \leftrightarrow PRO + 2 H_2O + 2 NAD$	-	-
R116	AA25	$AKG + O_2 + PRO \leftrightarrow CO_2 + HydPro + SUC$	-	-
R117	AA26	$ASP + ATP + H[+] + NADPH \rightarrow ADP + ASA + NADP +$ P_i	-	-
R118	AA27	$2 H[+] + ASA + GLU + NADH + PYR \leftrightarrow$ $AKG + DAP + H_2O + NAD$	-	-
R119	AA28	$DAP \leftrightarrow CO_2 + H[+] + LYS$	-	-
R120	AA29	$ASA + H[+] + NADPH \leftrightarrow HSER + NADP$	-	-
R121	AA30	$ATP + H_2O + HSER \rightarrow ADP + H[+] + P_i + THR$	-	-
R122	AA31	$AcCoA + CYS + H_2O + HSER \leftrightarrow$ $Ace + CoA + HCYS + H[+] + NH_4[+] + PYR$	-	-

R123	AA32	HCYS + MTHF \leftrightarrow H[+] + MET + THF	-	-
R124	AA33	4.306 ATP + 3.306 H ₂ O + 0.111 ALA + 0.094 GLY + 0.093 LEU + 0.059 PRO + 0.059 VAL + 0.058 LYS + 0.057 THR + 0.055 SER + 0.05 GLN + 0.05 GLU + 0.047 ARG + 0.047 ASN + 0.047 ASP + 0.045 PHE + 0.036 ILE + 0.031 TYR + 0.022 MET + 0.017 HIS + 0.013 HydPro + 0.012 CYS + 0.001 TRYP \rightarrow PROTEIN + 4.306 ADP + 4.306 Pi + 4.314 H[+]	-	-
R125	THF1	ATP + R5P \rightarrow AMP + H[+] + PRPP	-	-
R126	THF2	5FTHF + H[+] \leftrightarrow H ₂ O + MYLTHF	-	-
R127	THF3	H ₂ O + MYLTHF \leftrightarrow H[+] + N10FTHF	-	-
R128	THF4	ATP + FORM + THF \rightarrow ADP + N10FTHF + Pi	-	-
R129	THF5	MYLTHF + NADPH \leftrightarrow METHF + NADP	-	-
R130	THF6	H[+] + METHF + NADPH \leftrightarrow MTHF + NADP	-	-
R131	THF7	5FTHF + ATP + H ₂ O \rightarrow ADP + H[+] + N10FTHF + Pi	-	-
R132	THF8	FORM + H[+] + THF \leftrightarrow H ₂ O + N10FTHF	-	-
R133	THF9	DHF + H[+] + NADPH \leftrightarrow NADP + THF	-	-
R134	PA1	ACP + AcCoA + H[+] \leftrightarrow AcACP + CoA	-	-
R135	PA2	ATP + AcCoA + CO ₂ + H ₂ O \rightarrow ADP + H[+] + MalCoA + Pi	-	-
R136	PA3	ACP + MalCoA \leftrightarrow CoA + MalACP	-	-
R137	PA4	10 H[+] + 10 NADPH + 5 MalACP + AcACP \leftrightarrow C12:0ACP + 5 ACP + 5 CO ₂ + 5 H ₂ O + 10 NADP	-	-
R138	PA5	12 H[+] + 12 NADPH + 6 MalACP + AcACP \leftrightarrow C14:0ACP + 6 ACP + 6 CO ₂ + 6 H ₂ O + 12 NADP	-	-
R139	PA6	14 H[+] + 14 NADPH + 7 MalACP + AcACP \leftrightarrow C16:0ACP + 7 ACP + 7 CO ₂ + 7 H ₂ O + 14 NADP	-	-
R140	PA7	C16:0ACP + H[+] + NADH + O ₂ \leftrightarrow C16:1ACP + NAD + 2 H ₂ O	-	-
R141	PA8	C16:1ACP + H[+] + NADH + O ₂ \leftrightarrow C16:2ACP + NAD + 2 H ₂ O	-	-
R142	PA9	C16:2ACP + H[+] + NADH + O ₂ \leftrightarrow C16:3ACP + NAD + 2 H ₂ O	-	-
R143	PA10	16 H[+] + 16 NADPH + 8 MalACP + AcACP \leftrightarrow C18:0ACP + 8 ACP + 8 CO ₂ + 8 H ₂ O + 16 NADP	-	-
R145	PA11	C18:0ACP + H[+] + NADH + O ₂ \leftrightarrow C18:1ACP + NAD + 2 H ₂ O	-	-
R146	PA12	C18:1ACP + H[+] + NADH + O ₂ \leftrightarrow C18:2ACP + NAD + 2 H ₂ O	-	-
R147	PA13	C18:2ACP + H[+] + NADH + O ₂ \leftrightarrow C18:3ACP + NAD + 2 H ₂ O	-	-
R148	PA14	GLYC3P + 0.474 C16:0ACP + 0.446 C18:3ACP + 0.276 C18:2ACP + 0.253 C16:3ACP + 0.16 C18:1ACP + 0.148 C16:2ACP + 0.104 C12:0ACP + 0.051 C14:0ACP + 0.048 C18:0ACP + 0.04 C16:1ACP \leftrightarrow PA + 2 ACP + 2 H[+]	-	-
149	PA15	H[+] + O ₂ + NADH + C16:3ACP \rightarrow 2 H ₂ O + NAD + C16:4ACP	-	-
R150	TAG1	0.0186 C14:0ACP + 0.1275 C16:0ACP + 0.0387 C16:1ACP + 0.0137 C16:2ACP + 0.0191 C16:3ACP + 0.0019 C18:0ACP + 0.0753 C18:1ACP + 0.0967 C18:2ACP + 0.357 C18:3ACP + 0.2515 C16:4ACP \rightarrow ACP + FA	-	-
R151	TAG2	GLYC3P + FA \rightarrow AG3P	-	-
R152	TAG3	AG3P + FA \rightarrow DAG3P	-	-
R153	TAG4	H ₂ O + DAG3P \rightarrow DAG	-	-
R154	TAG5	DAG + FA \rightarrow TAG	-	-
R155	TAG6	0.3349 TAG \rightarrow TAG _p	-	-
R156	TAG7	0.3185 DAG \rightarrow DAG _p	-	-

R157	Ch1	12 H[+] + 8 ATP + 8 GLU + 8 NADPH + 2.5 O ₂ → PPorphyrin + 4 NH ₄ [+] + 6 CO ₂ + 8 AMP + 8 NADP + 8 PPi + 13 H ₂ O	-	-
R158	Ch2	18 H[+] + 15 NADPH + 8 ATP + 4 GAP + 4 PYR → Phytyl-PP + 4 ADP + 4 AMP + 4 CO ₂ + 7 PPi + 8 H ₂ O + 15 NADP	-	-
R159	Ch3	ATP + H ₂ O + MET → AdMET + H[+] + PPi + Pi	-	-
R160	Ch4	AdHCYS + H ₂ O ↔ Ad + HCYS	-	-
R161	Ch5	ATP + Ad → ADP + AMP + H[+]	-	-
R162	Ch6	4 NADPH + 2.5 O ₂ + 2 ATP + AdMET + Mg ²⁺ + PPorphyrin + Phytyl-PP → AdHCYS + Chlorophyll + PPi + 2 ADP + 2 H ₂ O + 2 Pi + 3 H[+] + 4 NADP	-	-
R163	NA1	4 ATP + 2 GLN + 2 H ₂ O + ASP + CO ₂ + GLY + N10FTHF + PRPP → AICAR + FUM + PPi + THF + 2 GLU + 4 ADP + 4 Pi + 7 H[+]	-	-
R164	NA2	ASP + CaP + H[+] + O ₂ + PRPP ↔ CO ₂ + H ₂ O + H ₂ O ₂ + PPi + Pi + UMP	-	-
R165	NA3	2 H ₂ O ₂ ↔ O ₂ + 2 H ₂ O	-	-
R166	NA4	ATP + UMP → ADP + UDP	-	-
R167	NA5	ATP + UDP ↔ ADP + UTP	-	-
R168	NA6	ATP + GLN + H ₂ O + UTP → ADP + CTP + GLU + Pi + 2 H[+]	-	-
R169	NA7	ATP + CDP ↔ ADP + CTP	-	-
R170	NA8	AICAR + N10FTHF ↔ H ₂ O + IMP + THF	-	-
R171	NA9	ATP + H ₂ O + IMP + NAD + NH ₄ [+] → AMP + GMP + NADH + PPi + 3 H[+]	-	-
R172	NA10	ATP + GMP → ADP + GDP	-	-
R173	NA11	ATP + GDP ↔ ADP + GTP	-	-
R174	NA12	ASP + GTP + IMP ↔ AMP + FUM + GDP + Pi + 2 H[+]	-	-
R175	NA13	ATP + H[+] + METHF + NADPH + UDP → ADP + DHF + H ₂ O + NADP + dTTP	-	-
R176	NA14	ATP + CDP + H[+] + NADPH → ADP + H ₂ O + NADP + dCTP	-	-
R177	NA15	ATP + GDP + H[+] + NADPH → ADP + H ₂ O + NADP + dGTP	-	-
R178	NA16	ATP + H[+] + NADPH ↔ H ₂ O + NADP + dATP	-	-
R179	NA17	2.372 H ₂ O + 1.372 ATP + 0.18 dATP + 0.18 dTTP + 0.32 dCTP + 0.32 dGTP → DNA + PPi + 1.372 ADP + 1.372 Pi + 2.372 H[+]	-	-
R180	NA18	1.4 H ₂ O + 0.56 ATP + 0.34 GTP + 0.16 UTP + 0.34 CTP → 0.4 ADP + 0.4 H[+] + 0.4 Pi + PPi + RNA	-	-
R182	Car1	cGAP + cPYR → CO ₂ + cDXP	2.2.1.7	R05636
R183	Car2	ATP + H[+] + 2 NADPH + CTP + cDXP → 2 H ₂ O + ADP + 2 NADP + PPi + CMP + cIPP	1.1.1.267 2.7.7.60	R05688 R05633
R184	Car3	ATP + H[+] + 2 NADPH + CTP + cDXP → 2 H ₂ O + ADP + 2 NADP + PPi + CMP + cDMAPP	2.7.1.148 4.6.1.12 1.17.7.1 1.17.1.2	R05634 R05637 R08689 R05884 R07219
R184	Car4	cIPP ↔ cDMAPP	5.3.3.2	R01123
R185	Car5	cDMAPP + cIPP → PPi + cGPP	2.5.1.1	R01658
R186	Car6	2 cIPP + cGPP → 2 PPi + cGGPP	2.5.1.10 2.5.1.29	R02003 R02061
R187	Car7	2 cGGPP → 2 PPi + cPHYT	2.5.1.32	R07916
R188	Car8	H ₂ O + NAD + cPHYT → H[+] + NADH + cZCAR	1.3.5.5	R04787
R189	Car9	2 O ₂ + 2 NADH + cZCAR → 4 H ₂ O + 2 NAD + cLYC	1.3.5.6	R04798 R04800
R190	Car10	cLYC → cBCAR	5.5.1.19	R03823
R191	Car11	2 H[+] + 2 O ₂ + 2 NADPH + cBCAR → 2 H ₂ O + 2 NADP + cZEA	1.14.13.129	R09747

140 Appendix C. Supplementary information for metabolic network reconstruction

R192	Car12	$2 \text{ H}[+] + 2 \text{ O}_2 + 2 \text{ NADH} + \text{ cZEA} \leftrightarrow 2 \text{ H}_2\text{O} + 2 \text{ NAD} + \text{ cVIO}$	1.14.13.90	R06956 R06947
R193	Car13	$\text{ cLYC} \rightarrow \text{ cACAR}$	5.5.1.18	R06963
R194	Car14	$\text{ cACAR} \rightarrow \text{ cLUT}$	5.5.1.19	R06962
R195	Car15	$0.1863 \text{ BCAR} \rightarrow 1 \text{ BCAR}_p$	1.14.13.129	R07530
R196	mu	$32.687 \text{ ATP} + 32.687 \text{ H}_2\text{O} + 0.6417 \text{ PROTEIN} + 0.2713 \text{ CARB} + 0.0453 \text{ PA} + 0.0305 \text{ RNA} + 0.0102 \text{ Chlorophyll} + 0.0011 \text{ DNA} \rightarrow \text{ Biomass} + 32.687 \text{ H}[+] + 32.687 \text{ ADP} + 32.687 \text{ Pi}$	1.14.99.45	R07531
R197	Glob	$0.771 \text{ cBCAR} + 0.075 \text{ TAG} + 0.154 \text{ DAG} \rightarrow \text{ Globule}$	-	-
R198	T1	$\text{ cDHAP} \leftrightarrow \text{ DHAP}$	-	-
R199	T2	$\text{ cGAP} \leftrightarrow \text{ GAP}$	-	-
R200	T3	$\text{ cPYR} \leftrightarrow \text{ PYR}$	-	-
R201	T4	$\text{ cPEP} \leftrightarrow \text{ PEP}$	-	-
R202	T5	$\text{ cMAL} \leftrightarrow \text{ MAL}$	-	-
R203	T6	$\text{ cASP} \leftrightarrow \text{ ASP}$	-	-
R204	T7	$\text{ cGLYCOL} \leftrightarrow \text{ GLYCOL}$	-	-
R205	T8	$\text{ cGLYC3P} \leftrightarrow \text{ GLYC3P}$	-	-
R206	T9	$\text{ cGLYC} \leftrightarrow \text{ GLYC}$	-	-
R207	T10	$\text{ mPYR} \leftrightarrow \text{ PYR}$	-	-
R208	T11	$\text{ mMAL} \leftrightarrow \text{ MAL}$	-	-
R209	T12	$\text{ mOXA} \leftrightarrow \text{ OXA}$	-	-
R210	T13	$\text{ mAKG} \leftrightarrow \text{ AKG}$	-	-
R211	T14	$3\text{PG} \rightarrow \text{ c3PG}$	-	-
R212	T15	$\text{ cAKG} \leftrightarrow \text{ AKG}$	-	-
R213	T16	$\text{ cGLU} \leftrightarrow \text{ GLU}$	-	-
R214	Ex1	$\text{ Light}_e x \rightarrow \text{ Light}$	-	-
R215	Ex2	$\text{ CO}_2_e x \leftrightarrow \text{ CO}_2$	-	-
R216	Ex3	$\text{ O}_2 \leftrightarrow \text{ O}_2_e x$	-	-
R217	Ex4	$\text{ SO}_4_e x \rightarrow \text{ SO}_4$	-	-
R218	Ex5	$\text{ NO}_3_e x \rightarrow \text{ NO}_3$	-	-
R219	Ex6	$\text{ NH}_4_e x \rightarrow \text{ NH}_4[+]$	-	-
R220	Ex7	$\text{ Mg}_2_e x \rightarrow \text{ Mg}_2[+]$	-	-
R221	Ex8	$\text{ Pi}_e x \leftrightarrow \text{ Pi}$	-	-
R222	Ex9	$\text{ H}_2\text{O}_e x \leftrightarrow \text{ H}_2\text{O}$	-	-

Table S2.: List of compounds in the carbon core metabolism.

No.	Symbol	Name
C001	13DPG	1,3-diPhosphoglycerate
C002	2OXOB	2-Oxobutanoate
C003	2PG	2-Phosphoglycerate
C004	3PG	Glycerate-3-phosphate
C005	5FTHF	5-Formyl-THF
C006	6PG	6-Phosphogluconate
C007	AcACP	Acetyl-ACP
C008	AcCOA	Acetyl-CoA
C009	Ace	Acetate
C010	ACP	Acetyl-carrier protein
C011	Ad	Adenosine
C012	AdHCYS	S-Adenosyl-L-homocysteine
C013	AdMET	S-Adenosyl-L-methionine
C014	ADP	Adenosine diphosphate
C015	ADP-G	ADP-Glucose
C016	AICAR	5-Aminoimidazole-4-carboxamide ribonucleine
C017	AKG	2-Oxoglutarate (alpha-ketoglutarate)
C018	ALA	Alanine
C019	AMP	Adenosine monophosphate
C020	ANTH	Anthranilate
C021	APS	Adenylyl sulfate
C022	ARG	Arginine
C023	ASA	L-Aspartic semialdehyde
C024	ASN	Asparagine
C025	ASP	Aspartate
C026	ATP	Adenosine triphosphate
C027	Biomass	Biomass
C028	Biomass _{ex}	Biomass (g)
C029	C12:0ACP	Dodecanoyl-ACP (Lauric acid)
C030	C14:0ACP	Tetradecanoyl-ACP (Myristic acid)
C031	C16:0ACP	Hexadecanoyl-ACP (Palmitic acid)
C032	C16:1ACP	Trans-Hexadec-2-enoyl-ACP (Palmitoleic acid)
C033	C16:2ACP	Hexadecadienoic acid
C034	C16:3ACP	Hexadecatrienoic acid
C035	C18:0ACP	Octadecanoyl-ACP (Stearic acid)
C036	C18:1ACP	Cis-11-ocadecanoate-ACP (Oleic acid)
C037	C18:2ACP	Linoleic acid
C038	C18:3ACP	Alpha-linoleic acid
C039	CaP	Carbamoyl phosphate
C040	CARB	Carbohydrate
C041	CDP	Cytidine diphosphate
C042	Chlorophyll	Chlorophyll
C043	CHO	Chorismate
C044	CIT	Citrate
C045	CMP	Cytidine monophosphate
C046	CDP	Cytidine diphosphate
C047	CTP	Cytidine triphosphate
C048	CO2	Carbon dioxide
C049	CO2 _{ex}	Carbon dioxide (extracellular)
C050	CoA	Coenzyme A
C051	CTP	Cytidine triphosphate
C052	CYS	Cysteine
C053	DAP	Diaminopimelate
C054	dATP	Deoxy ATP
C055	dCTP	Deoxy CTP
C056	dGTP	Deoxy GTP
C057	DHA	Dihydroxyacetone (Glycerone)
C058	DHAP	Dihydroxyacetone-P

C059	DHF	Dihydrofolate
C060	DMAPP	Dimethylallyl-pyrophosphate
C061	DNA	Deoxyribonucleic acid
C062	dTTP	Deoxy TTP
C063	DXP	Deoxy-xylulose 5-phosphate
C064	E4P	Erythrose 4-phosphate
C065	F16P	Fructose 1,6-bisphosphate
C066	F6P	Fructose 6-phosphate
C067	FAD	Flavin adenine dinucleotide oxidized
C068	FADH2	Flavin adenine dinucleotide reduced
C069	FORM	Formic acid
C070	FUM	Fumarate
C071	G1P	Glucose 1-phosphate
C072	G6P	Glucose 6-phosphate
C073	GA	Glyceraldehyde
C074	GAP	Glyceraldehyde 3-phosphate
C075	GDP	Guanosine diphosphate
C076	GGPP	Geranylgeranyl-pyrophosphate
C077	GLN	Glutamine
C078	GLU	Glutamate
C079	GLUC	Glucose
C080	GLY	Glycine
C081	GLYC	Glycerol
C082	GLYC3P	Glycerol 3-phosphate
C083	GLYCA	Glycerate
C084	GLY _C _{ex}	Glycerol (extracellular)
C085	GLYCOL	Glycolate
C086	GLYCOL2P	Glycolate-2P
C087	GLYOX	Glyoxylate
C088	GMP	Guanosine monophosphate
C089	GTP	Guanosine triphosphate
C090	H[+]	Proton
C091	H[+] _{ex}	Proton (extracellular)
C092	H2O	Water
C093	H2O2	Hydrogen peroxide
C094	H2O _{ex}	Water (extracellular)
C095	H2S	Hydrogen sulfide
C096	HCYS	Homocysteine
C097	HIS	Histidine
C098	HSER	Homoserine
C099	HydPro	Hydroxyproline
C100	HydPyr	3-Hydroxypyruvate
C101	ILE	Isoleucine
C102	IMP	Inosine monophosphate
C103	IPP	Isopentyl-pyrophosphate
C104	LEU	Leucine
C105	Light	Photons
C106	Light _{ex}	Photons (extracellular)
C107	LYC	Lycopene
C108	LYS	Lysine
C109	MAL	Malate
C110	MalCoA	Malonyl-CoA
C111	MET	Methionine
C112	METHF	5,10-Methylene-THF
C113	Mg2[+]	Magnesium
C114	Mg2[+] _{ex}	Magnesium (extracellular)
C115	MTHF	Methyl-THF
C116	MYLTHF	5,10-Methenyl-THF
C117	N10FTHF	10-Formyl-THF
C118	NAD	Nicotinamide oxidized
C119	NADH	Nicotinamide reduced

C120	NADP	Nicotinamidephosphate oxidized
C121	NADPH	Nicotinamidephosphate reduced
C122	NH4[+]	Ammonium
C123	NH4[+] _{ex}	Ammonium (extracellular)
C124	NO2	Nitrite
C125	NO3	Nitrate
C126	NO3 _{ex}	Nitrate (extracellular)
C127	O2	Oxygen
C128	O2 _{ex}	Oxygen (extracellular)
C129	OXA	Oxaloacetate
C130	PA	Phosphatidic acid
C131	PEP	Phosphoenolpyruvate
C132	PHE	Phenylalanine
C133	PHYT	Phytoene
C134	Phytol-PP	Phytol-diphosphate
C135	Pi	Orthophosphate
C136	Pi _{ex}	Orthophosphate (extracellular)
C137	PPi	Pyrophosphate
C138	PPorphyrin	Protoporphyrin
C139	PRE	Prephanate
C140	PRO	Proline
C141	PROTEIN	Protein
C142	PRPP	Phosphorybosylpyrophosphate
C143	PYR	Pyruvate
C144	R5P	Ribose 5-phosphate
C145	RNA	Ribonucleic acid
C146	Ru15DP	Ribulose 1,5-bisphosphate
C147	RU5P	Ribulose 5-phosphate
C148	S7P	Sedoheptulose 7-phosphate
C149	SER	Serine
C150	SO3	Sulphite
C151	SO4	Sulphate
C152	SO4 _{ex}	Sulphate (extracellular)
C153	STARCH	Starch
C154	STARCH _{ex}	Starch (extracellular)
C155	SUC	Succinate
C156	SUCCoA	Succinyl Coenzyme A
C157	THF	Tetrahydrofolate
C158	THR	Threonine
C159	TRYP	Tryptophan
C160	TYR	Tyrosine
C161	UDP	Uridine diphosphate
C162	UMP	Uridine monophosphate
C163	UTP	Uridine triphosphate
C164	VAL	Valine
C165	VIO	Violaxanthin
C166	X5P	Xylulose 5-phosphate
C167	ZCAR	Zeta-carotene

C.2 Metabolic network map of central carbon metabolism

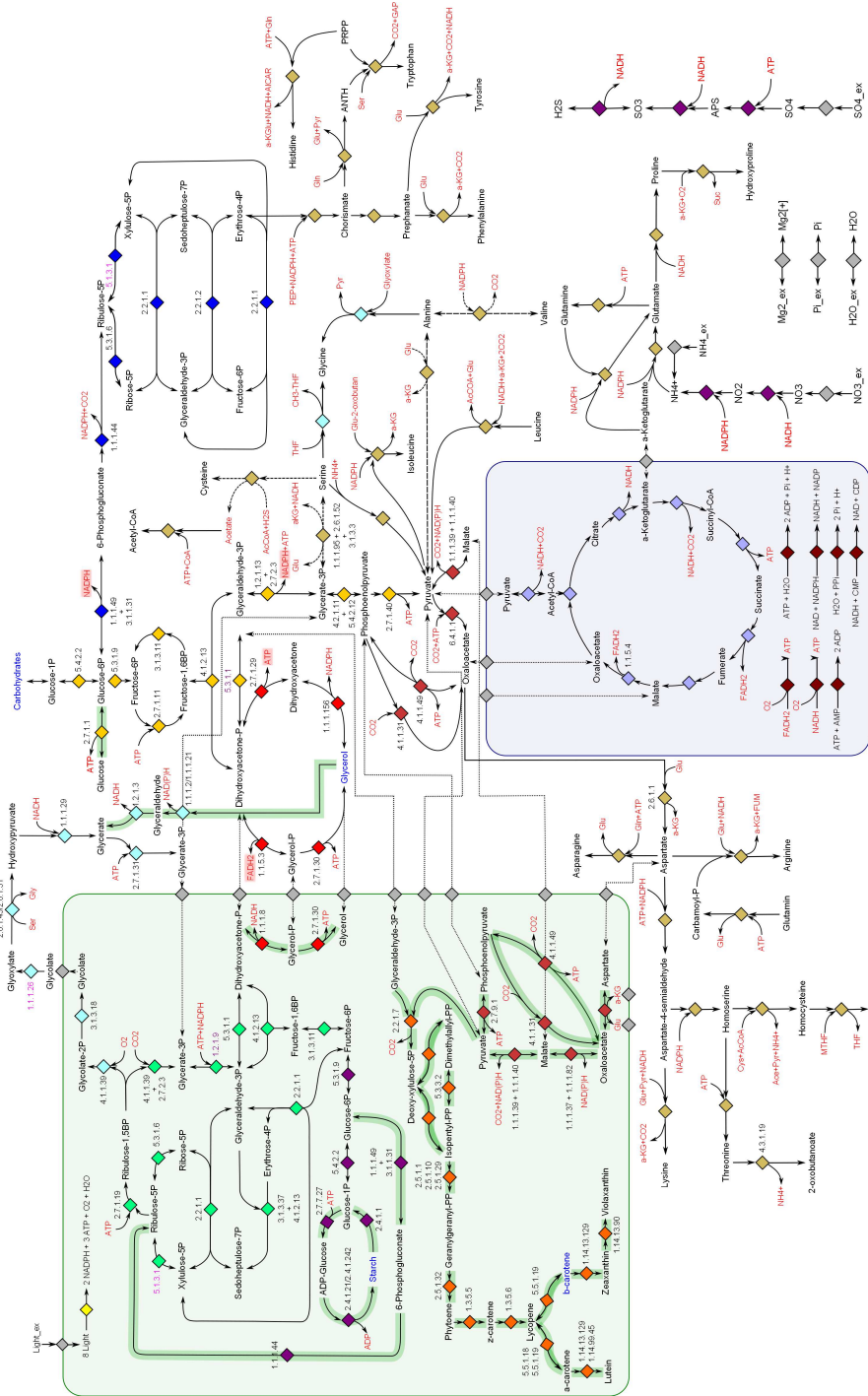


Figure S1: Network map of carbon core metabolism in the three considered compartments: Cytosol, chloroplast and mitochondrion.

Bibliography

- Abe, K., H. Hattori, and M. Hirano (2007). Accumulation and antioxidant activity of secondary carotenoids in the aerial microalga *Coelastrella striolata* var. *multistriata*. *Food Chemistry* 100(2), 656–661.
- Adesanya, V. O., M. P. Davey, S. A. Scott, and A. G. Smith (2014). Kinetic modelling of growth and storage molecule production in microalgae under mixotrophic and autotrophic conditions. *Bioresource Technology* 157C, 293–304.
- Andersen, R. A. (1992). Diversity of eukaryotic algae. *Biodiversity & Conservation* 1(4), 267–292.
- Bai, S. K., S. J. Lee, H. J. Na, K. S. Ha, J. A. Han, H. Lee, Y. G. Kwon, C. K. Chung, and Y. M. Kim (2005). β -carotene inhibits inflammatory gene expression in lipopolysaccharide-stimulated macrophages by suppressing redox-based NF- κ B activation. *Experimental & Molecular Medicine* 37(4), 323–34.
- Baker, N. R. (2008). Chlorophyll fluorescence: A probe of photosynthesis in vivo. *Annual Review of Plant Biology* 59, 89–113.
- Bakker, J. M., L. M. Aleese, G. Meijer, and G. von Helden (2003). Fingerprint IR spectroscopy to probe amino acid conformations in the gas phase. *Physical Review Letters* 91(20).
- Baroukh, C. (2014). *Metabolic modeling under non-balanced growth: Application to microalgae for biofuels production*. PhD thesis.
- Baroukh, C., R. Muñoz-Tamayo, J.-P. Steyer, and O. Bernard (2014). DRUM: A new framework for metabolic modeling under non-balanced growth. Application to the carbon metabolism of unicellular microalgae. *PLoS ONE* 9(8), e104499.
- Baroukh, C., R. Muñoz-Tamayo, J.-P. Steyer, and O. Bernard (2015). A state of the art of metabolic networks of unicellular microalgae and cyanobacteria for biofuel production. *Metabolic Engineering* 30, 49–60.
- Barra, L., R. Chandrasekaran, F. Corato, and C. Brunet (2014). The challenge of eco-physiological biodiversity for biotechnological applications of marine microalgae. *Marine Drugs* 12(3), 1641–1675.
- Baty, F. and M.-L. Delignette-Muller (2004). Estimating the bacterial lag time: Which model, which precision? *International Journal of Food Microbiology* 91(3), 261–277.
- Becker, S. A., A. M. Feist, M. L. Mo, G. Hannum, B. O. Palsson, and M. J. Herrgard (2007). Quantitative prediction of cellular metabolism with constraint-based mod-

- els: The COBRA toolbox. *Nature Protocols* 2(3), 727–38.
- Ben-Amotz, A., A. Katz, and M. Avron (1982). Accumulation of β -carotene in halo-tolerant algae: Purification and characterization of β -carotene-rich globules from *Dunaliella bardawil* (chlorophyceae). *Journal of Phycology* 18(4), 529–537.
- Ben-Amotz, A., A. Shaish, and M. Avron (1991). The biotechnology of cultivating *Dunaliella* for production of β -carotene rich algae. *Bioresource Technology* 38(2), 233–235.
- Berthomieu, C. and R. Hienerwadel (2009). Fourier transform infrared (FTIR) spectroscopy. *Photosynthesis Research* 101(2-3), 157–170.
- Biller, P. and A. B. Ross (2014). Pyrolysis GCMS as a novel analysis technique to determine the biochemical composition of microalgae. *Algal Research* 6, Part A(0), 91–97.
- Bjorkman, O. and B. Demmig (1987). Photon yield of O₂ evolution and chlorophyll fluorescence characteristics at 77 K among vascular plants of diverse origins. *Planta* 170(4), 489–504.
- Blanco, A. M., J. Moreno, J. A. Del Campo, J. Rivas, and M. G. Guerrero (2007). Outdoor cultivation of lutein-rich cells of *Muriellopsis* sp. in open ponds. *Applied microbiology and biotechnology* 73(6), 1259–66.
- Blanken, W., P. R. Postma, L. de Winter, R. H. Wijffels, and M. Janssen (2016). Predicting microalgae growth. *Algal Research* 14, 28–38.
- Bohnen, F. and T. Brück (2013). A critical review of algae process optimization using Design of Experiment methodologies. *JSM Biotechnol Bioeng* 1(3), 1015.
- Borowitzka, M. A. and C. J. Siva (2007). The taxonomy of the genus *Dunaliella* (Chlorophyta, Dunaliellales) with emphasis on the marine and halophilic species. *Journal of Applied Phycology* 19(5), 567–590.
- Bougaran, G., C. Rouxel, N. Dubois, R. Kaas, S. Grouas, E. Lukomska, J.-R. Le Coz, and J.-P. Cadoret (2012). Enhancement of neutral lipid productivity in the microalga *Isochrysis affinis Galbana* (T-Iso) by a mutation-selection procedure. *Biotechnology and Bioengineering* 109(11), 2737–2745.
- Boyle, N. R. and J. A. Morgan (2009). Flux balance analysis of primary metabolism in *Chlamydomonas reinhardtii*. *BMC Systems Biology* 3, 4.
- Brennan, L., A. Blanco Fernandez, A. S. Mostaert, and P. Owende (2012). Enhancement of BODIPY505/515 lipid fluorescence method for applications in biofuel-directed microalgae production. *Journal of Microbiological Methods* 90(2), 137–143.
- Burgard, A. P., E. V. Nikolaev, C. H. Schilling, and C. D. Maranas (2004). Flux coupling analysis of genome-scale metabolic network reconstructions. *Genome Research* 14(2), 301–12.
- Burgard, A. P., P. Pharkya, and C. D. Maranas (2003). Optknock: A bilevel programming framework for identifying gene knockout strategies for microbial strain optimization. *Biotechnology and Bioengineering* 84(6), 647–57.
- Burgula, Y., D. Khali, S. Kim, S. S. Krishnan, M. A. Cousin, J. P. Gore, B. L. Reuhs, and L. J. Mauer (2007). Review of mid-infrared Fourier transform-infrared spectroscopy applications for bacterial detection. *Journal of Rapid Methods and Automation in Mi-*

- crobiology* 15(2), 146–175.
- Butler, W. L. (1978). Energy distribution in the photochemical apparatus of photosynthesis. *Annual Review of Plant Physiology* 29, 345–378. ED.
- Carbonaro, M. and A. Nucara (2010). Secondary structure of food proteins by Fourier transform spectroscopy in the mid-infrared region. *Amino Acids* 38(3), 679–690.
- Chang, R. L., L. Ghamsari, A. Manichaikul, E. F. Hom, S. Balaji, W. Fu, Y. Shen, T. Hao, B. O. Palsson, K. Salehi-Ashtiani, and J. A. Papin (2011). Metabolic network reconstruction of *Chlamydomonas* offers insight into light-driven algal metabolism. *Molecular Systems Biology* 7, 518.
- Cheloni, G. and V. I. Slaveykova (2013). Optimization of the C11-BODIPY581/591 dye for the determination of lipid oxidation in *Chlamydomonas reinhardtii* by flow cytometry. *Cytometry Part A* 83(10), 952–961.
- Chen, H. and J. G. Jiang (2009). Osmotic responses of *Dunaliella* to the changes of salinity. *Journal of Cellular Physiology* 219(2), 251–8.
- Chen, W., C. W. Zhang, L. R. Song, M. Sommerfeld, and Q. Hu (2009). A high throughput Nile red method for quantitative measurement of neutral lipids in microalgae. *Journal of Microbiological Methods* 77(1), 41–47.
- Choi, S. K., Y. S. Park, D. K. Choi, and H. I. Chang (2008). Effects of astaxanthin on the production of NO and the expression of COX-2 and iNOS in LPS-stimulated BV2 microglial cells. *Journal of Microbiology and Biotechnology* 18(12), 1990–1996.
- Cifuentes, A. S., M. Gonzalez, M. Conejeros, V. Dellarossa, and O. Parra (1992). Growth and carotenogenesis in eight strains of *Dunaliella salina* Teodoresco from Chile. *Journal of Applied Phycology* 4(2), 111.
- Cloutier, M. and P. Wellstead (2010). The control systems structures of energy metabolism. *Journal of The Royal Society Interface* 7(45), 651–665.
- Cogne, G., M. Rugen, A. Bockmayr, M. Titica, C. G. Dussap, J. F. Cornet, and J. Legrand (2011). A model-based method for investigating bioenergetic processes in autotrophically growing eukaryotic microalgae: Application to the green algae *Chlamydomonas reinhardtii*. *Biotechnology Progress* 27(3), 631–40.
- Cooper, M. S., W. R. Hardin, T. W. Petersen, and R. A. Cattolico (2010). Visualizing “green oil” in live algal cells. *Journal of Bioscience and Bioengineering* 109(2), 198–201.
- Cordwell, S. J. (1999). Microbial genomes and “missing” enzymes: Redefining biochemical pathways. *Arch Microbiol* 172(5), 269–79.
- da Silva, T. L., C. A. Santos, and A. Reis (2009). Multi-parameter flow cytometry as a tool to monitor heterotrophic microalgal batch fermentations for oil production towards biodiesel. *Biotechnology and Bioprocess Engineering* 14(3), 330–337.
- Dal’Molin, C. G., L. E. Quek, R. W. Palfreyman, and L. K. Nielsen (2011). AlgaGEM - a genome-scale metabolic reconstruction of algae based on the *Chlamydomonas reinhardtii* genome. *BMC Genomics* 12(4), 1–10.
- Dashkova, V., E. Segev, D. Malashenkov, R. Kolter, I. Vorobjev, and N. S. Barteneva (2016). Microalgal cytometric analysis in the presence of endogenous autofluorescent pigments. *Algal Research* 19, 370–380.

- Davis, R., A. Aden, and P. T. Pienkos (2011). Techno-economic analysis of autotrophic microalgae for fuel production. *Applied Energy* 88(10), 3524–3531.
- Davis, R. W., B. J. Carvalho, H. D. T. Jones, and S. Singh (2015). The role of photo-osmotic adaptation in semi-continuous culture and lipid particle release from *Dunaliella viridis*. *Journal of Applied Phycology* 27(1), 109–123.
- de Winter, L., A. J. Klok, M. Cuaresma Franco, M. J. Barbosa, and R. H. Wijffels (2013). The synchronized cell cycle of *Neochloris oleoabundans* and its influence on biomass composition under constant light conditions. *Algal Research* 2(4), 313–320.
- Dean, A. P., D. C. Sigeo, B. Estrada, and J. K. Pittman (2010). Using FTIR spectroscopy for rapid determination of lipid accumulation in response to nitrogen limitation in freshwater microalgae. *Bioresource technology* 101(12), 4499–507.
- Del Vasto, M. (2015). *Organelle Genome Evolution Within The Green Algal Genus Dunaliella*. Master thesis.
- Del Vasto, M., F. Figueroa-Martinez, J. Featherston, M. A. Gonzalez, A. Reyes-Prieto, P. M. Durand, and D. R. Smith (2015). Massive and widespread organelle genomic expansion in the green algal genus *Dunaliella*. *Genome Biology and Evolution* 7(3), 656–663.
- Demmig-Adams, B. and W. W. Adams (2006). Photoprotection in an ecological context: The remarkable complexity of thermal energy dissipation. *New Phytologist* 172(1), 11–21.
- Droop, M. R. (1968). Vitamin B12 and marine ecology IV: Kinetics of uptake growth and inhibition in *Monochrysis lutheri*. *Journal of the Marine Biological Association of the United Kingdom* 48(3), 689–733.
- Edwards, J. S., R. U. Ibarra, and B. O. Palsson (2001). *In silico* predictions of *Escherichia coli* metabolic capabilities are consistent with experimental data. *Nature Biotechnology* 19(2), 125–130.
- Fabregas, J., J. Abalde, and C. Herrero (1989). Biochemical composition and growth of the marine microalga *Dunaliella tertiolecta* (Butcher) with different ammonium nitrogen concentrations as chloride, sulphate, nitrate and carbonate. *Aquaculture* 83(3), 289–304.
- Fachet, M., R. J. Flassig, L. Rihko-Struckmann, and K. Sundmacher (2014). A dynamic growth model of *Dunaliella salina*: Parameter identification and profile likelihood analysis. *Bioresource Technology* 173C, 21–31.
- Fachet, M., D. Hermsdorf, L. Rihko-Struckmann, and K. Sundmacher (2016). Flow cytometry enables dynamic tracking of algal stress response: A case study using carotenogenesis in *Dunaliella salina*. *Algal Research* 13, 227–234.
- Fassett, R. G. and J. S. Coombes (2012). Astaxanthin in cardiovascular health and disease. *Molecules* 17(2), 2030–48.
- Flassig, R. J., M. Fachet, K. Höffner, P. I. Barton, and K. Sundmacher (2016). Dynamic flux balance modeling to increase the production of high-value compounds in green microalgae. *Biotechnology for Biofuels* 9(1), 1–12.
- Flassig, R. J., I. Migal, E. v. der Zalm, L. Rihko-Struckmann, and K. Sundmacher (2015). Rational selection of experimental readout and intervention sites for reduc-

- ing uncertainties in computational model predictions. *BMC Bioinformatics* 16(1), 13.
- Gangl, D., J. A. Z. Zedler, P. D. Rajakumar, E. M. R. Martinez, A. Riseley, A. Wodarczyk, S. Purton, Y. Sakuragi, C. J. Howe, P. E. Jensen, and C. Robinson (2015). Biotechnological exploitation of microalgae. *Journal of Experimental Botany* 66(22), 6975–6990.
- Garcia-Camacho, F., A. Sanchez-Miron, E. Molina-Grima, F. Camacho-Rubio, and J. C. Merchuck (2012). A mechanistic model of photosynthesis in microalgae including photoacclimation dynamics. *Journal of theoretical biology* 304, 1–15.
- Geider, R. J., H. L. MacIntyre, and T. M. Kana (1998). A dynamic regulatory model of phytoplanktonic acclimation to light, nutrients, and temperature. *Limnology and Oceanography* 43(4), 679–694.
- Ghetti, F., H. Herrmann, D. P. Hder, and H. K. Seidlitz (1999). Spectral dependence of the inhibition of photosynthesis under simulated global radiation in the unicellular green alga *Dunaliella salina*. *Journal of Photochemistry and Photobiology B: Biology* 48(2), 166–173.
- Gimpel, J. A., V. Henriquez, and S. P. Mayfield (2015). In metabolic engineering of eukaryotic microalgae: Potential and challenges come with great diversity. *Frontiers in Microbiology* 6, 1376.
- Giordano, M., M. Kansiz, P. Heraud, J. Beardall, B. Wood, and D. McNaughton (2001). Fourier Transform Infrared spectroscopy as a novel tool to investigate changes in intracellular macromolecular pools in the marine microalga *Chaetoceros muellerii* (Bacillariophyceae). *Journal of Phycology* 37(2), 271–279.
- Goldman, J. C. and D. G. Peavey (1979). Steady-state growth and chemical composition of the marine chlorophyte *Dunaliella tertiolecta* in nitrogen-limited continuous cultures. *Applied and Environmental Microbiology* 38(5), 894–901.
- Gomez, J. A., K. Höffner, and P. I. Barton (2014). DFBAlab: A fast and reliable MATLAB code for dynamic flux balance analysis. *BMC Bioinformatics* 15, 409.
- Gomez, P. I. and M. A. Gonzalez (2005). The effect of temperature and irradiance on the growth and carotenogenic capacity of seven strains of *Dunaliella salina* (Chlorophyta) cultivated under laboratory conditions. *Biological research* 38(2-3), 151–62.
- Gonzalalez, M. A., P. I. Gomez, and J. E. W. Polle (2009). *Taxonomy and Phylogeny of the Genus Dunaliella* (1 ed.), Book section 15-43. Enfield: Science Publishers.
- Grafahrend-Belau, E., A. Junker, A. Eschenröder, J. Müller, F. Schreiber, and B. H. Junker (2013). Multiscale metabolic modeling: Dynamic flux balance analysis on a whole-plant scale. *Plant Physiology* 163(2), 637–647.
- Gregori, G., M. Denis, D. Lefevre, and B. Beker (2002). A flow cytometric approach to assess phytoplankton respiration. *Methods in Cell Science* 24(1-3), 99–106.
- Guiry, M. D. (2012). How many species of algae are there? *Journal of Phycology* 48(5), 1057–63.
- Günzler, H. and H.-U. Gremlich (2003). *IR-Spektroskopie: Eine Einführung* (4 ed.). Weinheim: Wiley-VCH.

- Hädicke, O. and S. Klamt (2010). CASOP: A computational approach for strain optimization aiming at high productivity. *Journal of Biotechnology* 147(2), 88–101.
- Halverson, K. J., I. Sucholeiki, T. T. Ashburn, and P. T. Lansbury (1991). Location of β -sheet-forming sequences in amyloid proteins by FTIR. *Journal of the American Chemical Society* 113(17), 6701–6703.
- Han, B. P. (2002). A mechanistic model of algal photoinhibition induced by photo-damage to Photosystem-II. *Journal of Theoretical Biology* 214(4), 519–27.
- Hannon, M., J. Gimpel, M. Tran, B. Rasala, and S. Mayfield (2010). Biofuels from algae: Challenges and potential. *Biofuels* 1(5), 763–784.
- Havlik, I., P. Lindner, T. Scheper, and K. F. Reardon (2013). On-line monitoring of large cultivations of microalgae and cyanobacteria. *Trends in Biotechnology* 31(7), 406–414.
- Hein, M., M. F. Pedersen, and K. Sand-Jensen (1995). Size-dependent nitrogen uptake in micro- and macroalgae. *Marine ecology progress series. Oldendorf* 118(1), 247–253.
- Hejazi, M. A., E. Holwerda, and R. H. Wijffels (2004). Milking microalga *Dunaliella salina* for β -carotene production in two-phase bioreactors. *Biotechnology and Bioengineering* 85(5), 475–81.
- Henson, M. A. and T. J. Hanly (2014). Dynamic flux balance analysis for synthetic microbial communities. *IET Syst Biol* 8(5), 214–29.
- Herrmann, H., D. P. Häder, and F. Ghetti (1997). Inhibition of photosynthesis by solar radiation in *Dunaliella salina*: Relative efficiencies of UV-B, UV-A and PAR. *Plant, Cell & Environment* 20(3), 359–365.
- Hildebrand, M., R. M. Abbriano, J. E. W. Polle, J. C. Traller, E. M. Trentacoste, S. R. Smith, and A. K. Davis (2013). Metabolic and cellular organization in evolutionarily diverse microalgae as related to biofuels production. *Current Opinion in Chemical Biology* 17(3), 506–514.
- Hindmarsh, A. C., P. N. Brown, K. E. Grant, S. L. Lee, R. Serban, D. E. Shumaker, and C. S. Woodward (2005). SUNDIALS: Suite of nonlinear and differential/algebraic equation solvers. *Acm Transactions on Mathematical Software* 31(3), 363–396.
- Höffner, K., S. M. Harwood, and P. I. Barton (2013). A reliable simulator for dynamic flux balance analysis. *Biotechnology and Bioengineering* 110(3), 792–802.
- Hucka, M., A. Finney, H. M. Sauro, H. Bolouri, J. C. Doyle, and H. Kitano (2003). The systems biology markup language (SBML): A medium for representation and exchange of biochemical network models. *Bioinformatics* 19(4), 524–531.
- Hyka, P., S. Lickova, P. Pribyl, K. Melzoch, and K. Kovar (2013). Flow cytometry for the development of biotechnological processes with microalgae. *Biotechnology Advances* 31(1), 2–16.
- Ibarra, R. U., J. S. Edwards, and B. O. Palsson (2002). *Escherichia coli* K-12 undergoes adaptive evolution to achieve in silico predicted optimal growth. *Nature* 420(6912), 186–189.
- Jahns, P., D. Latowski, and K. Strzalka (2009). Mechanism and regulation of the violaxanthin cycle: The role of antenna proteins and membrane lipids. *Biochimica et biophysica acta* 1787(1), 3–14.

- Jamers, A., M. Lenjou, P. Deraedt, D. Van Bockstaele, R. Blust, and W. de Coen (2009). Flow cytometric analysis of the cadmium-exposed green alga *Chlamydomonas reinhardtii* (Chlorophyceae). *European Journal of Phycology* 44(4), 541–550.
- Jin, E., K. Yokthongwattana, J. E. W. Polle, and A. Melis (2003). Role of the reversible Xanthophyll cycle in the Photosystem II damage and repair cycle in *Dunaliella salina*. *Plant Physiology* 132(1), 352–364.
- Jin, E. S. and J. E. W. Polle (2009). *Carotenoid Biosynthesis in Dunaliella (Chlorophyta)* (1 ed.), Book section 5, pp. 147–171. Enfield: Science Publishers.
- Kang, C. D., J. S. Lee, T. H. Park, and S. J. Sim (2007). Complementary limiting factors of astaxanthin synthesis during photoautotrophic induction of *Haematococcus pluvialis*: C/N ratio and light intensity. *Applied microbiology and biotechnology* 74(5), 987–994.
- Kim, J., M. Fabris, G. Baart, M. K. Kim, A. Goossens, W. Vyverman, P. G. Falkowski, and D. S. Lun (2016). Flux balance analysis of primary metabolism in the diatom *Phaeodactylum tricornutum*. *The Plant Journal: For Cell and Molecular Biology* 85(1), 161–76.
- Klamt, S., O. Hädicke, and A. von Kamp (2014). *Stoichiometric and Constraint-Based Analysis of Biochemical Reaction Networks*, Book section 5, pp. 263 – 316. Modeling and Simulation in Science, Engineering and Technology. Springer International Publishing.
- Klamt, S. and R. Mahadevan (2015). On the feasibility of growth-coupled product synthesis in microbial strains. *Metabolic Engineering* 30, 166–178.
- Klamt, S., J. Saez-Rodriguez, and E. D. Gilles (2007). Structural and functional analysis of cellular networks with CellNetAnalyzer. *BMC Systems Biology* 1, 2.
- Klamt, S., S. Schuster, and E. D. Gilles (2002). Calculability analysis in underdetermined metabolic networks illustrated by a model of the central metabolism in purple nonsulfur bacteria. *Biotechnology and Bioengineering* 77(7), 734–751.
- Kliphuis, A., A. Klok, D. Martens, P. Lamers, M. Janssen, and R. Wijffels (2011). Metabolic modeling of *Chlamydomonas reinhardtii*: Energy requirements for photoautotrophic growth and maintenance. *Journal of Applied Phycology* 24(2), 253–266.
- Klok, A. J., J. A. Verbaanderd, P. P. Lamers, D. E. Martens, A. Rinzema, and R. H. Wijffels (2013). A model for customising biomass composition in continuous microalgae production. *Bioresource Technology* 146(0), 89–100.
- Koller, M., A. Muhr, and G. Braunegg (2014). Microalgae as versatile cellular factories for valued products. *Algal Research* 6, Part A(0), 52–63.
- Koussa, J., A. Chaiboonchoe, and K. Salehi-Ashtiani (2014). Computational approaches for microalgal biofuel optimization: A review. *BioMed Research International* 2014, 12.
- Kreutz, C., A. Raue, D. Kaschek, and J. Timmer (2013). Profile likelihood in systems biology. *FEBS Journal* 280(11), 2564–2571.
- Krieger-Liszskay, A. (2005). Singlet oxygen production in photosynthesis. *Journal of Experimental Botany* 56(411), 337–346.

- Krujatz, F., A. Lode, S. Brüggemeier, K. Schütz, J. Kramer, T. Bley, M. Gelinsky, and J. Weber (2015). Green bioprinting: Viability and growth analysis of microalgae immobilized in 3D-plotted hydrogels versus suspension cultures. *Engineering in Life Sciences* 15(7), 678–688.
- Krumholz, E. W., H. Yang, P. Weisenhorn, C. S. Henry, and I. G. L. Libourel (2012). Genome-wide metabolic network reconstruction of the picoalga *Ostreococcus*. *Journal of Experimental Botany* 63(6), 2353–2362.
- Lamers, P. P., M. Janssen, R. C. H. De Vos, R. J. Bino, and R. H. Wijffels (2008). Exploring and exploiting carotenoid accumulation in *Dunaliella salina* for cell-factory applications. *Trends in Biotechnology* 26(11), 631–638.
- Lamers, P. P., M. Janssen, R. C. H. De Vos, R. J. Bino, and R. H. Wijffels (2012). Carotenoid and fatty acid metabolism in nitrogen-starved *Dunaliella salina*, a unicellular green microalga. *Journal of Biotechnology* 162(1), 21–27.
- Lamers, P. P., C. C. W. van de Laak, P. S. Kaasenbrood, J. Lorier, M. Janssen, R. C. H. De Vos, R. J. Bino, and R. H. Wijffels (2010). Carotenoid and fatty acid metabolism in light-stressed *Dunaliella salina*. *Biotechnology and Bioengineering* 106(4), 638–648.
- Laurens, L. M. L. and E. J. Wolfrum (2011). Feasibility of spectroscopic characterization of algal lipids: Chemometric correlation of NIR and FTIR spectra with exogenous lipids in algal biomass. *BioEnergy Research* 4(1), 22–35.
- Lee, D. Y., H. Yun, S. Park, and S. Y. Lee (2003). MetaFluxNet: The management of metabolic reaction information and quantitative metabolic flux analysis. *Bioinformatics* 19(16), 2144–6.
- Lee, E., M. Jalalizadeh, and Q. Zhang (2015). Growth kinetic models for microalgae cultivation: A review. *Algal Research* 12, 497–512.
- Lichtenthaler, H. K. (1999). The 1-Deoxy-D-Xylulose-5-Phosphate pathway of isoprenoid biosynthesis in plants. *Annual review of plant physiology and plant molecular biology* 50, 47–65.
- Lichtenthaler, H. K. (2001). Chlorophylls and carotenoids: Measurement and characterization by UV-VIS spectroscopy. *Current Protocols in Food Analytical Chemistry*.
- Liu, J., J. Mukherjee, J. J. Hawkes, and S. J. Wilkinson (2013). Optimization of lipid production for algal biodiesel in nitrogen stressed cells of *Dunaliella salina* using FTIR analysis. *Journal of Chemical Technology & Biotechnology* 88(10), 1807–1814.
- Lomas, M. W. and P. M. Glibert (2000). Comparison of nitrate uptake, storage and reduction in marine diatoms and flagellates. *Journal of Phycology* 36(5), 903–913.
- Long, S. P., S. Humphries, and P. G. Falkowski (1994). *Photoinhibition of photosynthesis in nature*, Volume 45 of *Annual Review of Plant Physiology and Plant Molecular Biology*, pp. 633–662.
- Lowry, O. H., N. J. Rosebrough, A. L. Farr, and R. J. Randall (1951). Protein measurement with the folin phenol reagent. *Journal of Biological Chemistry* 193(1), 265–275.
- Maarleveld, T. R., R. A. Khandelwal, B. G. Olivier, B. Teusink, and F. J. Bruggeman (2013). Basic concepts and principles of stoichiometric modeling of metabolic networks. *Biotechnology Journal* 8(9), 997–1008.

- MacIntyre, H. L., T. M. Kana, T. Anning, and R. J. Geider (2002). Photoacclimation of photosynthesis irradiance response curves and photosynthetic pigments in microalgae and cyanobacteria. *Journal of Phycology* 38(1), 17–38.
- Mahadevan, R. and C. H. Schilling (2003). The effects of alternate optimal solutions in constraint-based genome-scale metabolic models. *Metabolic Engineering* 5(4), 264–276.
- Mairet, F., O. Bernard, T. Lacour, and A. Sciandra (2011). Modeling microalgae growth in nitrogen limited photobioreactor for estimating biomass, carbohydrate and neutral lipid productivities. *Preprints of the 18th IFAC World Congress*, 10591–96.
- Mairet, F., O. Bernard, P. Masci, T. Lacour, and A. Sciandra (2011). Modelling neutral lipid production by the microalga *Isochrysis* aff. *galbana* under nitrogen limitation. *Bioresource Technology* 102(1), 142–149.
- Mairet, F., M. Titica, O. Bernard, and J. Pruvost (2010). Coupling biological and radiative models to describe microalgal growth in a photobioreactor. *IFAC Proceedings Volumes* 43(6), 168–173.
- Mallick, N., S. Mandal, A. K. Singh, M. Bishai, and A. Dash (2011). Green microalga *Chlorella vulgaris* as a potential feedstock for biodiesel. *Journal of Chemical Technology & Biotechnology* 87(1), 137–145.
- Manichaikul, A., L. Ghamsari, E. F. Hom, C. Lin, R. R. Murray, R. L. Chang, S. Balaji, T. Hao, Y. Shen, A. K. Chavali, I. Thiele, X. Yang, C. Fan, E. Mello, D. E. Hill, M. Vidal, K. Salehi-Ashtiani, and J. A. Papin (2009). Metabolic network analysis integrated with transcript verification for sequenced genomes. *Nature Methods* 6(8), 589–92.
- Markovits, A., M. P. Gianelli, R. Conejeros, and S. Erazo (1993). Strain selection for β -carotene production by *Dunaliella*. *World journal of microbiology & biotechnology* 9(5), 534–7.
- Maxwell, K. and G. N. Johnson (2000). Chlorophyll fluorescence - A practical guide. *Journal of Experimental Botany* 51(345), 659–668.
- Meeks, J. C. and R. W. Castenho (1971). Growth and photosynthesis in an extreme thermophile *Synechococcus lividus* (Cyanophyta). *Archiv Für Mikrobiologie* 78(1), 25–41.
- Mendoza, H., A. Martel, M. J. del Rio, and G. G. Reina (1999). Oleic acid is the main fatty acid related with carotenogenesis in *Dunaliella salina*. *Journal of Applied Phycology* 11(1), 15–19.
- Mendoza Guzmán, H., A. de la Jara Valido, K. Freijanes Presmanes, and L. Carmona Duarte (2012). Quick estimation of intraspecific variation of fatty acid composition in *Dunaliella salina* using flow cytometry and Nile Red. *Journal of Applied Phycology* 24(5), 1237–1243.
- Morgan-Kiss, R. M., J. C. Prisco, T. Pocock, L. Gudynaite-Savitch, and N. P. A. Huner (2006). Adaptation and acclimation of photosynthetic microorganisms to permanently cold environments. *Microbiology and Molecular Biology Reviews* 70(1), 222–+.
- Mulders, K. J. M., J. H. Janssen, D. E. Martens, R. H. Wijffels, and P. P. Lamers (2014). Effect of biomass concentration on secondary carotenoids and triacylglyc-

- erol (TAG) accumulation in nitrogen-depleted *Chlorella zofingiensis*. *Algal Research* 6, Part A, 8–16.
- Mulders, K. J. M., P. P. Lamers, D. E. Martens, and R. H. Wijffels (2014). Phototrophic pigment production with microalgae: Biological constraints and opportunities. *Journal of Phycology* 50(2), 229–242.
- Muñoz-Tamayo, R., P. Martinon, G. Bougaran, F. Mairet, and O. Bernard (2014). Getting the most out of it: Optimal experiments for parameter estimation of microalgae growth models. *Journal of Process Control* 24(6), 991–1001.
- Murchie, E. H. and T. Lawson (2013). Chlorophyll fluorescence analysis: A guide to good practice and understanding some new applications. *Journal of Experimental Botany* 64(13), 3983–98.
- Muthuraj, M., B. Palabhanvi, S. Misra, V. Kumar, K. Sivalingavasu, and D. Das (2013). Flux balance analysis of *Chlorella* sp. FC2 IITG under photoautotrophic and heterotrophic growth conditions. *Photosynthesis Research* 118(1-2), 167–79.
- Neidhardt, J., J. R. Benemann, L. Zhang, and A. Melis (1998). Photosystem-II repair and chloroplast recovery from irradiance stress: Relationship between chronic photoinhibition, light-harvesting chlorophyll antenna size and photosynthetic productivity in *Dunaliella salina* (green algae). *Photosynthesis Research* 56(2), 175–184.
- Olmos, J., J. Paniagua, and R. Contreras (2000). Molecular identification of *Dunaliella* sp. utilizing the 18S rDNA gene. *Letters in applied microbiology* 30(1), 80–4.
- Olson, R. J., D. Vaultot, and S. W. Chisholm (1985). Marine phytoplankton distributions measured using shipboard flow cytometry. *Deep Sea Research* 32(10), 1273–1280.
- Oren, A. (2010). Industrial and environmental applications of halophilic microorganisms. *Environmental Technology* 31(8-9), 825–834.
- Orosa, M., J. F. Valero, C. Herrero, and J. Abalde (2001). Comparison of the accumulation of astaxanthin in *Haematococcus pluvialis* and other green microalgae under n-starvation and high light conditions. *Biotechnology Letters* 23(13), 1079–1085.
- Orth, J. D., I. Thiele, and B. . Palsson (2010). What is flux balance analysis? *Nature Biotechnology* 28(3), 245–248.
- Packer, A., Y. Li, T. Andersen, Q. Hu, Y. Kuang, and M. Sommerfeld (2011). Growth and neutral lipid synthesis in green microalgae: A mathematical model. *Bioresource Technology* 102(1), 111–7.
- Pérez-Clemente, R., V. Vives, S. Zandalinas, M. López-Climent, V. Muñoz, and A. Gómez-Cadenas (2013). Biotechnological approaches to study plant responses to stress. *BioMed Research International* 2013, 10.
- Pick, U. (1999). *Dunaliella acidophila* - A most extreme acidophilic alga. Enigmatic microorganisms and life in extreme environments.
- Polle, J. E., K. K. Niyogi, and A. Melis (2001). Absence of lutein, violaxanthin and neoxanthin affects the functional chlorophyll antenna size of photosystem-II but not that of photosystem-I in the green alga *Chlamydomonas reinhardtii*. *Plant and Cell Physiology* 42(5), 482–91.

- Polle, J. E. W., D. Tran, and A. Ben-Amotz (2009). *History, Distribution, and Habitats of Algae of the Genus Dunaliella Teodoresco (Chlorophyceae)* (1 ed.), Book section 1-13. Enfield: Science Publishers.
- Quinn, J., L. de Winter, and T. Bradley (2011). Microalgae bulk growth model with application to industrial scale systems. *Bioresource Technology* 102(8), 5083–92.
- Rabbani, S., P. Beyer, J. Von Lintig, P. Hugueney, and H. Kleinig (1998). Induced β -carotene synthesis driven by triacylglycerol deposition in the unicellular alga *Dunaliella bardawil*. *Plant Physiology* 116(4), 1239–1248.
- Raue, A., C. Kreutz, T. Maiwald, J. Bachmann, M. Schilling, U. Klingmüller, and J. Timmer (2009). Structural and practical identifiability analysis of partially observed dynamical models by exploiting the profile likelihood. *Bioinformatics* 25(15), 1923–1929.
- Reijnders, M. J. M. F., B. M. Carreres, and P. J. Schaap (2015). Algal Omics: The functional annotation challenge. *Current Biotechnology* 4(4), 457–463.
- Reijnders, M. J. M. F., R. G. A. van Heck, C. M. C. Lam, M. A. Scaife, V. A. P. M. d. Santos, A. G. Smith, and P. J. Schaap (2014). Green genes: Bioinformatics and systems-biology innovations drive algal biotechnology. *Trends in Biotechnology* 32(12), 617–626.
- Research. Ph. D. thesis.
- Rubio, F. C., F. G. Camacho, J. M. Sevilla, Y. Chisti, and E. M. Grima (2003). A mechanistic model of photosynthesis in microalgae. *Biotechnology and bioengineering* 81(4), 459–73.
- Sanchez, J. F., J. M. Fernandez-Sevilla, F. G. Acien, M. C. Ceron, J. Perez-Parra, and E. Molina-Grima (2008). Biomass and lutein productivity of *Scenedesmus almeriensis*: Influence of irradiance, dilution rate and temperature. *Applied microbiology and biotechnology* 79(5), 719–29.
- Sanchez-Luna, L. D., R. P. Bezerra, M. C. Matsudo, S. Sato, A. Converti, and J. C. de Carvalho (2007). Influence of pH, temperature, and urea molar flowrate on *Arthrospira platensis* fed-batch cultivation: A kinetic and thermodynamic approach. *Biotechnology and Bioengineering* 96(4), 702–11.
- Schreiber, U. (1983). Chlorophyll fluorescence yield changes as a tool in plant physiology: I. The measuring system. *Photosynthesis Research* 4(4), 361–373.
- Schreiber, U., C. Klughammer, and J. Kolbowski (2011). High-end chlorophyll fluorescence analysis with the MULTI-COLOR-PAM. I. Various light qualities and their applications. *PAM Application Notes* 1, 1–21.
- Schuetz, R., L. Kuepfer, and U. Sauer (2007). Systematic evaluation of objective functions for predicting intracellular fluxes in *Escherichia coli*. *Molecular Systems Biology* 3, 119.
- Schuster, S., T. Dandekar, and D. A. Fell (1999). Detection of elementary flux modes in biochemical networks: A promising tool for pathway analysis and metabolic engineering. *Trends in Biotechnology* 17(2), 53–60.
- Schwender, J., C. Gemunden, and H. K. Lichtenthaler (2001). Chlorophyta exclusively use the 1-deoxyxylulose 5-phosphate/2-c-methylerythritol 4-phosphate pathway

- for the biosynthesis of isoprenoids. *Planta* 212(3), 416–23.
- Smith, D. R., R. W. Lee, J. C. Cushman, J. K. Magnuson, D. Tran, and J. E. W. Polle (2010). The *Dunaliella salina* organelle genomes: Large sequences, inflated with intronic and intergenic DNA. *BMC Plant Biology* 10.
- Srinivasan, S., W. R. Cluett, and R. Mahadevan (2015). Constructing kinetic models of metabolism at genome-scales: A review. *Biotechnology journal* 10(9), 1345–59.
- Stengel, D. B., S. Connan, and Z. A. Popper (2011). Algal chemodiversity and bioactivity: Sources of natural variability and implications for commercial application. *Biotechnology Advances* 29(5), 483–501.
- Steuer, R., H. Knoop, and R. Machne (2012). Modelling cyanobacteria: From metabolism to integrative models of phototrophic growth. *Journal of Experimental Botany* 63(6), 2259–2274.
- Tardif, M., A. Atteia, M. Specht, G. Cogne, N. Rolland, S. Brugiere, M. Hippler, M. Ferro, C. Bruley, G. Peltier, O. Vallon, and L. Cournac (2012). PredAlgo: A new subcellular localization prediction tool dedicated to green algae. *Molecular biology and evolution* 29(12), 3625–39.
- Thiele, I. and B. O. Palsson (2010). A protocol for generating a high-quality genome-scale metabolic reconstruction. *Nature Protocols* 5(1), 93–121.
- Thompson, P. A., P. J. Harrison, and J. N. C. Whyte (1990). Influence of irradiance on the fatty-acid composition of phytoplankton. *Journal of Phycology* 26(2), 278–288.
- Trinh, C. T., P. Unrean, and F. Srien (2008). Minimal *Escherichia coli* cell for the most efficient production of ethanol from hexoses and pentoses. *Applied and Environmental Microbiology* 74(12), 3634–43.
- Varela, J. C., H. Pereira, M. Vila, and R. Leon (2015). Production of carotenoids by microalgae: Achievements and challenges. *Photosynthesis Research*, 1–14.
- Varma, A. and B. O. Palsson (1994). Metabolic flux balancing: Basic concepts, scientific and practical use. *Nature Biotechnology* 12(10), 994–998.
- Veldhuis, M. J. W., G. W. Kraay, and K. R. Timmermans (2001). Cell death in phytoplankton: Correlation between changes in membrane permeability, photosynthetic activity, pigmentation and growth. *European Journal of Phycology* 36(2), 167–177.
- Vicker, M. G., J. Becker, G. Gebauer, W. Schill, and L. Rensing (1988). Circadian rhythms of cell cycle progress in the marine dinoflagellate *Gonyaulax polyedra*. *Chronobiology International* 5(1), 5–17.
- Vitova, M., J. Hendrychova, V. Cepak, and V. Zachleder (2005). Visualization of DNA-containing structures in various species of Chlorophyta, Rhodophyta and Cyanophyta using SYBR Green I dye. *Folia Microbiologica* 50(4), 333–340.
- Vo, T. and D. Tran (2014). Effects of salinity and light on growth of *Dunaliella* isolates. *Journal of Applied & Environmental Microbiology* 2(5), 208–211.
- Wagner, H., T. Jakob, and C. Wilhelm (2006). Balancing the energy flow from captured light to biomass under fluctuating light conditions. *New Phytologist* 169(1), 95–108.
- Wagner, H., Z. Liu, U. Langner, K. Stehfest, and C. Wilhelm (2010). The use of FTIR spectroscopy to assess quantitative changes in the biochemical composition of mi-

- croalgae. *Journal of biophotonics* 3(8-9), 557–66.
- Wang, L. and C. L. Weller (2006). Recent advances in extraction of nutraceuticals from plants. *Trends in Food Science & Technology* 17(6), 300–312.
- Webb, M. R. and A. Melis (1995). Chloroplast response in *Dunaliella salina* to irradiance stress - Effect on thylakoid membrane-protein assembly and function. *Plant Physiology* 107(3), 885–893.
- Wichuk, K., S. Brynjolfsson, and W. Fu (2014). Biotechnological production of value-added carotenoids from microalgae: Emerging technology and prospects. *Bioengineered* 5(3).
- Wilhelm, C., C. Büchel, J. Fisahn, R. Goss, T. Jakob, J. Laroche, J. Lavaud, M. Lohr, U. Riebesell, K. Stehfest, K. Valentin, and P. G. Kroth (2006). The regulation of carbon and nutrient assimilation in diatoms is significantly different from green algae. *Protist* 157(2), 91–124.
- Willemsen, A. M., D. M. Hendrickx, H. C. J. Hoefsloot, M. M. W. B. Hendriks, S. A. Wahl, B. Teusink, A. K. Smilde, and A. H. C. van Kampen (2015). MetDFBA: Incorporating time-resolved metabolomics measurements into dynamic flux balance analysis. *Molecular Biosystems* 11(1), 137–145.
- Winterbach, W., H. Wang, M. Reinders, P. Van Mieghem, and D. de Ridder (2011). Metabolic network destruction: Relating topology to robustness. *Nano Communication Networks* 2(23), 88–98.
- Wu, C., W. Xiong, J. Dai, and Q. Wu (2015). Genome-based metabolic mapping and ¹³C flux analysis reveal systematic properties of an oleaginous microalga *Chlorella protothecoides*. *Plant Physiology* 167(2), 586–99.
- Wu, H., A. von Kamp, V. Leoncikas, W. Mori, N. Sahin, A. Gevorgyan, C. Linley, M. Grabowski, A. A. Mannan, N. Stoy, G. R. Stewart, L. T. Ward, D. J. M. Lewis, J. Sroka, H. Matsuno, S. Klamt, H. V. Westerhoff, J. McFadden, N. J. Plant, and A. M. Kierzek (2016). MUFINS: Multi-formalism interaction network simulator. *Npj Systems Biology And Applications* 2, 16032.
- Xie, B., D. Stessman, J. H. Hart, H. Dong, Y. Wang, D. A. Wright, B. J. Nikolau, M. H. Spalding, and L. J. Halverson (2014). High-throughput fluorescence-activated cell sorting for lipid hyperaccumulating *Chlamydomonas reinhardtii* mutants. *Plant Biotechnology Journal* 12(7), 872–882.
- Xu, X. R., Z. Y. Zou, X. Xiao, Y. M. Huang, X. Wang, and X. M. Lin (2013). Effects of lutein supplement on serum inflammatory cytokines, ApoE and lipid profiles in early atherosclerosis population. *Journal of Atherosclerosis and Thrombosis* 20(2), 170–7.
- Yang, C., Q. Hua, and K. Shimizu (2000). Energetics and carbon metabolism during growth of microalgal cells under photoautotrophic, mixotrophic and cyclic light-autotrophic/dark-heterotrophic conditions. *Biochemical Engineering Journal* 6(2), 87–102.
- Zhang, J., Z. Sun, P. Sun, T. Chen, and F. Chen (2014). Microalgal carotenoids: Beneficial effects and potential in human health. *Food & Function* 5(3), 413–25.

Zhu, C. J. and Y. K. Lee (1997). Determination of biomass dry weight of marine microalgae. *Journal of Applied Phycology* 9(2), 189–194.

List of Figures

1.1. Schematic outline of the thesis	3
2.1. Carotenoid biosynthesis pathway in microalgae.	6
2.2. Overview of quenching mechanisms of carotenoid pigments.	7
2.3. Morphological changes in <i>D. salina</i> during carotenogenesis.	10
2.4. Microscopic pictures of carotenogenic and non-carotenogenic <i>D. salina</i> .	10
3.1. Measuring principle of flow cytometry.	14
3.2. Principle of PAM fluorometry.	16
4.1. Central carbon metabolism in <i>D. salina</i>	22
4.2. Photosynthesis-irradiance curve	28
4.3. Intracellular and extracellular effects in microalgal metabolism	30
4.4. Mathematical illustration of the DFBA workflow	31
5.1. Photobioreactor setup INFORS Labfors Lux and PSI FMT-150	34
5.2. Schematic view of INFORS Labfors Lux photobioreactor	35
5.3. Filtered carotenogenic and non-carotenogenic <i>D. salina</i> biomass	36
5.4. FTIR plate with blank and cell suspensions	39
6.1. Dynamics of cell density and pigment composition	44
6.2. Dynamics of biomass density and β -carotene density	45
6.3. Dynamics of chl <i>a/b</i> ratio and β -carotene/chl ratio	46
6.4. Relationship between cell granularity and β -carotene fraction	47
6.5. Dynamics of productivity and yield on light for biomass and pigments	48
6.6. Relationship between effective quantum yield and light intensity	50
6.7. Relationship between relative electron transport rate and light intensity	50
6.8. Photosynthetic performance to light intensity per cell (LL conditions) .	52
6.9. Photosynthetic performance to light intensity per cell (HL conditions) .	53
6.10. Photosynthetic performance to light intensity per cell (HL-ND conditions)	53
6.11. FTIR absorption spectra for standards and cells	55
6.12. FTIR absorption spectra under abiotic stress.	56
6.13. Macromolecular ratios in the inoculum and batch cultivations.	57
7.1. Dependency of $E_{X,dw}$ and ω_N on r_{Car}	62
7.2. Dependency of $E_{X,dw}$ and ω_N on μ_{max}	63
7.3. Dynamics of optical cross section of chl <i>a</i>	66

7.4.	Effect of stress type on β -carotene fraction, biomass and nitrogen density	68
7.5.	Effect of stress type on chlorophyll fraction and nitrogen quota	70
7.6.	Model validation for β -carotene fraction, biomass and nitrogen density	71
7.7.	Model validation for chlorophyll fraction and nitrogen quota	72
7.8.	Profile likelihood-based identifiability for all model parameters	73
8.1.	Network map of carbon core metabolism in the cytosol	78
8.2.	Network map of carbon core metabolism in the chloroplast	79
8.3.	Network map of carbon core metabolism in the mitochondrion	80
8.4.	Dynamics of β -carotene fraction, biomass and nitrogen density (DFBA)	86
8.5.	Dynamics of chlorophyll fraction and nitrogen quota (DFBA)	87
8.6.	Validation for β -carotene fraction, biomass and nitrogen density (DFBA)	88
8.7.	Validation for chlorophyll fraction and nitrogen quota (DFBA)	89
8.8.	Influence of nitrate density and feeding factor on growth and β -carotene	90
8.9.	Simulation results of the optimized fed-batch cultivation	91
8.10.	State space diagram of all cultivation experiments	93
8.11.	Simulation results of the continuous process at $3000 \mu\text{mol m}^{-2} \text{s}^{-1} \text{g}^{-1} \text{dw}$	94
8.12.	Simulation results of the continuous process at $1000 \mu\text{mol m}^{-2} \text{s}^{-1} \text{g}^{-1} \text{dw}$	95
9.1.	Relationship between ETR and light intensity in <i>D. parva</i>	100
9.2.	Correlation matrix for the biomass features of <i>D. salina</i> and <i>D. parva</i> . .	101
9.3.	Effect of stress type on β -carotene fraction, biomass and nitrogen density	102
9.4.	Effect of stress type on chlorophyll fraction and nitrogen quota	104
9.5.	Profile likelihood-based identifiability for all model parameters	105
S5.	Gating strategy for unstained cells	117
S6.	Calibration curves for FTIR analysis with respective standards	118
S1.	Dependency of $r_{N,\text{max}}$ on the remaining kinetic parameters for <i>D. salina</i>	125
S2.	Dependency of $K_{s,N}$ on the remaining kinetic parameters for <i>D. salina</i> .	126
S3.	Dependency of μ_{max} on the remaining kinetic parameters for <i>D. salina</i> .	126
S4.	Dependency of $K_{s,E}$ on the remaining kinetic parameters for <i>D. salina</i> .	127
S5.	Dependency of $K_{i,E}$ on the remaining kinetic parameters for <i>D. salina</i> .	127
S6.	Dependency of $E_{\text{car,crit}}$ on the remaining kinetic parameters for <i>D. salina</i>	128
S7.	Dependency of $r_{\text{car,E}}$ on the remaining kinetic parameters for <i>D. salina</i> .	128
S8.	Dependency of $r_{\text{car,N}}$ on the remaining kinetic parameters for <i>D. salina</i> .	129
S9.	Dependency of r_R on the remaining kinetic parameters for <i>D. salina</i> . .	129
S10.	Dependency of $r_{N,\text{max}}$ on the remaining kinetic parameters for <i>D. parva</i>	130
S11.	Dependency of μ_{max} on the remaining kinetic parameters for <i>D. parva</i> .	131
S12.	Dependency of $K_{s,E}$ on the remaining kinetic parameters for <i>D. parva</i> .	131
S13.	Dependency of $K_{i,E}$ on the remaining kinetic parameters for <i>D. parva</i> . .	132
S14.	Dependency of $E_{\text{car,crit}}$ on the remaining kinetic parameters for <i>D. parva</i>	132
S15.	Dependency of $r_{\text{car,E}}$ on the remaining kinetic parameters for <i>D. parva</i> .	133
S16.	Dependency of $r_{\text{car,N}}$ on the remaining kinetic parameters for <i>D. parva</i> .	133
S17.	Dependency of r_R on the remaining kinetic parameters for <i>D. parva</i> . . .	134
S1.	Network map of carbon core metabolism	144

List of Tables

2.1. Carotenoid content of different carotenoid-rich microalgae.	9
3.1. Fluorescent dyes for characterization of physiological properties.	15
3.2. Frequently used parameters in PAM analysis.	18
3.3. Band assignment for biomacromolecules in FTIR spectra of microalgae.	20
4.1. Existing metabolic networks for microalgae.	23
5.1. Reactor constants of INFORS Labfors Lux and PSI FMT-150	34
5.2. Standards for FTIR spectroscopy.	39
6.1. Overview of experimental conditions for batch cultures of <i>D. salina</i>	43
6.2. Performance of the batch cultivations	49
6.3. Overview of experimental conditions for PAM and FTIR.	49
6.4. Characteristic wavenumbers identified for <i>D. salina</i>	54
6.5. Comparison of FTIR with biochemical methods.	57
7.1. Summary of experimental conditions for model calibration.	60
7.2. Summary of biomass-specific parameters for <i>D. salina</i>	67
7.3. Summary of parameter values and confidence intervals for <i>D. salina</i>	67
8.1. Priority list order for the lexicographic linear programs	84
8.2. Biomass constants and parameter values for the DFBA model.	87
8.3. Performance of the fed-batch cultivation	92
8.4. Overview of exp. conditions for model-based continuous cultivations	92
8.5. Performance of the continuous cultivations	93
9.1. Size and weight comparison for <i>D. salina</i> and <i>D. parva</i>	99
9.2. Overview of experimental conditions for batch cultures of <i>D. parva</i>	99
9.3. Biotechnological performance of <i>D. parva</i> compared to <i>D. salina</i>	99
9.4. Summary of parameter values and confidence intervals for <i>D. parva</i>	104
S1. Emission ranges for the flow cytometric detector channels	116
S1. Overview of parameters from dynamic-kinetic model.	119
S2. Summary of biomass-specific parameters for <i>D. parva</i>	124
S1. List of reactions in the carbon core metabolism	135

S2. List of compounds in the carbon core metabolism.	141
--	-----

Publications and statements on authorship

Journal articles

M. Fachet, R. J. Flassig, L. Rihko-Struckmann, K. Sundmacher: A dynamic growth model of *Dunaliella salina*: Parameter identification and profile likelihood analysis, *Bioresource Technology*, 2014, 173C:21-31.

M. Fachet carried out the experiments, developed the model, analyzed the data and wrote the manuscript.

R. J. Flassig, **M. Fachet**, L. Rihko-Struckmann, K. Sundmacher: Robust process design for the bioproduction of β -carotene in green microalgae, *Computer Aided Chemical Engineering*, 2015, 37C:2117-2122.

M. Fachet formulated the model structure, analyzed the simulation results and wrote parts of the manuscript.

M. Fachet, D. Hermsdorf, L. Rihko-Struckmann, K. Sundmacher: Flow cytometry enables dynamic tracking of algal stress response: A case study using carotenogenesis in *Dunaliella salina*, *Algal Research*, 2016, 13:227-234.

M. Fachet carried out the experiments, analyzed the data and wrote the manuscript.

R. J. Flassig[†], **M. Fachet**[†], K. Höffner[†], P. I. Barton, K. Sundmacher: Dynamic flux balance modeling to increase the production of high-value compounds in green microalgae, *Biotechnology for Biofuels*, 2016, 9:165.

[†] Authors contributed equally.

M. Fachet carried out the experiments and wrote parts of the manuscript.

L. Rihko-Struckmann, M. Molnar, K. Pirwitz, **M. Fachet**, K. McBride, A. Zinser, K. Sundmacher: Recovery and separation of carbohydrate derivatives from the lipid extracted alga *Dunaliella* by mild liquefaction, *ACS Sustainable Chemistry & Engineering*, 2017, 5:588-595.

M. Fachet assisted in optimizing the experimental methods and revised the manuscript.

M. Fachet, R. J. Flassig, L. Rihko-Struckmann, K. Sundmacher: Carotenoid Production Process Using Green Microalgae of the *Dunaliella* Genus: Model-Based Analysis of Interspecies Variability, *accepted by Industrial & Engineering Chemistry Research*, 2017.

M. Fachet carried out the experiments, developed the model, analyzed the data and wrote the manuscript.

Conference proceedings

R. J. Flassig, **M. Fachet**, L. Rihko-Struckmann, K. Sundmacher: Robust process design for the bioproduction of β -carotene in green microalgae, *Proceedings of the 12th International Symposium on Process Systems Engineering and 25th European Symposium on Computer Aided Process Engineering*, Copenhagen, Denmark, 31 May - 4 June, 2015.

Conference talks and posters

M. Fachet, R. J. Flassig, D. Hermsdorf, L. Rihko-Struckmann, K. Sundmacher: Metabolic network construction and analysis in *Dunaliella salina*, *1st Young Algaeneers Symposium*, Wageningen, The Netherlands, 14 - 16 June, 2012. (Poster presentation).

M. Fachet, L. Rihko-Struckmann, K. Sundmacher: Fermentation of *Dunaliella salina* for β -carotene production: Modeling and optimization of bioreactor operation conditions, *9th European Congress of Chemical Engineering (ECCE) and 2nd European Congress of Applied Biotechnology (ECAB)*, The Hague, The Netherlands, 21 - 25 April, 2013. (Oral presentation).

M. Fachet, L. Rihko-Struckmann, K. Sundmacher: Analysis of cellular properties during carotenogenesis in *Dunaliella salina* using flow cytometry, *AlgnChem*, Montpellier, France, 31 March - 3 April, 2014. (Oral presentation).

M. Fachet, L. Rihko-Struckmann, K. Sundmacher: Analysis of cellular properties during carotenogenesis in *Dunaliella salina* using flow cytometry, *2nd Young Algaeneers Symposium*, Montpellier/Narbonne, France, 3 - 5 April, 2014. (Oral presentation).

M. Fachet, L. Rihko-Struckmann, K. Sundmacher: Biomass composition analysis of *Dunaliella salina* under carotenogenic conditions, *4th International Conference on Algal Biomass, Biofuels and Bioproducts*, Santa Fe, New Mexico, United States, 15 - 18 June, 2014. (Oral presentation).

M. Fachet, R. J. Flassig, L. Rihko-Struckmann, K. Sundmacher: Model-based process design for natural β -carotene: Accounting for parameter uncertainties and process design variabilities, *5th International Conference on Algal Biomass, Biofuels and Bioproducts*, Santa Diego, California, United States, 7 - 10 June, 2015. (Poster presentation).

M. Facht, L. Rihko-Struckmann, K. Sundmacher: Durchflusszytometrische Bioprozesskontrolle am Beispiel einer carotinoidbildenden Mikroalge, 8. *Bundesalgenstammtisch*, Garching, Germany, 7 - 8 September, 2015 and *Bioprocessing Days 2016*, Recklinghausen, Germany, 22 - 24 February, 2016. (Poster presentation).

K. Höffner, R. J. Flassig, **M. Facht**, S. Gladebeck, L. Rihko-Struckmann, K. Sundmacher: Model-based optimization of microalgal biorefineries by dynamic flux balance analysis (DFBA), *CAPE Forum 2016*, Sion, Switzerland, 30 March - 1 April, 2016. (Oral presentation).

R. J. Flassig, **M. Facht**, K. Höffner, K. Sundmacher: Dynamic flux balance modeling to increase the production of high-value compounds in green microalgae, *2nd Young Algaeneers Symposium and European Networks Conference on Algal and Plant Photosynthesis*, Qawra, Malta, 24 - 29 April, 2016. (Highlight talk and poster presentation).

Supervision of bachelor and master theses

1. T. Fries: *Analyse von Wachstumsraten und Biomassekomposition unter abiotischen Stressbedingungen in der halotoleranten Grünalge Dunaliella salina* (Bachelor thesis, 2012, Life Science Engineering)
2. M. Janasch: *Etablierung und Charakterisierung eines kontinuierlichen Fermentationsprozesses zur Induktion von Carotinoiden in Dunaliella salina* (Bachelor thesis, 2013, Biosystemtechnik)
3. J. Thormeier: *Metabolische Netzwerkanalyse des zentralen Kohlenstoffmetabolismus von Grünalgen mit dem CellNetAnalyzer* (Bachelor thesis, 2013, Biosystemtechnik)
4. J. Lärm: *Formulierung eines Fermentationsmodells für Biomassewachstum und Lipidakkumulation in Dunaliella salina* (Student research project, 2013, Systems Engineering and Engineering Cybernetics)
5. S. Gladebeck: *A dynamic growth model of Dunaliella salina: Simulation of continuous biomass growth with day-night light cycle* (Student research project, 2015, Systems Engineering and Engineering Cybernetics)
6. I. Harriehausen: *Analysis of Growth and Biomass-Composition of a Carotenoid Microalga in Batch Cultivations* (Bachelor thesis, 2015, Biosystemtechnik)
7. S. Gladebeck: *Modeling of Growth and Biomass composition of a carotenogenic microalga using Dynamic Flux Balance Analysis* (Master thesis, 2016, Systems Engineering and Engineering Cybernetics)

Curriculum Vitae

Personal Details

Name Melanie Facht
Date of birth 2 December 1986 in Leisnig
Address Turmschanzenstr. 17, 39114 Magdeburg

Profession

07/2011-03/2017 Max Planck Institute for Dynamics of Complex Technical Systems, Ph.D. student in the field of photobiotechnology within the Process Systems Engineering group supervised by Prof. Dr.-Ing. Kai Sundmacher and Dr. Liisa Rihko-Struckmann.
Thesis topic: *"Experimental and theoretical analysis of microalgal metabolism"*

Education

08/1998-06/2005 Martin-Luther-Gymnasium, Hartha
University Entrance Diploma
10/2005-06/2011 Otto von Guericke University, Magdeburg
Studies of Biosystems Engineering
10/2009-06/2011 Otto von Guericke University, Institute of Experimental Internal Medicine, Magdeburg
12/2010 Student Research Project
"Topoisomerase inhibitor-triggered nuclear shuttling of NF- κ B signaling components p65 and NEMO"
06/2011 Diploma Thesis
"Activation of IKK γ and RelA upon genotoxic stress"
06/2011 Degree: Diploma Engineer

Internship

03/2009-08/2009 Endress + Hauser Conducta, Waldheim
Internship
"Characterization of a microfluidic measuring module as a key component of a bioaffinity analyzer"